MODELLING DAMAGE FOR ELASTOPLASTICITY

A THESIS SUBMITTED TO
THE GRADUATE SCHOOL OF NATURAL AND APPLIED SCIENCES
OF
MIDDLE EAST TECHNICAL UNIVERSITY

BY

CELAL SOYARSLAN

IN PARTIAL FULFILLMENT OF THE REQUIREMENTS
FOR
THE DEGREE OF DOCTOR OF PHILOSOPHY
IN
CIVIL ENGINEERING

DECEMBER 2008

Approval of the thesis:

MODELLING DAMAGE FOR ELASTOPLASTICITY

submitted by **CELAL SOYARSLAN** in partial fulfillment of the requirements for the degree of
Doctor of Philosophy in Civil Engineering Department, Middle East Technical University by,

Prof. Dr. Canan Özgen
Dean, Graduate School of **Natural and Applied Sciences** _____

Prof. Dr. Güney Özcebe
Head of Department, **Civil Engineering** _____

Assoc. Prof. Dr. Uğurhan Akyüz
Supervisor, **Civil Engineering Dept., METU** _____

Prof. Dr. A. Erman Tekkaya
Co-supervisor, **Manufacturing Engineering Dept., Atılım** _____
University

Examining Committee Members:

Prof. Dr. Bilgin Kaftanoğlu
Manufacturing Engineering Dept., Atılım University _____

Assoc. Prof. Dr. Uğurhan Akyüz
Civil Engineering Dept., METU _____

Prof. Dr. Hakan Gür
Metallurgical and Materials Engineering Dept., METU _____

Assoc. Prof. Dr. Uğur Polat
Civil Engineering Dept., METU _____

Prof. Dr. Turgut Tokdemir
Engineering Sciences Dept., METU _____

Date: _____

I hereby declare that all information in this document has been obtained and presented in accordance with academic rules and ethical conduct. I also declare that, as required by these rules and conduct, I have fully cited and referenced all material and results that are not original to this work.

Name, Last Name: CELAL SOYARSLAN

Signature   :

ABSTRACT

MODELLING DAMAGE FOR ELASTOPLASTICITY

Soyarslan, Celal

Ph.D., Department of Civil Engineering

Supervisor   : Assoc. Prof. Dr. Uğurhan Akyüz

Co-Supervisor   : Prof. Dr. A. Erman Tekkaya

December 2008, 183 pages

A local isotropic damage coupled hyperelastic-plastic framework is formulated in *principal axes* where thermo-mechanical extensions are also addressed. It is shown that, in a functional setting, treatment of many damage growth models, including ones originated from phenomenological models (with formal thermodynamical derivations), micro-mechanical models or fracture criteria, proposed in the literature, is possible. *Quasi-unilateral damage evolutionary forms* are given with special emphasis on the feasibility of formulations in principal axes. Local integration procedures are summarized starting from a full set of seven equations which are simplified step by step initially to two and finally to one where different operator split methodologies such as elastic predictor-plastic/damage corrector (simultaneous plastic-damage solution scheme) and elastic predictor-plastic corrector-damage deteriorator (staggered plastic-damage solution scheme) are given. For regularization of the post peak response with softening due to damage and temperature, PERZYNA type viscosity is devised. Analytical forms accompanied with algorithmic expressions including the consistent material tangents are derived and the models are implemented as `UMAT` and `UMATHT` subroutines for ABAQUS/Standard, `VUMAT` subroutines for ABAQUS/Explicit and `UFINITE`

subroutines for MSC.Marc. The subroutines are used in certain application problems including numerical modeling of discrete internal cracks, namely chevron cracks, in direct forward extrusion process where comparison with the experimental facts show the predicting capability of the model, isoerror map production for accuracy assessment of the local integration methods, and development two novel necking triggering methods in the context of a damage coupled environment.

Keywords: continuum damage mechanics, ductile damage, finite elements, thermomechanics, extrusion cracks

ÖZ

ELASTOPLASTİSİTE İÇİN HASAR MODELLENMESİ

Soyarslan, Celal

Doktora, İnşaat Mühendisliğ Bölümü

Tez Yöneticisi : Doç. Dr. Uğurhan Akyüz

Ortak Tez Yöneticisi : Prof. Dr. A. Erman Tekkaya

Aralık 2008, 183 sayfa

İzotrop hasarla eşleşmiş yerel bir hiperelastik plastik çatı, termo-mekanik eklentilerle, asal eksenlerde formüle edilmiştir. Gösterilmiştir ki, fonksiyonel bir ortamda, fenomenolojik modelleri (termodinamik türetmeli), mikro-mekanik modelleri ya da kırılma kriterlerini orijin alan literatürde geçen bir çok hasar evrim modelini kullanmak olasıdır. *Yarı-tek yönlü hasar evrim formları*, asal eksenlerde formülasyonlarının elverişliliği işaret edilerek sunulmuştur. Lokal entegrasyon usulleri, elastik kestirimhasarlı plastik düzeltim (eş-zamanlı hasar ve plastisite çözüm metodu) ve elastik kestirim-plastik düzeltim-hasar hesabı (bindirmeli hasar ve plastisite çözüm metodu) gibi farklı operatör ayırma metodları da verilerek, yedi denklemden oluşan tam setin önce ikiye ve nihayetinde bire indirgenerek çözümüyle özetlenmiştir. Hasar ve termal etkiler nedeni ile yumuşamalı doruk sonrası tepkinin regülarizasyonunda PERZYNA tipi vizkozite kullanılmıştır. Analitik formlarla birlikte tutarlı malzeme tanjantlarını da içeren algoritmik ifadeler türetilmiş ve modeller ABAQUS/Standart için UMAT ve UMATHT, ABAQUS/Explicit için VUMAT ve MSC.Marc için UFINITE altyordamları olarak programlanmıştır. Altyordamlar, direkt ileriye ekstruzyonda, v-şeklinde kırık

da denilen, ayrık içsel kırıkların modellenmesi, ki deneysel sonuç karşılaştırmaları modelin kestirim kabiliyetini sergilemektedir, lokal entegrasyon yöntemlerinin kesinliğini değerlendiren eşhata haritasının oluşturulması, ve hasarla eşleşmiş bir ortamda iki yeni boyun verme tetikleyicisi metodun geliştirilmesini de içeren çeşitli uygulama problemlerinde kullanılmıştır.

Anahtar Kelimeler: sürekli ortamlar hasar mekaniği, sünek hasar, sonlu elemanlar, termo-mekanik, ekstruzyon kırıkları

I dedicate this thesis to my beloved grand mother Ayşe Turan.

ACKNOWLEDGMENTS

I would like to express my gratitude to my supervisors Assoc. Prof. Dr. Uğurhan Akyüz and Prof. Dr. -Ing. A. Erman Tekkaya. for their instructive comments in the supervision of the thesis.

I would like to express my special thanks and gratitude to Prof. Dr. Bilgin Kaftanoğlu, Prof. Dr. Turgut Tokdemir, Prof. Dr. Hakan Gür and Assoc. Prof. Dr. Uğur Polat for showing keen interest to the subject matter and accepting to read and review the thesis.

TABLE OF CONTENTS

LIST OF TABLES

TABLES

LIST OF FIGURES

FIGURES

CHAPTER 1

INTRODUCTION

1.1 Motivation

Disturbance of the material integrity in metal forming processes results in defected products. This, once seen in engineering structures under service loads, may result in catastrophic consequences. In the context of ductile fracture, material failure is a progressive process. This is to say, the soundness of the material under applied loads experiences a gradual reduction, where an initially intact material results in a ruptured one. Explanation of this complete history including the post cracking with propagation of occurred crack does not only constitute an academic motivation but also helps understanding the defected element behavior under service loads. It should also be noted that, although in metal forming crack propagation is of no importance, since a product with cracks has no use, there exist manufacturing technologies like machining and orthogonal cutting where the violation of the material integrity is intentionally introduced into the system.

Thus process design and life prediction of structural members requires a strong behavioral definition of the materials utilized. Since most engineering problems invariably include complexities that preclude use of analytical methods which result in closed form solutions, a rational definition of the material behavior does suffice only when accompanied with a numerical setup where the algorithmic forms makes the models accessible.

1.2 Aim and Scope

With this motivation, the aim of this study is to present a theoretical and numerical framework for ductile damage modeling for metal plasticity. The treatment is content with directional independence in material response which excludes any initial or deformation induced anisotropy. Besides it does not assume particular restrictions on the extent of strains. The theoretical side follows principles of thermodynamics, where purely mechanical (isothermal) and thermo-mechanical derivations are separately presented. Formulation of nonlinear isotropic hardening plasticity and combined nonlinear isotropic/linear kinematic hardening plasticity are given. As a post peak regularizer of the softening response, an over-stress type viscous formulation is discussed. The presentations are accompanied with intuitive application problems, involving those with discrete crack formations.

1.3 Modeling Material Weakening

Plasticity and damage are two softening mechanisms that differ on micro-mechanical foundations. The former entails crystal slip through dislocation movements. The latter, in the context of ductile damaging materials, requires a progressive deterioration process, which shows itself in three steps, namely nucleation, growth and coalescence of micro-voids. Nucleation of micro-voids results in free surface development and occurs around secondary phase particles or impurities with stress concentrations under plastic flow conditions by particle-matrix debonding, or by inclusion cracking. Positive hydrostatic stresses cause growth of nucleated and/or already existing micro-voids to decrease material homogenized stiffness and strength. Under increased loads the enlarged micro-voids tend to coalesce to form unified macro-crack (failure). This explains the fact that compressive stress fields promote deformation range whereas tri-axial stress fields lead premature cracks, see e.g. [149] and [142]. The steps involved in the deterioration process are illustrated in Figure 1.1. A broad review of governing mechanisms to give account for material deterioration can be found in [103].
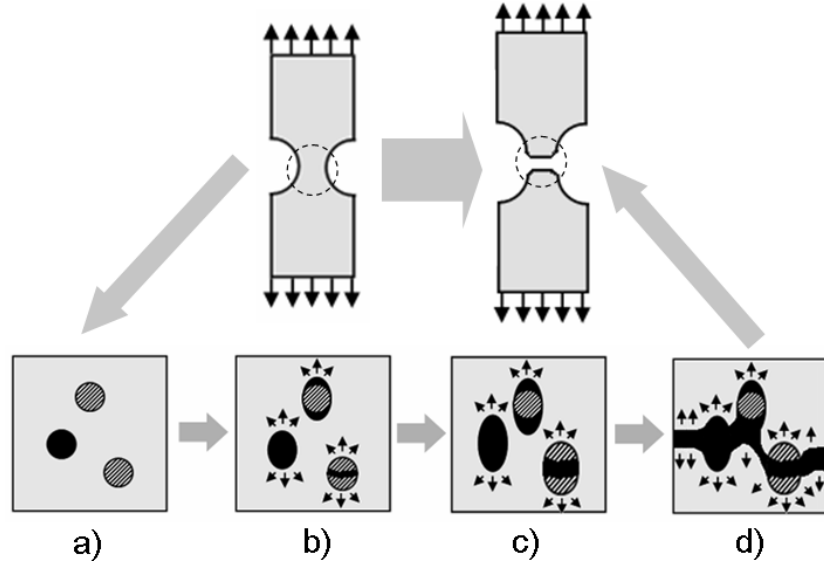
Figure 1.1: Progressive deterioration micro-mechanism depending on void nucleation, growth and coalescence.

The failure concept, which can be summarized as the complete loss of load carrying capacity, has been worked by three different approaches, which are fracture mechanics (FM), micro-based damage mechanics (MDM) and meso-based damage mechanics (i.e. continuum damage mechanics (CDM)). For an overview of the methods, the reader is referred to [24] and the references therein.

1.3.1 FM Models

FM takes into account an accumulated plastic work threshold for material failure. There are various models proposed in the literature, see e.g. [135] for OYANE criterion, [58] for FREUDENTHAL criterion, [46] for COCKROFT LATHAM criterion and finally [30] for BROZZO criterion, among others, which are listed in Table 1.1. On the table, $\boldsymbol{\sigma}$ represents the CAUCHY stress tensor whose maximum principal component is denoted by σ_1. The pressure is given by p. $\dot{\alpha}$ stands for the rate of equivalent plastic strain whereas A stands for a material parameter. B_1, B_2, B_3, B_4 represent material dependent fracture thresholds. According to the criteria, once the accumulated plastic work reaches one of these predefined critical values, fracture occurs.

Table 1.1: Certain fracture criteria.

Name	Equivalent plastic work	Threshold
OYANE	$\int \left[p / \sqrt{\boldsymbol{\sigma} : \boldsymbol{\sigma}} + A \right] \dot{\alpha} \, dt$	B_1
FREUDENTHAL	$\int \sqrt{\boldsymbol{\sigma} : \boldsymbol{\sigma}} \, \dot{\alpha} \, dt$	B_2
COCKROFT-LATHAM	$\int \sigma_1 \, \dot{\alpha} \, dt$	B_3
BROZZO	$\int 2 \, \sigma_1 / \left[3 \, (\sigma_1 - p) \right] \dot{\alpha} \, dt$	B_4

The computation of the given integrals is not coupled to deformation, thus may be explicitly computed. This uncoupled nature gives rise to practical implementation of the models into existing FE software without any effort. No additional equations to be satisfied incrementally/iteratively are introduced to the system, thus, mere burden becomes the trivial explicit integration of the plastic work, which provides algorithmic efficiency. Besides, the non-softening material behavior keeps the numerical setup well-posed. However, same uncoupled character constitutes the disadvantage as well. The deformation-damage uncoupling precludes mimicking the already mentioned *progressive* structure of the deterioration. In other words, throughout the deformation history, neither the load carrying capacity nor the stiffness of the material is lost up to rupture. This setting results in a binary material deterioration behavior, by which a material point is either intact or failed, which is not realistic on physical grounds.

1.3.2 MDM Models

MDM models are derived from analysis on isolated unit cells involving idealized defects as cracks, voids or second phase particles. A homogenization procedure is required to map gathered micro-mechanical behavior to continuum scale, by which it is possible to materialize the model in structural analysis. GURSON's damage model, [68], is a MDM model, based on a voided rigid plastic matrix. With the proposed modified plastic potential, the homogenized behavior stands for porous plasticity, where the physically obvious damage indicator variable is the void volume fraction (usually denoted by f). [186], modified this model to give account for the increase in the void growth rate with void coalescence, to create what is known today as GURSON-TVERGAARD-NEEDLEMAN model (hereafter GTN). Another MDM model, which is thermodynamically consistent and which is utilized largely in the literature can be given as ROUSSELIER model, [152]. The advantage of the MDM models are their clear

4

micro-mechanical motivations reflecting the complete physical phenomena. However, there are certain disadvantages noted in the literature. The determination of the material parameters is impractical [1]. Their primarily hydrostatic stress dependent structure cannot predict shear dominated failure, see e.g. [73]. [64] and more recently [126] constitute attempts to extent GURSON's damage model to shear-dominated failure. Although the shrinkage of the yield locus is reflected which results in the decrease in load carrying capacity with damage extent, the elastic stiffness degradation in unloading is not captured. Besides, the local conventional setting of MDM formulations give rise to spurious mesh dependence and nonphysical localization problems in numerical treatment of the post peak responses. Finally, the micro-mechanical construction of the formulation constitutes a barrier in transferability of the model to the materials having different micro-structures.

1.3.3 CDM Models

CDM, which constitutes the main subject matter of this thesis, making use of internal state variable theory of thermo-mechanics, solves the problem of material weakening with mathematical phenomenological constructs (i.e. damage variable) which stand for the internal variables responsible for irreversible micro-structural deterioration.

With its thermodynamic soundness and relative simplicity, the method has been extensively used to quantify many deterioration types such as elastic, plastic, brittle, ductile, creep and fatigue, for small and finite strains including directional, thermal and rate effects. Besides, nonlocal extensions based on integral averaging or gradient formulations have been proposed to cure the unphysical localization and pathological mesh dependency of the post peak response, in numerical simulations. The nature of the approach allows algorithmic treatment in a strain driven framework, which gives account for a convenient integration into existing nonlinear mechanical solvers, [35]. Such attempts, in the context of isotropic damage coupled finite plasticity, have been made by [165], [85], [86], [87], [181], [171], [61], [174], [107], [153]; and more recently with nonlocal extensions by [7], [5] and [116)]. Isotropic damage assumption takes at hand a randomly and statistically homogeneously distributed, shaped and oriented

---

[1] Calibration of material parameters are relatively easy for three parameter ROUSSELIER damage model.

micro-void cluster. This postulate of damage isotropy, has proved validity and efficiency for ductile damaging materials. In a general setting, distributed micro-cracks, i.e. damage, even in a homogeneous and isotropic body create induced anisotropic and inhomogeneous character of the overall response, [92]. For cases where the proportional loading conditions are violated, anisotropy is favored, [98]. Recently, in the finite strain context, thermodynamics based anisotropic formulations depending on multiplicative decomposition of metric transformation tensor are given in [31] and with nonlocal extensions in [32]. Frameworks with introduction of fictitious undamaged configurations are proposed by [117], [53] and [118] to resolve damage induced anisotropy. Another noteworthy framework, treating anisotropic (visco)damage coupled with (visco)plasticity and its nonlocal extensions can be found in [2] and [189], respectively. Recently, proposing functional forms for inelastic hardening variables in damage and plasticity, [190] resolves the coupled problem including directional effects.

The advantage of CDM is the existence of consistent derivation through thermodynamics of irreversible processes. Besides, these models are capable to reflect both the shrinkage of the admissible stress space and the elastic stiffness degradation with material deterioration. Like in the case of MDM models, this softening behavior in turn creates an ill-posed initial boundary value problem, with the loss of ellipticity for quasi-static cases, and loss of hyperbolicity for dynamic problems, where spurious mesh dependence and nonphysical localization problems are due for post peak responses.

The literature on CDM has reached to a mature level. Reader may refer to the texts of [98], [92], [169], and [99]. Additional references having chapters on the subject are [97], [50], [38] and [154].

1.3.3.1 Fundamental Hypotheses of Utilized Phenomenological Damage Models

In the current presentation, the formulations are based on the concept of effective stress and the principle of strain equivalence. In order to illustrate these members of the foundation, a geometrical insight into the meaning of the damage variable is possible by considering a one dimensional tensile test specimen which is represented

in two spaces one of which is physical and the other is fictitious, as given in Figure 1.2. Physical space stands for the actual case where the effect of micro-cracks and micro-voids persist, whereas the fictitious space is assumed to be defect-free.
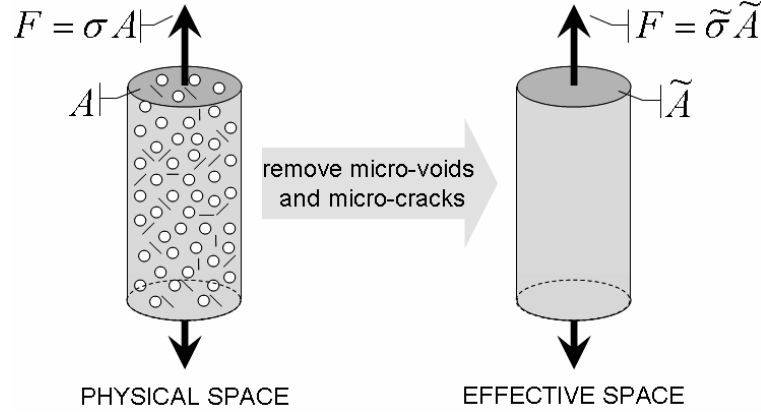
Figure 1.2: Effective stress concept.

Considering the cross section of the specimen, the nominal area, which takes place in the physical space, is represented by A, and the defect-free area, which takes place in the effective space, is represented by $\tilde{A}$. Once the damaged area, $A_D = A - \tilde{A}$, is scaled with A, one reaches an objective measure for damage, which verbally stands for the ratio of the damaged area to the total area, at the plane of interest,

$$D = \frac{A_D}{A}$$

with $D \in [0, 1]$, where the lower bound, $D = 0$, represents the intact material without any damage, and the upper bound, $D = 1$, represents complete rupture[2].

---

[2] A noteworthy point is that, although CDM provides a strong coupling environment where the progressive deterioration of the material is resolved, for high strength and low ductility materials (like high carbon steels), critical damage values (which denotes the local material failure) can be considerably small (D_{cr} can even be in the order of 0.05, see e.g. [188]. The micro-mechanical picture is in correlation to this fact, the critical void volume fraction for element failure is taken as $f = 0.05$ to $f = 0.2$, where $f = 1.0$ is never practically reached, [61]). This may lead to a FM-like uncoupled application. However, the model produced should be applicable to larger extent of materials together with less mathematical restrictions and provide soundness on physical grounds. Thus, in this study a fully coupled progressive deterioration mechanism is presented in chevron prediction.

The CAUCHY stress acting in the physical space is named as the nominal stress, whereas the effective CAUCHY stress, $\tilde{\boldsymbol{\sigma}}$, acts at the undefected material sub-scale, i.e. in the effective space. This phenomenological approach has the roots from the works of [88] and [144], where the creep rupture in metals is considered.

Once nominal-effective separation is introduced to the field variables, the construction of the constitutive setup in between dual forms constitutes the central problem. For this purpose, in the literature, certain equivalence principles, such as strain equivalence, stress equivalence and energy equivalence, are proposed. These have certain advantages and disadvantages over each-other, investigation of which is beyond the aim of the current work[3]. The strain equivalence principle, [95], as illustrated in Figure 1.3, states the equivalence of the strain under actual nominal stresses with the strain computed at the fictitious undamaged state under effective stresses. In other words, it assumes the validity of canonical constitutive forms, once the stress measure is selected in terms of the effective one.
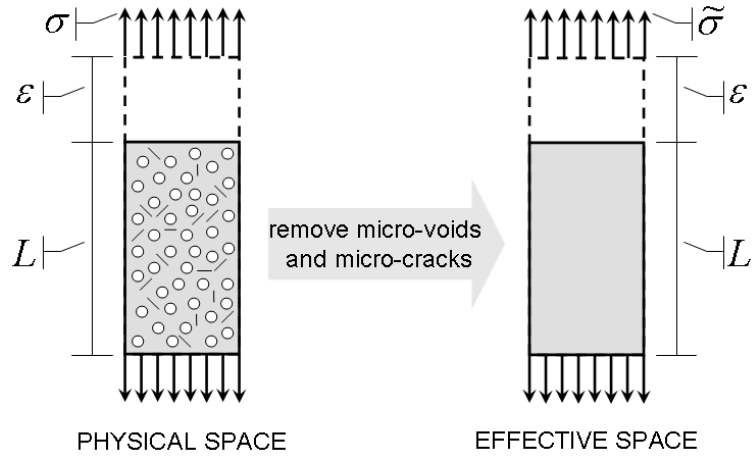
Figure 1.3: Principle of strain equivalence.

---

[3] We content with noting that, the principle of energy equivalence is especially utilized together with anisotropic damage modeling.

1.4   Organization of the Thesis

The thesis is organized in the form of a collection of the following self-contained chapters,

In Chapter 2, a local, isotropic damage coupled hyperelastic-plastic framework is formulated in principal axes using an eigenbases representation. It is shown that, in a functional setting, treatment of many damage growth models, including ones originated from phenomenological models (with formal thermodynamical derivations), micro-mechanics or fracture criteria, proposed in the literature, is possible. Quasi-unilateral damage evolutionary forms are given with special emphasis on the feasibility of formulations in principal axes. Moreover local integration procedures are summarized starting from a full equation set which are simplified step by step initially to two and finally to one. Also different operator split methodologies such as elastic predictor-plastic/damage corrector (simultaneous plastic-damage solution scheme) and elastic predictor-plastic corrector-damage deteriorator (staggered plastic-damage solution scheme) are given. Besides possible extensions to involve linear kinematic hardening are formulated in a thermodynamically consistent manner. To this end regarding consistent material moduli are derived. The model is implemented as a user defined material subroutine `UMAT` for ABAQUS/Standard and `UFINITE` MSC.Marc and tested for a set of sample problems evaluating the accuracy and predictive capabilities of the developed algorithms in a purely mechanical setting.

In Chapter 3, a thermo-mechanical framework for damage-coupled finite (visco) plasticity with nonlinear isotropic hardening is presented in an eigenvalue representation. The formulation makes use of the internal variable theory of thermodynamics and, following in the footsteps of [162], introduces inelastic entropy as an additional state variable. It is shown that, given a temperature dependent damage dissipation potential, the evolution of inelastic entropy assumes a split form relating to plastic and damage portions, respectively. For regularization of the doubly induced softening due to damage and temperature, a simple PERZYNA type viscosity is devised. Analytical forms, which provide an account of the effect of damage on heat conduction, and provide a thermo-mechanical framework accompanied by algorithmic forms for a staggered scheme based on the so-called isothermal split, are derived. A possible setting

for the adiabatic formulation is also presented. The model is implemented as `UMAT` and `UMATHT` subroutines for ABAQUS/Standard and used in a set of application problems, among which, two novel necking triggering methods (similar to the thermal and geometric imperfection methods) are introduced in the context of a damage coupled environment.

In Chapter 4, materializing Continuum Damage Mechanics (CDM), numerical modeling of discrete internal cracks, namely central bursts, in direct forward extrusion process is presented. For this purpose, a thermodynamically consistent LEMAITRE-variant damage model with quasi-unilateral evolution which is coupled with hyperelastic-plasticity is utilized. With `VUMAT` subroutine combined with an element deletion method and with a `UMAT` subroutine combined with an appropriately implemented ramped element degradation method, the model is used in the simulation of central crack formations in forward extrusion of 100Cr6 with single reduction and Cf53 with double reduction, using explicit and implicit FE schemes, respectively. On the physical side, relative predictive performances are observed. The investigations reveal that, in application of the quasi-unilateral conditions, the crack closure parameter has an indispensable effect on the damage accumulation zones by determining their internal or superficial character. Combining a suitably selected crack closure parameter with the element deletion procedure, discrete cracks are obtained. The periodicity of the cracks shows well accordance with the experimental facts. Besides, investigations on the effect of many process parameters on the final distribution of mechanical fields are presented. Moreover, it is demonstrated that, application of counter pressure introduces a marked decrease in the central damage accumulation, which in turn increases the formability of the material through keeping the tensile triaxiality in tolerable limits. It is also shown that, for a crack involving process, through systematic increase of the counter pressure, the crack sizes diminish; where at a certain level of counter pressure chevron cracks can be completely avoided.

Finally, Chapter 5 shortly summarizes the thesis work and addresses the future perspectives.

1.5 A Word on Notation

Throughout the thesis, following notations will be used. Assuming $\mathbf{a}$, $\mathbf{b}$, and $\mathbf{c}$ as three second order tensors, together with the EINSTEIN's summation convention on repeated indices, $\mathbf{c} = \mathbf{a} \bullet \mathbf{b}$ represents the product with $[\mathbf{c}]_{ik} = [\mathbf{a}]_{ij}[\mathbf{b}]_{jk}$. $d = \mathbf{a} : \mathbf{b}$ represents the inner product with $d = [\mathbf{a}]_{ij}[\mathbf{b}]_{ij}$ where d is a scalar. $\mathbb{E} = \mathbf{a} \otimes \mathbf{b}$, $\mathbb{F} = \mathbf{a} \oplus \mathbf{b}$ and $\mathbb{G} = \mathbf{a} \ominus \mathbf{b}$ represent the tensor products with $[\mathbb{E}]_{ijkl}=[\mathbf{a}]_{ij}[\mathbf{b}]_{kl}$, $[\mathbb{F}]_{ijkl}=[\mathbf{a}]_{ik}[\mathbf{b}]_{jl}$ and $[\mathbb{G}]_{ijkl}=[\mathbf{a}]_{il}[\mathbf{b}]_{jk}$, where $\mathbb{E}$, $\mathbb{F}$ and $\mathbb{G}$ represent fourth order tensors. $[\bigstar]^{t}$ and $[\bigstar]^{-1}$ denote the transpose and the inverse of $[\bigstar]$, respectively. DIV$[\bigstar]$, GRAD$[\bigstar]$ and div$[\bigstar]$, grad$[\bigstar]$ respectively designate the divergence and gradient operators with respect to the coordinates in the reference and current configurations. $[\bigstar]^{\text{sym}}$ and $[\bigstar]^{\text{skw}}$ are associated with the symmetric and skew-symmetric parts of $[\bigstar]$ respectively, with $[\bigstar] = [\bigstar]^{\text{sym}} + [\bigstar]^{\text{skw}}$.

CHAPTER 2

ISOTHERMAL FORMULATION

2.1 Introduction

The purpose of this Chapter is to present, in an EUCLIDEAN setting, a sound finite strain hyperelastic-plastic framework coupled with *local* isotropic damage, formulated in the principal axes. For this purpose, using the concepts of effective stress, [88] and [144], and principle of strain equivalence, [95], a strongly coupled plasticity and damage formulation is followed through a single yield function. With this, damage occurrence is strictly accompanied by plastic flow which is realistic for ductile damage.

The computational features of the current framework that are worth mentioning can be listed as follows:

- Presented framework in principal axes provides convenience in formulation of the damage coupled finite hyperelastic-plasticity reducing the tensorial differentials to simple scalar differentials, [80]. This simplicity is especially apparent in consistent linearization of the problem,

- The principal axes representation of the damage (pseudo)conjugate variable can readily be extended to give account for the formulation of the active-passive conditions, which serves handiness compared to tensorial representations,

- There are no particular restrictions on the forms of the governing functions of plasticity in terms of nonlinear isotropic hardening,

- With the proposed functional setting, there are also no particular restrictions on the damage evolutionary forms as well. Possible forms, that can be treated

in this setting, include damage models derived from various damage dissipation potentials. Besides, exploiting the proportionality of the plastic multiplier and the equivalent plastic strain rate for a class of plasticity models, without violating the second principle of thermodynamics, it is possible to expand the existing set of damage models together with a broad range of possible progressive deterioration formulations, including fracture criteria based and micro-mechanically based ones.

- The complete numerical setting is constructed on eigen-bases rather then eigenvectors, which is more efficient, as far as especially the fourth order tangent moduli computations are concerned, [119].

- The local integration schemes, which results in different operator-split methodologies such as elastic predictor-plastic/damage corrector type (simultaneous plastic/damage solution scheme) and elastic predictor-plastic corrector-damage deteriorator type (staggered plastic/damage solution scheme), are thoroughly presented. These schemes are supported with systematic reductions applied to the total number of governing equations at the local stress update problem.

This chapter has the following outline. Local constitutive forms are derived in § 2.2 in a thermodynamic consistency and a functional damage rate form, which unifies the ductile damage models utilized in the literature, is proposed. In § 2.2.3, a model problem with J_2 plasticity and a LEMAITRE variant damage model is presented together with unilateral damage evolutionary forms formulated in principal stress space. Numerical aspects, including the algorithmic forms and the consistent tangent moduli are given in § 3.3. The example problems take place in § 2.4.

2.2 Theory

2.2.1 Multiplicative Factorization

With reference to Figure 2.1, let $\mathbf{x} \in \mathbb{R}^3$ and $\mathbf{X} \in \mathbb{R}^3$ designate the positions of the particle in the current configuration, $\mathfrak{B} \subset \mathbb{R}^3$, and the reference configuration, $\boldsymbol{\varphi}(\mathfrak{B}) \subset \mathbb{R}^3$, respectively. $\mathbf{F}$ is the deformation gradient via $\mathbf{F} = \partial_{\mathbf{X}} \mathbf{x}$. The motion $\boldsymbol{\varphi}(\mathbf{X}, t)$:

$\mathfrak{B} \times \mathbb{R} \to \mathbb{R}^3$ is responsible for the mapping $\mathbf{x} = \boldsymbol{\varphi}(\mathbf{X}, t)$.
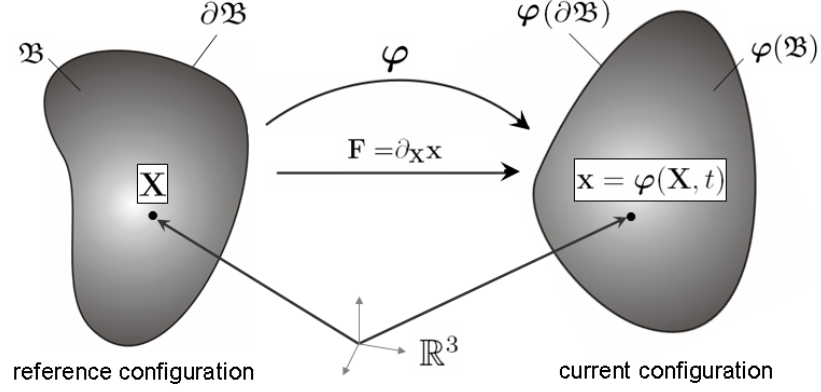
Figure 2.1: Description of motion and configurations.

The multiplicative framework, according to the kinematics of [94], is micro-mechanically justified in [11] for single crystals, where the same setup preserves validity for the use together with the macroscopic phenomenological theory of polycrystalline media due to similarity of deformation mechanisms between single and polycrystals, [140]. Multiplicative kinematics postulates the local multiplicative decomposition of the deformation gradient into elastic and plastic portions as [1],

$$\mathbf{F} = \mathbf{F}^e \bullet \mathbf{F}^p. \tag{2.1}$$

The illustration of this decomposition, together with valid EULERIAN and LAGRANGIAN strain measures is given in Figure 2.2. The local character of this factorization is reflected by the circles which represent the neighborhood of the regarding placements.

---

[1]   Arguments on the non-uniqueness of this decomposition, stemming from the arbitrariness of the intermediate configuration, can be found in e.g. [50, p. 398], [106, pp. 455–456] and [163, pp. 337–338] among others. The definition of proper state variables to give account for an appropriate finite strain multiplicative framework, supplying the invariance requirement, is a rather much debated issue and it is beyond the scope of the current study. Here, merely, the exploitation of [163, pp. 337–338] is followed. Accordingly, together with the isotropy condition the orientation of the intermediate configuration is irrelevant. Thus the non-uniqueness of the decomposition does not arise as a problem in this context and does not affect the derivations once the stored energy is constructed in terms of $\mathbf{b}^e$. A recent investigation on the internal dissipation inequalities for finite strain constitutive laws together with their theoretical and numerical consequences is given in [102].
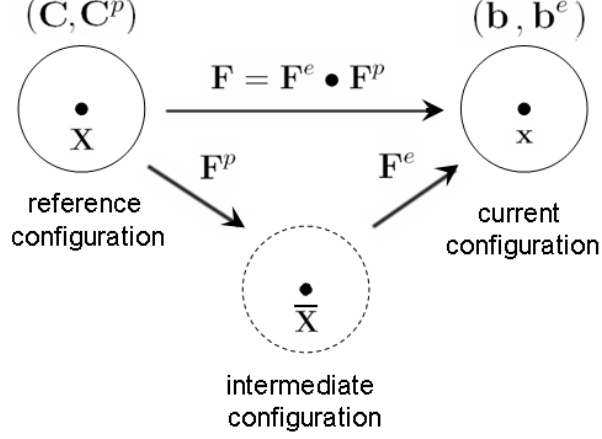
Figure 2.2: Multiplicative kinematics of LEE.

For numerical modeling of this formulation, to give account for finite strain elasto-plastic formulation, see e.g. [158], [159], [161] and [164] among others. The principal axes formulation of finite (visco)plasticity, in manifold and EUCLIDEAN settings[2], can be found in [79], [80], [81] and the references therein.

2.2.2 Thermodynamic Framework

In coupling isotropic damage with plasticity using multiplicative kinematics, it is started with the definition of free energy potentials, where isotropic hardening plasticity is taken into account only. Expansion of the current setting to kinematic hardening is given in the following pages. Merging the finite strain plasticity framework of [163] and thermodynamics of internal variables, [98], in definition of damage including processes, an additively decoupled total free energy, Ψ, in terms of elastic and isotropic hardening plastic portions, i.e. Ψ^e and $\Psi^{p,iso}$, respectively, is selected as follows,

$$\Psi(\mathbf{b}^e, \alpha, D) = \Psi^e(\mathbf{b}^e, D) + \Psi^{p,iso}(\alpha), \text{ with } \Psi^e(\mathbf{b}^e, D) = (1 - D)\,\tilde{\Psi}^e(\mathbf{b}^e). \qquad (2.2)$$

In Equation 2.2, $\mathbf{b}^e$ and α denote the elastic left CAUCHY-GREEN deformation tensor and the isotropic hardening (strain like) internal variable, respectively. $D \in [0, 1]$,

---

[2] Advantage of a manifold formalism, together with a coordinate free representation, where the framework is equipped with a metric, is obvious (e.g. for space curved membranes and shells). EU-CLIDEAN setting, where 3D, 2D plane stress, plane strain and axi-symmetric formulations of continuum are due, constitutes a particular choice of coordinate representation where the metric boils down to a unit tensor.

represents the isotropic damage variable and has a clear geometrical definition as the damaged area density at the plane of attention, [88]. Effective elastic potential, i.e. $\tilde{\Psi}^e(\mathbf{b}^e)$, is the free elastic energy of the fictitious undamaged continuum. In this setting damage is coupled to elasticity with state coupling.

In pure local mechanical form, a non-negative dissipation, which is the difference between the local stress power and the local rate of change of free energy, according to the second principle of thermodynamics, can be set as follows,

$$\Omega = \tau : \mathbf{d} - \underbrace{\{\partial_t \Psi^e + \partial_t \Psi^{p,iso}\}}_{=\partial_t \Psi} \geq 0, \tag{2.3}$$

with $\partial_t [\bigstar] := \partial [\bigstar] / \partial t$, and $\mathbf{d} := \mathrm{sym}[\mathbf{l}]$ representing the rate of deformation tensor which is the work conjugate of the KIRCHHOFF stress tensor, where $\mathbf{l} := \partial_t \mathbf{F} \bullet \mathbf{F}^{-1}$ denotes the spatial velocity gradient. (2.3) gives the state equations between dual variables, after proper modifications,

$$\tau = 2(1-D)\partial_{\mathbf{b}^e}\tilde{\Psi}^e \bullet \mathbf{b}^e, \tag{2.4}$$

$$q = -\partial_\alpha \Psi = -\partial_\alpha \Psi^{p,iso}, \tag{2.5}$$

$$Y^d = -\partial_D \Psi = \tilde{\Psi}^e. \tag{2.6}$$

where, q is responsible for isotropic hardening, in the form of yield locus expansion, and Y^d is the thermodynamically formal damage conjugate variable, in the form of the elastic strain energy energy release rate. This form is in accordance with the canonical LEMAITRE damage model. Using the effective KIRCHHOFF stress definition as, $\tilde{\tau} = \tau/(1-D)$, it is seen that, due to the strain equivalence principle, the effective stresses do not depend explicitly on D. Substituting (2.4), (2.5) and (2.6) in (2.3), the following dissipation potential expression is carried out,

$$\Omega = -\tau : [\frac{1}{2}\pounds_v\mathbf{b}^e \bullet \mathbf{b}^{e,-1}] + \underbrace{[-\partial_\alpha \Psi^{p,iso}]}_{=:q} \partial_t\alpha + \underbrace{[-\partial_D \Psi]}_{=:Y^d} \partial_t D, \tag{2.7}$$

where $\pounds_v[\bigstar]$ stands for the objective LIE derivative of $[\bigstar]$, [109]. The evolutionary forms are defined postulating a combined loading function, in an additively decoupled combination of the plastic potential, i.e. $\tilde{\phi}$, and a damage dissipation potential, i.e. ϕ^d,

$$\phi^t(\tau, q, Y^d; \alpha, D) = \tilde{\phi}(\tilde{\tau}, q) + \phi^d(Y^d; \alpha, D). \tag{2.8}$$

16

The plastic flow is physically possible at undamaged material sub-scale, which corresponds to the formulation of $\tilde{\phi}$ in the effective KIRCHHOFF stress space. Following the hypothesis of generalized standard materials, which proposes the existence of normality rules, [111], one derives the plastic flow rule and the rate expressions for α and D as,

$$\pounds_v \mathbf{b}^e = -2 \frac{\dot{\gamma}}{(1-D)} \partial_{\tilde{\tau}} \tilde{\phi} \bullet \mathbf{b}^e, \qquad (2.9)$$

$$\partial_t \alpha = \dot{\gamma} \, \partial_q \tilde{\phi}, \qquad (2.10)$$

$$\partial_t D = \dot{\gamma} \, \partial_{Y^d} \phi^d, \qquad (2.11)$$

which are conventional, associative evolutionary rules. In the following, plastic isotropic hardening and many damage softening forms are unified within respective functional settings.

2.2.2.1 Functional Isotropic Hardening Forms

Selection of the form for the plastic potential will naturally yield a set of state equations for isotropic hardening plasticity. For (2.5), a generalized function, $K'(\alpha) := -\partial_\alpha \Psi^{p,iso}$ with $q = K'(\alpha)$, can be defined using various forms proposed in the literature as given in Table 2.1.

Table 2.1: Plasticity isotropic hardening models in the functional setting.

ID	Name	$K'(\alpha)$
A.	Linear	$K \alpha$
B.	Saturation	$K \alpha + (\tau_\infty - \tau_0)(1 - \exp[-\delta \alpha])$
C.	SWIFT	$\tau_0 [(c + \alpha) - 1]$
D.	RAMBERG-OSGOOD	$K \alpha^n$
E.	Logarithmic	$\tau_0 [\ln(c + \alpha) - 1]$

On the table, K stands for the linear hardening parameter, whereas τ_0 and τ_∞ represent yield stress and saturation stress, respectively. δ and c constitute other material constants.

2.2.2.2 Functional Damage Rate Forms

Following thermodynamics of internal variables, and using the effective stress concept, strain equivalence principle, state coupling with elasticity and kinematic coupling with plasticity, different isotropic damage evolutionary models can be postulated proposing different damage dissipation potentials, i.e. ϕ^d. Eventual integration of the derived rate forms supplies diverse patterns for damage curves with increasing plastic strain. Together with proposing an exponential ductile continuum damage model, [39] presents a comparative study showing relative performances of some damage models utilized in literature. The models such as LEMAITRE damage model, [96], TAI's damage model, [182], CHANDRAKANTH and PANDEY's damage model, [39] and [40], are capable of reflecting concave-up type damage evolution with plastic strain. On the other hand, there are more general damage models, by taking into account the dependence of damage dissipation potential on equivalent plastic strains, give rise to a potential of mimicking a larger range of nonlinear damage evolutionary forms, ranging from concave-down to concave-up. The model of TIE-JUN, [184], and the model of BONORA, [23], later validated in [24] for low alloy steels under various triaxialities and in [25] for ferritic steels, are of this kind. [23] shows that for Al2024 and Al-Li alloys, where the damage evolution rate is dominated by the nucleation process, which includes nucleation of multiple voids, damage accumulation patterns other than concave-up are observed.

Derivation of a dissipation potential may not seem to be an easy task. Without formally tracking the scheme given in § 2.2.2, a consistent definition of damage rate, which does not violate the CLAUSIUS DUHEM inequality, is possible (i.e. no damage healing, $\dot{D} > 0$). This gives rise to a broad range of progressive damage evolutionary forms such as the three invariant damage model, given in [97], also used in [155] for chevron predictions in cold axi-symmetric extrusion or those based on fracture criteria or some micro-mechanical damage models. An example for the fracture criteria based CDM model may be given as the triaxiality dependent damage model of [63], also used in [116)], which proposes the progressive deterioration counterpart of the OYANE's ductile fracture criterion originally proposed in [136]. For this class of models, as progressive counterparts of accumulated plastic work dependent models,

it is possible to exploit FREUDENTHAL criterion, [58], COCKROFT LATHAM criterion, [46], or BROZZO criterion, [30]. The phenomenological CDM version of the micro-mechanically based void growth model of [149], given in [65] and also used in [51], constitutes an example for the micro-mechanically based CDM model.

The possibility of collecting the mentioned damage forms in a unified framework, together with a functional setting, suitable for the current finite plasticity in principal axes, forms the main motivation of this section. This has the apparent advantage of robust implementation of a user defined material routine for a broad range of damage models with minimum effort.

To set the stage, in the internal variable setting, damage growth models are postulated to have the following generalized functional form, without specifying any particular damage potential, i.e. ϕ^d,

$$\dot{D} = f(\boldsymbol{\tau}; \boldsymbol{\xi}, D), \tag{2.12}$$

where $\boldsymbol{\xi}$ represents the vector of hardening internal variables (possibly together with their rates) in the form of scalars/tensors (e.g. isotropic/kinematic hardening variables respectively). In the present strong plastic-damage coupled environment, in the absence of kinematic hardening, following modification of (2.12) holds, making use of the proportionality of $\dot{\gamma}$ and $\dot{\alpha}$,

$$\dot{D} = \dot{\gamma}\, g(Y; \alpha, D), \text{ with } Y = Y(\tilde{\tau}). \tag{2.13}$$

Additional function Y may seem superfluous, however the form (2.13) is proposed to catch an accordance with the thermodynamically formally derived damage rate form given in (2.11), together with $g = \partial_{Y^d}\phi^d / \partial_q \tilde{\phi}$, and $Y = Y^d$. Hence (2.13) covers all thermodynamically consistent damage models where $\phi^d = \phi^d(Y^d; \alpha, D)$, including those mentioned at the beginning of the section. Moreover, (2.13) may emerge as many functional forms in Y, where Y, an isotropic function of $\tilde{\tau}^3$, is not necessarily a formal damage work conjugate variable[4]. Table 2.2 lists some of the damage growth rules used in the literature in the context of ductile damage mentioned in the previous paragraphs, which are modified to fit (2.13), in the current finite strain framework. Model E constitutes a generalization of the model proposed in [65]. The

---

[3] Thus, Y can be represented in terms of principal stresses, i.e. $\tilde{\tau}_1, \tilde{\tau}_2, \tilde{\tau}_3$, and it is feasible to be tackled in a principal axes formulation.
[4] Y, where $Y \neq -\partial_D\Omega$, is named as damage pseudo-conjugate variable.

components $\tilde{p}$, $\tilde{\tau}_1$ and $\tilde{\tau}_{eq}$ represent the effective KIRCHHOFF type pressure, maximum principal KIRCHHOFF stress and equivalent VON MISES stress respectively. All the other variables except for Y, α and D refer to the appropriate material parameters defined in the original references.

2.2.3 Application to A Model Problem

2.2.3.1 Spectral Representations

Starting with, the link between the tensorial forms and the principal values are constructed through the following spectral decompositions,

$$\mathbf{b}^e = \sum_{A=1}^{3} b_A^e \, \mathbf{m}^A, \ \ \boldsymbol{\epsilon}^e = \sum_{A=1}^{3} \epsilon_A^e \, \mathbf{m}^A, \ \ \boldsymbol{\tau} = \sum_{A=1}^{3} \tau_A \, \mathbf{m}^A, \ \ \mathbf{s} = \sum_{A=1}^{3} s_A \, \mathbf{m}^A, \qquad (2.14)$$

where $\boldsymbol{\epsilon}^e$ denotes the elastic logarithmic strain tensor and $\mathbf{s}$ represents the deviatoric KIRCHHOFF stress tensor together with the respective eigenvalues (principal values) as ϵ_A^e and s_A. Thanks to isotropy, among the tensors given in (2.14), identical eigen-bases, i.e. $\mathbf{m}^A = \boldsymbol{\nu}^A \otimes \boldsymbol{\nu}^A$, are shared, where $\boldsymbol{\nu}^A$ represents the corresponding eigenvectors with $(A = 1, 2, 3)$. The principal values of the logarithmic elastic strains are defined in terms of elastic principal stretches, i.e. λ_A^e, as, $\epsilon_A^e = \log[\lambda_A^e]$. The deviatoric portion of $\lambda_A^e = \sqrt{b_A^e}$ and ϵ_A^e are represented by $\bar{\lambda}_A^e$ and $\bar{\epsilon}_A^e$. respectively.

In what follows, the presented framework is specialized for a specific model including a hyperelastic potential quadratic in logarithmic elastic strains represented by principal stretches, VON MISES plasticity represented in principal effective stress space and a quasi-unilaterally evolving LEMAITRE variant damage model. Initially the derivations are made for mere isotropic hardening plasticity. Formulations for kinematic hardening follow for the sake of completeness.

Table 2.2: Damage models in the functional setting.

ID	Reference	$g = g(Y; \alpha, D)$	$Y = Y(\tilde{\tau})$
A.	Lemaitre (1985)	$(Y/S_0)^s$	$Y^d(\tilde{\tau})$
B.	Lemaitre and Chaboche (1990)	$(Y/S_0)^s/(1-D)^b$	$\alpha_1 \langle \tilde{p} \rangle + \alpha_2 \langle \tilde{\tau}_1 \rangle + (1 - \alpha_1 - \alpha_2) \tilde{\tau}_{eq}$
C.	Tai (1990)	$D(Y/S_0)$	$Y^d(\tilde{\tau})$
D.	Tie-Jun (1990)	$(Y/S_0)\, 1/[(1 - \alpha/\alpha_{cr})^{(1-b)} \alpha^{(2/n)}]$	$Y^d(\tilde{\tau})$
E.	Gunawardena et al.(1991)	$(m_1 + m_2 D) \exp[(3/2) Y]$	$\langle \tilde{p}/\tilde{\tau}_{eq} \rangle$
F.	Chandrakanth and Pandey (1993)	$(Y/S_0) [1/(1-D)^n - (1-D)]$	$Y^d(\tilde{\tau})$
G.	Dhar et al. (1996)	$a_0 + (a_1 + a_2 D) Y^S/(1-D)^q$	$Y^d(\tilde{\tau})$
H.	Bonora (1997)	$(Y/S_0) (D_{cr} - D)^{(q-1/q)}/[(1-D) \alpha^{(2+n)/n}]$	$Y^d(\tilde{\tau})$
I.	Goijaerts et al.(2001)	$\langle 1 + aY \rangle \alpha$	$\tilde{p}/\tilde{\tau}_{eq}$

2.2.3.2 Free Energies and Regarding State Laws

For isothermal conditions, one postulates the following deviatoric volumetric split for the effective elastic potential,

$$\tilde{\Psi}^e(\mathbf{b}^e) := \tilde{\Psi}^{e,vol}(J^e) + \tilde{\Psi}^{e,dev}(\bar{\lambda}^e_A), \ (A = 1, 2, 3), \tag{2.15}$$

where the frame invariance lets one use the principals of the tensor arguments in representation of the isotropic functions,

$$\tilde{\Psi}^{e,vol}(J^e) \ := \ \frac{1}{2} H \log[J^e]^2, \tag{2.16}$$

$$\tilde{\Psi}^{e,dev}(\bar{\lambda}^e_A) \ := \ \mu \left(\log[\lambda^e_1]^2 + \log[\lambda^e_2]^2 + \log[\lambda^e_3]^2\right)$$

$$= \ \mu \left(\bar{\epsilon}^{e,2}_1 + \bar{\epsilon}^{e,2}_2 + \bar{\epsilon}^{e,2}_3\right). \tag{2.17}$$

This quadratic form, although preserves validity for a large class of materials up to moderately large deformations [3], [4], does not satisfy the polyconvexity condition [102]. For the plastic portion, following isotropic hardening potential is common which is associated with the combined linear and saturation type hardening,

$$\Psi^{p,iso}(\alpha) := \frac{1}{2} K \, \alpha^2 + (K_\infty - K_0) \, (\delta + \exp[-\delta\alpha]/\delta). \tag{2.18}$$

Accordingly, one finds the following state equation for τ,

$$\tau \ = \ (1 - D)[\underbrace{H\{\mathrm{tr}[\epsilon^{\mathbf{e}}]\}}_{=:\tilde{p}} \mathbf{1} + \underbrace{2\mu \, \bar{\epsilon}^e}_{=:\tilde{\mathbf{s}}}], \tag{2.19}$$

where $\tilde{p} = (\tilde{\tau}_1 + \tilde{\tau}_2 + \tilde{\tau}_3)/3$. One also may derive,

$$q \ = \ K \, \alpha + (K_\infty - K_0) \, (1 - \exp[-\delta\alpha]), \tag{2.20}$$

$$Y^d \ = \ \tilde{\Psi}^{e,vol}(J^e) + \tilde{\Psi}^{e,dev}(\bar{\lambda}^e_A). \tag{2.21}$$

2.2.3.3 Dissipation Potentials and Regarding Evolutionary Forms

The definition of the yield potential, which is of VON MISES type, is made in the effective KIRCHHOFF stress space in terms of the principal values of the effective KIRCHHOFF stresses, as,

$$\tilde{\phi}(\tilde{\tau}_A, q) := \sqrt{\frac{2}{3}} \, (\tilde{\tau}_1^2 + \tilde{\tau}_2^2 + \tilde{\tau}_3^2 - \tilde{\tau}_1 \, \tilde{\tau}_2 - \tilde{\tau}_1 \, \tilde{\tau}_3 - \tilde{\tau}_2 \, \tilde{\tau}_3)^{\frac{1}{2}} - \sqrt{\frac{2}{3}} \, y(q) \leq 0, \tag{2.22}$$

where $y(q) = (\tau_0 + q)$ represents the hardening/softening function for isothermal conditions, and τ_0 is the initial yield stress of the virgin material. Using this weakly[5] coupled potential, the expressions for $\partial_{\tilde{\tau}} \tilde{\phi}$ and $\partial_q \tilde{\phi}$, taking place in (2.9) and (2.10) respectively, can be derived as follows,

$$\partial_{\tilde{\boldsymbol{\tau}}} \tilde{\phi} = \sum_{A=1}^{3} \tilde{n}_A \, \boldsymbol{\nu}^A \otimes \boldsymbol{\nu}^A \quad \Rightarrow \quad \pounds_v \mathbf{b}^e = -2 \, \frac{\dot{\gamma}}{(1-D)} (\sum_{A=1}^{3} \tilde{n}_A \, \boldsymbol{\nu}^A \otimes \boldsymbol{\nu}^A) \bullet \mathbf{b}^e, \quad (2.23)$$

$$\partial_q \tilde{\phi} = \sqrt{\frac{2}{3}} \quad \Rightarrow \quad \partial_t \alpha = \dot{\gamma} \sqrt{\frac{2}{3}}, \quad (2.24)$$

where $\tilde{n}_A = \partial_{\tilde{\tau}_A} \tilde{\phi} = s_A / \sqrt[2]{s_1^2 + s_2^2 + s_3^2}$. Pay attention to the fact that the eigen-bases for the effective and the homogenized stresses are equivalent, i.e. $\mathbf{m}^A = \boldsymbol{\nu}^A \otimes \boldsymbol{\nu}^A \equiv \tilde{\mathbf{m}}^A = \tilde{\boldsymbol{\nu}}^A \otimes \tilde{\boldsymbol{\nu}}^A$.

2.2.3.4 A Lemaitre Variant Damage Model

For the damage evolutionary form, preserving generality $g(Y; \alpha, D)$ with $Y = Y^d$, i.e. the formal damage conjugate variable defined in (2.6), is selected, as in the case of LEMAITRE damage model. (2.21), which is given in elastic logarithmic strains, can be reformulated in the effective principal KIRCHHOFF stress space together with (2.19), to give $Y^d(\tilde{\tau}_A)$, $(A = 1, 2, 3)$ as follows,

$$Y^d(\tilde{\tau}_A) = \frac{1+\nu}{2E} \left(\tilde{\tau}_1^2 + \tilde{\tau}_2^2 + \tilde{\tau}_3^2 \right) - \frac{\nu}{2E} \left(\tilde{\tau}_1 + \tilde{\tau}_2 + \tilde{\tau}_3 \right)^2, \quad (2.25)$$

or shortly

$$Y^d(\tilde{\tau}_A) = \frac{1+\nu}{2E} \left(\tilde{\tau}_1^2 + \tilde{\tau}_2^2 + \tilde{\tau}_3^2 \right) - \frac{9\nu}{2E} \, \tilde{p}^2, \quad (2.26)$$

where $\tilde{p} = (\tilde{\tau}_1 + \tilde{\tau}_2 + \tilde{\tau}_3)/3$. This form involves the effect of triaxiality intrinsically as follows

$$Y^d = \frac{\tilde{\tau}_{eq}^2 \, R_v}{2E}, \quad (2.27)$$

where R^v is the triaxiality function,

$$R_v = \frac{2}{3} \left(1 + \nu \right) + 3 \left(1 - 2\nu \right) \left(\frac{\tilde{p}}{\tilde{\tau}_{eq}} \right), \quad (2.28)$$

---

[5] Here, weakly coupled refers to no hardening-damage coupling, where merely the effective stress contributions take place in the yield function but not the effective counterparts of the hardening variables, [20]. The plasticity-damage coupling is referred to as strong on the other hand due to the use of a single plastic potential coupled to damage, restricting damage by not allowing its growth without accompanying plastic flow. Comparison of possible coupling mechanisms can be found in [107].

and $\tilde{\tau}_{eq}$ is the equivalent **von Mises** stress which is defined in terms of principal components as $\tilde{\tau}_{eq} = (\tilde{\tau}_1^2 + \tilde{\tau}_2^2 + \tilde{\tau}_3^2 - \tilde{\tau}_1 \tilde{\tau}_2 - \tilde{\tau}_1 \tilde{\tau}_3 - \tilde{\tau}_2 \tilde{\tau}_3)^{1/2}$.

Remark 2.2.1 *In the original* LEMAITRE *damage model, the conjugate damage force, Y^d, is defined as, [98]*

$$Y^d = \frac{1+\nu}{2E(1-D)^2}\boldsymbol{\tau} : \boldsymbol{\tau} - \frac{\nu}{2E(1-D)^2}tr[\boldsymbol{\tau}]^2,$$

which is identical to (2.25) with the effective stress definition.

2.2.3.5 Quasi-Unilateral Damage Evolution

Physical facts show that, the damage evolution is amplified in tensile conditions whereas under compressive loads the rates of deterioration dramatically reduce. This is due to the partial micro-crack closure. Accordingly, quasi-unilateral damage takes into account evolution fully in tension and partially (or none) in compression. For a 3D stress state, the tensile and the compressive characters of the tensor components may not be apparent. For this purpose, two common resolutions are due.

The former, being a rather simplistic approach, proposed in [178] and [141] where the damage accumulation rate for cyclic plasticity is analyzed, relies on the character of the triaxiality (or equivalently the hydrostatic stress component). Hence, damage accumulates under positive (tensile) hydrostatic stresses where the damaged material stiffness is utilized. For negative triaxialities on the other hand, neither damage accumulates (not even partially), nor a reduction in the tangent is given account for.

In the latter more rigorous method, decision is made using the distinct principal tensor (stress or strain) components. Accordingly, the tensile and compressive principal tensor components are sought, where, for the extraction of these components, use of projection operators are proposed, see, e.g. [104] and [92], as well as spectral decompositions, see, e.g. [199]. In view of that, the damage conjugate variable definitions are refined to support quasi-lateral damage evolutionary forms, fully contributed by tensile stresses and partially contributed by compressive stresses, parameterized by the crack closure parameter.

Two methods have relative advantages and disadvantages. The form given in [178] and

[141] is very efficient and supplies rapid qualification of the evolutionary conditions. Besides, it does not require a crack closure parameter. However, this simplicity may be seen as a drawback of the method, where there is no space for partial damage evolution under compressive hydrostatic stresses. As far as the void nucleation with shear decohesion under compressive stresses is taken into account, this requirement may be seen over-restrictive. The principal stress/strain projection method on the other hand intrinsically takes into account these mechanisms to a certain level governed by the crack closure parameter. However, the method results in a more complicated algorithm as far as the computation of the evolutionary forms and the material tangents are concerned.

The advantage of the current framework using the principal stress space formulation comes to scene at this stage with its ease of application of the quasi-unilateral damage evolutionary forms (i.e. active/passive damage evolutionary conditions). Since the existing formulation is already a principal axes one, it is naturally devised for the active/passive conditions, thus does not necessitate an additional labor for extracting the principal tensile and principal compressive portions of stress tensors with projection operators or spectral decompositions. Accordingly, one may propose the following refined damage conjugate variable to give account for the quasi-lateral damage evolution, with fully contributed by tensile stresses and partially contributed by compressive stresses as,

$$
\begin{aligned}
Y^{d,+}(\tilde{\tau}_A) = {} & \frac{1+\nu}{2E} \left(\langle \tilde{\tau}_1 \rangle^2 + \langle \tilde{\tau}_2 \rangle^2 + \langle \tilde{\tau}_3 \rangle^2 \right) - \frac{9\nu}{2E} \langle \tilde{p} \rangle^2 \\
& + \frac{h\,(1+\nu)}{2E} \left(\langle -\tilde{\tau}_1 \rangle^2 + \langle -\tilde{\tau}_2 \rangle^2 + \langle -\tilde{\tau}_3 \rangle^2 \right) - \frac{9h\,\nu}{2E} \langle -\tilde{p} \rangle^2,
\end{aligned}
\tag{2.29}
$$

where $\langle \bigstar \rangle$ is the MACAULEY bracket with $\langle \bigstar \rangle := 1/2\,(\bigstar + |\bigstar|)$ and $h \in [0,1]$ is the crack closure parameter. The two extremes where $h = 0$ and $h = 1$ correspond to complete and no crack closure respectively, where for steels h is generally taken as 0.2, [98]. The use of effective principal KIRCHHOFF stresses highly simplifies not only the form of the expressions, but also the consequent derivations. This apparent simplicity is applicable to all of the isotropic damage models given in Table 2.2, where $Y(\tilde{\tau})$ is reformulated as $Y(\tilde{\tau}_A)$ with $(A = 1, 2, 3)$. In the current framework, unlike [99, p. 105], identical damage independent effective stress definition for elasticity and plasticity is used.

Application of the quasi-unilateral conditions with anisotropic damage is prone to certain anomalies, which is beyond the purpose of the current study. For a general perspective, the reader is referred to [38] and the references therein.

2.2.4 Expansion to Kinematic Hardening

Inclusion of kinematic hardening is made in the simplest manner by introducing an additional term to the plastic free energy in (2.2). Accordingly, an additively decoupled form into isotropic, i.e. $\Psi^{p,iso}$, and kinematic, i.e. $\Psi^{p,kin}$, portions are assumed, such as,

$$\Psi^p(\alpha, \mathbf{z}) = \Psi^{p,iso}(\alpha) + \Psi^{p,kin}(\mathbf{z}), \tag{2.30}$$

where an additional dissipation term due to the kinematic hardening, $\Omega^{p,kin}$, is added to the pure local mechanical inequality,

$$\Omega = \boldsymbol{\tau} : [-\frac{1}{2}\pounds_v \mathbf{b}^e \bullet \mathbf{b}^{e,-1}] + \Omega^{p,kin}(\mathbf{z}) + q\,\partial_t\alpha + Y^d\,\partial_t D \geq 0, \tag{2.31}$$

with $\mathbf{z}$ and $\boldsymbol{\beta}$ being kinematic hardening strain-like and stress-like variables, respectively. $\boldsymbol{\beta}$ is also called the backstress, associated with the center of the yield surface, i.e. elastic range. Geometrical interpretation of the isotropic, kinematic and combined isotropic/kinematic hardening models are respectively given in Figure 2.3.a, Figure 2.3.b and Figure 2.3.c in the Π plane, defined at the effective KIRCHHOFF stress space, for an initially virgin yield locus, given by the dashed circles. More complicated hardening models can be developed by distorting the locus by accompanied plastic flow.

For kinematic hardening, in the context of multiplicative kinematics, two possible approaches that are proposed in the literature, which are named as Model A and Model B, are utilized. Model A is due to [81] and Model B is due to [102], where the details are in Table 2.3.
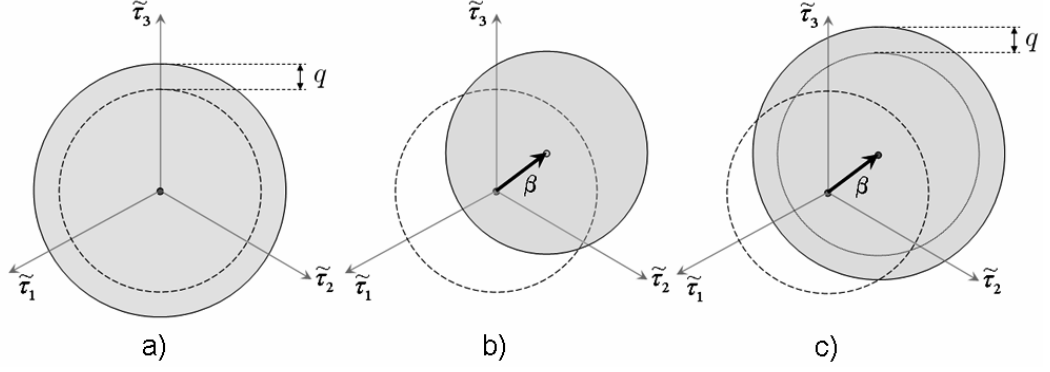
Figure 2.3: Yield locus evolution in Π plane, a) Isotropic hardening, b) Kinematic hardening, c) Combined isotropic/kinematic hardening.

Table 2.3: Utilized kinematic hardening models.

Expression	Model A	Model B
$\boldsymbol{\beta}$	$2\partial_{\mathbf{z}}\Psi \bullet \mathbf{z}$	$\partial_{\mathbf{z}}\Psi$
$\Omega^{p,kin}$	$\boldsymbol{\beta} : \left[-\frac{1}{2}\pounds_v\mathbf{z} \bullet \mathbf{z}^{-1}\right]$	$\boldsymbol{\beta} : \left[-\overset{\triangle}{\boldsymbol{\xi}}\right]$
Objective rate	$\pounds_v\mathbf{z} = \dot{\mathbf{z}} - \mathbf{l} \bullet \mathbf{z} - \mathbf{z} \bullet \mathbf{l}^t$	$\overset{\triangle}{\mathbf{z}} = \sum\limits_{A=1}^{3} \dot{z}_A\,\boldsymbol{\nu}^A \otimes \boldsymbol{\nu}^A$

In both of the formulations, it is hypothesed that, $\mathbf{b}^e$ is coaxial with $\mathbf{z}$, (equivalently, so are $\boldsymbol{\tau}$ and $\boldsymbol{\beta}$). Also $\mathbf{z}$ and $\boldsymbol{\beta}$ are deviatoric and symmetric tensors. Accordingly following expressions are valid,

$$\mathbf{z} = \sum_{A=1}^{3} z_A\,\boldsymbol{\nu}^A \otimes \boldsymbol{\nu}^A; \qquad z_A = \gamma_A^2, \tag{2.32}$$

$$\boldsymbol{\beta} = \sum_{A=1}^{3} \beta_A\,\boldsymbol{\nu}^A \otimes \boldsymbol{\nu}^A. \tag{2.33}$$

In Model A, the form of the KIRCHHOFF type kinematic hardening stress like variable is analogous to the KIRCHHOFF stress definition. The dissipation potential is constructed in terms of LIE derivative of $\mathbf{z}$. This form is direct extension of the dissipation potential to give account for damage derived in the reference configuration in [81], as,

$$0 \leq \Omega := -\mathbf{S} : \frac{1}{2}\mathbf{C} \bullet \partial_t\mathbf{G}^p \bullet \mathbf{G}^{p,-1} - \mathbf{A} : \frac{1}{2}\mathbf{C} \bullet \partial_t\boldsymbol{\Xi} \bullet \boldsymbol{\Xi}^{-1} + q\,\partial_t\alpha + Y^d\,\partial_t D, \tag{2.34}$$

where $\mathbf{z} = \mathbf{F} \bullet \mathbf{\Xi} \bullet \mathbf{F}^t$, $\boldsymbol{\beta} = \mathbf{F} \bullet \mathbf{A} \bullet \mathbf{F}^t$, $\mathbf{b}^e = \mathbf{F} \bullet \mathbf{G}^p \bullet \mathbf{F}^t$. Accordingly one finds

$$\underbrace{\partial_t \mathbf{b}^e - \mathbf{l} \bullet \mathbf{b}^e - \mathbf{b^e} \bullet \mathbf{l}^t}_{=: \mathcal{L}_v \mathbf{b}^e} = \mathbf{F} \bullet \partial_\mathbf{t} \mathbf{G^p} \bullet \mathbf{F^t}, \tag{2.35}$$

$$\underbrace{\partial_t \mathbf{z} - \mathbf{l} \bullet \mathbf{z} - \mathbf{z} \bullet \mathbf{l}^t}_{=: \mathcal{L}_v \mathbf{z}} = \mathbf{F} \bullet \partial_\mathbf{t} \mathbf{\Xi} \bullet \mathbf{F^t}. \tag{2.36}$$

Except for the trivial case of $q\,\partial_t\alpha \equiv q\,\partial_t\alpha$, $Y^d\,\partial_t D \equiv Y^d\,\partial_t D$, for scalars, one can derive the following equivalences to complete the case,

$$-\mathbf{S} : \frac{1}{2}\mathbf{C} \bullet \partial_t \mathbf{G}^p \bullet \mathbf{G}^{p,-1} \equiv \boldsymbol{\tau} : [-\frac{1}{2}\mathcal{L}_v \mathbf{b}^e \bullet \mathbf{b}^{e,-1}], \tag{2.37}$$

$$-\mathbf{A} : \frac{1}{2}\mathbf{C} \bullet \partial_t \mathbf{\Xi} \bullet \mathbf{\Xi}^{-1} \equiv \boldsymbol{\beta} : \left[-\frac{1}{2}\mathcal{L}_v \mathbf{z} \bullet \mathbf{z}^{-1}\right], \tag{2.38}$$

where the details of the derivations are given in Appendix C. In Model B, the conventional form of the state laws is utilized, where the objective rate of the strain like variable in the dissipation potential expression is in a corotational rate form. As seen in both of the models, the definition for the back stress, with $2\partial_\mathbf{z}\Psi \bullet \mathbf{z}$ or $\partial_\mathbf{z}\Psi$ for Model A and B, respectively, strictly depends on the form of $\Psi^{p,kin}(\mathbf{z})$.

The flow rules are carried out through the dissipation potentials which involve the back stress, $\boldsymbol{\beta}$, as an additional argument,

$$\phi^t(\boldsymbol{\tau}, \boldsymbol{\beta}, q, Y^d; \alpha, D) = \tilde{\phi}(\tilde{\boldsymbol{\tau}}, \boldsymbol{\beta}, q) + \phi^d(Y^d; \alpha, D). \tag{2.39}$$

Existing flow equations does not alter, whereas the evolutionary forms for $\mathbf{z}$, in Model A and Model B yield two objective rate forms. For Model A, together with the normality condition, one derives

$$\mathcal{L}_v \mathbf{z} = -2\,\dot{\gamma}\,\partial_{\boldsymbol{\beta}}\tilde{\phi} \bullet \mathbf{z}, \tag{2.40}$$

whereas for Model B, one carries out,

$$\overset{\triangle}{\mathbf{z}} = -\dot{\gamma}\,\partial_{\boldsymbol{\beta}}\tilde{\phi}. \tag{2.41}$$

2.2.4.1   Model Free Energies and Dissipation Potentials

As model free energy definitions, for Model A, a form, quadratic in logarithmic kinematic hardening strains, i.e. $\boldsymbol{\kappa} = \log[\boldsymbol{\gamma}]$ is utilized, where $\gamma_A = \sqrt{z_A}$ stands for the kinematic hardening stretch with the deviatoric portion represented, [81]. For

Model B a form quadratic in kinematic hardening strain-like variable, $\mathbf{z}$, is selected, [102]. These two forms are generalizations of the PRAGER-ZIEGLER type of kinematic hardening to the finite strain regimes,

$$\Psi^{p,kin}(\gamma_A) = \begin{cases} \frac{1}{3}C\,(\log[\gamma_1]^2 + \log[\gamma_2]^2 + \log[\gamma_3]^2); & \text{Model A}; \\ \frac{1}{3}C(\gamma_1^4 + \gamma_2^4 + \gamma_3^4), \text{ with } z_A^2 = \gamma_A^4; & \text{Model B}. \end{cases} \tag{2.42}$$

Accordingly one finds the following state equations for $\boldsymbol{\beta}$,

$$\boldsymbol{\beta} = \begin{cases} \frac{2}{3}C\,\boldsymbol{\kappa}; & \text{Model A}; \\ \frac{2}{3}C\,\mathbf{z}; & \text{Model B}. \end{cases} \tag{2.43}$$

The definition of the yield potential, which is of VON MISES type, is made in the effective KIRCHHOFF stress space in terms of the principal values of the effective KIRCHHOFF stresses and KIRCHHOFF type back-stress as,

$$\tilde{\phi}(\tilde{s}_A, \beta_A, q) := [(\tilde{s}_1 - \beta_1)^2 + (\tilde{s}_2 - \beta_2)^2 + (\tilde{s}_3 - \beta_3)^2]^{1/2} - \sqrt{\frac{2}{3}}\,y(q) \le 0. \tag{2.44}$$

Utilizing above form, evolutionary forms can be handled as follows,

$$\partial_{\tilde{\boldsymbol{\tau}}}\tilde{\phi} = \sum_{A=1}^{3} \tilde{n}_A\,\boldsymbol{\nu}^A \otimes \boldsymbol{\nu}^A \;\Rightarrow\; \mathcal{L}_v\mathbf{b}^e = -2\,\frac{\dot{\gamma}}{(1-D)}(\sum_{A=1}^{3} \tilde{n}_A\,\boldsymbol{\nu}^A \otimes \boldsymbol{\nu}^A) \bullet \mathbf{b}^e, \tag{2.45}$$

$$\partial_{\boldsymbol{\beta}}\tilde{\phi} = \sum_{A=1}^{3} \tilde{n}_A\,\boldsymbol{\nu}^A \otimes \boldsymbol{\nu}^A \;\Rightarrow\; \begin{cases} \mathcal{L}_v\mathbf{z} = -2\,\dot{\gamma}\,(\sum_{A=1}^{3} \tilde{n}_A\,\boldsymbol{\nu}^A \otimes \boldsymbol{\nu}^A) \bullet \mathbf{z}; & \text{Model A}; \\ \overset{\triangle}{\mathbf{z}} = -\dot{\gamma}\,\sum_{A=1}^{3} \tilde{n}_A\,\boldsymbol{\nu}^A \otimes \boldsymbol{\nu}^A; & \text{Model B}. \end{cases} \tag{2.46}$$

where $\tilde{n}_A = \partial_{\tilde{\tau}_A}\tilde{\phi} = \xi_A/\sqrt[2]{\xi_1^2 + \xi_2^2 + \xi_3^2}$, with $\xi_A = \tilde{s}_A - \beta_A$. Pay attention to the fact that the eigen-bases for the effective and the homogenized stresses are equivalent, i.e. $\mathbf{m}^A = \boldsymbol{\nu}^A \otimes \boldsymbol{\nu}^A \equiv \tilde{\mathbf{m}}^A = \tilde{\boldsymbol{\nu}}^A \otimes \tilde{\boldsymbol{\nu}}^A$.

2.3 Numerical Implementation

2.3.1 FE Formulation of the Coupled IBVP

In an EULERIAN description, the local equation of motion is constructed as,

$$\text{div } \boldsymbol{\sigma} + \rho\boldsymbol{\zeta} = \rho\boldsymbol{\gamma}. \tag{2.47}$$

where $\boldsymbol{\sigma}$ denotes the CAUCHY stress tensor defined at current configuration. ρ is the density, whereas $\boldsymbol{\zeta}$ and $\boldsymbol{\gamma}$ are the body forces and accelerations respectively.

Following a (Bubnov-)Galerkin approach, both sides are multiplied by a sufficiently smooth virtual displacement field, $\boldsymbol{\eta}$, integrate at the current configuration and apply the divergence theorem to carry out a weak statement of the quasi static (global) equilibrium of the body, where accelerations are neglected (i.e. $\boldsymbol{\gamma} = \mathbf{0}$),

$$g(\boldsymbol{\varphi}, \boldsymbol{\eta}) = \int_{\boldsymbol{\varphi}(\mathfrak{B})} \boldsymbol{\sigma} : [\mathrm{grad}\boldsymbol{\eta}]^{\mathrm{sym}} \, dv - \int_{\boldsymbol{\varphi}(\mathfrak{B})} \rho\boldsymbol{\zeta} \bullet \boldsymbol{\eta} \, dv - \int_{\boldsymbol{\varphi}(\partial\mathfrak{B}_\sigma)} \bar{\mathbf{t}} \bullet \boldsymbol{\eta} \, da = 0, \quad (2.48)$$

where $\bar{\mathbf{t}}$ denotes the surface tractions. Linearization of the given weak form, for only the internal virtual work, in the direction of $\boldsymbol{\varphi}$, i.e. $Dg(\boldsymbol{\varphi}, \boldsymbol{\eta})\bullet\mathrm{d}\boldsymbol{\varphi}$ is,

$$\begin{aligned} Dg(\boldsymbol{\varphi}, \boldsymbol{\eta}) \bullet \mathrm{d}\boldsymbol{\varphi} &= \int_{\boldsymbol{\varphi}(\mathfrak{B})} [\mathrm{grad}\boldsymbol{\eta}]^{\mathrm{sym}} : \mathbf{c} : [\mathrm{grad}\boldsymbol{\varphi}]^{\mathrm{sym}} \, dv \\ &+ \int_{\boldsymbol{\varphi}(\mathfrak{B})} \mathrm{grad}\boldsymbol{\eta} \bullet \boldsymbol{\sigma} \bullet \mathrm{grad}\boldsymbol{\varphi} \, dv. \end{aligned} \quad (2.49)$$

On the right hand side, the first term is due to material stiffness and the second term is due to geometric stiffness. A consistent derivation of $\mathbf{c}$, i.e. spatial material tangent, is vital for quadratic convergence quality of the Newton-Raphson method, which is listed in §2.3.3.

2.3.2 Algorithmic Treatment of the Time Discrete Forms

In the following, isotropic damage coupled hyperelastic-plastic framework formulated in principal axes, local integration procedures are summarized starting from a full set of seven equations which are simplified systematically at first to two and finally to one. In addition, possible operator-split methodologies, which emanate from product formulas, such as elastic predictor-plastic/damage corrector (simultaneous plastic-damage solution scheme) and elastic predictor-plastic corrector-damage deteriorator (staggered plastic-damage solution scheme) are given. Isoerror maps, listed in § 2.4, are utilized for the accuracy and stability evaluation taking into account the effect of various process parameters.

The accessibility of any mathematical material model to the engineering practice in the solution of random complex problems is possible invariably through implementing user material subroutines into existing finite element software. For a quasi static problem, these subroutines require stress, internal variable and material tangent matrix updates at the end of the time step. This scheme is generally named as the return mapping,

which boils down to a radial return for isotropic VON MISES type yield loci, [93]. Such a scheme generally requires simultaneous satisfaction of a set of differential equations, in the form of the rates of inelastic variables, mostly of nonlinear character which requires satisfaction of B-stability, [160]. A general approach for solving this set is application of the NEWTON-RAPHSON method together with a backward-EULER integration. For quasi-static problems, this helps definition of the global algorithmic moduli also, which may not be the case for different integration methods, such as those belonging to RK family, [194]. On the local integration schemes for inelasticity, there is a vast amount of literature. Among others, [93] and [131] can be given as examples which studies local integration schemes for pure plasticity. [163] includes an indepth treatment of the subject. [170], [194] and [128] constitute examples for damage coupled plasticity. For a larger evaluation of the methods, user is referred to [194] and the references therein. The NEWTON-RAPHSON method requires the analytical derivation of local system JACOBIAN which may not be possible for complicated material models. As the mathematical rigor in the material model is increased, certain justifications may be possible from the accuracy. Accordingly, numerical evaluation of the JACOBIAN is possible, see e.g. [120] or [138]. Another option is application of quasi-NEWTON type methods, [54]. Making use of staggered routines which falls into the class of product formulas, [45], is one remedy which has certain advantages:

- Since the staggering breaks up the coupled environment of the system, the off-diagonal terms in the JACOBIAN are not computed. This subtracts from the local computational load for the integration, which results in a considerable time gain in staggered schemes. This is more apparent in the dynamic explicit analysis where the global tangent is not utilized in the analysis thus the pure computational time depends on the performance of the local integration routines.

- For the staggered portions, different time steps and different numerical integration methods can be devised among staggered integration steps,

- It is easy to implement a staggered routine into the existing return mapping routines. Unlike the monolithic schemes the modifications are decreased to minimum where the code changes are limited to explicit implementations (like independent function additions) rather than implicit ones. [6],

---

[6] For example, in the adiabatic processes where high velocity loading is due, the heat cannot find

- In the context of damage mechanics, where isotropic damage variable is due, the advantage of staggering the plastic correction and damage deterioration may not be apparent, where two scalar nonlinear equations are due. However as far as anisotropy is concerned, the efficiency is obvious, where the dimension of the problem is significantly increased due to additional tensorial components, see e.g. [54].

Besides the having proved the mentioned advantages, staggered routines are only conditionally stable thus require accuracy and stability analysis. The accuracy requirements may need smaller time steps, compared to monolithic schemes. The aim of this study is to assess the stability and accuracy of the staggered routines in continuum damage mechanics for finite strains. The stability and the accuracy of the use of product formulas in the context of simultaneous differential equation solutions were investigated by [45]. In the context of damage coupled plasticity, such staggered algorithms are proposed by[165], [85], [86] for isotropic damage models where multi-surface damage-plasticity models are utilized. For anisotropic damage models, [54] investigates the performance of staggered schemes. [128] also applies another approach in damage integration. As a tool to evaluate the numerical accuracy, isoerror maps are utilized, which are known to lack the mathematical rigor however show reasonable performance. Isoerror analysis is used by [93] and [131] for pure plasticity and [170] and [194] for damage coupled plasticity. The presentation in [194] utilizes a small strain framework. Besides none of these studies involve the application of a staggered approach. In the present study, for a finite strain hyperelastic plastic model coupled to a LEMAITRE variant damage model, the parametric effects, such as degree of nonlinearity of the damage function (where the concave up and down models are diagnosed), the effect of the initial damage in the system, on the accuracy and stability of the staggered integration are evaluated. The latter is of special importance. Although the physical evidences prove that failure may occur far below the upper

---

time to conduct or convect over the problem domain. This lack of conduction leads to a simplified case of solution in the local integration in the expense of increasing number of equations handled at the radial return. The heat equation is treated now at its strong form where the derivation of the weak form is not required. Such schemes, which are implemented in the dynamic explicit codes, once treated by staggered routines, this amount to four step elastic predictor/plastic corrector/damage deteriorator/temperature deteriorator type algorithm. Whereas the physics of the problem is complicated, once a plastic return map routine is available, expansion to damage and thermal coupling is a matter addition of two uncoupled initial value problems.

mathematical limit of damage which is $D = 1$, numerical instabilities may occur for $D \geq 0.80$, [99]. A functional damage framework is utilized which gives the possibility to observe the response of different damage models.

These methods emerge as a special form of the closest point projection which boils down to the radial return mapping when VON MISES yield surface is utilized, [164], [93]. The radial return map in a damage coupled framework takes place in the effective KIRCHHOFF stress space. Using the effective KIRCHHOFF stress definition as, $\tilde{\tau} = \tau/(1-D)$, it is seen that, due to the strain equivalence principle, the effective stresses do not depend explicitly on D.

$[\bigstar]_n$ and $[\bigstar]_{n+1}$ give the definitions of any state variable denoted by $[\bigstar]$, at times t_n and t_{n+1} respectively. It is assumed that the state variables at time t_n are known and using the deformation computed at $\Delta t = t_{n+1} - t_n$, the state at time t_{n+1} is sought for. Using a strain driven process, an elastic trial left CAUCHY GREEN deformation tensor, $\mathbf{b}^{e,tri}$, at time t_{n+1}, can be defined making use of relative deformation gradient tensor at current step, i.e. $\mathbf{f}_{n+1}$, with $\mathbf{f}_{n+1} = \mathbf{F}_{n+1} \bullet \mathbf{F}_n^{-1}$, and elastic left CAUCHY GREEN deformation tensor of the previous step, i.e. $\mathbf{b}_n^e$, as follows,

$$\mathbf{b}_{n+1}^{e,tri} = \mathbf{f}_{n+1} \bullet \mathbf{b}_n^e \bullet \mathbf{f}_{n+1}^t. \tag{2.50}$$

The spectral decomposition of $\mathbf{b}_{n+1}^{e,tri}$ reads, with $b_{n+1,A}^e = \lambda_{n+1,A}^{e,tri,2}$,

$$\mathbf{b}_{n+1}^{e,tri} = \sum_{A=1}^{3} \lambda_{tri,A}^{e,2} \, \mathbf{m}_{n+1}^{tri,A}. \tag{2.51}$$

Following [167], the eigen-bases, $\mathbf{m}_{n+1}^{tri,A}$, can be explicitly given as,

$$\mathbf{m}_{n+1}^{tri,A} = \frac{\mathbf{b}_{n+1}^{e,tri} \bullet \mathbf{b}_{n+1}^{e,tri} - (I_1 - \lambda_{n+1,A}^{e,tri,2}) \, \mathbf{b}_{n+1}^{e,tri} + I_3 \, \lambda_{n+1,A}^{e,tri,-2} \, \mathbf{1}}{D_A}, \tag{2.52}$$

where $\mathbf{1}$ is the second order identity tensor. D_A is defined as,

$$D_A = 2\lambda_{n+1,A}^{e,tri,4} - I_1 \lambda_{n+1,A}^{e,tri,2} + I_3 \lambda_{n+1,A}^{e,tri,-2}, \tag{2.53}$$

using the following invariant definitions for I_1, I_2 and I_3,

$$I_1 = \lambda_{n+1,1}^{e,tri,2} + \lambda_{n+1,2}^{e,tri,2} + \lambda_{n+1,3}^{e,tri,2}, \tag{2.54}$$

$$I_2 = \lambda_{n+1,1}^{e,tri,2} \lambda_{n+1,2}^{e,tri,2} + \lambda_{n+1,1}^{e,tri,2} \lambda_{n+1,3}^{e,tri,2} + \lambda_{n+1,2}^{e,tri,2} \lambda_{n+1,3}^{e,tri,2}, \tag{2.55}$$

$$I_3 = \lambda_{n+1,1}^{e,tri,2} \lambda_{n+1,2}^{e,tri,2} \lambda_{n+1,3}^{e,tri,2}. \tag{2.56}$$

(2.52) is restricted to the case of discrete eigenvalues, i.e. $\lambda_{n+1,1}^{e,tri} \neq \lambda_{n+1,2}^{e,tri} \neq \lambda_{n+1,3}^{e,tri}$. The case of coincident or nearly coincident eigenvalues are treated with the perturbation technique presented in § 2.3.3. The algorithmic counterpart of the flow rule (2.9) is,

$$\mathcal{L}_v \mathbf{b}_{n+1}^e = -2 \frac{\dot{\gamma}_{n+1}}{(1 - D_{n+1})} \left. \partial_{\tilde{\tau}} \tilde{\phi} \right|_{n+1} \bullet \mathbf{b}_{n+1}^e, \tag{2.57}$$

where for a typical time step Δt, using $\Delta \gamma := \Delta t \dot{\gamma}_{n+1}$, the exponential mapping approximation for integration of flow rule, as a solution of the first order differential equation (2.57), yields[7],

$$\mathbf{b}_{n+1}^e = \exp \left[-2 \frac{\Delta \gamma}{(1 - D_{n+1})} \left. \partial_{\tilde{\tau}} \tilde{\phi} \right|_{n+1} \right] \bullet \mathbf{b}_{n+1}^{e,tri}. \tag{2.58}$$

Rewriting (2.58) to constitute the principal stretches, one carries out,

$$\lambda_{n+1,A}^e = \exp \left[-\frac{\Delta \gamma}{(1 - D_{n+1})} \left. \frac{\partial \tilde{\phi}}{\partial \tilde{\tau}_A} \right|_{n+1} \right] \lambda_{n+1,A}^{e,tri}. \tag{2.59}$$

Taking the natural logarithms of both sides,

$$\epsilon_{n+1,A}^e = \epsilon_{n+1,A}^{e,tri} - \frac{\Delta \gamma}{(1 - D_{n+1})} \left. \frac{\partial \tilde{\phi}}{\partial \tilde{\tau}_A} \right|_{n+1}, \tag{2.60}$$

gives rise to the following form,

$$\epsilon_{n+1,A}^e = \epsilon_{n+1,A}^{e,tri} - \Delta \epsilon_{n+1,A}^p, \tag{2.61}$$

where the principal logarithmic plastic strain increments are defined as follows,

$$\Delta \epsilon_{n+1,A}^p = \frac{\Delta \gamma}{(1 - D_{n+1})} \left. \frac{\partial \tilde{\phi}}{\partial \tilde{\tau}_A} \right|_{n+1}. \tag{2.62}$$

It is noteworthy that, making use of the HENCKY model, from a multiplicative decomposition of the deformation gradient into elastic and plastic portions one comes up with the damage coupled counterpart of the canonical stress-space return mapping algorithm of the small strain elasto-plasticity. Using (2.57), the plastic/damage correction of trial elastic logarithmic strains in (2.60) furnishes the following definitions for the current total effective principal KIRCHHOFF stresses,

$$\tilde{\tau}_{n+1,A} = \tilde{\tau}_{n+1,A}^{tri} - 2\mu \frac{\Delta \gamma}{(1 - D_{n+1})} \, n_{n+1,A}, \text{ with } \tilde{\tau}_{n+1,A}^{tri} = \tilde{p} + \tilde{s}_{n+1,A}^{tri}, \tag{2.63}$$

and for the corrected current deviatoric effective principal KIRCHHOFF stresses,

$$\tilde{s}_{n+1,A} = \tilde{s}_{n+1,A}^{tri} - 2\mu \frac{\Delta \gamma}{(1 - D_{n+1})} \, n_{n+1,A}, \text{ with } \tilde{s}_{n+1,A}^{tri} = 2\mu \, \bar{\epsilon}_{n+1,A}^{e,tri}. \tag{2.64}$$

---

[7] See Appendix C.2.5 as a reminder, for a general treatment for the exponential mapping.

2.3.2.1 Simultaneous Local Integration Schemes

In what follows, the coupled nonlinear equation set of the local integration problem, for a known constant displacement increment, is presented. The solution results in a two-step operator-split with a simultaneous plastic/damage correction for a given elastic prediction, i.e. (2.50). Table 2.7 shows the schematic illustration of the problem.

Table 2.4: Two-step operator-split with a simultaneous plastic/damage correction.

Total		Elastic Predictor		Plastic/Damage Corrector	
$\begin{cases} \partial_t \boldsymbol{\epsilon} \neq 0 \\ \pounds_v \mathbf{b}^e \neq 0 \\ \partial_t \alpha \neq 0 \\ \partial_t D \neq 0 \end{cases}$	$=$	$\begin{cases} \partial_t \boldsymbol{\epsilon} \neq 0 \\ \pounds_v \mathbf{b}^e = 0 \\ \partial_t \alpha = 0 \\ \partial_t D = 0 \end{cases}$	$+$	$\begin{cases} \partial_t \boldsymbol{\epsilon} = 0 \\ \pounds_v \mathbf{b}^e \neq 0 \\ \partial_t \alpha \neq 0 \\ \partial_t D \neq 0 \end{cases}$	$.$

Techniques, used in reduction of totally seven coupled equations, initially to two and finally to one, are also given. For this purpose, one necessitates the subsequent definition of the yield function computed at the current step,

$$\tilde{\phi}_{n+1} := \|\tilde{\mathbf{s}}_{n+1}\| - \sqrt{\frac{2}{3}} \, y \, (q_{n+1}) = 0. \tag{2.65}$$

Defining a family of generalized mid-point integration rules parameterized in θ, as, $[\bigstar]_{n+1} = [\bigstar]_n + \Delta t \, [\dot{\bigstar}]_{n+\theta}$, with $[\dot{\bigstar}]_{n+\theta} = (1 - \theta) \, [\dot{\bigstar}]_n + \theta \, [\dot{\bigstar}]_{n+1}$, for an arbitrary variable denoted by $[\bigstar]$, one may supply the rather trivial integration of the scalars α and D. This method is second order accurate for $\theta = 1/2$, [110], whereas $\theta = 1$ gives account for the first order accurate and unconditionally stable backward EULER method which is highly efficient in the integration of α, in computational plasticity, [83], and utilized in this section. The techniques, used in reduction of totally seven coupled equations, initially to two and finally to one, are also given. In the simultaneous local integration schemes, implicit backward EULER method is utilized for both plasticity and damage, which reads,

$$\alpha_{n+1} \quad = \quad \alpha_n + \Delta t \, \dot{\alpha}_{n+1} = \alpha_n + \sqrt{\frac{2}{3}} \, \Delta\gamma, \tag{2.66}$$

$$D_{n+1} \quad = \quad D_n + \Delta t \, \dot{D}_{n+1} = D_n + \Delta\gamma \, g_{n+1}, \tag{2.67}$$

with $g_{n+1} = g(Y_{n+1}^{d,+}; \alpha_{n+1}, D_{n+1})$, where, $Y_{n+1}^{d,+} = Y_{n+1}^{d,+}(\alpha_{n+1}, D_{n+1})$. In a residual setting, using the effective stresses definition with (2.63), for the current and the trial principal stress components, the complete simultaneous set of equations can be given as,

$$
\mathbf{r}_{n+1} = \mathbf{r}_{n+1}(\mathbf{x}_{n+1}) = \left\{ \begin{array}{c} \tau_{n+1,1} - \tau_{n+1,1}^{tri} + 2\mu\Delta\gamma \; n_{n+1,1} \\[4pt] \tau_{n+1,2} - \tau_{n+1,2}^{tri} + 2\mu\Delta\gamma \; n_{n+1,2} \\[4pt] \tau_{n+1,3} - \tau_{n+1,3}^{tri} + 2\mu\Delta\gamma \; n_{n+1,3} \\[4pt] \alpha_{n+1} - \alpha_n - \sqrt{\tfrac{2}{3}}\,\Delta\gamma \\[4pt] q_{n+1} - K'(\alpha_{n+1}) \\[4pt] \tilde{\phi}_{n+1} := \|\tilde{\mathbf{s}}_{n+1}\| - \sqrt{\tfrac{2}{3}}\,y(q_{n+1}) \\[4pt] D_{n+1} - D_n - \Delta\gamma\;g_{n+1} \end{array} \right\} \; ; \quad \mathbf{x}_{n+1} \left\{ \begin{array}{c} \tau_{n+1,1} \\[4pt] \tau_{n+1,2} \\[4pt] \tau_{n+1,3} \\[4pt] \Delta\gamma \\[4pt] D_{n+1} \\[4pt] \alpha_{n+1} \\[4pt] q_{n+1} \end{array} \right\} .
$$
(2.68)

where $\mathbf{r}_{n+1}(\mathbf{x}_{n+1}) = \mathbf{0}$. The array of unknowns is represented by $\mathbf{x}_{n+1}$. This set of nonlinear equations can be treated with the standard NEWTON-RAPHSON solution scheme. Accordingly the linearized version of the equations can be given as $\mathrm{d}\mathbf{r}_{n+1} = \mathbf{Dr}_{n+1} \bullet \mathrm{d}\mathbf{x}_{n+1}$, where the Jacobian of the system is denoted by $\mathbf{Dr}_{n+1}$, with,

$$
\mathbf{Dr}_{n+1} = \begin{bmatrix} \frac{\partial r_{1,n+1}}{\partial \tau_{n+1,1}} & \frac{\partial r_{1,n+1}}{\partial \tau_{n+1,2}} & \frac{\partial r_{1,n+1}}{\partial \tau_{n+1,3}} & \frac{\partial r_{1,n+1}}{\partial \Delta\gamma} & \frac{\partial r_{1,n+1}}{\partial D_{n+1}} & \frac{\partial r_{1,n+1}}{\partial \alpha_{n+1}} & \frac{\partial r_{1,n+1}}{\partial q_{n+1}} \\[6pt] \frac{\partial r_{2,n+1}}{\partial \tau_{n+1,1}} & \frac{\partial r_{2,n+1}}{\partial \tau_{n+1,2}} & \frac{\partial r_{2,n+1}}{\partial \tau_{n+1,3}} & \frac{\partial r_{2,n+1}}{\partial \Delta\gamma} & \frac{\partial r_{2,n+1}}{\partial D_{n+1}} & \frac{\partial r_{2,n+1}}{\partial \alpha_{n+1}} & \frac{\partial r_{2,n+1}}{\partial q_{n+1}} \\[6pt] \frac{\partial r_{3,n+1}}{\partial \tau_{n+1,1}} & \frac{\partial r_{3,n+1}}{\partial \tau_{n+1,2}} & \frac{\partial r_{3,n+1}}{\partial \tau_{n+1,3}} & \frac{\partial r_{3,n+1}}{\partial \Delta\gamma} & \frac{\partial r_{3,n+1}}{\partial D_{n+1}} & \frac{\partial r_{3,n+1}}{\partial \alpha_{n+1}} & \frac{\partial r_{3,n+1}}{\partial q_{n+1}} \\[6pt] \frac{\partial r_{4,n+1}}{\partial \tau_{n+1,1}} & \frac{\partial r_{4,n+1}}{\partial \tau_{n+1,2}} & \frac{\partial r_{4,n+1}}{\partial \tau_{n+1,3}} & \frac{\partial r_{4,n+1}}{\partial \Delta\gamma} & \frac{\partial r_{4,n+1}}{\partial D_{n+1}} & \frac{\partial r_{4,n+1}}{\partial \alpha_{n+1}} & \frac{\partial r_{4,n+1}}{\partial q_{n+1}} \\[6pt] \frac{\partial r_{5,n+1}}{\partial \tau_{n+1,1}} & \frac{\partial r_{5,n+1}}{\partial \tau_{n+1,2}} & \frac{\partial r_{5,n+1}}{\partial \tau_{n+1,3}} & \frac{\partial r_{5,n+1}}{\partial \Delta\gamma} & \frac{\partial r_{5,n+1}}{\partial D_{n+1}} & \frac{\partial r_{5,n+1}}{\partial \alpha_{n+1}} & \frac{\partial r_{5,n+1}}{\partial q_{n+1}} \\[6pt] \frac{\partial r_{6,n+1}}{\partial \tau_{n+1,1}} & \frac{\partial r_{6,n+1}}{\partial \tau_{n+1,2}} & \frac{\partial r_{6,n+1}}{\partial \tau_{n+1,3}} & \frac{\partial r_{6,n+1}}{\partial \Delta\gamma} & \frac{\partial r_{6,n+1}}{\partial D_{n+1}} & \frac{\partial r_{6,n+1}}{\partial \alpha_{n+1}} & \frac{\partial r_{6,n+1}}{\partial q_{n+1}} \\[6pt] \frac{\partial r_{7,n+1}}{\partial \tau_{n+1,1}} & \frac{\partial r_{7,n+1}}{\partial \tau_{n+1,2}} & \frac{\partial r_{7,n+1}}{\partial \tau_{n+1,3}} & \frac{\partial r_{7,n+1}}{\partial \Delta\gamma} & \frac{\partial r_{7,n+1}}{\partial D_{n+1}} & \frac{\partial r_{7,n+1}}{\partial \alpha_{n+1}} & \frac{\partial r_{7,n+1}}{\partial q_{n+1}} \end{bmatrix} .
$$
(2.69)

Using $\mathbf{Dr}_{n+1}^{-1} \bullet \mathrm{d}r_{n+1} = \mathrm{d}\mathbf{x}_{n+1}$, the solution for $\mathbf{x}_{n+1}$, which constitutes the local return mapping realized at each GAUSS point, can be carried out with the following iterative scheme,

$$
\mathbf{x}_{n+1}^{(k+1)} = \mathbf{x}_{n+1}^{(k)} - \delta^{(k)}\,\mathbf{Dr}_{n+1}^{-1,(k)} \bullet \mathbf{r}_{n+1}^{(k)},
$$
(2.70)

where $\delta^{(k)} \in (0, 1]$ is the proper line-search parameter.

The linearization of the global FE equilibrium equations requires a slight difference in

the definition of the vector of residuals and the vector of unknowns as,

$$\mathbf{r}_{n+1} = \mathbf{r}_{n+1}(\hat{\mathbf{x}}_{n+1}) = \mathbf{0}; \quad \hat{\mathbf{x}}_{n+1} \begin{Bmatrix} \epsilon_{n+1,\,1} \\ \epsilon_{n+1,\,2} \\ \epsilon_{n+1,\,3} \\ \tau_{n+1,\,1} \\ \tau_{n+1,\,2} \\ \tau_{n+1,\,3} \\ \Delta\gamma \\ D_{n+1} \\ \alpha_{n+1} \\ q_{n+1} \end{Bmatrix}. \tag{2.71}$$

With this current manipulation, the total differential of $\mathbf{r}_{n+1}$ with $\mathrm{d}\mathbf{r}_{n+1} = \mathbf{0}$, yields the consistent tangent. At this level, the number of the components of the JACOBIAN for governing equations is considerable. Further refinements are possible with little effort.

Reduction to Two Equations: Following [166], the local governing equations collected in (2.68) can be reduced, particularly for the chosen yield criterion, making use of the substitution, $\tilde{s}_{n+1,\,A} = \|\tilde{\mathbf{s}}_{n+1}\| \, n_{n+1,\,A}$

$$\|\tilde{\mathbf{s}}_{n+1}\| \, n_{n+1,\,A} = \left\|\tilde{\mathbf{s}}_{n+1}^{tri}\right\| \, n_{n+1,\,A}^{tri} - 2\mu \frac{\Delta\gamma}{(1 - D_{n+1})} \, n_{n+1,\,A}. \tag{2.72}$$

Table 2.5: Scheme for the elastic predictor.

---

1. Database at $\mathbf{x} \in \mathfrak{B}$, $\qquad \mathbf{b}_n^e, \ \alpha_n, \ D_n$

2. Given the current one, i.e. $\mathbf{F}_{n+1}$, compute the relative deformation gradient,
$\mathbf{f}_{n+1} = \mathbf{F}_{n+1} \bullet \mathbf{F}_n^{-1}$

3. Compute the trial elastic left Cauchy Green deformation tensor,

$$\boldsymbol{b}_{n+1}^{e,\,tri} \quad = \quad \mathbf{F}_{n+1} \bullet \mathbf{b}_n^e \bullet \mathbf{F}_{n+1}^t$$

4. Apply the spectral decomposition,

$$\mathbf{b}_{n+1}^{tri,\,A} = \sum_{A=1}^{3} b_{n+1,\,A}^{e,\,tri} \, \mathbf{m}_{n+1}^{tri,\,A}, \ \text{ with } \lambda_{n+1,\,A}^{e,\,tri} = (b_{n+1,\,A}^{e,\,tri})^{1/2}$$

with the following definition for eigen-bases,

$$\boldsymbol{m}_{n+1}^{tri,\,A} = \frac{\mathbf{b}_{n+1}^{e,\,tri} \bullet \mathbf{b}_{n+1}^{e,\,tri} - (I_1 - \lambda_{n+1,\,A}^{e,\,tri,\,2}) \, \mathbf{b}_{n+1}^{e,\,tri} + I_3 \, \lambda_{n+1,\,A}^{e,\,tri,\,-2} \, \mathbf{1}}{D_A}$$

which is computed for perturbed eigen-values for sufficiently close principal stretches.

5. Compute the trial elastic logarithmic strains,

$$\epsilon_{n+1,\,A}^{e,\,tri} = \ln(\lambda_{n+1,\,A}^{e,\,tri})$$

6. Compute the effective principal Kirchhoff stress predictions,

$$\begin{aligned}
\tilde{\tau}_{n+1,\,A}^{tri} &= \tilde{p}_{n+1} + \tilde{s}_{n+1,\,A}^{tri} \\
\tilde{p}_{n+1} &= H \, \log\left[J_{n+1}\right] \\
\tilde{s}_{n+1,\,A}^{tri} &= 2\mu \, \bar{\epsilon}_{n+1,\,A}^{e,\,tri}.
\end{aligned}$$

Applying the following arrangements,

$$\left(\|\tilde{\mathbf{s}}_{n+1}\| + 2\mu \frac{\Delta\gamma}{(1 - D_{n+1})} \right) n_{n+1,\,A} = \left\| \tilde{\mathbf{s}}_{n+1}^{tri} \right\| n_{n+1,\,A}^{tri}, \tag{2.73}$$

and exploiting the condition of collinear flow and the trial KIRCHHOFF stress tensor, where, $\mathbf{n}_{n+1} \equiv \mathbf{n}_{n+1}^{tri}$, [166], the uniqueness of the spectral decomposition yields,

$$n_{n+1,\,A}^{tri} \, \mathbf{m}_{n+1}^{tri,\,A} = n_{n+1,\,A} \, \mathbf{m}_{n+1}^{A}, \tag{2.74}$$

which gives $\mathbf{m}_{n+1}^{tri,\,A} \equiv \mathbf{m}_{n+1}^{A}$ and $n_{n+1,\,A} \equiv n_{n+1,\,A}^{tri}$. Utilizing this equivalence one can write,

$$\|\tilde{\mathbf{s}}_{n+1}\| + 2\mu \frac{\Delta\gamma}{(1 - D_{n+1})} = \left\| \tilde{\mathbf{s}}_{n+1}^{tri} \right\|. \tag{2.75}$$

Finally, representing the hardening/softening function definition in terms of the plastic

multiplier, yields the following reduced form, with $\mathbf{r}_{n+1} = \mathbf{r}_{n+1}(\mathbf{x}_{n+1})$,

$$
\mathbf{r}_{n+1} =
\left\{
\begin{array}{c}
\sqrt{\frac{2}{3}}\left\{\tau_0 + K'(\alpha_n + \sqrt{\frac{2}{3}}\Delta\gamma)\right\}- \\[6pt]
- \left\|\tilde{\mathbf{s}}_{n+1}^{\,tri}\right\| + 2\mu \dfrac{\Delta\gamma}{(1 - D_{n+1})} \\[10pt]
D_{n+1} - D_n - \Delta\gamma \; g_{n+1}
\end{array}
\right\} ;
\tag{2.76}
$$

$$
\kappa_{n+1} =
\left\{
\begin{array}{c}
\Delta\gamma \\[6pt]
D_{n+1}
\end{array}
\right\}.
\tag{2.77}
$$

where, for the local return mapping problem, $\mathbf{r}_{n+1}(\mathbf{x}_{n+1}) = \mathbf{0}$, with the number of unknowns, reduced from 7 to 2. The iterative scheme given in (2.70) is used in the solution of the reduced nonlinear problem with the following JACOBIAN definition,

$$
\mathbf{Dr}_{n+1} =
\left[
\begin{array}{cc}
\dfrac{\partial r_{1,\,n+1}}{\partial \Delta\gamma} & \dfrac{\partial r_{1,\,n+1}}{\partial D_{n+1}} \\[12pt]
\dfrac{\partial r_{2,\,n+1}}{\partial \Delta\gamma} & \dfrac{\partial r_{2,\,n+1}}{\partial D_{n+1}}
\end{array}
\right].
\tag{2.78}
$$

For the more general global problem,

$$
\mathbf{r}_{n+1} = \mathbf{r}_{n+1}(\hat{\mathbf{x}}_{n+1}) = \mathbf{0}; \quad \hat{\mathbf{x}}_{n+1}
\left\{
\begin{array}{c}
\epsilon_{n+1,\,1} \\[6pt]
\epsilon_{n+1,\,2} \\[6pt]
\epsilon_{n+1,\,3} \\[6pt]
\Delta\gamma \\[6pt]
D_{n+1}
\end{array}
\right\}.
\tag{2.79}
$$

with the vanishing total differential, $\mathrm{d}\mathbf{r}_{n+1} = \mathbf{0}$,

$$
\mathrm{d}r_{1,\,n+1} = \sum_{A=1}^{3} \frac{\partial r_{1,\,n+1}}{\partial \epsilon_{n+1,\,A}}\,\mathrm{d}\epsilon_{n+1,\,A} + \frac{\partial r_{1,\,n+1}}{\partial \Delta\gamma}\,\mathrm{d}\Delta\gamma + \frac{\partial r_{1,\,n+1}}{\partial D_{n+1}}\,\mathrm{d}D_{n+1} = 0, \tag{2.80}
$$

$$
\mathrm{d}r_{2,\,n+1} = \sum_{A=1}^{3} \frac{\partial r_{2,\,n+1}}{\partial \epsilon_{n+1,\,A}}\,\mathrm{d}\epsilon_{n+1,\,A} + \frac{\partial r_{2,\,n+1}}{\partial \Delta\gamma}\,\mathrm{d}\Delta\gamma + \frac{\partial r_{2,\,n+1}}{\partial D_{n+1}}\,\mathrm{d}D_{n+1} = 0. \tag{2.81}
$$

with $\mathrm{d}\epsilon_{n+1,\,A}/\mathrm{d}\epsilon_{n+1,\,B} = \delta_{AB}$, one carries out,

$$
\left\{
\begin{array}{c}
\dfrac{\partial r_{1,\,n+1}}{\partial \epsilon_{n+1,\,A}} \\[12pt]
\dfrac{\partial r_{2,\,n+1}}{\partial \epsilon_{n+1,\,A}}
\end{array}
\right\} = -\mathbf{Dr}_{n+1} \bullet
\left\{
\begin{array}{c}
\dfrac{\mathrm{d}\Delta\gamma}{\mathrm{d}\epsilon_{n+1,\,A}} \\[12pt]
\dfrac{\mathrm{d}D_{n+1}}{\mathrm{d}\epsilon_{n+1,\,A}}
\end{array}
\right\},
\tag{2.82}
$$

to give the following expression to be used in the algorithmic tangent moduli of the linearized global equilibrium problem,

$$
\left\{
\begin{array}{c}
\dfrac{\mathrm{d}\Delta\gamma}{\mathrm{d}\epsilon_{n+1,\,A}} \\[12pt]
\dfrac{\mathrm{d}D_{n+1}}{\mathbf{d}\epsilon_{n+1,\,A}}
\end{array}
\right\} = -\mathbf{Dr}_{n+1}^{-1} \bullet
\left\{
\begin{array}{c}
\dfrac{\partial r_{1,\,n+1}}{\partial \epsilon_{n+1,\,A}} \\[12pt]
\dfrac{\partial r_{2,\,n+1}}{\partial \epsilon_{n+1,\,A}}
\end{array}
\right\}.
\tag{2.83}
$$

39

Derivations for the components of the local JACOBIAN, i.e. $\mathbf{Dr}_{n+1}$, are listed in Appendix C, preserving the functional setting. The algorithmic treatment of the simultaneous approach with reduced two equation system is summarized in Table 2.6.

Table 2.6: Scheme for the return-mapping algorithm for two-step operator-split (Elastic predictor-plastic/damage corrector type algorithm).

1. Process Table 2.5. (Elastic predictor),
2. Check for plastic-damage loading on effective Kirchhoff stress space,

$$\tilde{\phi}_{n+1}^{tri} = \{(\tilde{s}_{n+1,1}^{tri})^2 + (\tilde{s}_{n+1,2}^{tri})^2 + (\tilde{s}_{n+1,3}^{tri})^2\}^{1/2} - \sqrt{\frac{2}{3}}\{\tau_0 + K(\alpha_n)\}$$

   IF $\tilde{\phi}_{n+1}^{tri} \leq 0$ **THEN**
Set $(\bullet)_{n+1} = (\bullet)_{n+1}^{tri}$, **EXIT**. (Elastic step)
ELSE
GOTO 3. (Plastic-damage corrector)
ENDIF
3. Find the plastic multiplier and the damage, $\Delta\gamma^{(0)} = 0, D_{n+1}^{(0)} = D_n$, with linesearch,

$$\left\{ \begin{array}{c} \Delta\gamma^{(k+1)} \\ D_{n+1}^{(k+1)} \end{array} \right\} = \left\{ \begin{array}{c} \Delta\gamma^{(k)} \\ D_{n+1}^{(k)} \end{array} \right\}$$

$$- \frac{\delta^{(k)}}{\Delta_{n+1}^{(k)}} \left[\begin{array}{cc} \left(\dfrac{\partial r_{2,n+1}}{\partial D_{n+1}}\right)^{(k)} & -\left(\dfrac{\partial r_{1,n+1}}{\partial D_{n+1}}\right)^{(k)} \\ -\left(\dfrac{\partial r_{2,n+1}}{\partial \Delta\gamma}\right)^{(k)} & \left(\dfrac{\partial r_{1,n+1}}{\partial \Delta\gamma}\right)^{(k)} \end{array} \right] \bullet \left\{ \begin{array}{c} r_{1,n+1}^{(k)} \\ r_{2,n+1}^{(k)} \end{array} \right\}$$

   with $\Delta_{n+1}^{(k)} = \det(\mathbf{Dr}_{n+1}^{(k)})$ and $\delta^{(k)} \in (0,1]$ which denotes the proper line-search parameter. **4.** Return map with the *plastic/damage correction*,

$$\tilde{s}_{n+1,A} = \tilde{s}_{n+1,A}^{tri} - 2\mu \frac{\Delta\gamma}{(1-D_{n+1})} \frac{\tilde{s}_{n+1,A}^{tri}}{\|\tilde{s}_{n+1}^{tri}\|}$$

$$\alpha_{n+1} = \alpha_n + \sqrt{\frac{2}{3}}\Delta\gamma$$

5. Find the homogenized *total* Kirchhoff stresses,

$$\tau_{n+1,A} = (1-D_{n+1})(\tilde{s}_{n+1,A} + \tilde{p}_{n+1})$$

6. Update the intermediate configuration,

$$b_{n+1,A}^e = J^{\frac{2}{3}}\exp\left[\frac{\tilde{s}_{n+1,A}}{\mu}\right], \text{ with } \mathbf{b}_{n+1}^e = \sum_{A=1}^{3} b_{n+1,A}^e \mathbf{m}_{n+1}^{tri,A}$$

Reduction to a Single Equation: Following [172], one can further reduce the number of equations, making use of the condition where, D_{n+1} can explicitly be represented in terms of $\Delta\gamma$, as follows,

$$D_{n+1}(\Delta\gamma) = 1 - 2\mu\,\Delta\gamma\,\frac{1}{\left\|\tilde{\mathbf{s}}_{n+1}^{tri}\right\| - \sqrt{\frac{2}{3}}\left\{\tau_0 + K'(\alpha_n + \sqrt{\frac{2}{3}}\,\Delta\gamma)\right\}}. \qquad (2.84)$$

Substituting (2.84) in (2.67), one may carry out a single highly nonlinear equation, in the residual form,

$$r_{n+1} = D_{n+1}(\Delta\gamma) - D_n - \Delta\gamma\,g(D_{n+1}(\Delta\gamma), Y_{n+1}(\Delta\gamma)), \qquad (2.85)$$

where $r_{n+1} = r_{n+1}(\kappa_{n+1}) = 0$. The local problem is solved following similar steps as before, with $\kappa_{n+1} = \Delta\gamma$ and $dr_{n+1} = (\partial r_{n+1}/\partial\Delta\gamma)\,d\kappa_{n+1}$. For the global problem,

$$r_{n+1} = r_{n+1}(\hat{\mathbf{x}}_{n+1}) = \mathbf{0}; \quad \hat{\mathbf{x}}_{n+1}\left\{\begin{array}{c} \epsilon_{n+1,\,1} \\ \epsilon_{n+1,\,2} \\ \epsilon_{n+1,\,3} \\ \Delta\gamma \end{array}\right\}. \qquad (2.86)$$

the vanishing total differential, $dr_{n+1} = 0$, reads,

$$dr_{n+1} = \sum_{A=1}^{3}\frac{\partial r_{n+1}}{\partial\epsilon_{n+1,\,A}}\,d\epsilon_{n+1,\,A} + \frac{\partial r_{n+1}}{\partial\Delta\gamma}\,d\Delta\gamma = 0, \qquad (2.87)$$

which gives the following expression, used in the algorithmic material tangent moduli,

$$\frac{d\Delta\gamma}{d\epsilon_{n+1,\,A}} = -(\partial r_{n+1}\partial\Delta\gamma)^{-1}\frac{\partial r_{n+1}}{\partial\epsilon_{n+1,\,A}}, \qquad (2.88)$$

where the derivation of $dD_{n+1}/d\epsilon_{n+1,\,A}$ requires the application of the chain rule of differentiation, using (2.84), as follows,

$$\frac{dD_{n+1}}{d\epsilon_{n+1,\,A}} = \frac{\partial D_{n+1}}{\partial\Delta\gamma}\frac{\partial\Delta\gamma}{\partial\epsilon_{n+1,\,A}}, \qquad (2.89)$$

which concludes the simultaneous plasticity-damage solution schemes.

2.3.2.2 Staggered Local Integration Schemes

The plastic/damage corrector phase can be taken in a staggered approach where an initial plastic correction is done without damage evolution and damage is realized under frozen plasticity conditions. The result is a three-step, elastic predictor, plastic

corrector and damage deteriorator type algorithm, which results in a quite handy code. This is because simultaneous satisfaction of the whole equation set, given in (2.68), is not required. The efficiency of such an approach, by bypassing the obligation of concurrent fulfillment of two nonlinear equations, is also mentioned in [85], in the context of a two surface damage coupled plasticity model.

To solve the system of equations in a staggered manner, one has to numerically decouple the plastic correction and the damage deterioration steps. Below setting shows the schematic illustration of the problem.

Table 2.7: Three-step operator-split with a staggered plastic/damage correction.

Total	Elastic Predictor	Plastic Corrector	Damage Deteriorator
$\left\{\begin{array}{l}\partial_t \boldsymbol{\epsilon} \neq 0 \\ \mathcal{L}_v \mathbf{b}^e \neq 0 \\ \partial_t \alpha \neq 0 \\ \partial_t D \neq 0\end{array}\right\} =$	$\left\{\begin{array}{l}\partial_t \boldsymbol{\epsilon} \neq 0 \\ \mathcal{L}_v \mathbf{b}^e = 0 \\ \partial_t \alpha = 0 \\ \partial_t D = 0\end{array}\right\} +$	$\left\{\begin{array}{l}\partial_t \boldsymbol{\epsilon} = 0 \\ \mathcal{L}_v \mathbf{b}^e \neq 0 \\ \partial_t \alpha \neq 0 \\ \partial_t D = 0\end{array}\right\} +$	$\left\{\begin{array}{l}\partial_t \boldsymbol{\epsilon} = 0 \\ \mathcal{L}_v \mathbf{b}^e = 0 \\ \partial_t \alpha = 0 \\ \partial_t D \neq 0\end{array}\right\} .$

Accordingly the plastic correction under frozen damage conditions, i.e. $D = D_n$, reads,

$$
\mathbf{r}_{n+1} = \mathbf{r}_{n+1}(\mathbf{x}_{n+1}) \left\{\begin{array}{l} \tau_{n+1,\,1} - \tau^{tri}_{n+1,\,1} + 2\mu\Delta\gamma\; n_{n+1,1} \\[4pt] \tau_{n+1,\,2} - \tau^{tri}_{n+1,\,2} + 2\mu\Delta\gamma\; n_{n+1,2} \\[4pt] \tau_{n+1,\,3} - \tau^{tri}_{n+1,\,3} + 2\mu\Delta\gamma\; n_{n+1,3} \\[4pt] \alpha_{n+1} - \alpha_n - \sqrt{\tfrac{2}{3}}\,\Delta\gamma \\[4pt] q_{n+1} - K'(\alpha_{n+1}) \\[4pt] \tilde{\phi}_{n+1} := \|\tilde{\mathbf{s}}_{n+1}\| - \sqrt{\tfrac{2}{3}}\,y\,(q_{n+1}) \end{array}\right\} \;;\quad \mathbf{x}_{n+1} \left\{\begin{array}{l} \tau_{n+1,\,1} \\[4pt] \tau_{n+1,\,2} \\[4pt] \tau_{n+1,\,3} \\[4pt] \Delta\gamma \\[4pt] \alpha_{n+1} \\[4pt] q_{n+1} \end{array}\right\} .
$$

(2.90)

where $\mathbf{r}_{n+1}(\mathbf{x}_{n+1}) = \mathbf{0}$. Following the solution of this set, the damage integration under constant plastic flow, for the recently found $\Delta\gamma$, takes place, with the following modified general mid-point integration,

$$
D_{n+1} = D_n + \Delta\gamma\;[(1-\theta)\,g_n + \theta\,g_{n+\theta}]\,, \tag{2.91}
$$

where $g_n = g(Y_n^{d,+}; \alpha_{n+1}, D_n)$ with $Y_n^{d,+} = Y^{d,+}(\alpha_{n+1}, D_n)$, and $g_{n+\theta} = g(Y_{n+\theta}^{d,+}; \alpha_{n+1}, D_{n+\theta})$ with $Y_{n+\theta}^{d,+} = Y^{d,+}(\alpha_{n+1}, D_{n+\theta})$. In these forms, the requirement of the

use of the currently converged equivalent plastic strains, i.e. α_{n+1}, of the plastic correction step, should be emphasized. (2.91) is merely solved for D_{n+1}. As a final stage, damage deterioration is applied to the plastically corrected homogenized principal stresses, exploiting the effective stress definition as follows,

$$\tau_{n+1, A} = (1 - D_{n+1}) \frac{\tau_{n+1, A}}{(1 - D_n)}. \tag{2.92}$$

Reducing the number of equations, the decoupled residuals for plastic correction and damage integration can be simply written as follows,

$$\mathbf{r}_{n+1} = \left\{ \begin{array}{c} \sqrt{\tfrac{2}{3}} \{\tau_0 + K'(\alpha_n + \sqrt{\tfrac{2}{3}} \Delta\gamma)\} - \left\| \tilde{\mathbf{s}}_{n+1}^{tri} \right\| + 2\mu \frac{\Delta\gamma}{(1-D_n)} \\ D_{n+1} - D_n - \Delta\gamma \; [(1 - \theta) \, g_n + \theta \, g_{n+\theta}] \end{array} \right\}, \tag{2.93}$$

where $\mathbf{r}_{n+1} = \mathbf{0}$. With the uncoupled nature of the staggered approach, plasticity evolves under constant damage and damage evolves under the recently converged constant plastic multiplier. The linearized version can be given in a compact form as follows,

$$\left\{ \begin{array}{c} \mathrm{d}r_{1,n+1} \\ \mathrm{d}r_{2,n+1} \end{array} \right\} = \left[\begin{array}{cc} \left. \frac{\partial r_{1,n+1}}{\partial \Delta\gamma} \right|_{D=D_n} & 0 \\ 0 & \left. \frac{\partial r_{2,n+1}}{\partial D_{n+1}} \right|_{\alpha=\alpha_{n+1}} \end{array} \right] \bullet \left\{ \begin{array}{c} \mathrm{d}\Delta\gamma \\ \mathrm{d}D_{n+1} \end{array} \right\}. \tag{2.94}$$

For the global more general problem, using (2.83) together with (2.94) reveals the following explicitly derived forms, which will be used in the algorithmic material tangent computations,

$$\left\{ \begin{array}{c} \frac{\mathrm{d}\Delta\gamma}{\mathrm{d}\epsilon_{n+1, A}} \\ \frac{\mathrm{d}D_{n+1}}{\mathrm{d}\epsilon_{n+1, A}} \end{array} \right\} = - \left\{ \begin{array}{c} \left(\frac{\partial r_{1,n+1}}{\partial \Delta\gamma} \right)^{-1} \left. \frac{\partial r_{1,n+1}}{\partial \epsilon_{n+1, A}} \right|_{D=D_n} \\ \left(\frac{\partial r_{2,n+1}}{\partial D_{n+1}} \right)^{-1} \left. \frac{\partial r_{2,n+1}}{\partial \epsilon_{n+1, A}} \right|_{\alpha=\alpha_{n+1}} \end{array} \right\}. \tag{2.95}$$

The algorithmic treatment of the staggered approach is summarized in Table 2.8. The efficiency of the use of staggered approach together with an explicit damage integration, with significantly reduced number of operations, is apparent for the explicit FE solution procedures, where the process time is controlled mainly by the local integration computations. Now, the algorithmic moduli derivations for the global solution schemes, which supplies the quadratic convergence of the iterative procedure once the sufficiently close initial guess is realized, [166], are visited.

Table 2.8: Scheme for the return-mapping algorithm for staggered scheme with three-step operator-split (Elastic predictor-plastic corrector-damage deteriorator type algorithm).

---

1. Process Table 2.5. (Elastic predictor),
2. Check for plastic loading on effective Kirchhoff stress space,

$$\tilde{\phi}_{n+1}^{tri} = \{(\tilde{s}_{n+1,1}^{tri})^2 + (\tilde{s}_{n+1,2}^{tri})^2 + (\tilde{s}_{n+1,3}^{tri})^2\}^{1/2} - \sqrt{\frac{2}{3}}\{\tau_0 + K(\alpha_n)\}$$

    IF $\tilde{\phi}_{n+1}^{tri} \leq 0$ **THEN**
Set $(\bullet)_{n+1} = (\bullet)_{n+1}^{tri}$, **EXIT**. (Elastic step)
ELSE
GOTO 3. (Plastic corrector)
ENDIF
3. Find the plastic multiplier, $\Delta\gamma^{(0)} = 0$,

$$\Delta\gamma^{(k+1)} = \Delta\gamma^{(k)} - \left.\frac{\partial r_{1,n+1}}{\partial\Delta\gamma}\right|_{D=D_n}^{(k)} r_{1,n+1}|_{D=D_n}^{(k)}$$

4. *Correct plastically* the effective Kirchhoff stresses,

$$\tilde{s}_{n+1,A} = \tilde{s}_{n+1,A}^{tri} - 2\mu\frac{\Delta\gamma}{(1-D_n)}\frac{\tilde{s}_{n+1,A}^{tri}}{\|\tilde{s}_{n+1}^{tri}\|}$$

$$\alpha_{n+1} = \alpha_n + \sqrt{\frac{2}{3}}\Delta\gamma$$

5. Find the current damage, $D_{n+1}^{(0)} = D_n$, with line-search,

$$D_{n+1}^{(m+1)} = D_{n+1}^{(m)} - \delta^{(m)}\left.\frac{\partial r_{2,n+1}}{\partial D_{n+1}}\right|_{\alpha=\alpha_{n+1}}^{(m)} r_{2,n+1}|_{\alpha=\alpha_{n+1}}^{(m)}$$

    with $\delta^{(m)} \in (0,1]$, which denotes the proper line-search parameter.
6. Apply the *damage deterioration*,

$$\tau_{n+1,A} = (1-D_{n+1})(\tilde{s}_{n+1,A} + \tilde{p}_{n+1})$$

7. Update the intermediate configuration,

$$b_{n+1,A}^e = J^{\frac{2}{3}}\exp\left[\frac{\tilde{s}_{n+1,A}}{\mu}\right], \quad\text{with}\quad \mathbf{b}_{n+1}^e = \sum_{A=1}^{3} b_{n+1,A}^e \mathbf{m}_{n+1}^{tri,A}.$$

2.3.3   Consistent Tangent Moduli

In the global more general problem, $\boldsymbol{\tau} = \boldsymbol{\tau}(\epsilon, \Delta\gamma(\epsilon), D(\epsilon))$, where the spectral decomposition of the homogenized KIRCHHOFF stress tensor, i.e. $\boldsymbol{\tau}_{n+1} = (1 - D_{n+1})\tilde{\boldsymbol{\tau}}_{n+1}$,

for $t = t_{n+1}$ is,

$$\boldsymbol{\tau}_{n+1} = \sum_{A=1}^{3} \tau_{n+1,A} \, \mathbf{m}_{n+1}^{tri,A}. \tag{2.96}$$

Following relation gives the definition of the spatial elasto-plastic-damage tangent moduli, [161],

$$c_{ijkl} = 2 \, F_{iI} \, F_{jJ} \, F_{kK} \, F_{lL} \, \frac{\partial S_{IJ}}{\partial C_{KL}}, \tag{2.97}$$

which is a push-forward transformation of material tangent. $\mathbf{S} = \mathbf{F}^{-1} \bullet \boldsymbol{\tau} \bullet \mathbf{F}^{-T}$, is the Second PIOLA KIRCHHOFF stress tensor, i.e. the pull-back transform of the KIRCHHOFF stress tensor and $\mathbf{C}$ is the right CAUCHY-GREEN deformation tensor. An explicit representation of the tensor can be given as,

$$\mathbb{C} = \sum_{A=1}^{3} \sum_{B=1}^{3} a_{n+1,AB}^{epd} \, \mathbf{m}_{n+1}^{tri,A} \otimes \mathbf{m}_{n+1}^{tri,B} + 2 \sum_{A=1}^{3} \tau_{n+1,A} \widehat{\mathbb{C}}_{n+1}^{tri,A}. \tag{2.98}$$

Starting with the first part of (3.84), $a_{n+1,AB}^{epd}$ is the following 3×3 matrix [8],

$$a_{n+1,AB}^{epd} = \frac{\mathrm{d}\tau_{n+1,A}}{\mathrm{d}\epsilon_{n+1,B}^{tri}}, \tag{2.99}$$

the computation of which requires the following chain rule of differentiation,

$$\frac{\mathrm{d}\tau_{n+1,A}}{\mathrm{d}\epsilon_{n+1,B}^{tri}} = \frac{\partial \tau_{n+1,A}}{\partial \epsilon_{n+1,B}^{tri}} + \frac{\partial \tau_{n+1,A}}{\partial \Delta\gamma} \frac{\partial \Delta\gamma}{\partial \epsilon_{n+1,B}^{tri}} + \frac{\partial \tau_{n+1,A}}{\partial D_{n+1}} \frac{\partial D_{n+1}}{\partial \epsilon_{n+1,B}^{tri}}, \tag{2.100}$$

with

$$\frac{\partial \tau_{n+1,A}}{\partial \epsilon_{n+1,B}^{tri}} = (1 - D_{n+1}) \frac{\partial \tau_{n+1,A}^{tri}}{\partial \epsilon_{n+1,B}^{tri}} - 2\mu\Delta\gamma \, \frac{\partial n_{n+1,A}}{\partial \epsilon_{n+1,B}^{tri}} \tag{2.101}$$

$$\frac{\partial \tau_{n+1,A}}{\partial \Delta\gamma} = -2\mu \, n_{n+1,A} \tag{2.102}$$

$$\frac{\partial \tau_{n+1,A}}{\partial D_{n+1}} = -\tau_{n+1,A}^{tri}. \tag{2.103}$$

Using $\delta_{AB}^{dev} = \delta_{AB} - \frac{1}{3}$, with δ_{AB} representing the KRONECKER delta which is given as,

$$\delta_{AB} = \begin{cases} 1, & \text{if } A = B; \\ 0, & \text{otherwise.} \end{cases} \tag{2.104}$$

one can find,

$$\frac{\partial \tau_{n+1,A}^{tri}}{\partial \epsilon_{n+1,B}^{tri}} = H + 2\mu\delta_{AB}^{dev}, \tag{2.105}$$

$$\frac{\partial n_{n+1,A}}{\partial \epsilon_{n+1,B}^{tri}} = \frac{2\mu}{\|\tilde{\mathbf{s}}_{n+1}^{tri}\|} \{\delta_{AB}^{dev} - n_{n+1,A} \, n_{n+1,B}\}. \tag{2.106}$$

---

[8] Taking the differential of the trial logarithmic elastic strains, i.e. $\boldsymbol{\epsilon}_{n+1}^{e,tri} = \boldsymbol{\epsilon}_{n+1} - \boldsymbol{\epsilon}_{n}^{p}$, will result in, $\mathrm{d}\boldsymbol{\epsilon}_{n+1}^{e,tri} = \mathrm{d}\boldsymbol{\epsilon}_{n+1} - \mathrm{d}\boldsymbol{\epsilon}_{n}^{p}$. Since for $t = t_{n+1}$, $\mathrm{d}\boldsymbol{\epsilon}_{n}^{p} = 0$, $\mathrm{d}\boldsymbol{\epsilon}_{n+1}^{e,tri} = \mathrm{d}\boldsymbol{\epsilon}_{n+1}$.

In § 2.3.2.1 and § 2.3.2.2, the expressions, $\partial\Delta\gamma/\partial\boldsymbol{\epsilon}_{n+1}$ and $\partial D_{n+1}/\partial\boldsymbol{\epsilon}_{n+1}$ in principal components, are already supplied for different integration schemes. Exploiting the previously derived $\mathrm{d}\boldsymbol{\epsilon}_{n+1}^{e,tri} = \mathrm{d}\boldsymbol{\epsilon}_{n+1}$, the outcomes for $\partial\Delta\gamma/\partial\boldsymbol{\epsilon}_{n+1}^{e,tri}$ and $\partial D_{n+1}/\partial\boldsymbol{\epsilon}_{n+1}^{e,tri}$ can be found. Accordingly, making use of (2.83) for the simultaneous scheme with two equations, (2.88) and (2.89) for the simultaneous scheme with a single equation, and finally (2.95) for the staggered approach with two equations, with the substitution $\partial\boldsymbol{\epsilon}_{n+1} \rightarrow \partial\boldsymbol{\epsilon}_{n+1}^{e,tri}$, is sufficient. Unreduced sets involve rather lengthy derivations, which are not included here.

It is noteworthy that, in case of no damage coupling, $\mathbf{a}_{n+1}^{epd}$ boils down to $\mathbf{a}_{n+1}^{ep}$ given in [161], for nonlinear isotropic hardening finite plasticity formulated in principal axes.

Coming to the second part of (3.84), $\widehat{\mathbb{C}}_{n+1}^{tri,A}$ is the spectral direction variation in the form of eigen-dyad derivatives with respect to the Eulerian metric tensor (rotation of the eigen-bases). The derivation reveals the following expression with eigen-projections[9], see, e.g. [167] and [161].

$$
\begin{aligned}
\widehat{\mathbb{C}}_{n+1}^{tri,A} = &\frac{1}{D_A}[\mathbb{I}^{\mathbf{b}_{n+1}^{e,tri}} - \mathbf{b}_{n+1}^{e,tri} \otimes \mathbf{b}_{n+1}^{e,tri} + I_3\,\lambda_{n+1,A}^{e,tri,-2}\,(\mathbf{1}\otimes\mathbf{1} - \mathbb{I})] \\
&+ \frac{1}{D_A}[\lambda_{n+1,A}^{e,tri,2}\,(\mathbf{b}_{n+1}^{e,tri} \otimes \mathbf{m}_{n+1}^{tri,A} + \mathbf{m}_{n+1}^{tri,A} \otimes \mathbf{b}_{n+1}^{e,tri}) \\
&- \frac{1}{2}D_A'\,\lambda_{n+1,A}^{e,tri}\mathbf{m}_{n+1}^{tri,A} \otimes \mathbf{m}_{n+1}^{tri,A}] \\
&- \frac{1}{D_A}[I_3\,\lambda_{n+1,A}^{e,tri,-2}\,(\mathbf{1}\otimes\mathbf{m}_{n+1}^{tri,A} + \mathbf{m}_{n+1}^{tri,A}\otimes\mathbf{1})],
\end{aligned}
\tag{2.107}
$$

where,

$$
\mathbb{I} = \frac{1}{2}(\mathbf{1}\oplus\mathbf{1} + \mathbf{1}\ominus\mathbf{1}),
\tag{2.108}
$$

$$
\mathbb{I}^{\mathbf{b}_{n+1}^{e,tri}} = \frac{1}{2}(\mathbf{b}_{n+1}^{e,tri}\oplus\mathbf{b}_{n+1}^{e,tri} + \mathbf{b}_{n+1}^{e,tri}\ominus\mathbf{b}_{n+1}^{e,tri}),
\tag{2.109}
$$

and,

$$
D_A' = 8\lambda_{n+1,A}^{e,tri,3} - 2I_1\lambda_{n+1,A}^{e,tri} - 2I_3\lambda_{n+1,A}^{e,tri,-3}.
\tag{2.110}
$$

(2.73) and (2.107) require computation of D_A, which is given in (2.53). An explicit designation of D_A may be furnished as, $D_A = (\lambda_{n+1,A}^{e,tri,2} - \lambda_{n+1,B}^{e,tri,2})(\lambda_{n+1,A}^{e,tri,2} - \lambda_{n+1,C}^{e,tri,2})$, where an even permutation of indices $(1,2,3)$ is denoted by (A,B,C), [167]. (2.73) and (2.107), suffer from singularities or ill-conditioning, for equal or nearly equal

---

[9] The fourth order tensor can also be computed using eigenvectors. [121] shows that an use of eigen-bases ends up with a faster computation.

eigenvalues, respectively, with $D_A \to 0$. In treatment of such cases, different methods, analytical or numerical, are suggested. As an analytical approach, [130, pp. 338–341], in the context of eigen-vector formulation, uses systematic application of the L'HOSPITAL rule to create special expressions for diverse situations. Coming to the numerical methods, the use of perturbation schemes are common, where equal or numerically close eigenvalues are perturbed to have distinct values. This enables treatment of these special cases in the general class of distinct eigenvalues, making use of (2.73) and (2.107). In the current study, due to its feasibility, this latter approach is used. Accordingly for sufficiently close $\lambda^{e,tri}_{n+1,\,A}$ and $\lambda^{e,tri}_{n+1,\,B}$, the following perturbation scheme is applied, [119],

$$\begin{Bmatrix} \lambda^{e,tri}_{n+1,\,A} \\ \lambda^{e,tri}_{n+1,\,B} \\ \lambda^{e,tri}_{n+1,\,C} \end{Bmatrix} = \begin{Bmatrix} (1+\delta)\,\lambda^{e,tri}_{n+1,\,A} \\ (1-\delta)\,\lambda^{e,tri}_{n+1,\,B} \\ 1/[(1+\delta)(1-\delta)]\,\lambda^{e,tri}_{n+1,\,C} \end{Bmatrix}, \text{ with } \delta \ll 1. \qquad (2.111)$$

2.3.4 Expansion to Kinematic Hardening

For the sake of completeness, the algorithmic forms for the simultaneous scheme are involved for combined isotropic kinematic hardening plasticity coupled with damage. Accordingly, the definition of the trial state additionally requires,

$$\mathbf{z}^{tri}_{n+1} = \mathbf{z}_n. \qquad (2.112)$$

The spectral decomposition of $\mathbf{z}^{tri}_{n+1,\,A}$ read, $z^{tri}_{n+1,\,A} = \gamma^{tri,\,2}_{n+1,\,A} = \gamma^2_{n,\,A}$, for both Model A and Model B,

$$\mathbf{z}^{tri}_{n+1} = \sum_{A=1}^{3} \gamma^{tri,\,2}_{n+1,\,A}\,\boldsymbol{\nu}^{tri,\,A}_{n+1} \otimes \boldsymbol{\nu}^{tri,\,A}_{n+1}, \qquad (2.113)$$

where the algorithmic counterpart of the evolution equation of the kinematic hardening strain like variable is,

$$\begin{aligned} \mathcal{L}_v \mathbf{z}_{n+1} &= -2\,\dot{\gamma}_{n+1}\,\partial_{\boldsymbol{\beta}}\tilde{\phi}\Big|_{n+1} \bullet \mathbf{z}_{n+1}; \quad \text{Model A;} \\ \overset{\triangle}{\mathbf{z}}_{n+1} &= -\dot{\gamma}_{n+1}\,\partial_{\boldsymbol{\beta}}\tilde{\phi}\Big|_{n+1}; \qquad\qquad \text{Model B.} \end{aligned} \qquad (2.114)$$

Utilizing exponential mapping and backward EULER method for integration of Model A and Model B, respectively, one has,

$$\begin{aligned} \mathbf{z}_{n+1} &= \exp\left[2\,\Delta\gamma\,\partial_{\boldsymbol{\beta}}\tilde{\phi}\Big|_{n+1}\right] \bullet \mathbf{z}^{tri}_{n+1}; \quad \text{Model A;} \\ \mathbf{z}_{n+1} &= \mathbf{z}^{tri}_{n+1} + \Delta\gamma\,\partial_{\boldsymbol{\beta}}\tilde{\phi}\Big|_{n+1}; \qquad\quad \text{Model B.} \end{aligned} \qquad (2.115)$$

Refining (2.115) to constitute the principal stretches, one carries out,

$$\gamma_{n+1,\,A} = \exp\left[\Delta\gamma \left.\frac{\partial\tilde{\phi}}{\partial\beta_A}\right|_{n+1}\right] \gamma_{n+1,\,A}^{tri}; \quad \text{Model A};$$

$$\gamma_{n+1,\,A} = \gamma_{n+1,\,A}^{tri} + \Delta\gamma \left.\frac{\partial\tilde{\phi}}{\partial\beta_A}\right|_{n+1}; \qquad \text{Model B}. \tag{2.116}$$

For Model A, taking the natural logarithms of both sides, one obtains the following relation,

$$\kappa_{n+1,\,A} = \kappa_{n+1,\,A}^{tri} + \Delta\gamma \left.\frac{\partial\tilde{\phi}}{\partial\beta_A}\right|_{n+1}, \tag{2.117}$$

Eventually one has,

$$\kappa_{n+1,\,A} = \kappa_{n+1,\,A}^{tri} - \Delta\kappa_{n+1,\,A}; \quad \text{Model A};$$

$$z_{n+1,\,A} = z_{n+1,\,A}^{tri} - \Delta z_{n+1,\,A}^{p}; \quad \text{Model B}. \tag{2.118}$$

where the principal strain corrections read,

$$\Delta\kappa_{n+1,\,A} = \Delta\gamma \left.\frac{\partial\tilde{\phi}}{\partial\beta_A}\right|_{n+1}; \quad \text{Model A};$$

$$\Delta z_{n+1,\,A} = \Delta\gamma \left.\frac{\partial\tilde{\phi}}{\partial\beta_A}\right|_{n+1}; \quad \text{Model B}. \tag{2.119}$$

In the current setting, since the back stress and the stress tensors commute, the exponential mapping is exactly satisfied, [57], and the use of the principal components rather than tensorial descriptions become available. Unless the coaxiality is presumed, the reduction of the forms to the principal space is not possible.

It is noteworthy that since the stress corrections in the deviatoric KIRCHHOFF stress space for the back stress give identical results for Model A and Model B, such as,

$$\beta_{n+1,\,A} = \beta_{n+1,\,A}^{tri} + \frac{2}{3}C\,\Delta\gamma\,n_{n+1,\,A}. \tag{2.120}$$

Final equation to be satisfied is the yield function computed at the current step,

$$\tilde{\phi}_{n+1} := \|\boldsymbol{\xi}_{n+1}\| - \sqrt{\frac{2}{3}}\,y\,(q_{n+1}) = 0. \tag{2.121}$$

In a residual setting, using the effective stresses definition with (2.63), for the current and the trial principal stress components, the complete simultaneous set of equations

can be given as,

$$
\mathbf{r}_{n+1} =
\begin{Bmatrix}
\tau_{n+1,A} - \tau^{tri}_{n+1,A} + 2\mu\Delta\gamma\, n_{n+1,A} \\
\beta_{n+1,A} - \beta^{tri}_{n+1,A} - (2/3)C(\theta)\,\Delta\gamma\, n_{n+1,A} \\
\alpha_{n+1} - \alpha_n - \sqrt{\tfrac{2}{3}}\,\Delta\gamma \\
q_{n+1} - K'(\alpha_{n+1}) \\
\tilde{\phi}_{n+1} := \|\boldsymbol{\xi}_{n+1}\| - \sqrt{\tfrac{2}{3}}\, y\,(q_{n+1}) \\
D_{n+1} - D_n - \Delta\gamma\, g_{n+1}
\end{Bmatrix}
\; ; \quad
\mathbf{x}_{n+1}
\begin{Bmatrix}
\tau_{n+1,A} \\
\beta_{n+1,A} \\
\Delta\gamma \\
D_{n+1} \\
\alpha_{n+1} \\
q_{n+1}
\end{Bmatrix}.
\tag{2.122}
$$

with $(A = 1,2,3)$. where $\mathbf{r}_{n+1}(\mathbf{x}_{n+1}) = \mathbf{0}$. Following [166], the local governing equations collected in (2.122) can be reduced, particularly for the chosen yield criterion, making use of the substitution, $\xi_{n+1,A} = \|\boldsymbol{\xi}_{n+1}\|\, n_{n+1,A}$

$$
\tilde{\mathbf{s}}_{n+1} - \boldsymbol{\beta}_{n+1} = \tilde{\mathbf{s}}^{tri}_{n+1} - \boldsymbol{\beta}^{tri}_{n+1} - \left\{ 2\mu\,\frac{\Delta\gamma}{(1-D_{n+1})} + \frac{2}{3}C\,\Delta\gamma \right\}\mathbf{n}_{n+1}, \tag{2.123}
$$

$$
\|\boldsymbol{\xi}_{n+1}\|\, n_{n+1,A} = \|\boldsymbol{\xi}^{tri}_{n+1}\|\, n^{tri}_{n+1,A} \\
- \left\{ 2\mu\,\frac{\Delta\gamma}{(1-D_{n+1})} + \frac{2}{3}C\,\Delta\gamma \right\} n_{n+1,A}. \tag{2.124}
$$

Applying the following arrangements,

$$
\left(\|\boldsymbol{\xi}_{n+1}\| + 2\mu\,\frac{\Delta\gamma}{(1-D_{n+1})} + \frac{2}{3}C\,\Delta\gamma \right) n_{n+1,A} = \|\boldsymbol{\xi}^{tri}_{n+1}\|\, n^{tri}_{n+1,A}, \tag{2.125}
$$

and exploiting the condition of collinear flow and the trial KIRCHHOFF stress tensor, where, $\mathbf{n}_{n+1} \equiv \mathbf{n}^{tri}_{n+1}$, [166], the uniqueness of the spectral decomposition yields,

$$
n^{tri}_{n+1,A}\,\mathbf{m}^{tri,A}_{n+1} = n_{n+1,A}\,\mathbf{m}^{A}_{n+1}, \tag{2.126}
$$

which gives $\mathbf{m}^{tri,A}_{n+1} \equiv \mathbf{m}^{A}_{n+1}$ and $n_{n+1,A} \equiv n^{tri}_{n+1,A}$. Utilizing this equivalence, one can write,

$$
\|\boldsymbol{\xi}_{n+1}\| + 2\mu\,\frac{\Delta\gamma}{(1-D_{n+1})} + \frac{2}{3}C\,\Delta\gamma = \|\boldsymbol{\xi}^{tri}_{n+1}\|. \tag{2.127}
$$

Finally, representing the hardening/softening function definition in terms of the plastic multiplier, yields the following reduced form,

$$
\mathbf{r}_{n+1} = \mathbf{r}_{n+1}(\mathbf{x}_{n+1}) =
\begin{Bmatrix}
\sqrt{\tfrac{2}{3}}\left\{ \tau_0 + K'(\alpha_n + \sqrt{\tfrac{2}{3}}\,\Delta\gamma) \right\} \\
\quad - \|\boldsymbol{\xi}^{tri}_{n+1}\| + 2\mu\,\dfrac{\Delta\gamma}{(1-D_{n+1})} + \dfrac{2}{3}C\,\Delta\gamma \\
D_{n+1} - D_n - \Delta\gamma\, g_{n+1}
\end{Bmatrix}
; \tag{2.128}
$$

$$
\mathbf{x}_{n+1} =
\begin{Bmatrix}
\Delta\gamma \\
D_{n+1}
\end{Bmatrix}.
\tag{2.129}
$$

where, for the local return mapping problem follows identical steps with the previously proposed simultaneous routines.

2.4 Application Problems

The given framework is implemented as a user defined material subroutines, `UMAT` for ABAQUS/Standard, `VUMAT` for ABAQUS/Explicit and UFINITE[10], for MSC.Marc, for return mapping in the company of reduced equation couple, together with the simultaneous and the staggered solution schemes which are listed in Table 2.6 and Table 2.8. The staggered solution schemes are supplied with forward (explicit) and backward (implicit) EULER integration for the D. The codes are materialized in accuracy and efficiency assessment of the integration routines and in the simulation of a set of axi-symmetric application problems. Throughout the simulations, a saturation type isotropic hardening function is utilized for plasticity, which is given as,

$$K'(\alpha) = K\,\alpha + (K_\infty - K_0)\,(1 - \exp\left[-\delta\,\alpha\right]).$$

For damage evolution, following simplified LEMAITRE model is selected,

$$g(Y; \alpha, D) = \frac{a}{(1-D)}\,Y,$$

with $Y = Y^{d,+}$.

2.4.1 Geometrical Interpretation and Accuracy and Efficiency Assessment of the Return Map Algorithms

In this first set of application problems, the geometrical insight into the simultaneous and staggered return mapping algorithms is presented. Moreover accuracy and efficiency assessment studies are given which shows relative reliability and performance of the methods for a given strain increment.

---

[10] `UFINITE` serves a suitable environment for isotropic finite strain elasto-plasticity defined by principal stretches. Implementation details of `UFINITE` are well documented in [125, Chp. 3, pp. 280–282].

2.4.1.1 Geometrical Interpretation

Damage softening and isotropic plastic hardening are in competition for a damage coupled plasticity. A geometrical insight into the problem may be supplied by presenting the iterative return map for a given trial stress state on the Π plane. For this purpose, following hypothetical material properties given in Table 2.9, which gives geometrically clear resultants, are selected. Besides, an initial 1D stress state on the yield surface is selected, free of any initial plastic strains or damage.

Table 2.9: Material parameters for the example problem.

Parameter	Symbol	Magnitude	Unit
Bulk modulus	H	175	GPa
Shear modulus	μ	80.7692	GPa
Flow stress	τ_0	0.750	GPa
Saturation stress	τ_∞	5	GPa
Linear hardening	K	0.1	GPa
Hardening exponent	δ	10	-
Damage multiplier	a	30	-

Resultant return mapping patterns for a set of strain increments on the Π plane are given for the simultaneous integration algorithm in Figure 2.4. It is seen that an arbitrary elastic trial state is followed by a single plastic/damage correction step. The first observation is the radial character of the return map, where any trial stress state is mapped with a direction normal to the circular yield locus. A noteworthy fact is that, the yield locus on the effective stress space is expanding with plastic hardening whereas damage effect results in a shrinkage on the yield locus represented at the homogenized stress space.

Once the same problem is repeated for the staggered routine, the pattern given in Figure 2.5 is carried out. This time, the radial return requires two additional steps,
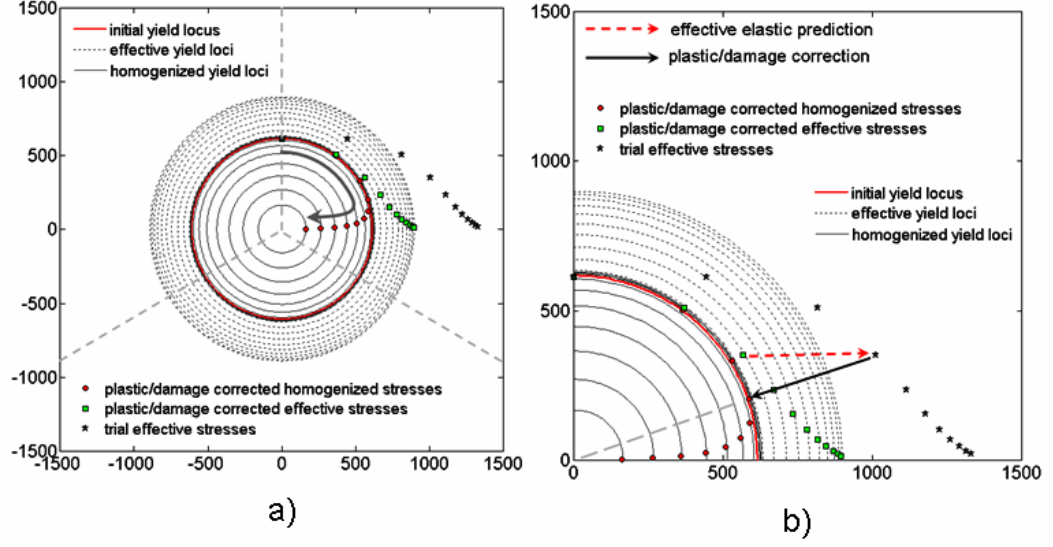
Figure 2.4: Geometrical representation of the return map for the simultaneous integration scheme.

named as plastic correction and damage deterioration, for an arbitrary elastic trial state. Other observations follows the previous solution's results where the difference in between Figure 2.4 and Figure 2.5 is hardly observed which shows the performance of a staggered routine which assumes uncoupled plasticity and damage.
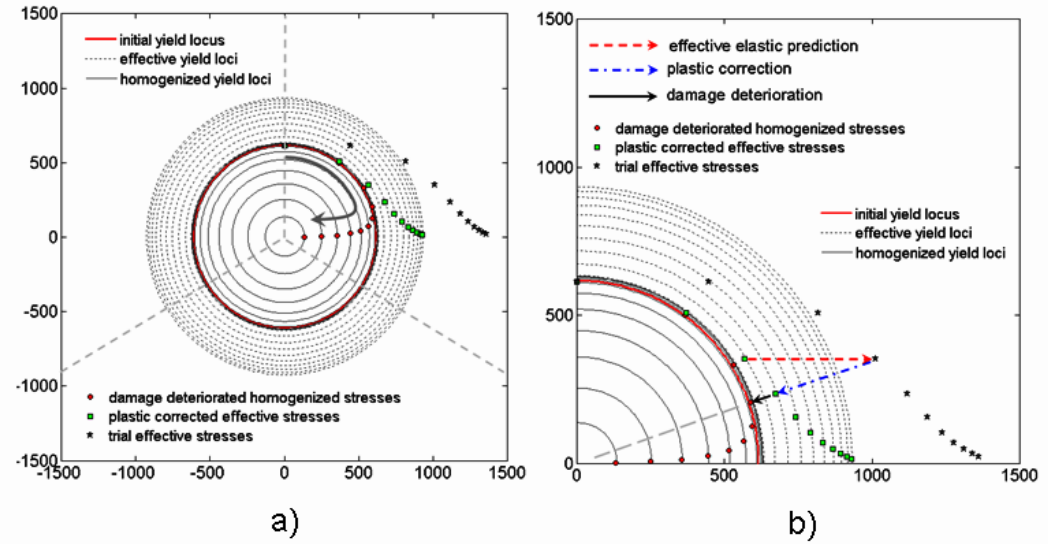
Figure 2.5: Geometrical representation of the return map for the staggered integration scheme.

2.4.1.2 Accuracy Assessment - Isoerror Maps

Isoerror maps lack mathematical rigor however they are very effective in evaluation of the accuracy of the integration routines. The effect of damage integration approaches, such as simultaneous or staggered implicit/explicit, damage functional degree of non-linearity and initial damage on the effect of integration accuracies, is investigated. The material parameters utilized are in variance with those of the previous case where $\tau_\infty=1$ GPa and $a=1.5$ are utilized.

Use of isoerror maps goes back to [93]. An example use may be seen in [131] among others. In damage mechanics, use of isoerror maps is seen in [194]. In the current context, the method is applied for a 3D case. Test point locations are shown Figure 2.6 for the effective KIRCHHOFF stress space where totally four conditions, namely I-A, I-B, II-A and II-B, are analyzed.
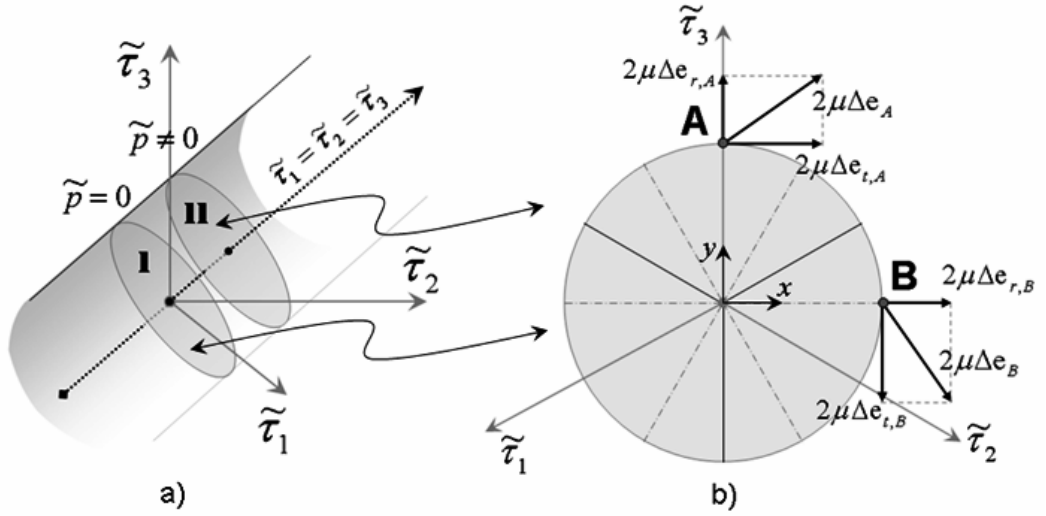
Figure 2.6: Representation of the test points on the Π plane.

I stands for the stress states for no initial pressure and II stands for the pressurized initial state, as seen in selected planes in HAIGH-WESTERGAARD space in Figure 2.6.a. Pressurized cases are to investigate the effect of initial pressure on damage evolution. Figure 2.6.b represents the yield locus on the Π plane, where the marked

point A stands for the uniaxial stress state whereas point B stands for the state with pure shear condition. Deviatoric loads, on the Π plane, tangential and normal to the circular yield locus, as shown in Figure 2.6.b, are applied for the test points and regarding isoerror maps are plotted. Any point on the Π plane on the yield locus can be uniquely defined for a given pressure, LODE angle and yield stress. Depending on the x and y coordinates of the point on the yield locus, the initial principal stress state definition given in (2.130) can be derived for a given pressure, p, and yield stress, τ_0, [76, p. 18],

$$\tilde{\boldsymbol{\tau}}^p = \mathbf{W} \bullet \mathbf{v}, \tag{2.130}$$

where following definitions are valid

$$\tilde{\boldsymbol{\tau}}^p = \left\{ \begin{array}{c} \tilde{\tau}_1 \\ \tilde{\tau}_2 \\ \tilde{\tau}_3 \end{array} \right\}, \quad \mathbf{W} = \left[\begin{array}{ccc} -1/2 & -1/6 & 1 \\ 1/2 & -1/6 & 1 \\ 0 & 1/3 & 1 \end{array} \right], \tag{2.131}$$

together with the specialized $\mathbf{v}$ values, $\mathbf{v}_A$ and $\mathbf{v}_B$, for points A and B, respectively, which are given as,

$$\mathbf{v}_A = \left\{ \begin{array}{c} 0 \\ 2\tau_0 \\ p \end{array} \right\}, \quad \mathbf{v}_B = \left\{ \begin{array}{c} 2\tau_0/\sqrt{3} \\ 0 \\ p \end{array} \right\}. \tag{2.132}$$

Accordingly, for points I-A, I-B, II-A, II-B, the initial stress and strain states are quantitatively given in Table 2.10, for $\tau_0 = 750$ MPa,

Table 2.10: Initial conditions of the selected points.

Test Point	$\tilde{\boldsymbol{\tau}} = \left\{ \begin{array}{ccc} \tilde{\tau}_1, & \tilde{\tau}_2, & \tilde{\tau}_3 \end{array} \right\}^t$	$\boldsymbol{\epsilon}^e = \left\{ \begin{array}{ccc} \epsilon_1^e, & \epsilon_2^e, & \epsilon_3^e \end{array} \right\}^t$
I-A	$\left\{ \begin{array}{c} -250 \\ -250 \\ 500 \end{array} \right\}$	$\left\{ \begin{array}{c} -1.547619047619048\text{e-}003 \\ -1.547619047619048\text{e-}003 \\ 3.095238095238095\text{e-}003 \end{array} \right\}$
I-B	$\left\{ \begin{array}{c} -4.330127018922194\text{e+}002 \\ 4.330127018922194\text{e+}002 \\ 0 \end{array} \right\}$	$\left\{ \begin{array}{c} -2.680554821237549\text{e-}003 \\ 2.680554821237549\text{e-}003 \\ 0 \end{array} \right\}$
II-A	$\left\{ \begin{array}{c} 0 \\ 0 \\ 750 \end{array} \right\}$	$\left\{ \begin{array}{c} -1.071428571428571\text{e-}003 \\ 1.071428571428571\text{e-}003 \\ 3.571428571428571\text{e-}003 \end{array} \right\}$
II-B	$\left\{ \begin{array}{c} -1.830127018922193\text{e+}002 \\ 6.830127018922194\text{e+}002 \\ 2.500000000000000\text{e+}002 \end{array} \right\}$	$\left\{ \begin{array}{c} -2.204364345047072\text{e-}003 \\ 3.156745297428025\text{e-}003 \\ 4.761904761904762\text{e-}004 \end{array} \right\}$

As seen for cases of I no initial pressure is due and for II initial pressure with $\tau_0/3$ is assigned. Since the loads applied lie on the deviatoric Π plane, they also are deviatoric. In numerical accuracy assessment of the integration algorithms, true percent relative errors are computed for different fields. For the stress field, the definition of the error in stress, $\mathfrak{ERR}_\tau$, follows as,

$$\mathfrak{ERR}_\tau = \frac{\sqrt{[\tau_{exact} - \tau_{approximate}] : [\tau_{exact} - \tau_{approximate}]}}{\sqrt{\tau_{exact} : \tau_{exact}}} \times 100. \qquad (2.133)$$

Error is also computed for D and α, which is the radial location of the point on the circular yield surface. For these scalar fields, error formulation utilizes the conventional form. Accordingly for $[\bigstar]$ representing any one of D or α, the error $\mathfrak{ERR}_\bigstar$ becomes,

$$\mathfrak{ERR}_\bigstar = \frac{|\bigstar_{exact} - \bigstar_{approximate}|}{|\bigstar_{exact}|} \times 100. \qquad (2.134)$$

In above computations approximate values are computed with a single step application of the algorithm for the given loading whereas the exact values utilizes 1000 steps, following the common approach in the literature. A 5 percent error can be taken as an acceptable threshold in evaluation of the results. Resultant isoerror maps are given in Figures 2.7, 2.8, 2.9 and 2.10 for test points I-A, II-A, I-B and II-B, respectively. In the representations, columns 1 to 3, respectively designate the isoerror plots for effective stress, equivalent plastic strain and damage errors. Coming to the rows, simultaneous, staggered implicit and staggered explicit schemes are respectively given in row a, b and c.

The difference in the results for difference test points is hardly recognizable. Among the results for integration routines, it is seen that for small strain increments the difference is not obvious however for large strain increments the difference gets importance. Thus one should utilize staggered explicit routines only for small strain increments. In this setting, increasing the number of steps to gain accuracy may increase the computational time thus tempting staggered routine may not be so efficient. However, the result is problem specific. It is shown that once the coupling in between damage and plasticity is omitted, the implicit integration of damage can only increase the damage integration quality to a certain level especially for large loading steps.
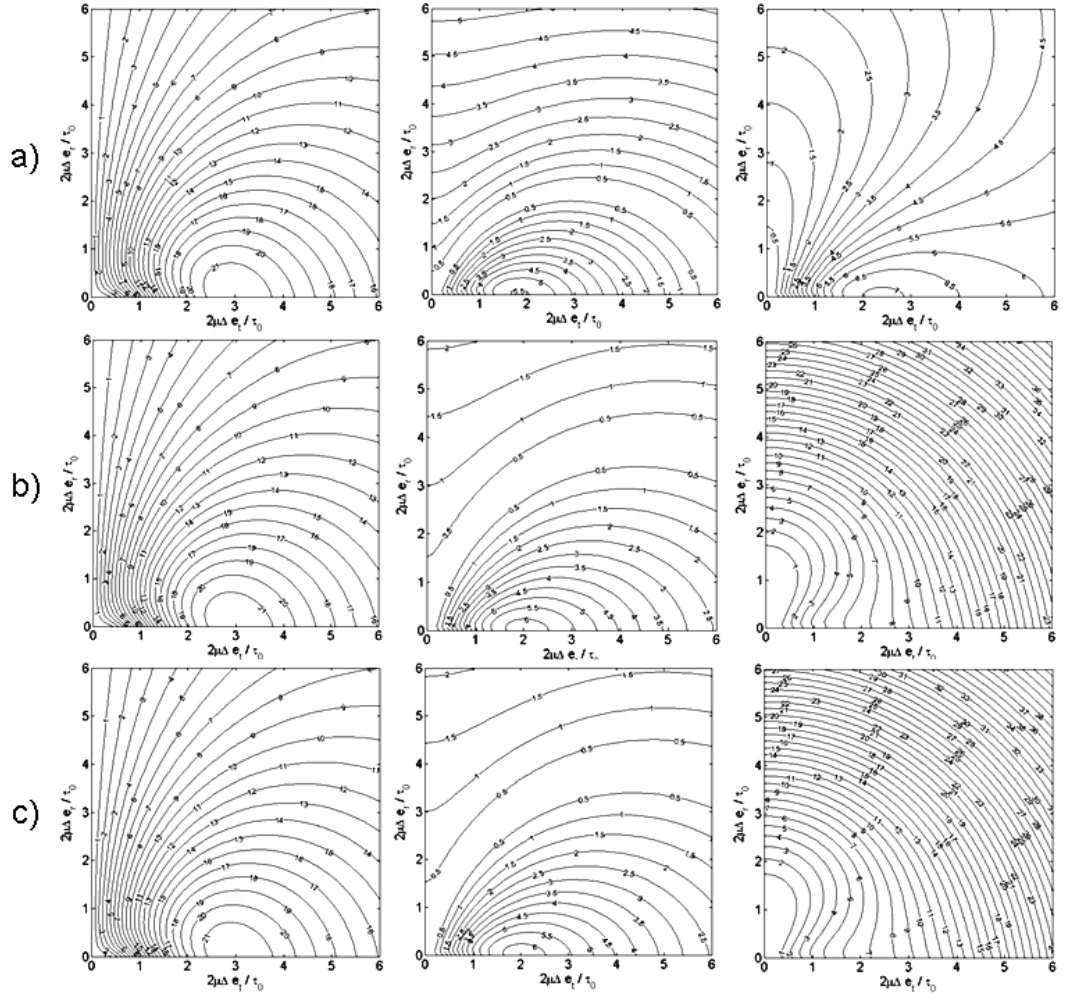
Figure 2.7: Isoerror maps for accuracy assessment of integration algorithms for case I-A.
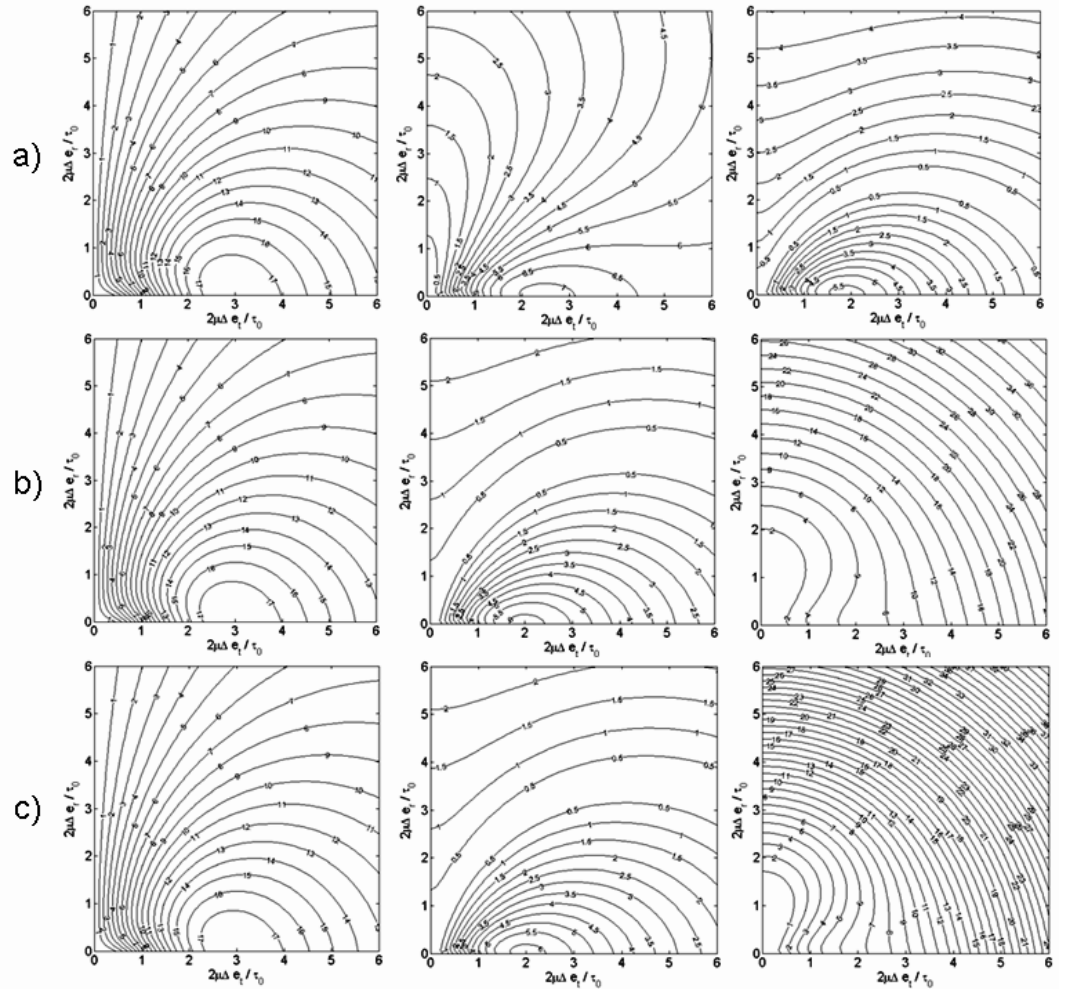
Figure 2.8: Isoerror maps for accuracy assessment of integration algorithms for case II-A.
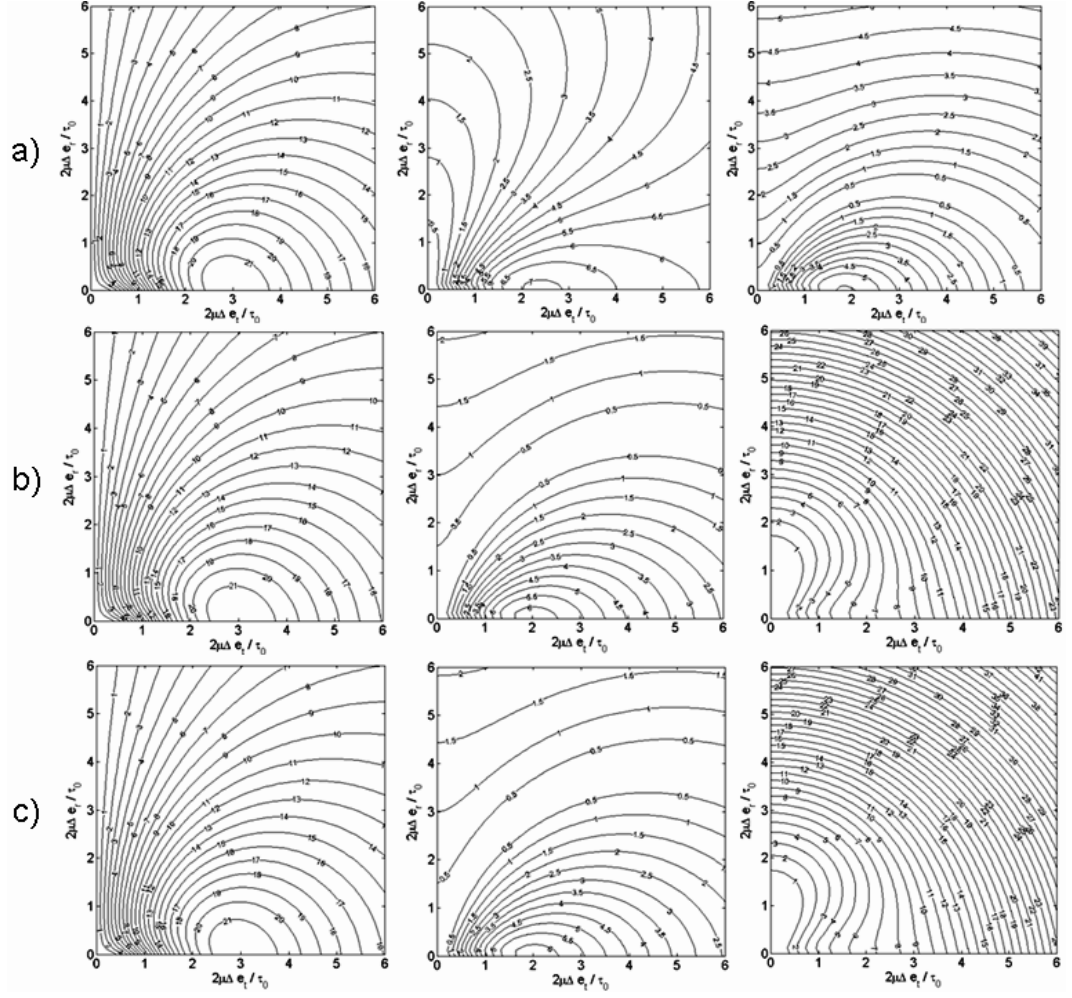
Figure 2.9: Isoerror maps for accuracy assessment of integration algorithms for case I-B.
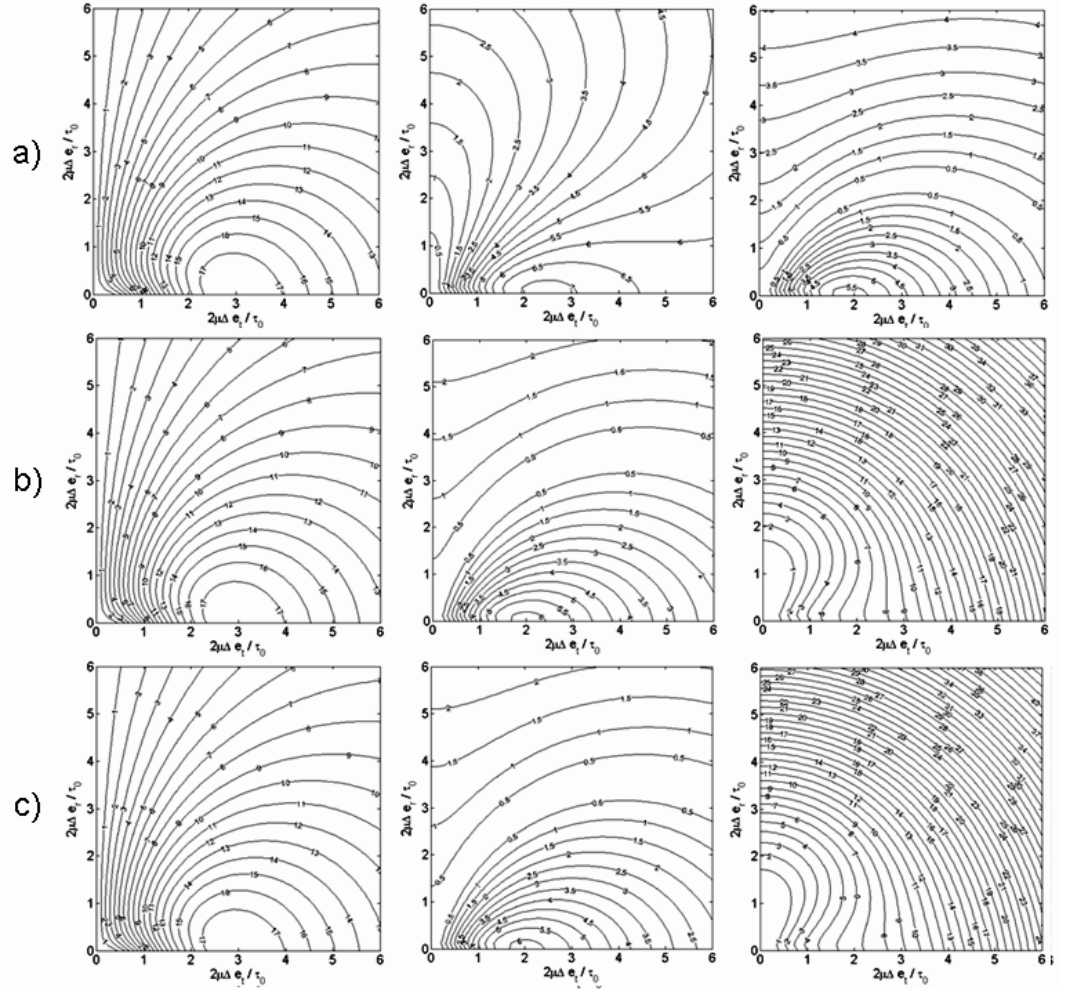
Figure 2.10: Isoerror maps for accuracy assessment of integration algorithms for case II-B.

2.4.1.3 Efficiency Assessment - Convergence Tests

In this section, the concentration is devoted to the number of iterations required in different solution algorithms for a given initial condition and applied load step. For a point lying on the yield locus a logarithmic strain based loading with a magnitude of 0.015 in radial and tangential directions are applied, which for an exact solution creates, a final equivalent plastic strain of 0.018925584826 and damage of 0.033566948053. In the solutions, a convergence threshold of 10e-6 is utilized.

Table 2.11 lists of the equivalent plastic strain and damage values at each iteration for the simultaneous scheme with two reduced equations. As seen, desired precision is satisfied at the sixth iteration.

Table 2.11: Convergence of equivalent plastic strain and damage through iterations, simultaneous scheme.

Iteration	α	D
1	4.706284481469381E-003	0.621381030670264
2	1.459249815639381E-002	2.202923716197214E-002
3	1.863027071136262E-002	8.214544668329469E-003
4	1.819276851166353E-002	3.457503808154121E-002
5	1.819101038280528E-002	3.458794550210217E-002
6	1.819101021947922E-002	3.458795530809459E-002

The residuals of the reduced equations are given in Table 2.12 from which the quadratic convergence quality of the local integration scheme is observed.

Table 2.12: Convergence of the residuals through iterations, simultaneous scheme.

Iteration	r_1	r_2
1	-1674.96750537952	0.334483800874814
2	-1015.13544326820	-0.157043547448021
3	-14.1780168970472	-2.787756928654985E-002
4	0.406715354483822	2.728864735388609E-005
5	-5.422106369223911E-006	-1.037531647402057E-008
6	-9.094947017729282E-013	-1.387778780781446E-017

For the same problem, once a staggered routine is utilized, plastic integration is followed by damage integration. Accordingly, the plastic correction, which is identical for implicit and explicit damage integration, results in the convergence behavior, which requires only three iterations for convergence, due to the character of hardening plasticity models, as given in Table 2.13.

Table 2.13: Convergence of the equivalent plastic strain and residual through iterations, plastic correction phase of the staggered scheme.

Iteration	α	r_1
1	1.882513792587752E-002	-3.40026247673541
2	1.883826792142717E-002	-1.457530743209645E-006
3	1.883826792705538E-002	0.000000000000000E+000

With an implicit damage integration, convergence is captured in three iterations as given in Table 2.14.

Table 2.14: Convergence of the damage and residual through iterations, damage deterioration phase of the staggered scheme.

Iteration	D	r_2
1	2.339278937801977E-002	-5.682196415299837E-004
2	2.378950956521546E-002	-1.997380615348376E-007
3	2.378964911673556E-002	-2.477532068390076E-014

For explicit damage integration, obviously the first line of the implicit damage integration may be taken, which stands for a forward damage integration. The results show that, maximum error in damage is observed in the explicit damage integration together with the staggered routine. Since number of iterations is a direct measure of number of floating point calculations, it has an indispensable effect on the overall computational time required thus the efficiency. However, although total number of iterations seems identical in simultaneous and staggered routine with implicit damage integration, number of floating point operations of the simultaneous routine is larger due to the requirement for additional computations of the off diagonal members of the

JACOBIAN. It should be noted that, although their implementation is much easier, as the coupled terms of the JACOBIAN are not computed, there is a trade off between accuracy and efficiency for staggered routines. Thus, the selection of whether a fully coupled or uncoupled solution scheme depends on the problem nature which is related to the degree of nonlinearity of the damage function, and degree of coupling between plasticity and damage. As the results represent, for favorable conditions staggered routines with explicit integration may be quite efficient. This property is valid especially for dynamic explicit problems where the time steps in global solution may be quite small which satisfies the conditional stability of the global problem.

2.4.2 Necking of an Axi-symmetric Bar

This example is well documented in the literature, see, e.g. [181], [161]. The problem illustrates the necking of an axi-symmetric bar with a total length of 53.334 and radius of 6.413. In order to trigger necking a total 98.2% radial reduction is introduced to the center, which is linearly distributed throughout the length of the bar. This way, the bifurcation problem, where the necking can emanate at any section, is transferred into a limit load problem, [80]. The geometry of the modeled quarter, 20x10 FE mesh (20 elements on longitudinal direction, 10 elements on radial direction) and the boundary conditions can be seen in Figure 2.11. It should be noted that, this problem does not reflect the active-passive conditions of damage evolution, as it is mainly an overall tensile processes.

The problem is solved for damage coupled and no damage (plain VON MISES plasticity) cases where damage coupled simulations are conducted using simultaneous and staggered solution schemes with two local equations, presented in the previous sections. For the staggered schemes, explicit and implicit damage integration procedures are followed. In the simulations, 250 load steps are applied for a total top displacement of $\Delta u = 7.68$. Premature failure (termination before increment 250) is observed in damage coupled models, whereas for the no damage case all load increments are successfully applied.
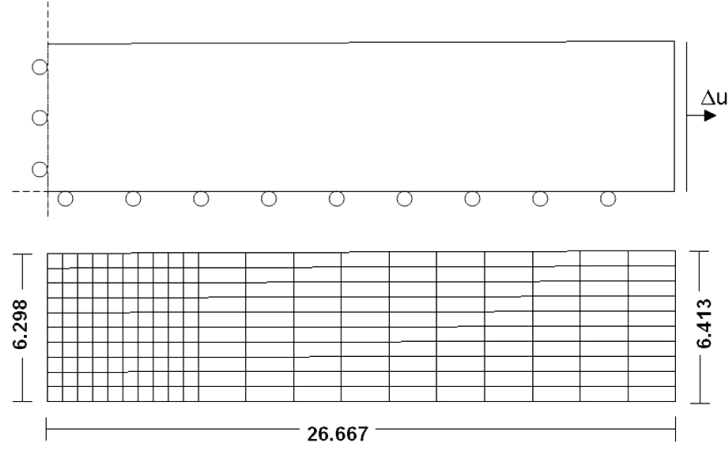
Figure 2.11: 20x10 mesh, boundary conditions and the geometry for the simulation of necking of an axi-symmetric bar.

A large strain, updated LAGRANGE formulation is selected where multiplicative decomposition is set as a plasticity procedure. Mechanical Element 10, with a selective integration scheme is used for axi-symmetric analyses [11].

The material parameters, fully compatible with [181], are given in Table 2.15. Unless otherwise stated, these parameters apply for all the other example problems.

Table 2.15: Material parameters for the example problem.

Parameter	Symbol	Magnitude	Unit
Bulk modulus	H	164.206	GPa
Shear modulus	μ	80.1938	GPa
Flow stress	τ_0	0.450	GPa
Saturation stress	τ_∞	0.715	GPa
Linear hardening	K	0.12914	GPa
Hardening exponent	δ	16.93	-
Damage multiplier	a	200	-

---

[11] It should be noted that the derivations of this chapter are made within the context of standard FE formulations. The plastic incompressibility acts as an over-constraint on the pressure field which results in locking of the standard finite elements. MSC.Marc, utilizes a mixed formulation, to be more specific a two-field, perturbed LAGRANGIAN form of a variational principle, for treatment of quasi-incompressibility, in the multiplicative framework. The formulations are well documented in [124, Chp. 5, pp. 158–162]. Since proposing a variational structure is beyond the scope of this thesis, we are contented with a suitable application of the exactly derived forms to the given framework in the space of approximation errors.

Damage and equivalent plastic strain distributions, just before the fracture, at Δu=4.9152, computed with the simultaneous scheme, are given in Figure 2.12. At the mid zone of the bar, due to the localized deformation together with necking, equivalent plastic strains and damage shows a marked accumulation. Moreover, it is observed that the distribution of highly localized damage has a central character which causes the local failure. This finding is in correlation with the actual experimental facts, where center constitutes the zone of ductile failure initiation (cup-cone fracture). Unlike [181], where a deviatoric variant of LEMAITRE damage model is utilized, the patterns of damage and equivalent plastic strains show a certain deviation. This is due to dominating effect of the triaxiality in the current model. For metal plasticity, disregarding the volumetric response is not realistic on physical grounds.
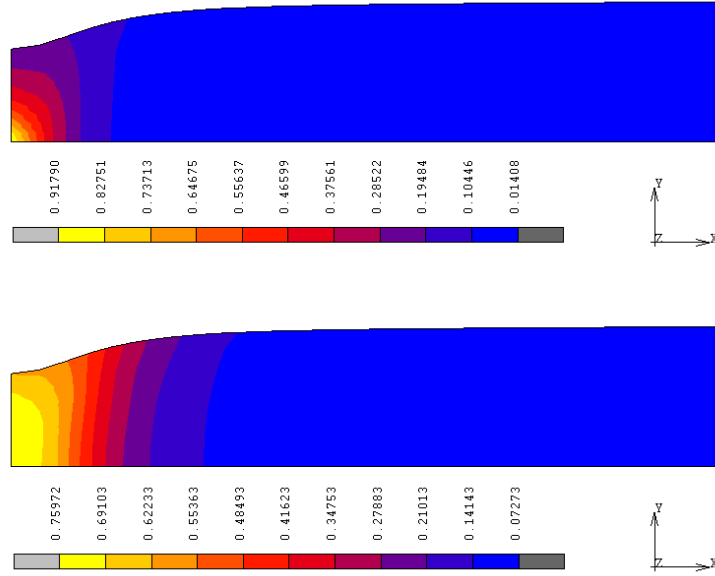
Figure 2.12: Contour plots for the damage coupled model at Δu=4.9152 (simultaneous two equation solution scheme), (top) Damage distribution, (bottom) Equivalent plastic strain distribution.

The load-displacement curves in Figure 2.13 show that, introduction of damage coupling results in a steeper post peak response with a premature termination of the analysis at smaller strains. This anticipated result with a considerable loss in ductility, is due to the strength loss of the material with damage deterioration. The same figure also shows that, the resultant responses for the simulated local integration schemes,

64

such as simultaneous, staggered with explicit damage integration and staggered with implicit damage integration, do not deviate from each other. This is primarily due to the selected functional forms for plasticity and damage and used material parameters, which govern the mathematical character of the problem at the space of unknowns, in terms of the degrees of functional nonlinearities. Besides, utilized sufficiently large number of loading steps has a stabilizing effect by improving the accuracy of the explicit damage integration steps. Use of implicit plastic integration as a first step for both of the staggered cases helps as well. The excessive number of tests conducted by the researchers show that, simultaneous scheme and the damage implicit integration in the staggered scheme should be supplied with appropriately defined line-searches and backtracking. For this purpose, Table 2.6 and Table 2.8 use particular NEWTON iteration steps, scaled with a line-search parameter, regarding these cases.
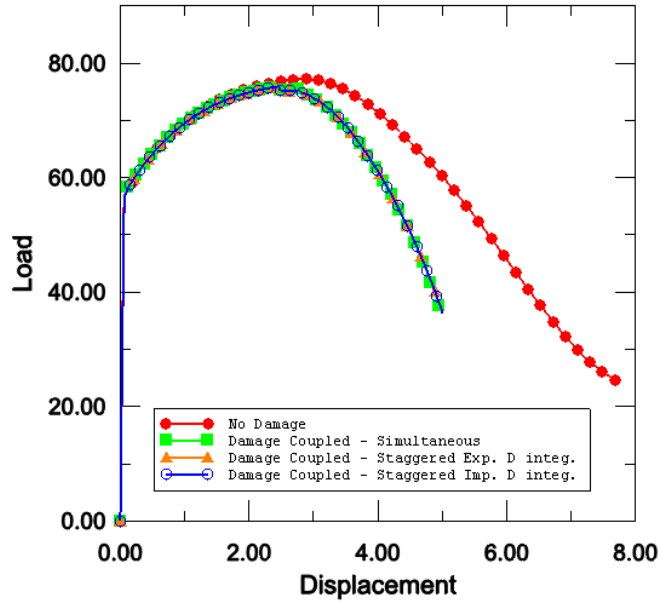
Figure 2.13: Load-displacement curves for damage coupled and non-damaged plasticity models.

2.4.3 Axi-symmetric Tension of a Notched Specimen

This example includes a notched specimen under tensile loading. The notch creates a radius dependent nonuniform stress state, which affects the damage deriving mechanisms. The geometry is the one utilized in [37] and [187]. Dimensions, the FE mesh and the imposed boundary conditions are given in Figure 2.14. In the simulations 250 load steps are applied for a total top displacement of Δu=1.00. Just like the previous one, this problem is also solved for damage coupled (with simultaneous and staggered schemes) and no damage cases. Due to its overall tensile character, this problem also does not reflect the effect of quasi-unilateral damage evolution.
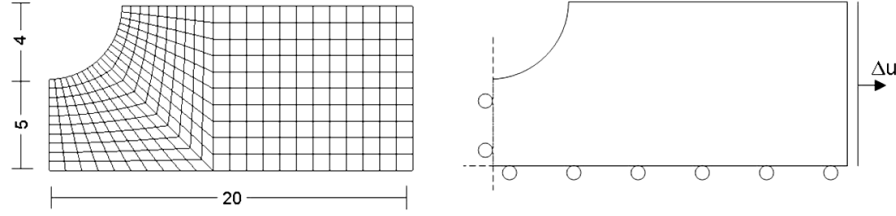
Figure 2.14: Mesh, boundary conditions and the geometry for the simulation of axi-symmetric tension of a notched specimen.

The results follow a similar fashion with the ones recorded in the literature as far as the damage evolution throughout the tensile process is taken into account. An initially notch concentrated damage, tends to slowly move towards the center and localize. This triaxiality dependent trend throughout the deformation history, given in Figure 2.15, is in complete accordance with the experimental evidences showing central failure initiation for certain notch geometries, [74].

The load-displacement curves in Figure 2.16 (left) show that, deteriorative mechanism of damage results in a softer response for damage coupled models compared to no damage case. The deviation between damage coupled and no damage cases' curves
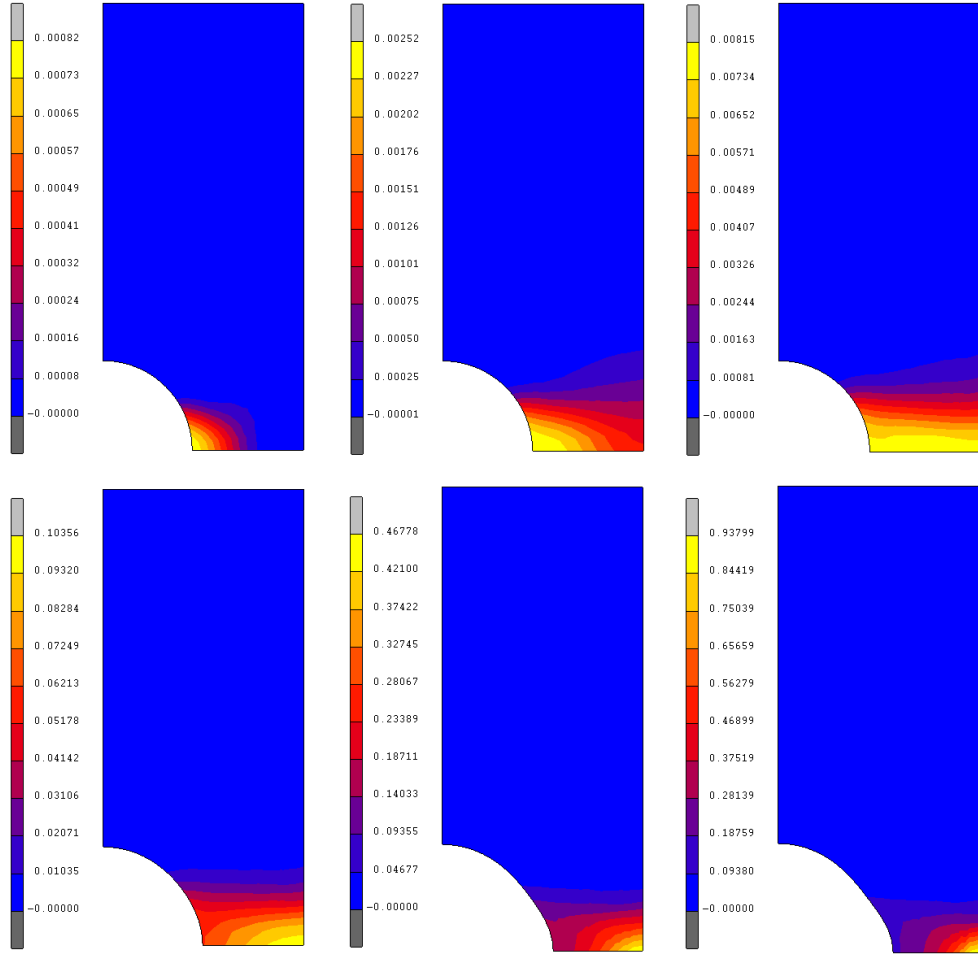
Figure 2.15: Contour plots of the Damage distribution at different steps (simultaneous two equation solution scheme), (top row, from left to right) Δu=0.032, 0.052 and 0.104, (bottom row, from left to right) Δu=0.440, 0.800 and 0.916.

increase with increasing damage accumulation controlled by the plastic deformation. The response curves for the utilized local integration schemes are in complete correlation within each other with the identical reasons listed for the previous example. Figure 2.16 (right) shows the damage histories computed at the notch center with different integration schemes, which also are in perfect harmony. The curves get steeper, with a concave up structure, towards the local failure point, where damage reaches the limit value, i.e. $D = 1$. This marked increase in damage increments near failure creates numerical difficulties in implicit schemes, [187], where the use of line-search becomes indispensable.
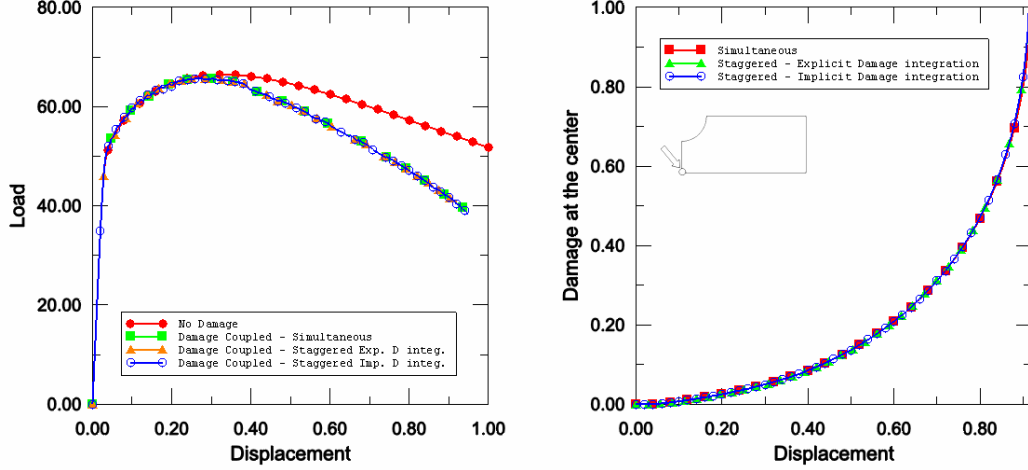
Figure 2.16: History plots, (left) Load-displacement curves for damage coupled and non-damaged plasticity models, (right) Damage evolution at center for various local integration schemes.

2.4.4 Upsetting of an Axi-symmetric Billet

Final problem is concerned with the upsetting of an axi-symmetric billet, which aims to investigate the effect of crack closure effect on the resultant damage distributions. For this purpose, on a cylindrical billet with a total undeformed length of 30.0 and radius of 10.0, two simulations are realized one of which involves the crack closure effect with the crack closure parameter, $h = 0.01$, and the other does not give account for the quasi-unilateral damage evolution. The geometry, mesh and imposed boundary conditions are given in Figure 2.17. At the die-billet interface, tangential movement is completely restrained using the glue contact option. A similar problem is studied for isotropic porous plasticity in [174]. The material parameters are the ones listed in Table 2.15, with a slight difference with $a = 2.0$. In determination of the results, the simultaneous local integration scheme with two equations, is utilized.

The upsetting is realized for over 60% height reduction. With the applied friction conditions, which provides a perfect stick at the die-billet interface, barreling occurs. Figure 2.18 (left) shows the deformed FE mesh at $\Delta u = 9.126$. The equivalent plastic
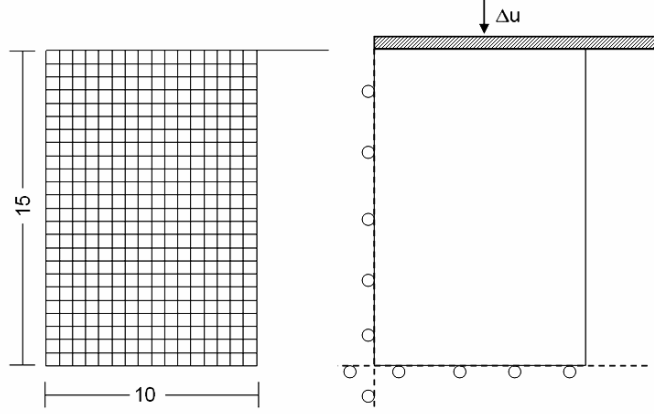
Figure 2.17: Mesh, boundary conditions and the geometry for the simulation of up-setting of an axi-symmetric billet.

strain contours plotted for two simulations, with and without crack closure effect, show a complete accordance as seen in Figure 2.18 (right) and (middle) respectively. With J_2 theory, the plastic flow and the accumulated equivalent plastic strains, which stands for the numerical construct for the micro-mechanical dislocation pile-ups, are functions of the distortional elastic energies. In the damage coupled framework, the plasticity is assumed to perform on the effective material subscale. Mathematically, this is realized by the damage free effective stress space formulation of plasticity, where for low levels of damage, the effective isochoric energies do not deviate considerably, which reveals the correlation of these plots.

A marked difference, in terms of intensity and distribution, is observed in the final damage contours between two simulations as seen in Figure 2.19. The reason for the difference in intensities, where the damage model without quasi-unilateral conditions has a peak damage value of more than 15 times of the model with crack closure effect for Δu=9.126, is apparent. Without incorporation of the crack closure effect, the intensity of damage increments utilize complete elastic energy release without making distinction about the governing stress terms' compressive or tensile characters, which results in a higher rate of accumulation. With crack closure effect however,

69
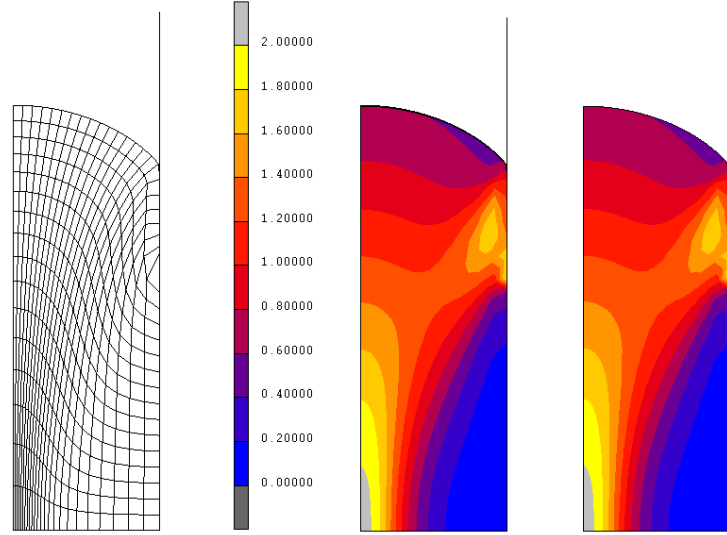
Figure 2.18: Resultants at $\Delta u=9.126$ (simultaneous two equation solution scheme), (left) Deformed mesh, (middle) Equivalent plastic strain distribution without crack closure effect, (right) Equivalent plastic strain distribution with crack closure effect, h = 0:01.
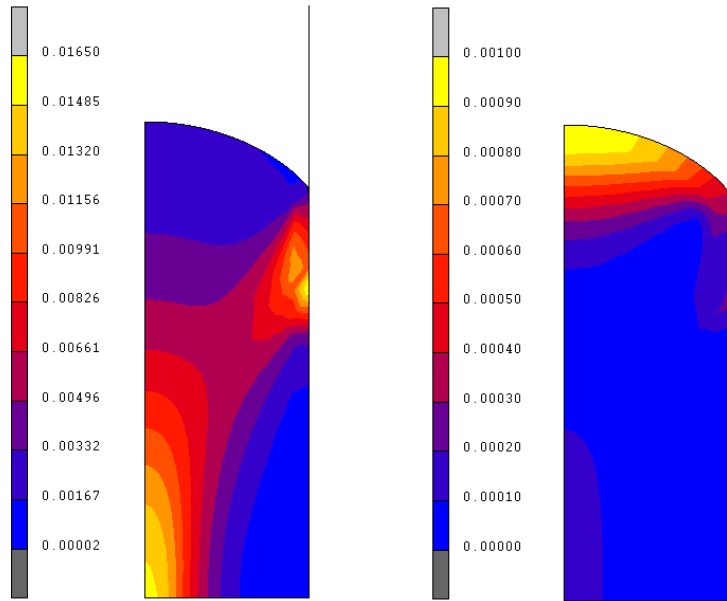
Figure 2.19: Contour plots of the Damage distribution at $\Delta u=9.126$ (simultaneous two equation solution scheme), (left) without crack closure effect, (right) with crack closure effect, h = 0:01.

although the involvement of the energy release due to tensile principal stresses is complete, for compressive principal stresses it is only partial, where the extent of its contribution is scaled by the selected crack closure parameter. On the deviation in

distributions, following comments can be made. As Figures 2.18 and 2.19 reveal, the damage distribution primarily follows a pattern similar to the ones of the equivalent plastic strains, in the absence of the crack closure effect. This anticipated result is due to the strong-coupled plasticity-damage framework.

Figure 2.20, which shows the stress state, at Δu=9.126, in terms of three principal components of CAUCHY type, is helpful in evaluation of the case with crack closure effect. Comparison of the zones of the positive principal stresses, which are purposely highlighted in Figure 2.20, and the damage accumulations given in Figure 2.19 (right), one may conclude that, in the advancing steps of frictional upsetting, together with barreling, the tensile pressures at the equator line has a dominating role on the damage evolution if the crack closure effect is incorporated. Occurrence of surface cracks due to barreling in frictional upsetting processes is a known experimental fact. Consequently, recalling previously mentioned ductile damage micro-mechanism, formed of micro-voids nucleation, growth and coalescence, use of quasi-unilateral evolutionary conditions is motivated. Accordingly, in engineering practice, utilizing a combined experimental-numerical procedure, in the definition of an appropriate crack closure parameter is vital. Utilizing this fact, one may also make a final remark on the obvious role of friction on the eventual damage distributions, [174]. For the frictionless upsetting where a homogeneous deformation is due, a quasi-unilaterally evolving damage model with the current utilization predicts a homogeneous damage accumulation, which is merely due to partially contributed uniform compressive stresses, where the extent of this contribution depends solely on the selected crack closure parameter.

2.5   Conclusion

In this chapter, a local, damage coupled isotropic finite strain hyperelastic-plastic framework is formulated in the principal axes, in a EUCLIDEAN setting. The unified functional framework for the governing functions of isotropic hardening plasticity and damage does not assume particular restrictions on the forms. This gives rise to implementation of a broad range of isotropic hardening plasticity and damage models,
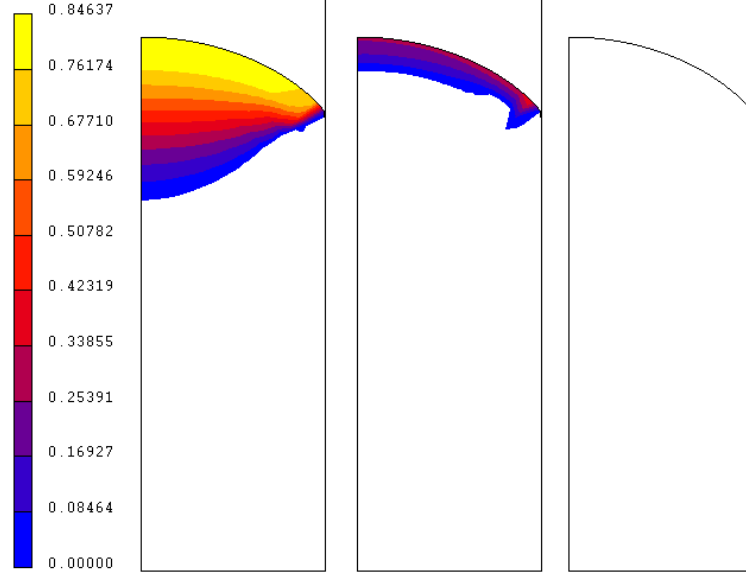
Figure 2.20: Positive portions of the maximum, intermediate and minimum (from left to right) Cauchy type principal stresses, at Δu=9.126 (simultaneous equation solution scheme.

strongly coupled through a single yield surface. Extensions to include linear kinematic hardening plasticity is also presented. It is shown that, principal axes formulation provides convenience not only in finite hyperelastic-plastic framework, reducing tensorial differentials to simple differentials with respect to scalars, but also in active-passive damage evolutionary conditions. In addition, simultaneous and staggered local integration algorithms are presented, which results in two and three-step operator-split methodologies. The framework is supplied with consistently derived material moduli and implemented as a user defined material subroutine for MSC.Marc, which is used in a set of example problems. On physical grounds, simulation results designating fracture initiation zones in tensile dominant processes with the effect of triaxiality, and in frictional upsetting with incorporation of the quasi-unilateral conditions, follow the experimental facts on ductile failure mechanisms.

On numerical grounds, isoerror maps are produced to evaluate the accuracy of the proposed algorithms. The correlation of the results between simultaneous and staggered schemes for selected damage model for sufficiently small time steps, motivates the use of numerically cheaper staggered local integration approach with explicit damage integration. An apparent gain in terms of computation time can be obtained, partic-

ularly in the context of explicit FE procedures, where the overall computational time is dominantly governed by the local return mapping at integration points. This possibility is investigated by the researchers for bulk metal forming simulations, conducted with the developed subroutines for explicit commercial FE solvers in which powerful contact algorithms are available. An apparent gain in terms of computation time can be obtained, particularly in the context of explicit FE procedures, where the overall computational time is dominantly governed by the local return mapping at integration points. This possibility is investigated by the researchers for bulk metal forming simulations, conducted with the developed subroutines for explicit commercial FE solvers in which powerful contact algorithms are available.

CHAPTER 3

THERMO-INELASTIC FORMULATION

3.1 Introduction

In a thermo-mechanical problem, heat is produced by dissipated mechanical work in addition to external heat sources if any exist. Produced heat is conducted/convected over the problem domain where rate sensitivity is applicable even to rate-independent models due to the time-dependence of heat flux, [198]. In order to solve the coupled problem for deformation and temperature one has to take into account a set of complicated mutual interactions among fields. In the absence of damage, problems of interest in thermoplasticity often display a two sided coupling, which according to [162] exhibits the following effects:

- The influence of the thermal field on the mechanical field

  - Thermal expansion

  - Temperature induced elastic softening, temperature dependence of elastic material properties

  - Temperature induced plastic softening, yield locus shrinkage

- The influence of the mechanical field on the thermal field

  - Geometric coupling on heat flux

  - Heat generation by plastic dissipation

  - Structural elastic heating (GOUGH-JOULE Effect)

In the current context, plasticity and damage accounts for the irreversible dissipative processes. In addition to the mentioned above, conditions that must be analyzed in the presence of damage include:

- The action of the damage field on the other mechanical fields

  - Damage induced elastic softening, deteriorated elastic stiffness
  - Damage induced yield locus shrinkage

- The influence of the damage field on the thermal field

  - Heat generation by damage dissipation
  - Damage dependent heat flux

- The influence of the thermal field on the damage field

  - Direct effect through temperature dependence of the damage dissipation functions,
  - Indirect effect through reconstruction of other damage deriving mechanical fields (e.g. triaxiality).

This highly complicated picture is the norm rather than the exception for many engineering applications. In the context of isotropic damage coupled finite plasticity, different numerical models are presented by [165], [85], [86], [87], [181], [171], [107], [5], among others. These frameworks, however, are presented in a purely isothermal setting. [48] presents a damage coupled finite strain thermoplastic framework utilizing GURSON damage model, whereas LEMAITRE damage model is presented in [154], [155] and [100]. These involve the hypoelastic formulations relying on objective stress integrators. Formulations based on multiplicative framework are given in [59] where a continuum sensitivity method is developed for porous metal plasticity using GURSON damage model. In the mentioned applications, the effect of damage on the heat conduction is not reflected. However, at micro-scale the deterioration of the material continuity through void nucleation, growth and coalescence inherently affects conduction quality. At the extreme where $D = 1$ the conduction is naturally precluded whereas the convection on the produced free surface is due. Mathematically this is supplied by a damage dependent heat conduction coefficient, [60].

Bracketing anisotropy and reducing the symmetry class to simple isotropy, the current chapter aims to formulate a consistent thermodynamic framework for finite multiplicative thermoplasticity coupled with damage which gives account for the listed mutual effects. Recently, in the finite strain context depending on pure mechanical theory, thermodynamics based anisotropic formulations depending on multiplicative decomposition of metric transformation tensor are given in [31]. Frameworks with introduction of fictitious undamaged configurations are proposed by [117], [53], [118]. Present formulation expands on representation of the damage-coupled framework given in [173] (which uses a dynamic explicit setup) to include thermal coupling together with a quasi-static formulation. Finite strain kinematics utilizes multiplicative split of the deformation gradient into elastic and plastic portions. A principal axes formulation is used based on a hyperelastic potential quadratic in HENCKY strains and nonlinear isotropic hardening VON MISES plasticity (which is typical for metals). This way, the stress from properly articulated definition of elastic potential supplies a precise elastic prediction. The total hyperelastic relations for the stress, have proved reliability for the cases where small elastic strain assumption may fall short, like in the case of high velocity impact and explosion, in which high elastic dilatations may be observed. Besides, hypoelastic stress formulations lead dissipation for even elastic cycles, [196]. The treatment of scalars rather than tensors, together with the principal axes formulation, serves handiness. The present formulation of finite kinematics is resolved in eigenvectors rather than eigenbases. In eigenbases representation, the determination of discrete eigenvalues are not required as the closed form solution for the eigenbases is due, [161], whereas in the eigenvalue solution, eigenvalues have to be computed utilizing the eigenvalue problem, [148]. In resolution of damage, conventional isotropic LEMAITRE damage model is selected, where the effective stress concept, [88] and [144], together with strain equivalence principle, [95], form the bases.

The thermodynamic framework is formed along the same lines with [162]. Exploiting the additivity or extensive property of the entropy, its decomposition into the elastic and inelastic portions is postulated. It is shown that, together with temperature dependent plastic and damage dissipation potentials, the internal variable inelastic entropy has a natural split form in plastic and damage portions. This amounts to a generalization of the postulated results suggested by [162] to the case of damage

76

coupling. Consequently, not only the plastic structural changes but also the damage structural changes are consistently linked to their regarding entropies. [14] also argues thermo-mechanical resolutions along the same lines with [162], however for anisotropic concrete damage. An interesting irreversible thermodynamics theory is presented in [16], where the entropy production is utilized as a metric for damage evolution, and consequently phenomenological damage potential definitions are bypassed, unlike the present study.

The numerical resolution of the thermo-mechanical problem is addressed as well, where a staggered scheme with the so-called isothermal split is utilized. Accordingly, the mechanical problem is realized under fixed temperature and the thermal problem under fixed configuration, both utilizing the other's result as their own boundary conditions. Although the isothermal split is practically implemented into the existing codes and serves certain numerical advantages such as adoption of different time scales to uncoupled mechanical and thermal steps; it, however, is, at its best, only conditionally stable. Another staggered resolution, the adiabatic split, based on an isentropic mechanical step, overcomes this problem of conditionality. For a detailed analysis involving the comparison of staggered and simultaneous thermo-mechanical resolutions, the reader may refer to [198], [162], [9], [10] and the references therein. A covariant principal axis formulation of the same framework is given in [81]. More recently, [34] expands the formulations and application problems to give account for temperature dependent elastic properties. Thermoplasticity with kinematic hardening is investigated in [69]. These applications exclude the void growth mechanism, i.e. damage, and accompanying softening in metallic materials. A thermo-plastic framework with a staggered resolution is presented in [70)] for porous plasticity. [176] addresses the numerical consequences isothermal and isentropic split for a nonlocal thermo-damage model. Finally, [133, pp. 637–672] supplies detailed information on the various methodologies of the solution of thermo-mechanical problems.

Numerical solution of the post-peak responses of material models including softening regimes via finite element procedures is prone to mesh sensitivity and related nonphysical localization. This is described as the loss of ellipticity in the context of quasi-static problems. In this regard, for a physically admissible solution, the material models should be enhanced with localization limiters, which keep the numerical prob-

lem well-posed. In the current study, strain hardening effects are in competition with a doubly softening mechanism induced by damage and temperature. Thus, a simple PERZYNA type viscous regularization is adopted into the existing framework in the spirit of [147] and [168]. Accordingly, the initial boundary value problem subjected to this doubly softening mechanism is kept well-posed. The effect of devising material rate dependence on the change of the character of the governing differential equation is presented in [127], in which it is shown that, in the context of quasi-static problems, the ellipticity loss is precluded by the incorporation of the viscosity and the pathological mesh sensitivity is thus healed. However, as shown in the application problems, this localization limitation property of the viscous regularization schemes is limited to certain deformation levels. More advanced models, such as gradient type localization limiters, are presented, in a pure mechanical setting, by [7], [37] and [116)] for isotropic damage models. [32] expands the nonlocal framework to anisotropic models. Treatment of anisotropic (visco)damage coupled with (visco)plasticity can be found in [2]. With nonlocal extensions, an isotropic GURSON damage model coupled thermo-plastic framework is presented in [70)]. More general thermo-mechanical frameworks with viscous and nonlocal enhancements accompanying anisotropic damage take place in [189] and [190].

This chapter has the following outline. Local constitutive forms are derived in § 3.2 in a thermodynamic consistency. Numerical aspects, including the FE formulation of the coupled thermo-mechanical problem, algorithmic forms and the consistent tangent moduli are given in § 3.3. § 3.4 constructs the formulations for adiabatic conditions. The example problems take place in § 3.5. Two damage triggering methods depending on the imposed conditions on damage field are presented, which, to the authors knowledge, haven't been presented in the literature yet. Besides the localization prevention characteristics of the viscous regularization in existence of two softening mechanism are investigated. ABAQUS implementation details are presented in Appendix B.

3.2 Theory

Based on the kinematic assumptions presented in Chapter 2, and following the rational thermodynamics approach followed by [162], the internal energy, $e(\mathbf{F}^e, \xi, \eta^e)$, is

postulated where η^e stands for the elastic entropy associated with the lattice and ξ denotes the vector of strain like internal variables responsible for irreversible mechanisms. For thermo-mechanical applications, an additively decoupled form of total entropy, η, with $\eta = \eta^e + \eta^{pd}$ is claimed, utilizing its extensive property. η^{pd} is the inelastic (configurational) entropy, which stands for the scalar internal variable, conjugate to the temperature, associated with the dissipative mechanisms such as plasticity, hardening and damage. Through the associative evolutionary forms emanating from conventional normality conditions together with a temperature dependent damage dissipation potential, one ends up with a natural additive split, $\eta^{pd} = \eta^p + \eta^d$, where the inelastic entropy is found as the summation of the plastic, η^p, and damage, η^d, entropies. With this phenomenological statement, the interpretation of the evolution of inelastic entropy is made in terms of the flow stress changes in a plastic process, and the damage dissipation potential changes, which is a nonlinear function of the elastic energy release rate, in a damage process, with respect to temperature. By this way, the framework given in [162] is expanded to give account for damage induced effects. Hence, η^p is linked to the irreversible plastic structural changes, such as dislocation motion and lattice defects and η^d is linked to the dissipative micro-structural changes accompanied by nucleation, growth and coalescence of micro-voids and micro-cracks. Both of η^p and η^d do involve inputs to the total entropy which are not covered by the inputs of the mechanical dissipation.

In the current context, the vector of strain like internal variables is defined as $\boldsymbol{\xi} = \{\alpha, D\}^t$, with α and $D \in [0, 1]$ being responsible for isotropic hardening and damage, respectively. Invariance requirements for constitutive model under arbitrary rigid body rotations on the intermediate configuration motivate the use of $e(\mathbf{F}^e, \boldsymbol{\xi}, \eta^e) \mapsto e(\mathbf{b}^e, \boldsymbol{\xi}, \eta^e)$, where $\mathbf{b}^e$ represents the elastic left CAUCHY-GREEN deformation tensor, with $\mathbf{b}^e = \mathbf{F}^e \bullet \mathbf{F}^{e,t}$. One may apply the LEGENDRE transformation to derive, $e(\mathbf{b}^e, \boldsymbol{\xi}, \eta^e) = \Psi(\mathbf{b}^e, \boldsymbol{\xi}, \theta) + \theta\eta^e$, in which $\Psi(\mathbf{b}^e, \boldsymbol{\xi}, \theta)$ represents the HELMHOLTZ free energy, which is set in terms of the absolute temperature, θ, instead of elastic entropy. An additively decoupled form of $\Psi(\mathbf{b}^e, \boldsymbol{\xi}, \theta)$ reads

$$\Psi(\mathbf{b}^e, \xi, \theta) := \Psi^e(\mathbf{b}^e, D) + \Psi^{td}(J^e, \theta, D) + \Psi^t(\theta) + \Psi^p(\alpha, \theta), \qquad (3.1)$$

where $\Psi^e(\mathbf{b}^e, D)$ denotes the damage affected pure elastic free energy[1]. $\Psi^p(\alpha, \theta)$ stands

---

[1] To supply this form, for the sake of simplicity, temperature independent elastic material param-

for the plastic free energy blocked in the dislocations. $\Psi^t(\theta)$ is associated with the purely thermal entropy. Elastic structural entropy is constructed through the thermo-dilatational potential, $\Psi^{td}(J^e, \theta, D)$. The relations between the nominal (homogenized) and the effective free energies follow

$$\Psi^e(\mathbf{b}^e, D) \;\; = \;\; (1-D)\,\tilde{\Psi}^e(\mathbf{b}^e), \tag{3.2}$$

$$\Psi^{td}(J^e, \theta, D) \;\; = \;\; (1-D)\,\tilde{\Psi}^{td}(J^e, \theta), \tag{3.3}$$

with, $\left[\tilde{\bigstar}\right] := \left[\bigstar\right]/(1-D)$, where $\left[\tilde{\bigstar}\right]$ and $\left[\bigstar\right]$ are associated with the effective and nominal forms of any tensorial or scalar quantity. Effective forms act on the intact material subscale whereas nominal forms reflect mathematically homogenized behavior under the influence of damage deterioration.

3.2.1 Equations of State

The second principle of thermodynamics for a thermo-mechanical problem postulates a nonnegative difference between the local stress power and the local rate of change of free energy. This, as a measure for the thermodynamic admissibility, supplies the following so-called the Clausius-Duhem inequality,

$$0 \leq \Omega = \boldsymbol{\tau} : \mathbf{d} + \theta\frac{\partial \eta}{\partial t} - \frac{\partial e}{\partial t} - \frac{1}{\theta}\mathbf{q} \bullet \mathbf{g}, \tag{3.4}$$

where $\boldsymbol{\tau}$ is the Kirchhoff stress tensor which is the work conjugate of the spatial rate of deformation tensor, $\mathbf{d} := \mathrm{sym}\left[\mathbf{l}\right]$, with $\mathbf{l} := \partial\mathbf{F}/\partial t \bullet \mathbf{F}^{-1}$ denoting the spatial velocity gradient. $\mathbf{q}$ stands for the Kirchhoff type heat flux, analogous with the weighted Cauchy stress. $\mathbf{g}$ is associated with the spatial gradient of θ with $\mathbf{g} := \nabla\theta$. This inequality can be split into two more restrictive inequalities, namely, the local thermo-mechanical, i.e reduced Clausius-Planck form, and the conductive thermal, i.e. Fourier Form,

$$\Omega = \Omega^{lthm} + \Omega^{cth} \geq 0, \;\; \Omega^{lthm} \geq 0, \;\; \Omega^{cth} \geq 0. \tag{3.5}$$

where the respective dissipation potentials are denoted by Ω^{lthm} and Ω^{cth}, with

$$\Omega^{lthm} \;\; := \;\; \boldsymbol{\tau} : \mathbf{d} + \theta\frac{\partial \eta}{\partial t} - \frac{\partial e}{\partial t}, \tag{3.6}$$

$$\Omega^{cth} \;\; := \;\; -\frac{1}{\theta}\mathbf{q} \bullet \mathbf{g}. \tag{3.7}$$

eters are assumed, $\mu(\theta) \mapsto \mu$, $H(\theta) \mapsto H$. For a treatment including temperature dependent elastic constants for thermoplasticity, see [34].

Natural satisfaction of the condition, $\Omega^{cth} \geq 0$, is supplied with (3.55) of § 3.2.5. The remaining inequality, $\Omega^{lthm} \geq 0$, postulates a stronger form of the original setup. By making appropriate substitutions for Ω^{lthm} and using previously postulated LEGENDRE transformation, one has,

$$\frac{\partial e}{\partial t} = \frac{\partial \Psi}{\partial t} + \frac{\partial \theta}{\partial t}\eta^e + \frac{\partial \eta^e}{\partial t}\theta. \tag{3.8}$$

Using the main inequality, (3.5.b) supplies,

$$0 \leq \Omega^{lthm} = \tau : \mathbf{d} + \theta \underbrace{\left[\frac{\partial \eta}{\partial t} - \frac{\partial \eta^e}{\partial t}\right]}_{=\frac{\partial \eta^{pd}}{\partial t}} - \frac{\partial \Psi}{\partial t} - \frac{\partial \theta}{\partial t}\eta^e. \tag{3.9}$$

Applying the chain rule of differentiation

$$\frac{\partial \Psi}{\partial t} = \frac{\partial \Psi}{\partial \mathbf{b}^e} : \frac{\partial \mathbf{b}^e}{\partial t} + \frac{\partial \Psi}{\partial \boldsymbol{\xi}} \bullet \frac{\partial \boldsymbol{\xi}}{\partial t} + \frac{\partial \Psi}{\partial \theta}\frac{\partial \theta}{\partial t}, \tag{3.10}$$

with

$$\frac{\partial \mathbf{b}^e}{\partial t} = \pounds_v \mathbf{b}^e + \mathbf{l} \bullet \mathbf{b}^e + \mathbf{b}^e \bullet \mathbf{l}^t, \tag{3.11}$$

where $\pounds_v [\bigstar]$ stands for the objective LIE derivative of $[\bigstar]$ via,

$$\pounds_v \mathbf{b}^e = \mathbf{F} \bullet \frac{\partial \mathbf{G}^p}{\partial t} \bullet \mathbf{F}^t, \tag{3.12}$$

in which $\mathbf{G}^p := \mathbf{C}^{p,-1} = \mathbf{F}^{p,-1} \bullet \mathbf{F}^{p,-t}$, [109]. $\mathbf{C}^p$ is the plastic right CAUCHY-GREEN deformation tensor whose inverse is designated by $\mathbf{G}^p$. Substituting (3.11) back into (3.9), together with certain manipulations, one finds,

$$0 \leq \Omega^{lthm} = \underbrace{\left[\tau - 2\frac{\partial \Psi}{\partial \mathbf{b}^e}\bullet\mathbf{b}^e\right]}_{=0} : \mathbf{d} + \underbrace{2\frac{\partial \Psi}{\partial \mathbf{b}^e}\bullet\mathbf{b}^e}_{=:\tau} : \left[-\frac{1}{2}\pounds_v\mathbf{b}^e \bullet \mathbf{b}^{e,-1}\right] + \theta\frac{\partial\eta^{pd}}{\partial t}$$
$$+ \left[-\frac{\partial\Psi}{\partial\boldsymbol{\xi}}\right] \bullet \frac{\partial\boldsymbol{\xi}}{\partial t} + \underbrace{\left[-\frac{\partial\Psi}{\partial\theta} - \eta^e\right]}_{=0}\frac{\partial\theta}{\partial t}. \tag{3.13}$$

Accordingly following state equations are derived,

$$\boldsymbol{\tau} = \frac{\partial\Psi}{\partial\mathbf{b}^e} \bullet \mathbf{b}^e, \quad \boldsymbol{\varsigma} = -\frac{\partial\Psi}{\partial\boldsymbol{\xi}}, \quad \eta^e = -\frac{\partial\Psi}{\partial\theta}, \tag{3.14}$$

where elastic entropy is found out to be the conjugate variable of the temperature. $\boldsymbol{\varsigma}$ is the vector of stress like internal variables which are dual with $\boldsymbol{\xi}$, where $\boldsymbol{\varsigma} = \{q, Y^d\}^t$. q is responsible for isotropic hardening in the form of yield locus expansion whereas Y^d is the thermodynamically formal damage conjugate variable. Substitution of the derived

state equations yields the following reduced dissipation inequality, whose maximization furnishes the base for state variable evolution equations,

$$0 \leq \Omega^{lthm} = \boldsymbol{\tau} : \left[-\frac{1}{2} \pounds_v \mathbf{b}^e \bullet \mathbf{b}^{e,-1} \right] + \underbrace{\left[-\frac{\partial \Psi}{\partial \alpha} \right]}_{=:q} \frac{\partial \alpha}{\partial t} + \underbrace{\left[-\frac{\partial \Psi}{\partial D} \right]}_{=:Y^d} \frac{\partial D}{\partial t} + \theta \frac{\partial \eta^{pd}}{\partial t}, \quad (3.15)$$

Specified additively decoupled potentials given in (3.1) result in the following explicit representations for the state equations[2],

$$\boldsymbol{\tau} = (1-D) \left[\frac{\partial \tilde{\Psi}^e}{\partial \mathbf{b}^e} + \frac{\partial \tilde{\Psi}^{td}}{\partial \mathbf{b}^e} \right] \bullet \mathbf{b}^e, \quad (3.16)$$

$$q = -\frac{\partial \Psi^p}{\partial \alpha}, \quad (3.17)$$

$$Y^d = \tilde{\Psi}^e + \tilde{\Psi}^{td}, \quad (3.18)$$

$$\eta^e = -(1-D)\frac{\partial \tilde{\Psi}^{td}}{\partial \theta} - \frac{\partial \Psi^t}{\partial \theta} - \frac{\partial \Psi^p}{\partial \theta}. \quad (3.19)$$

Due to its dependence on $\tilde{\Psi}^{td}$, the definition of total KIRCHHOFF stress tensor gives account for additional temperature dependent dilatational terms, compared to the isothermal solution. Also in this setting, damage conjugate variable includes thermally motivated portions, as an extension of the canonical LEMAITRE damage model. Meanwhile, the strain equivalence principle gives that the effective KIRCHHOFF stress, i.e. $\tilde{\boldsymbol{\tau}} = \boldsymbol{\tau}/(1-D)$, does not explicitly depend on D.

---

[2] A remarkable fact is that, once the temperature dependence of the elasticity parameters are taken into account, one has $\tilde{\Psi}^e = \tilde{\Psi}^e(\mathbf{b}^e, \theta)$, and

$$\eta^e = -(1-D)\left[\frac{\partial \tilde{\Psi}^e}{\partial \theta} + \frac{\partial \tilde{\Psi}^{td}}{\partial \theta} \right] - \frac{\partial \Psi^t}{\partial \theta} - \frac{\partial \Psi^p}{\partial \theta}.$$

3.2.2 Equations of Evolution

The local thermo-mechanical dissipation, Ω^{lthm}, that should be maximized, can be split into mechanical, Ω^{mech}, and thermal, Ω^{ther}, portions[3], [47],

$$0 \leq \Omega^{lthm} := \underbrace{\boldsymbol{\tau} : \left[-\frac{1}{2} \pounds_v \mathbf{b}^e \bullet \mathbf{b}^{e,-1} \right] + q\,\frac{\partial \alpha}{\partial t} + Y^d\,\frac{\partial D}{\partial t}}_{=:\Omega^{mech}} + \underbrace{\theta\,\frac{\partial \eta^{pd}}{\partial t}}_{=:\Omega^{ther}}. \qquad (3.20)$$

The evolutionary forms exploit the standard arguments of the maximization of the inelastic dissipation, [105], where the plastic yield potential as a constraint function is now modified to involve the damage dissipation potential as well. The hypothesis of generalized standard materials, which proposes the existence of normality rules, [111], applies equally valid. Accordingly, a loading function, ϕ^t, additively decoupled into a temperature dependent plastic potential, $\tilde{\phi}$, and a temperature dependent damage dissipative potential, ϕ^d, is postulated,

$$\phi^t(\boldsymbol{\tau}, q, Y^d; D, \theta) = \tilde{\phi}(\tilde{\boldsymbol{\tau}}, q; \theta) + \phi^d(Y^d; D, \theta). \qquad (3.21)$$

Owing to the fact that the plastic flow is physically possible at undamaged material sub-scale, the formulation of $\tilde{\phi}$ takes place in the effective KIRCHHOFF stress space. Within the context of isotropy, associated plasticity is recovered, where the plastic flow represented by the flow rule is coaxial with the KIRCHHOFF stress,

$$\pounds_v \mathbf{b}^e = -2\,\frac{\dot{\gamma}}{(1-D)}\,\frac{\partial \tilde{\phi}}{\partial \tilde{\boldsymbol{\tau}}} \bullet \mathbf{b}^e, \qquad (3.22)$$

---

[3] Utilizing $\Omega^{mech} = \Omega^{mech,p} + \Omega^{mech,d}$, with,

$$\Omega^{mech,p} = \boldsymbol{\tau} : \left[-\frac{1}{2} \pounds_v \mathbf{b}^e \bullet \mathbf{b}^{e,-1} \right] + q\,\frac{\partial \alpha}{\partial t},$$

and

$$\Omega^{mech,d} = Y^d\,\frac{\partial D}{\partial t},$$

this form accounts for

$$\Omega^{lthm} + \Omega^{mech,p} + \Omega^{mech,d} \geq 0.$$

which is implied by the additive decomposition $\eta = \eta^e + \eta^p + \eta^d$, and which is in accordance with Equation 29 of [189].

where $\dot{\gamma}$ is the single plastic multiplier. Coming to the rates of the scalar internal variables, α, D and η^{pd}, one derives,

$$\frac{\partial \alpha}{\partial t} = \dot{\gamma} \frac{\partial \tilde{\phi}}{\partial q}, \tag{3.23}$$

$$\frac{\partial D}{\partial t} = \dot{\gamma} \frac{\partial \phi^d}{\partial Y^d}, \tag{3.24}$$

$$\frac{\partial \eta^{pd}}{\partial t} = \dot{\gamma} \left[\frac{\partial \tilde{\phi}}{\partial \theta} + \frac{\partial \phi^d}{\partial \theta} \right]. \tag{3.25}$$

which are conventional, associative evolutionary rules. Since the growth of both α and D depend on $\dot{\gamma}$, damage concurrently occurs with plasticity. In the context of inelastic dissipation maximization postulate, multi-surface damage-plasticity models, which give account for separate plastic and damage multipliers, in the form of LA-GRANGE multipliers, damage evolution in absence of plastic flow is possible, [75]]. Current treatment supplies the source of kinematic coupling between plasticity and damage. Such an application has proved convenient in ductile metal damage, where the dislocation pile-ups supply as a void nucleation source. This definition also postulates that the evolution of the inelastic entropy depends on both the plasticity and the damage dissipation potentials, which is an expanded version of [162], in which no damage mechanism is taken into account. It is remarkable that, one may represent the inelastic entropy production in an additive form in terms of plastic and damage parts as follows,

$$\frac{\partial \eta^{pd}}{\partial t} = \frac{\partial \eta^p}{\partial t} + \frac{\partial \eta^d}{\partial t}, \quad \frac{\partial \eta^p}{\partial t} = \dot{\gamma} \frac{\partial \tilde{\phi}}{\partial \theta}, \quad \frac{\partial \eta^d}{\partial t} = \dot{\gamma} \frac{\partial \phi^d}{\partial \theta}. \tag{3.26}$$

For the sake of completeness, KUHN-TUCKER optimality conditions end this section.

$$\dot{\gamma} \geq 0, \quad \tilde{\phi}(\tilde{\boldsymbol{\tau}}, q; \theta) \leq 0, \quad \dot{\gamma}\tilde{\phi}(\tilde{\boldsymbol{\tau}}, q; \theta) = 0. \tag{3.27}$$

3.2.3 Viscous Regularization and the Penalty Method

It is a well known fact that softening regimes are prone to numerical difficulties. These difficulties show themselves as non-uniqueness of the solution or mesh-non-objectivity which is frequently pronounced as pathological mesh dependency. These can be regularized, however partially, through encountering viscosity. In the context of damage-coupled plasticity, using PERZYNA type rate dependence, single surface overstress type viscous forms are utilized by [147] and [168] among others. It is

notable that taking a viscous plasticity model affects the structure of the damage evolutionary form through a single plastic potential and enforces it to have a viscous character also. In this method, the viscoplastic multiplier, $\dot{\gamma}^{vp}$, is not found via the consistency condition, $\partial\tilde{\phi}/\partial t = 0$, but computed through an overstress form,

$$\dot{\gamma}^{vp} = \frac{\langle\tilde{\phi}\rangle}{\eta},$$

with $\langle\bigstar\rangle$ standing for the MACAULAY brackets where $\langle\bigstar\rangle = 1/2\left[\bigstar + |\bigstar|\right]$. The viscosity parameter, η, should be selected as sufficiently small positive number to mimic instantaneous plasticity with care, not to create numerical difficulties. This formulation of plasticity falls in the class of penalty formulations rather than LAGRANGE multiplier methods. For $\eta \mapsto 0$ inviscid plasticity is recovered, whereas instantaneous elasticity is obtained for $\eta \mapsto \infty^4$. From now on, the evolutionary forms are subjected to the modification $\dot{\gamma} \mapsto \dot{\gamma}^{vp}$, to involve regularizing rate effects.

3.2.4 The Temperature Evolution Equation

Following temperature evolution equation constitutes the boundary value problem for temperature,

$$C_v\frac{\partial\theta}{\partial t} = \Omega^{mech} - \mathfrak{H} - J\mathrm{div}\left[\frac{\mathbf{q}}{J}\right] + R, \tag{3.28}$$

where C_v denotes the specific heat and $\mathfrak{H}$ denotes the elastic-plastic-damage structural heating which is related to the latent (non-dissipative) elastic and inelastic structural changes. R and $\mathbf{q}$ represent the heat source and the KIRCHHOFF type heat flux, respectively, both of which are omitted in adiabatic processes. The temperature evolution equation can be found through the local energy balance equation, i.e. the first principle of thermodynamics,

$$-J\mathrm{div}\left[\frac{\mathbf{q}}{J}\right] + R \geq \frac{\partial e}{\partial t} - \boldsymbol{\tau} : \mathbf{d}. \tag{3.29}$$

Substituting the local thermo-mechanical dissipation definition

$$\Omega^{lthm} := \boldsymbol{\tau} : \mathbf{d} + \theta\frac{\partial\eta}{\partial t} - \frac{\partial e}{\partial t} \Rightarrow \frac{\partial e}{\partial t} - \boldsymbol{\tau} : \mathbf{d} = -\Omega^{lthm} + \theta\frac{\partial\eta}{\partial t}, \tag{3.30}$$

---

4   Treatment of creep can be carried out the same setting, exploiting the equivalence of both elastoviscoplastic and creep formulations. Creep may be seen as a special case of viscoplasticity where the elastic domain is null, [179].

and using $\Omega^{lthm} = \Omega^{mech} + \Omega^{ther}$, where $\Omega^{ther} = \theta \left[\partial \eta^{pd} / \partial t \right]$, and $[\partial \eta / \partial t] = [\partial \eta^e / \partial t] + \left[\partial \eta^{pd} / \partial t \right]$, one has,

$$\frac{\partial e}{\partial t} - \boldsymbol{\tau} : \mathbf{d} = -\Omega^{mech} + \theta \left[\frac{\partial \eta}{\partial t} - \frac{\partial \eta^{pd}}{\partial t} \right]. \tag{3.31}$$

Since $\eta^e = \eta - \eta^{pd} = -\partial \Psi / \partial \theta$ and $[\partial \Psi / \partial t] = \boldsymbol{\tau} : \mathbf{d} - \Omega^{mech} + [\partial \theta / \partial t] \eta^e$, one carries out,

$$\theta \left[\frac{\partial \eta}{\partial t} - \frac{\partial \eta^{pd}}{\partial t} \right] = \underbrace{\left[-\theta \frac{\partial}{\partial \theta} \left[\boldsymbol{\tau} : \mathbf{d} - \Omega^{mech} \right] \right]}_{=: \mathfrak{H}} + \frac{\partial \theta}{\partial t} \underbrace{\left[-\theta \frac{\partial^2 \Psi}{\partial \theta^2} \right]}_{=: C_v}. \tag{3.32}$$

Note that, (3.32) checks with [162]. However in the preceding form, Ω^{mech} inherently involves damage effects. Moreover $\mathfrak{H}$ is found as,

$$\mathfrak{H} = -\theta \left\{ \frac{\partial}{\partial \theta} \left[\frac{\partial \Psi}{\partial \mathbf{b}^e} \right] : \frac{\partial \mathbf{b}^e}{\partial t} + \frac{\partial}{\partial \theta} \left[\frac{\partial \Psi}{\partial \alpha} \right] \frac{\partial \alpha}{\partial t} + \frac{\partial}{\partial \theta} \left[\frac{\partial \Psi}{\partial D} \right] \frac{\partial D}{\partial t} \right\}. \tag{3.33}$$

3.2.5 Application to a Model Problem

In this section the potentials are specified in order to derive the explicit representations of the state laws and the evolutionary equations. For elasticity, one may postulate a deviatoric-volumetric split for the effective elastic potential, $\tilde{\Psi}^e(\mathbf{b}^e) = \tilde{\Psi}^{e,vol}(J^e) + \tilde{\Psi}^{e,dev}(\bar{\lambda}_A^e)$, $(A = 1, 2, 3)$, where use of the principals of the tensor arguments in representation of the isotropic tensor functions is possible,

$$\tilde{\Psi}^{e,vol}(J^e) := \frac{1}{2} H \log[J^e]^2, \tag{3.34}$$

$$\tilde{\Psi}^{e,dev}(\bar{\lambda}_A^e) := \mu \left(\log[\bar{\lambda}_1^e]^2 + \log[\bar{\lambda}_2^e]^2 + \log[\bar{\lambda}_3^e]^2 \right) \tag{3.35}$$

$$= \mu \left(\bar{\epsilon}_1^{e,2} + \bar{\epsilon}_2^{e,2} + \bar{\epsilon}_3^{e,2} \right).$$

with H and μ being the bulk and the shear modulus, respectively. $\lambda_A^e = \sqrt{b_A^e}$ stands for the principal elastic stretch with the deviatoric portion represented by $\bar{\lambda}_A^e$. ϵ^e denotes the elastic logarithmic strain tensor with principals represented by ϵ_A^e. This quadratic form in terms of HENCKY measure of elastic strains although preserves validity for a large class of materials up to moderately large deformations, [196], does not satisfy the polyconvexity condition [102]. The deviatoric contribution of the elastic logarithmic strain tensor and its principal components are denoted by, $\bar{\epsilon}^e$ and $\bar{\epsilon}_A^e$, respectively.

For the plastic portion, following isotropic hardening potential is common which is associated with a combined linear and saturation type. In the presence of thermal coupling, this potential reads,

$$\Psi^{p,iso}(\alpha,\theta) = \frac{1}{2}K(\theta)\,\alpha^2 + \tau_{0,\infty}(\theta)\left[\delta + \frac{\exp[-\delta\alpha]}{\delta}\right], \qquad (3.36)$$

with, $\tau_{0,\infty}(\theta) := \tau_{\infty}(\theta) - \tau_0(\theta)$, where and $\tau_0(\theta)$ and $\tau_{\infty}(\theta)$ denote the initial and the final yield stress of the material at temperature θ, respectively. Following [162], linear thermal softening, with hardening softening parameter, ω_h, acting on plasticity parameters is assumed,

$$\begin{aligned} \tau_0(\theta) &= \tau_0(\theta_0)\left[1 - \omega_h(\theta - \theta_0)\right], & (3.37) \\ K(\theta) &= K(\theta_0)\left[1 - \omega_h(\theta - \theta_0)\right], \\ \tau_{0,\infty}(\theta) &= \tau_{0,\infty}(\theta_0)\left[1 - \omega_h(\theta - \theta_0)\right]. \end{aligned}$$

Volumetric elastic deformation is associated with the thermal effects through the following thermo-dilatational potential,

$$\tilde{\Psi}^{td}(J^e,\theta) = -3\,H\,\alpha^t\frac{\log[J^e]}{J^e}(\theta - \theta_0). \qquad (3.38)$$

Pure thermal potential is defined as

$$\Psi^t(\theta) = C_v\left[(\theta - \theta_0) - \theta\,\log\left[\frac{\theta}{\theta_0}\right]\right], \qquad (3.39)$$

which satisfies the condition, $-C_v = \left[\partial^2\tilde{\Psi}^t/\partial\theta^2\right]$. These definitions let one find the following state equation for the homogenized KIRCHHOFF stress,

$$\boldsymbol{\tau} = (1 - D)\left[\underbrace{H\left\{\text{tr}[\boldsymbol{\epsilon}^e] - 3\,\alpha^t(\theta - \theta_0)\frac{1 - \log[J^e]}{J^e}\right\}}_{=:\tilde{p}}\mathbf{1} + \underbrace{2\mu\,\bar{\boldsymbol{\epsilon}}^e}_{=:\tilde{\mathbf{s}}}\right], \qquad (3.40)$$

where $\tilde{p} = (\tilde{\tau}_1 + \tilde{\tau}_2 + \tilde{\tau}_3)/3$ and $\tilde{\mathbf{s}}$ represent the temperature dependent effective KIRCHHOFF type hydrostatic stress and the deviatoric effective KIRCHHOFF stress tensor, respectively. The eigenvalues of the latter is denoted by $\tilde{s}_A$. Thanks to isotropy, $\boldsymbol{\epsilon}^e$ and $\tilde{\mathbf{s}}$ are coaxial thus share identical eigenbases, $\mathbf{m}^A = \boldsymbol{\nu}^A \otimes \boldsymbol{\nu}^A$, where $\boldsymbol{\nu}^A$ represents the corresponding eigenvectors with $(A = 1, 2, 3)$. As a consequence of the preceding

definitions, the rest of the state equations read,

$$q = -K(\theta)\,\alpha - [\tau_\infty(\theta) - \tau_0(\theta)]\,[1 - \exp[-\delta\alpha]]\,, \tag{3.41}$$

$$Y^d = \frac{1}{2}\,H\,\log[J^e]^2 + \mu\,(\bar{\epsilon}_1^{e,2} + \bar{\epsilon}_2^{e,2} + \bar{\epsilon}_3^{e,2}) - 3\,H\,\alpha^t\frac{\log[J^e]}{J^e}(\theta - \theta_0), \tag{3.42}$$

$$\eta^e = \frac{1}{2}\omega_h K(\theta_0)\,\alpha^2 + \omega_h\tau_{0,\infty}(\theta_0)\left[\delta + \frac{\exp[-\delta\alpha]}{\delta}\right] \tag{3.43}$$
$$+ (1 - D)3\,H\,\alpha^t\frac{\log[J^e]}{J^e} + C_v\log\left[\frac{\theta}{\theta_0}\right].$$

The damage conjugate variable, Y^d, is associated with the temperature dependent total thermo-elastic energy release rate. The expression for η^e is in accordance with the one given in [81, Equation 70], except for the fact that it includes the damage effect at the third term on the right hand side of equivalence. The definition of the yield potential, which is of J_2 type, is made in the effective KIRCHHOFF stress space in terms of the principal values of the effective KIRCHHOFF stress and a two parameter simple damage dissipation potential, chosen as a power function in Y^d, is utilized for the damage dissipation, which read,

$$\tilde{\phi}(\tilde{s}_A, q; \theta) := [\tilde{s}_1^2 + \tilde{s}_2^2 + \tilde{s}_3^2]^{1/2} - \sqrt{\frac{2}{3}}\,y(q, \theta) \le 0, \tag{3.44}$$

$$\phi^d(Y^d; D, \theta) := \frac{a(\theta)}{(s+1)}\frac{1}{(1-D)}\left[\frac{Y^d}{a(\theta)}\right]^{s+1}, \tag{3.45}$$

with $y(q, \theta) = [\tau_0(\theta) - q(\alpha, \theta)]$ representing the hardening/softening function for thermo-coupled conditions. A linear temperature dependence is chosen for the damage parameter, $a(\theta)$, via

$$a(\theta) = a(\theta_0)\,[1 - \omega_d(\theta - \theta_0)]\,. \tag{3.46}$$

Consequently, with the definition of $\partial\tilde{\phi}/\partial\tilde{\tau}$, the plastic flow rule can be defined,

$$\frac{\partial\tilde{\phi}}{\partial\tilde{\tau}} = \sum_{A=1}^3 \tilde{n}_A\,\boldsymbol{\nu}^A \otimes \boldsymbol{\nu}^A \Rightarrow \pounds_v\mathbf{b}^e = -2\frac{\dot{\gamma}^{vp}}{(1-D)}\left[\sum_{A=1}^3 \tilde{n}_A\,\boldsymbol{\nu}^A \otimes \boldsymbol{\nu}^A\right] \bullet \mathbf{b}^e, \tag{3.47}$$

where $\tilde{n}_A = \partial\tilde{\phi}/\partial\tilde{\tau}_A = \tilde{s}_A/\sqrt[2]{\tilde{s}_1^2 + \tilde{s}_2^2 + \tilde{s}_3^2}$. It is notable that the eigenbases for the effective and the homogenized stresses are equivalent, i.e. $\boldsymbol{\nu}^A \otimes \boldsymbol{\nu}^A \equiv \tilde{\boldsymbol{\nu}}^A \otimes \tilde{\boldsymbol{\nu}}^A$. The rates of the scalar strain like variables, α and D, read,

$$\frac{\partial\tilde{\phi}}{\partial q} = -\sqrt{\frac{2}{3}} \qquad \Rightarrow \frac{\partial\alpha}{\partial t} = -\dot{\gamma}^{vp}\sqrt{\frac{2}{3}},$$
$$\frac{\partial\phi^d}{\partial Y^d} = \frac{1}{(1-D)}\left[\frac{Y^d}{a(\theta)}\right]^s \qquad \Rightarrow \frac{\partial D}{\partial t} = \dot{\gamma}^{vp}\frac{1}{(1-D)}\left[\frac{Y^d}{a(\theta)}\right]^s. \tag{3.48}$$

Following similar arguments, the growth of the plastic portion of the inelastic entropy reads,

$$\frac{\partial \eta^p}{\partial t} = \dot{\gamma}^{vp} \sqrt{\frac{2}{3}} \left[\omega_0 \tau_0(\theta_0) - \omega_h q(\alpha, \theta_0) \right], \tag{3.49}$$

which is identical to [162]. The growth of the inelastic entropy associated with damage is,

$$\frac{\partial \eta^d}{\partial t} = \dot{\gamma}^{vp} \frac{1}{(1-D)} \left[\frac{Y^d}{a(\theta)} \right]^s \left[\omega_d a(\theta_0) \frac{Y^d}{a(\theta)} - 3 H \alpha^t \frac{\log[J^e]}{J^e} \right]. \tag{3.50}$$

The details of these derivations are given in Appendix C. The expressions add up to the rate of total inelastic entropy production, $\partial \eta^{pd}/\partial t$, utilizing (3.26). The second principle of thermodynamics places a restriction on the definition of the thermal dissipation via $\Omega^{ther} = \theta \left[\partial \eta^{pd}/\partial t \right] \geq 0$. Accordingly one may suggest two stronger inequalities, such as $\partial \tilde{\phi}/\partial \theta \geq 0$ and $\partial \phi^d/\partial \theta \geq 0$. The former is naturally satisfied, where in the view of (3.37) thermal softening of the plastic potential, is addressed[5]. This condition, also named as the yield locus contraction with temperature, reflects the experimental evidences.

Following simplification, introduced in [162], is invariably valid for the current damage-coupled plasticity,

$$\Omega^{mech,p} = \dot{\gamma}^{vp} \sqrt{\frac{2}{3}} \tau_0(\theta),$$

where the details of this derivation can be found in Appendix C. Together with the definition of damage dissipation,

$$\Omega^{mech,d} := Y^d \underbrace{\frac{\partial D}{\partial t}}_{\dot{\gamma} \frac{\partial \phi^d}{\partial Y^d}} = \dot{\gamma}^{vp} \frac{a(\theta)}{(1-D)} \left[\frac{Y^d}{a(\theta)} \right]^{s+1}, \tag{3.51}$$

---

[5] For two-surface damage coupled plasticity models, where independent plasticity-damage evolution can be observed, analogical to the plasticity, damage softening amounts for the thermal contraction of the separately defined damage surface which is related to the free surface energy of the micro-void/micro-crack formation.

one may find the following total mechanical dissipation[6], Ω^{mech},

$$\Omega^{mech} = \Omega^{mech,p} + \Omega^{mech,d} = \dot{\gamma}^{vp} \left[\sqrt{\frac{2}{3}} \tau_0(\theta) + \frac{a(\theta)}{(1-D)} \left[\frac{Y^d}{a(\theta)} \right]^{s+1} \right]. \qquad (3.52)$$

This expression has a crucial importance in the current thermo-inelastic framework. Besides constituting the heat source, it also accounts for the term that is used in linearization of the weak form of the thermal problem.

Coming to the time sensitive thermal dissipation analysis, a damage affected potential, Φ, is utilized, [60],

$$\Phi = (1-D)\tilde{\Phi}; \quad \tilde{\Phi} = -\frac{1}{2}k\,\mathbf{g} \bullet \mathbf{g}, \qquad (3.53)$$

where k is the (isotropic) heat conduction coefficient. This equation eventually defines the following damage affected heat flux vector, which is in the form of the classical FOURIER's linear heat flow equation,

$$\mathbf{q} = -\frac{\partial \Phi}{\partial \mathbf{g}} = -(1-D)k\,\mathbf{g} \Rightarrow \mathbf{q} = -(1-D)k\,\mathbf{g}. \qquad (3.54)$$

Substituting the values in the conductive thermal FOURIER inequality, supplies,

$$\Omega^{cth} = -\frac{1}{\theta}\mathbf{q} \bullet \mathbf{g} = (1-D)\frac{1}{\theta}k\,\mathbf{g} \bullet \mathbf{g} \geq \mathbf{0}. \qquad (3.55)$$

It is clearly seen that this inequality is unconditionally satisfied for a positive heat conduction coefficient, $k > \mathbf{0}$.

3.3 Numerical Implementation

3.3.1 FE Formulation of the Coupled IBVP

Let $\mathbf{P} := \boldsymbol{\tau} \bullet \mathbf{F}^{-t}$ stand for the first (unsymmetric) PIOLA-KIRCHHOFF stress and $\mathbf{Q} := \mathbf{F}^{-1} \bullet \mathbf{q}$ stand for the heat flux of equivalent type, analogically. Utilizing the

---

[6] In the presence of damage, since $\Omega^{mech,d} \ll \Omega^{mech,p}$, it may be advocated that, $Y^d \, \partial D / \partial t \approx 0$. With this cancelation one has,

$$\Omega^{mech} \approx \Omega^{mech,p}.$$

Also, following the experimental observations of [183], for instantaneous plasticity, one may construct a modified plastic mechanical dissipation, $\Omega^{mech} \longmapsto \breve{\Omega}^{mech,p}$, in terms of the plastic power,

$$\breve{\Omega}^{mech,p} := \varkappa \left[\dot{\gamma}^{vp} \sqrt{\frac{2}{3}} y(q,\theta) \right].$$

where the so-called TAYLOR-QUINNEY empirical constant, $\varkappa \in [0,1]$, defines the extent of the plastic power which is defined as the plastic dissipation. $\varkappa$ is commonly selected in the range $0.85 \leq \varkappa \leq 0.95$.

PIOLA transform, one has $J\mathrm{div}\left[\mathbf{q}/J\right] \mapsto \mathrm{DIV}[\mathbf{Q}]$ and $J\mathrm{div}\left[\boldsymbol{\tau}/J\right] \mapsto \mathrm{DIV}[\mathbf{P}]$, with $J = \det[\mathbf{F}]$. The primary unknowns of the thermo-mechanical problem, $\{\boldsymbol{\varphi}, \mathbf{v}, \theta\}^t$, with $\mathbf{v}$ denoting the velocity vector, are resolved at the global solution stage by considering the following coupled differential equation set constructed at the reference configuration,

$$\left\{ \begin{array}{c} \partial\boldsymbol{\varphi}/\partial t - \mathbf{v} \\ \mathrm{DIV}\left[\mathbf{P}\right] + \boldsymbol{\zeta} - \rho_0\dot{\mathbf{v}} \\ C_v\left[\partial\theta/\partial t\right] - \Omega^{mech} + \mathfrak{H} + \mathrm{DIV}\left[\mathbf{Q}\right] - R \end{array} \right\} = \mathbf{0}. \tag{3.56}$$

Apart from the trivial velocity vector definition given in the first row; in a residual setting, the second and third rows stand for the local equation of motion and the first law of thermodynamics, which supplies the equation for thermal condition. $\dot{\mathbf{v}}$ is the acceleration vector and ρ_0 is the referential density. $\boldsymbol{\zeta}$ denotes the body forces. The boundary conditions for the problem can be listed as follows,

$$\boldsymbol{\varphi} = \bar{\boldsymbol{\varphi}} \text{ at } \partial\mathfrak{B}^{\varphi}; \quad \bar{\mathbf{T}} = \mathbf{P} \bullet \mathbf{N} \text{ at } \partial\mathfrak{B}^{\sigma}; \quad \partial\mathfrak{B}^{\varphi} \cap \partial\mathfrak{B}^{\sigma} = \varnothing; \quad \partial\mathfrak{B}^{\varphi} \cup \partial\mathfrak{B}^{\sigma} = \partial\mathfrak{B}.$$

$$\theta = \bar{\theta} \text{ at } \partial\mathfrak{B}^{\theta}; \quad \bar{\mathbf{Q}} = \mathbf{Q} \bullet \mathbf{N} \text{ at } \partial\mathfrak{B}^{q}; \quad \partial\mathfrak{B}^{\theta} \cap \partial\mathfrak{B}^{q} = \varnothing; \quad \partial\mathfrak{B}^{\theta} \cup \partial\mathfrak{B}^{q} = \partial\mathfrak{B}.$$

$$\tag{3.57}$$

with $\mathbf{N}$ being the outward unit normal to the boundary, $\partial\mathfrak{B}$, in the reference configuration $\partial\mathfrak{B}^{\varphi} \subset \partial\mathfrak{B}$ and $\partial\mathfrak{B}^{\theta} \subset \partial\mathfrak{B}$ denote the parts of the boundary on which the DIRICHLET boundary conditions are specified with the prescribed displacements, $\bar{\boldsymbol{\varphi}}$, and temperatures, $\bar{\theta}$, respectively. With the prescribed tractions, $\bar{\mathbf{T}}$, and the outward normal heat flux, $\bar{\mathbf{Q}}$, NEUMANN type boundary conditions respectively act on the boundary parts $\partial\mathfrak{B}^{\sigma} \subset \partial\mathfrak{B}$ and $\partial\mathfrak{B}^{q} \subset \partial\mathfrak{B}$. The conditions satisfied on these boundary parts are given in (3.57). In the current context, temperature increase is merely associated with the mechanical dissipation due to irreversible processes such as plasticity and damage. Accordingly, the heat source and the temperature variations due to elastic loading are omitted, by canceling R and $\mathfrak{H}$ respectively, to give $C_v\left[\partial\theta/\partial t\right] - \Omega^{mech} + \mathrm{DIV}[\mathbf{Q}] = 0$.

(3.56) can be solved in a monolithic or a staggered manner. Monolithic scheme stands for concurrent satisfaction of the equation set to describe the unknowns, where the system is solved in a fully coupled manner. For this approach, see e.g. [8] and [162]. For the simultaneous solution of the global problem, consequent numerically costly tangent stiffness matrix of thermoplasticity is usually not symmetric. Besides since the difference of the orders of the thermal and mechanical problems, it is not well-

conditioned and needs post processing. In the staggered approach, the coupling is split into mechanical and thermal branches and corresponding equations are solved with successive decrease of mechanical and thermal residuum, where the linear momentum and the energy conservation requirements are satisfied, respectively. If the former mechanical step is realized under constant temperature, then the split is called an isothermal split. The isothermal staggered approaches are numerically cheaper at the expense of numerical instability risk. Unconditionally stable algorithms may be produced by following an isentropic mechanical step, in which the total entropy is held constant. The code may take advantage of using different time scales for the split mechanical and thermal steps which is not possible with monolithic approaches. Details of the staggered split algorithms may be found in [162] and the follow-up studies [198], [9], [10]. For kinematic hardening thermoplasticity, staggered approach is utilized by [69]. Similar generalizations of the staggered approach to damage involved analysis can be found in [174] and [70)]. It should be noted that, the quadratic convergence quality of the NEWTON-RAPHSON scheme is preserved only for the simultaneous approach, whereas the staggered algorithm does provide only super-linear convergence, [162], [198].

3.3.1.1 Staggered Solution Scheme

In solution of the above problem, an isothermal staggered solution scheme is followed, where an isothermal mechanical step is followed by a thermal step on fixed configuration.

Mechanical Step For the mechanical problem, the equation is modified as follows in order to preclude the temperature evolution,

$$\left\{ \begin{array}{c} \partial\boldsymbol{\varphi}/\partial t - \mathbf{v} \\ \mathrm{DIV}\left[\mathbf{P}\right] + \boldsymbol{\zeta} - \rho_0\dot{\mathbf{v}} \\ C_v\left[\partial\theta/\partial t\right] \end{array} \right\} = \mathbf{0}, \tag{3.58}$$

Following a GALERKIN approach, both sides are multiplied by a sufficiently smooth virtual displacement field, $\boldsymbol{\eta}_u$, and integrate at the reference configuration. Applying integration by parts followed by the divergence theorem gives the following internal

part of the mechanical weak statement,

$$g_{\boldsymbol{\eta}_u}^{\text{int}}(\boldsymbol{\eta}_u; \boldsymbol{\varphi}) = \int_{\mathfrak{B}_0} \boldsymbol{\tau} : [\text{grad}\boldsymbol{\eta}_u]^{\text{sym}} \, dV, \qquad (3.59)$$

Linearization of the internal virtual work in the direction of displacement increment $\mathbf{u}$, i.e. $Dg(\boldsymbol{\varphi}, \boldsymbol{\eta}_u)[\mathbf{u}]$, reads,

$$Dg_{\boldsymbol{\eta}_u}^{\text{int}}(\boldsymbol{\eta}_u; \boldsymbol{\varphi})[\mathbf{u}] := \left.\frac{\mathrm{d}}{\mathrm{d}\varepsilon}\right|_{\varepsilon=0} g_{\boldsymbol{\eta}_u}^{\text{int}}(\boldsymbol{\eta}_u; \boldsymbol{\varphi} + \varepsilon\mathbf{u}). \qquad (3.60)$$

Time discrete forms of the above split at the quasi-static limit with, $\rho_0 \mapsto 0$, is constructed through a backward-EULER scheme. In the following, $[\bigstar]_n$ and $[\bigstar]_{n+1}$ give the definitions of any variable denoted by $[\bigstar]$, at time t_n and t_{n+1} respectively. $[\check{\bigstar}]_{n+1}$ stands for the regarding definition at the end of the isothermal mechanical step. It is assumed that the state variables at time t_n are known and using the deformation and temperature computed at $\Delta t = t_{n+1} - t_n$, through a split scheme, the state at time t_{n+1} is sought for. Accordingly, the isothermal mechanical step realized under constant temperature, $\check{\theta}_{n+1} \mapsto \theta_n$, reads

$$\left\{ \begin{array}{c} \check{\boldsymbol{\varphi}}_{n+1} - \boldsymbol{\varphi}_n - \mathbf{u}_{n+1} \\ \text{DIV} \left[\check{\mathbf{P}}_{n+1}\right] + \boldsymbol{\zeta}_{n+1} \\ \check{\theta}_{n+1} - \theta_n \end{array} \right\} = \mathbf{0}. \qquad (3.61)$$

Consequently, one carries out the following linearization, for the internal part of the mechanical weak form,

$$\begin{aligned} K_{MM}(\boldsymbol{\eta}_u, \mathbf{u}_{n+1}) := Dg_{\boldsymbol{\eta}_u}^{\text{int}} = &\int_{\mathfrak{B}} [\text{grad}\boldsymbol{\eta}_u]^{\text{sym}} : \mathbf{c}_{MM,n+1} : [\text{grad}\mathbf{u}_{n+1}]^{\text{sym}} \, dV \\ &+ \int_{\mathfrak{B}} \text{grad}\boldsymbol{\eta}_u \bullet \boldsymbol{\tau}_{n+1} \bullet \text{grad}\mathbf{u}_{n+1} \, dV, \end{aligned} \qquad (3.62)$$

which gives the isothermal stiffness matrix, with the assembly following a spatial discretization. On the right hand side, the first term is due to material stiffness and the second term is due to geometric stiffness. A consistent derivation of $\mathbf{c}_{MM,n+1}$, the spatial material tangent matrix, is vital for quadratic convergence quality of the NEWTON-RAPHSON method. Together with the solution of this step, appropriate updates are realized to give, $\{\mathbf{b}_n^e, \boldsymbol{\xi}_n, \theta_n\} \mapsto \{\check{\mathbf{b}}_{n+1}^e, \check{\boldsymbol{\xi}}_{n+1}, \check{\theta}_{n+1}\}$.

93

Thermal Step After isothermal mechanical convergence is supplied, the thermal step is solved for

$$\left\{ \begin{array}{c} \mathbf{v} \\ \dot{\mathbf{v}} \\ C_v \left[\partial\theta/\partial t\right] - \Omega^{mech} + \mathrm{DIV}\left[\mathbf{Q}\right] \end{array} \right\} = \mathbf{0}, \tag{3.63}$$

Analogically to the mechanical problem under fixed temperature, the weak statement[7] for the thermal problem can be carried out by multiplying both sides of the thermal equation with a continuous temperature field, η_ϱ. Following similar steps as given in the preceding equations, the weak statement for the internal part of the energy balance is carried out,

$$g_{\eta_\varrho}^{\mathrm{int}}(\eta_\varrho; \theta) = \int_{\mathfrak{B}} \eta_\varrho C_v \frac{\partial\theta}{\partial t} dV - \int_{\mathfrak{B}} \eta_\varrho \Omega^{mech} dV + \int_{\mathfrak{B}} \eta_\varrho \bullet k\nabla\theta \, dV. \tag{3.64}$$

This expression is consistently linearized in the direction of temperature change ϱ, to give

$$Dg_{\eta_\varrho}^{\mathrm{int}}(\eta_\varrho; \theta)[\varrho] := \frac{\mathrm{d}}{\mathrm{d}\varepsilon}\bigg|_{\varepsilon=0} g_{\eta_\varrho}^{\mathrm{int}}(\eta_\varrho; \theta + \varepsilon\varrho). \tag{3.65}$$

Introducing the time discretization for the thermal step at fixed configuration, together with backward-EULER method, one has,

$$\left\{ \begin{array}{c} \boldsymbol{\varphi}_{n+1} - \check{\boldsymbol{\varphi}}_{n+1} \\ \mathbf{v}_{n+1} - \check{\mathbf{v}}_{n+1} \\ C_v \left[\theta_{n+1} - \check{\theta}_{n+1}\right]/\Delta t - \Omega_{n+1}^{mech} + \mathrm{DIV}\left[\mathbf{Q}_{n+1}\right] \end{array} \right\} = \mathbf{0}. \tag{3.66}$$

Together with this setting, the linearization of the internal part yields,

$$\begin{aligned} K_{TT}(\eta_\varrho, \varrho_{n+1}) := Dg_{\eta_\varrho}^{\mathrm{int}} = & \int_{\mathfrak{B}} \eta_\varrho \left[\frac{C_v}{\Delta t} - \frac{\partial\Omega_{n+1}^{mech}}{\partial\theta_{n+1}}\right] \varrho_{n+1} \, dV \\ & + \int_{\mathfrak{B}} \nabla\eta_\varrho \bullet k\nabla\varrho_{n+1} \, dV, \end{aligned} \tag{3.67}$$

where $\mathrm{d}\Omega_{n+1}^{mech}/\mathrm{d}\theta_{n+1} =: c_{TT,n+1}$ is called the thermo-inelastic coupling modulus. The derivation of this term is crucial for application of the NEWTON-RAPHSON scheme for the thermal portion of the problem. At this step, the variable update is realized with,
$\left\{\check{\mathbf{b}}_{n+1}^e, \check{\boldsymbol{\xi}}_{n+1}, \check{\theta}_{n+1}\right\} \mapsto \left\{\mathbf{b}_{n+1}^e, \boldsymbol{\xi}_{n+1}, \theta_{n+1}\right\}$.

---

[7] It should be noted that, for an adiabatic case which is assumed for processes taking place in a very short time duration, the heat source and the heat dissipation through conduction are omitted. Consequently, the thermal resolution can be made at material level, at an expense of an increased dimension of the local unknowns array. This is conducted utilizing the strong form of the energy balance equation without a need for tracking a GALERKIN approach. The usual trend is the application of the backward-EULER method in the integration of the temporal evolutionary forms.

Throughout the preceding global solution scheme, switching between the split problems, mutual effects of thermal and mechanical fields on each other are reflected. Accordingly temperature change induced by inelastic dissipative mechanisms such as plasticity and damage are taken into account as well as softening and expansion induced by temperature. Besides heat conduction is affected by deformation and damage.

3.3.2 Return Mapping

Update of the state variables with local integration follows a two-step operator-split with a simultaneous plastic/damage correction for a given elastic prediction. Using a strain driven process, elastic trial left CAUCHY-GREEN deformation tensor, $\mathbf{b}^{e,\,tri}$, can be defined at time t_{n+1}, making use of relative deformation gradient tensor at current step, i.e. $\mathbf{f}_{n+1}$, with $\mathbf{f}_{n+1} = \mathbf{F}_{n+1} \bullet \mathbf{F}_n^{-1}$, and elastic left CAUCHY-GREEN deformation tensor of the previous step, i.e. $\mathbf{b}_n^e$, as follows,

$$\mathbf{b}_{n+1}^{e,\,tri} = \mathbf{f}_{n+1} \bullet \mathbf{b}_n^e \bullet \mathbf{f}_{n+1}^t; \text{ where } \mathbf{b}_{n+1}^{e,\,tri} = \sum_{A=1}^{3} \lambda_{n+1,\,A}^{e,\,tri,\,2}\, \nu_{n+1}^{tri,\,A} \otimes \nu_{n+1}^{tri,\,A}. \tag{3.68}$$

Construction of the algorithmic counterpart of the continuum equations and applying the exponential mapping approximation for flow rule integration, utilizing the coaxiality of the plastic flow and the elastic trial state, yields the following plastic-damage correction on trial elastic principal strains, where the strain corrections in the form of the principal plastic strain increments, $\Delta\epsilon_{n+1,\,A}^p$, are defined as follows,

$$\epsilon_{n+1,\,A}^e = \epsilon_{n+1,\,A}^{e,\,tri} - \underbrace{\frac{\Delta\gamma}{(1 - D_{n+1})}\, \left.\frac{\partial\tilde{\phi}}{\partial\tilde{\tau}_A}\right|_{n+1}}_{\Delta\epsilon_{n+1,\,A}^p}, \tag{3.69}$$

with $\Delta\gamma = \Delta t\, \dot{\gamma}_{n+1}^{vp}$. For α and D, implicit backward-EULER method yields,

$$\alpha_{n+1} = \alpha_n + \sqrt{\frac{2}{3}}\,\Delta\gamma, \tag{3.70}$$

$$D_{n+1} = D_n + \Delta\gamma \frac{1}{(1 - D_{n+1})} \left[\frac{Y_{n+1}^d}{a(\theta_{n+1})}\right]^s. \tag{3.71}$$

The components of the inelastic entropy also exploit the backward-EULER method. Accordingly the plastic portion reads,

$$\eta_{n+1}^p = \eta_n^p + \Delta\gamma\sqrt{\frac{2}{3}}\, \left[\omega_0\tau_0(\theta_0) - \omega_h q(\alpha_{n+1}, \theta_0)\right], \tag{3.72}$$

and the damage portion reads,

$$\eta_{n+1}^d = \eta_n^d + \Delta\gamma \frac{1}{(1-D_{n+1})} \left[\frac{Y_{n+1}^d}{a(\theta_{n+1})} \right]^s \left[\omega_d a(\theta_0) \frac{Y_{n+1}^d}{a(\theta_{n+1})} - 3\,H\,\alpha^t \frac{\log[J_{n+1}^e]}{J_{n+1}^e} \right],$$
(3.73)

which add up to $\eta_{n+1}^{pd} = \eta_{n+1}^p + \eta_{n+1}^d$. It is remarkable that, the local integration expressions for η_{n+1}^p and η_{n+1}^d have explicit representations in $\Delta\gamma$ and D_{n+1}. Thus, setting the inelastic entropy as an additional internal variable does not complicate the local integration scheme and conventional finite thermoplastic algorithmic structure presented in [162], even for damage-coupled conditions. Resultant plastic/damage correction of principal KIRCHHOFF stresses yield,

$$\tilde{\tau}_{n+1,\,A} = \tilde{\tau}_{n+1,\,A}^{tri} - 2\mu \frac{\Delta\gamma}{(1-D_{n+1})}\,n_{n+1,\,A}, \;\; \text{with } \tilde{\tau}_{n+1,\,A}^{tri} = \tilde{p} + \tilde{s}_{n+1,\,A}^{tri}.$$
(3.74)

Plastic potential, which forms the constraint condition reads,

$$\tilde{\phi}_{n+1} := \|\tilde{s}_{n+1}\| - \sqrt{\frac{2}{3}}\,y\,(q_{n+1}, \theta_{n+1}) = 0.$$
(3.75)

3.3.2.1 Solution of Equations of Local Integration

Following [166], local governing equations collected so far can be reduced, particularly for the chosen yield criterion, making use of the substitution, $\tilde{s}_{n+1,\,A} = \|\tilde{s}_{n+1}\|\,n_{n+1,\,A}$, and exploiting the condition of collinear flow and the trial KIRCHHOFF stress tensor, finally, representing the hardening/softening function definition in terms of the plastic multiplier, to reach,

$$\mathbf{r}_{n+1}(\mathbf{x}_{n+1}) = \left\{ \begin{array}{c} \sqrt{\dfrac{2}{3}} \left[\tau_0(\theta_{n+1}) + K'(\alpha_n + \sqrt{\dfrac{2}{3}}\,\Delta\gamma\,, \theta_{n+1}) \right] \\[6pt] - \|\tilde{s}_{n+1}^{tri}\| + 2\mu \dfrac{\Delta\gamma}{(1-D_{n+1})} + \dfrac{\eta}{\Delta t}\Delta\gamma \\[8pt] D_{n+1} - D_n - \Delta\gamma \dfrac{1}{(1-D_{n+1})} \left[\dfrac{Y_{n+1}^d}{a(\theta_{n+1})} \right]^s \end{array} \right\},$$
(3.76)

where $\mathbf{r}_{n+1} = \mathbf{r}_{n+1}(\mathbf{x}_{n+1}) = \mathbf{0}$. In above, $-q = K'(\alpha,\theta) = \partial K(\alpha,\theta)/\partial\alpha|_\theta$ is utilized. The array of unknowns is represented by $\mathbf{x}_{n+1} = \{\Delta\gamma, D_{n+1}\}^t$. (3.76) can be treated with the standard NEWTON-RAPHSON solution scheme. Accordingly, the linearized version of the equations is given as $d\mathbf{r}_{n+1} = \mathbf{Dr}_{n+1} \bullet d\mathbf{x}_{n+1}$, where $\mathbf{Dr}_{n+1}$ denotes the

Jacobian of the system which reads,

$$\mathbf{Dr}_{n+1} = \begin{bmatrix} \dfrac{\partial r_{1,\,n+1}}{\partial \Delta\gamma} & \dfrac{\partial r_{1,\,n+1}}{\partial D_{n+1}} \\[2ex] \dfrac{\partial r_{2,\,n+1}}{\partial \Delta\gamma} & \dfrac{\partial r_{2,\,n+1}}{\partial D_{n+1}} \end{bmatrix}, \tag{3.77}$$

where the component derivations are given in the Appendix C. Using $\mathbf{Dr}_{n+1}^{-1} \bullet \mathrm{d}r_{n+1} = \mathrm{d}x_{n+1}$, the solution for $\mathbf{x}_{n+1}$, which constitutes the local return mapping realized at each GAUSS point, can be carried out with the following iterative scheme,

$$\mathbf{x}_{n+1}^{(k+1)} = \mathbf{x}_{n+1}^{(k)} - \delta^{(k)}\, \mathbf{Dr}_{n+1}^{-1,\,(k)} \bullet \mathbf{r}_{n+1}^{(k)}, \tag{3.78}$$

where $\delta^{(k)} \in (0, 1]$ is the proper line-search parameter.

3.3.3 Algorithmic Tangent Matrices

For the monolithic solution of the global equilibrium problem of coupled thermo-mechanical analysis, one has,

$$\mathbf{r}_{n+1} = \mathbf{r}_{n+1}(\hat{\mathbf{x}}_{n+1}) = \mathbf{0}; \quad \hat{\mathbf{x}}_{n+1} \begin{Bmatrix} \epsilon_{n+1,\,A} \\ \theta_{n+1} \\ \Delta\gamma \\ D_{n+1} \end{Bmatrix}. \tag{3.79}$$

where $\Delta\gamma = \Delta\gamma(\epsilon_{n+1}, \theta_{n+1})$ and $D_{n+1} = D_{n+1}(\epsilon_{n+1}, \theta_{n+1})$. A mechanical-thermal staggered approach introduces following simplifications into the solution scheme.

3.3.3.1 Mechanical Pass

Mechanical pass is realized under constant temperature, where $\theta_{n+1} = \check{\theta}$ which results in $\Delta\gamma = \Delta\gamma(\epsilon_{n+1})|_{\theta=\check{\theta}}$ and $D_{n+1} = D(\epsilon_{n+1})|_{\theta=\check{\theta}}$. For this stage,

$$\mathbf{r}_{n+1} = \mathbf{r}_{n+1}(\hat{\mathbf{x}}_{n+1}) = \mathbf{0}; \quad \hat{\mathbf{x}}_{n+1} \begin{Bmatrix} \epsilon_{n+1,\,A} \\ \Delta\gamma \\ D_{n+1} \end{Bmatrix}\Bigg|_{\theta_{n+1}=\check{\theta}}. \tag{3.80}$$

with the vanishing total differential, $\mathrm{d}\mathbf{r} = \mathbf{0}$, yields

$$\begin{Bmatrix} \dfrac{\mathrm{d}\Delta\gamma}{\mathrm{d}\epsilon_{n+1,\,A}} \\[2ex] \dfrac{\mathrm{d}D_{n+1}}{\mathrm{d}\epsilon_{n+1,\,A}} \end{Bmatrix} = -\mathbf{Dr}_{n+1}^{-1} \bullet \begin{Bmatrix} \dfrac{\partial r_{1,\,n+1}}{\partial \epsilon_{n+1,\,A}} \\[2ex] \dfrac{\partial r_{2,\,n+1}}{\partial \epsilon_{n+1,\,A}} \end{Bmatrix}. \tag{3.81}$$

Accordingly the computation of the mechanical tangent matrix, in the form of the spatial elastoplastic-damage tangent moduli, [161], reads

$$c_{MM,ijkl} = 2\, F_{iI}\, F_{jJ}\, F_{kK}\, F_{lL}\, C_{IJKL},$$
(3.82)

which is a push-forward transformation of Lagrangian constitutive moduli, $\mathfrak{C}_{IJKL}$, which is defined by,

$$\mathfrak{C}_{IJKL} = \frac{\partial S_{IJ}}{\partial C_{KL}},$$
(3.83)

where $\mathbf{S} = \mathbf{F}^{-1} \bullet \boldsymbol{\tau} \bullet \mathbf{F}^{-t}$, is the second PIOLA KIRCHHOFF stress tensor, i.e. the pull-back transform of the KIRCHHOFF stress tensor and $\mathbf{C}$ is the right CAUCHY-GREEN deformation tensor. An explicit representation of $\mathbf{c}_{MM,n+1}$ can be given as,

$$\mathbf{c}_{MM,n+1} J_{n+1} = \sum_{A=1}^{3} \sum_{B=1}^{3} a_{n+1,\,AB}^{epd}\, \boldsymbol{\nu}_{n+1}^{tri,A} \otimes \boldsymbol{\nu}_{n+1}^{tri,A} \otimes \boldsymbol{\nu}_{n+1}^{tri,B} \otimes \boldsymbol{\nu}_{n+1}^{tri,B}$$
$$- \sum_{A=1}^{3} 2(1-D)\tilde{\tau}_{n+1,A} \boldsymbol{\nu}_{n+1}^{tri,A} \otimes \boldsymbol{\nu}_{n+1}^{tri,A} \otimes \boldsymbol{\nu}_{n+1}^{tri,A} \otimes \boldsymbol{\nu}_{n+1}^{tri,A}$$
$$+ \sum_{A=1}^{3} \sum_{\substack{B=1 \\ A \neq B}}^{3} \vartheta_{AB} \boldsymbol{\nu}_{n+1}^{tri,A} \otimes \boldsymbol{\nu}_{n+1}^{tri,B} \otimes \boldsymbol{\nu}_{n+1}^{tri,A} \otimes \boldsymbol{\nu}_{n+1}^{tri,B}.$$
(3.84)

Utilizing the condition $\mathrm{d}\boldsymbol{\epsilon}_{n+1} \mapsto \mathrm{d}\boldsymbol{\epsilon}_{n+1}^{e,\,tri}$, $a_{n+1,\,AB}^{epd}$ is posed as the following 3×3 matrix,

$$a_{n+1,\,AB}^{epd} = \frac{\mathrm{d}\tau_{n+1,\,A}}{\mathrm{d}\epsilon_{n+1,\,B}^{e,\,tri}}.$$
(3.85)

Since the mechanical step in the staggered approach assumes

$$\boldsymbol{\tau}_{n+1}(\boldsymbol{\epsilon}_{n+1}, \theta_{n+1}, \Delta\gamma\,(\boldsymbol{\epsilon}_{n+1}, \theta_{n+1}), D(\boldsymbol{\epsilon}_{n+1}, \theta_{n+1}))$$
$$\mapsto \boldsymbol{\tau}_{n+1}(\boldsymbol{\epsilon}_{n+1}, \Delta\gamma\,(\boldsymbol{\epsilon}_{n+1}), D(\boldsymbol{\epsilon}_{n+1}))|_{\theta=\tilde{\theta}}\,,$$
(3.86)

the computation of $a_{n+1,\,AB}^{epd}$ requires the following chain rule of differentiation,

$$\frac{\mathrm{d}\tau_{n+1,\,A}}{\mathrm{d}\epsilon_{n+1,\,B}^{e,\,tri}} = \frac{\partial \tau_{n+1,\,A}}{\partial \epsilon_{n+1,\,B}^{e,\,tri}} + \frac{\partial \tau_{n+1,\,A}}{\partial \Delta\gamma} \frac{\mathrm{d}\Delta\gamma}{\mathrm{d}\epsilon_{n+1,\,B}^{e,\,tri}} + \frac{\partial \tau_{n+1,\,A}}{\partial D_{n+1}} \frac{\mathrm{d}D_{n+1}}{\mathrm{d}\epsilon_{n+1,\,B}^{e,\,tri}},$$
(3.87)

where the details of the derivation are given in Appendix C and the definitions for $\mathrm{d}\Delta\gamma/\mathrm{d}\epsilon_{n+1,\,B}^{tri}$ and $\mathrm{d}D_{n+1}/\mathrm{d}\epsilon_{n+1,\,B}^{tri}$ require (3.81). The designation of ϑ_{AB} is given as

$$\vartheta_{AB} = 2\frac{\tau_{n+1,\,A}\lambda_{n+1,\,B}^{e,\,tri,2} - \tau_{n+1,\,B}\lambda_{n+1,\,A}^{e,\,tri,2}}{\lambda_{n+1,\,A}^{e,\,tri,2} - \lambda_{n+1,\,B}^{e,\,tri,2}},$$
(3.88)

which suffers from singularity or ill-conditioning, for equal or nearly equal eigenvalues, respectively, where $\lambda_{n+1,\,A}^{e,\,tri} - \lambda_{n+1,\,B}^{e,\,tri} \mapsto 0$. [130, pp. 338–341] includes an

analytical treatment of such cases in the context of finite elasticity materializing L'Hospital rule. Accordingly, as also shown in [22, pp. 138–138, p. 202], for $\lambda_{n+1,A}^e = \lambda_{n+1,B}^e$, the definition of ϑ_{AB} boils down to $\vartheta_{AB} = 2\mu - 2\tau_{n+1,A}$. However, for inelasticity, the application of the L'Hospital rule is not straightforward and requires significant computational time. Thus, numerical perturbation technique serves an efficient substitute. Consequently, equal or numerically close eigenvalues with, $\lambda_{n+1,A}^{e,tri} \simeq \lambda_{n+1,B}^{e,tri}$, are perturbed with a perturbation factor[8], $\delta \ll 1$, which gives $\lambda_{n+1,A}^{e,tri} \mapsto (1+\delta)\,\lambda_{n+1,A}^{e,tri}$, $\lambda_{n+1,B}^{e,tri} \mapsto (1-\delta)\,\lambda_{n+1,B}^{e,tri}$, and for volumetric consistency $\lambda_{n+1,C}^{e,tri} \mapsto 1/[(1+\delta)(1-\delta)]\,\lambda_{n+1,C}^{e,tri}$, [119].

3.3.3.2 Thermal Pass

Coming to the second pass, the configuration is held fixed, $\epsilon_{n+1,A} = \breve{\epsilon}_A$, which results in $\Delta\gamma = \Delta\gamma(\theta_{n+1})|_{\epsilon=\breve{\epsilon}}$ and $D_{n+1} = D(\theta_{n+1})|_{\epsilon=\breve{\epsilon}}$. Consequently one has,

$$\mathbf{r}_{n+1} = \mathbf{r}_{n+1}(\hat{\mathbf{x}}_{n+1}) = \mathbf{0}; \quad \hat{\mathbf{x}}_{n+1} \left.\left\{ \begin{array}{c} \theta \\ \Delta\gamma \\ D_{n+1} \end{array} \right\}\right|_{\epsilon_{n+1,A}=\breve{\epsilon}_A} . \tag{3.89}$$

Analogous to the mechanical step, exploitation of the condition, $d\mathbf{r} = \mathbf{0}$, reads,

$$\left\{ \begin{array}{c} \dfrac{d\Delta\gamma}{d\theta_{n+1}} \\ \dfrac{dD_{n+1}}{d\theta_{n+1}} \end{array} \right\} = -\mathbf{Dr}_{n+1}^{-1} \bullet \left\{ \begin{array}{c} \dfrac{\partial r_{1,n+1}}{\partial\theta_{n+1}} \\ \dfrac{\partial r_{2,n+1}}{\partial\theta_{n+1}} \end{array} \right\}. \tag{3.90}$$

It should be noted that, in both the mechanical pass and the thermal pass the internal variables are changing. The thermal portion is due only if there exists plastic flow and induced damage. Accordingly the Jacobian for the thermal problem, c_{TT}, becomes,

$$c_{TT,n+1} := \frac{d\Omega_{n+1}^{mech}}{d\theta_{n+1}}, \tag{3.91}$$

where the mechanical dissipation at the current increment is,

$$\Omega_{n+1}^{mech} = \frac{\Delta\gamma}{\Delta t}\left[\sqrt{\frac{2}{3}}\tau_0(\theta_{n+1}) + \frac{a(\theta_{n+1})}{(1-D_{n+1})}\left[\frac{Y_{n+1}^d}{a(\theta_{n+1})}\right]^{s+1}\right]. \tag{3.92}$$

Since the thermal step is realized under fixed configuration, one assumes,

$$\begin{aligned} \Omega_{n+1}^{mech}&(\boldsymbol{\epsilon}_{n+1}, \theta_{n+1}, \Delta\gamma\,(\boldsymbol{\epsilon}_{n+1}, \theta_{n+1}), D(\boldsymbol{\epsilon}_{n+1}, \theta_{n+1})) \\ &\mapsto \Omega_{n+1}^{mech}(\theta_{n+1}, \Delta\gamma\,(\theta_{n+1}), D(\theta_{n+1}))\Big|_{\boldsymbol{\epsilon}=\breve{\epsilon}}. \end{aligned} \tag{3.93}$$

---

[8] δ=1.0e-12 constitutes a reasonable assumption.

Accordingly one has,

$$c_{TT,n+1} := \frac{\partial \Omega^{mech}}{\partial \theta_{n+1}} + \frac{\partial \Omega^{mech}}{\partial \Delta\gamma} \frac{\mathrm{d}\Delta\gamma}{\mathrm{d}\theta_{n+1}} + \frac{\partial \Omega^{mech}}{\partial D_{n+1}} \frac{\mathrm{d}D_{n+1}}{\mathrm{d}\theta_{n+1}}. \qquad (3.94)$$

The details of the derivation are given in Appendix C and the definitions for $\mathrm{d}\Delta\gamma/\mathrm{d}\theta_{n+1}$ and $\mathrm{d}D_{n+1}/\mathrm{d}\theta_{n+1}$ require (3.90). This concludes the numerical setup.

3.4 Adiabatic Conditions

For processes which takes place in very small time zones, such as high velocity impact or explosion, heat cannot find time to be conducted over the problem domain. Besides large dilatational changes may occur due to high pressures, [196], which makes use of total hyperelastic stress formulation more reasonable compared to hypoelasticity. When the heat flux is omitted, system can be modeled under adiabatic conditions. Accordingly, since no boundary value problem for temperature is due, the heat equation can be solved in material level. The only difference is that the local equations become a bit more rigorous, [133]. Accordingly, the reduced set of two local equations is increased to three, to become,

$$\mathbf{r}_{n+1} = \mathbf{r}_{n+1}(\mathbf{x}_{n+1}) = \left\{ \begin{array}{c} \sqrt{\frac{2}{3}}\left\{\tau_0(\theta_{n+1}) + K'(\alpha_n + \sqrt{\frac{2}{3}}\Delta\gamma)\right\} \\ -\left\|\tilde{\mathbf{s}}_{n+1}^{tri}\right\| + 2\mu\frac{\Delta\gamma}{(1-D_{n+1})} \\ D_{n+1} - D_n - \Delta\gamma\frac{1}{(1-D_{n+1})^m}\left(\frac{Y_{n+1}^d}{S}\right)^s \\ \theta_{n+1} - \theta_n - \frac{1}{\rho c}\Delta t\,\chi(\rho\dot{w}_{n+1}) \end{array} \right\} ; \quad (3.95)$$

$$\mathbf{x}_{n+1} = \left\{ \begin{array}{c} \Delta\gamma \\ D_{n+1} \\ \theta_{n+1} \end{array} \right\}. \qquad (3.96)$$

where the solution of simultaneous equations require a systematic application of the NEWTON-RAPHSON method where

$$\mathbf{Dr}_{n+1} = \begin{bmatrix} \dfrac{\partial r_{1,n+1}}{\partial \Delta\gamma} & \dfrac{\partial r_{1,n+1}}{\partial D_{n+1}} & \dfrac{\partial r_{1,n+1}}{\partial \theta_{n+1}} \\[2mm] \dfrac{\partial r_{2,n+1}}{\partial \Delta\gamma} & \dfrac{\partial r_{2,n+1}}{\partial D_{n+1}} & \dfrac{\partial r_{2,n+1}}{\partial \theta_{n+1}} \\[2mm] \dfrac{\partial r_{3,n+1}}{\partial \Delta\gamma} & \dfrac{\partial r_{3,n+1}}{\partial D_{n+1}} & \dfrac{\partial r_{3,n+1}}{\partial \theta_{n+1}} \end{bmatrix}. \qquad (3.97)$$

It should be noted that, for high velocity processes, such as machining or impact and penetration problems, strain rate dependence should be involved in the material

100

formulation. Accordingly, strain rate hardening is taken into account. As a consequence, the macroscopic material behavior gives account for a competing mechanism in between strain hardening, strain rate hardening, thermal softening and damage softening. A damage coupled version of the JOHNSON-COOK model, [84], which is an expansion of already utilized hardening/softening function, $y(q, \theta)$, to give account for the thermal and strain rate effects is a widely used alternative for this choice[9]. In the current context, to include strain rate effects, previously presented hardening/softening form can be modified to involve strain rate hardening effects as follows,

$$y(q, \theta) = [\tau_0(\theta) - q(\alpha)] \left[1 + C \log \left[\frac{\dot{\alpha}}{\dot{\alpha_0}} \right] \right] \left[1 - \frac{(\theta - \theta_0)}{(\theta_m - \theta_0)} \right], \qquad (3.98)$$

where C is a material parameter scaling the strain rate effect. $\dot{\alpha_0}$ denotes the reference plastic strain rate. θ_0 and θ_m represent reference and melting temperatures, respectively.

3.5 Application Problems

Preceding algorithmic resolutions are implemented as ABAQUS subroutines where the implementation details are included in Appendix B. In what follows, a set of example problems solved with these subroutines are given.

3.5.1 Necking of an Axi-symmetric Bar

Necking of an axi-symmetric bar is investigated in the context of damage-coupled thermoplastic framework. Contrary to the common idea, in the FE simulations with a typical free contracting (shear-free grip conditions) tensile test specimen of a certain gauge length, central refinement of the mesh does not suffice to transform the bifurcation problem, where the necking can emanate at any section, to a limit load problem. This is due to the fact that, necking emanation requires the break up of the stress uniformity. For this purpose, two necking triggering methods widely used in the literature are the geometric imperfection method and the thermal triggering method. The

---

[9] Such an approach is utilized by many researchers, see e.g. [28] and [29], for an application on a projectile penetration into steel plate problem. Another application for the JOHNSON-COOK model may be given as the hard machining simulations, where large strains, high strain rates and high temperatures are experienced, see e.g. [66] and [67].

former requires a reduction of the central area, linearly varied over the half-length as utilized in [181], [161] and [80], among others. In the latter, fixed temperature boundary conditions applied at both ends are utilized as a necking triggering mechanism, which was first studied by [198], then repeated in [162], [81] and [34], among others. Fixing the temperature at the boundary nodes precludes further thermal softening at specimen end regions, and with the softening in internal regions stress uniformity is broken down[10].

Inspired by these two methods, two additional necking triggering methodologies which relies on the imposed conditions on the damage field over the problem domain, are proposed. Accordingly, either the elements at the central band are deteriorated by a slight initial appropriately selected damage value, or the ones at the boundary bands are assigned to non-increasing and zero damage. The former is analogically similar to the geometric imperfection method whereas in the latter case, with the absence of damage evolution, the boundary band elements boil down to plain thermoplastic ones. Thus it is analogous to the thermal triggering method where the damage softening at the boundary elements is precluded and due to further damage softening in the internal elements the stress uniformity is lost.

In the following analyses, four of the methods mentioned above are utilized. Figure 3.1 shows the geometrical setup and boundary conditions where only one quarter is modeled exploiting symmetry and axi-symmetry. In the geometrical imperfection method the radius of face B is selected as 98.2% of the radius of face A. A displacement controlled simulation is performed where the displacement, Δu, is assigned to face A as seen in Figure 3.1.b. For the thermal boundary conditions the heat flux is blocked at the faces. The elements are assumed to have a reference absolute temperature of $\theta_0 =293$ (K). For the thermal triggering method only, as seen in Figure 3.1.c, face A is assigned with a fixed temperature of 293 (K) equal to the reference temperature.

Figure 3.2 shows 10×20 (10 elements in radial direction and 20 elements in longitu-

---

[10] Restraining the extraction of the specimen end faces (grip conditions with shear) is another way to overcome the uniform stress distribution.
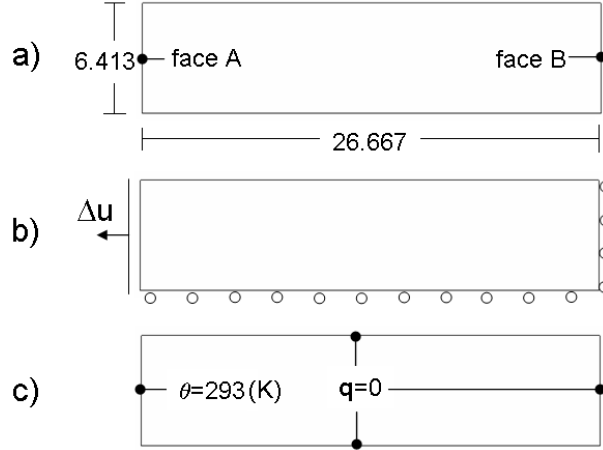
Figure 3.1: Geometry and the boundary conditions for the tensile tests.

dinal direction) mesh composed of element CAX4T, which is a 4-node axi-symmetric thermally coupled quadrangular element with bilinear displacement and temperature interpolations. For the central damage deterioration method (hereafter damage triggering type 1), an initial nonzero damage field, smoothly varied over a certain length, is introduced at the central zone. Accordingly, the regions numbered with $n = 1, 2, 3, 4, 5$ in Figure 3.2.a are deteriorated by an initial damage of, $D = 2^{(1-n)} \times 10^{-6}$. The rest of the domain has zero initial damage. For the necking triggering method which relies on the imposed damage conditions at support regions (hereafter damage triggering type 2), the GAUSS points at the elements of zone 6, seen in Figure 3.2.b, are selected as purely thermoplastic; that is to say, uncoupled to damage.
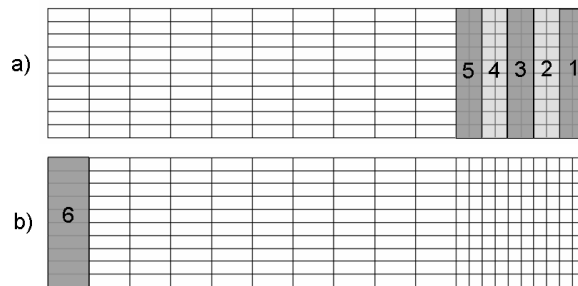

Figure 3.2: The regions, on 10x20 mesh, on which the damage conditions are imposed, for regarding necking triggering methods.

The material parameters used in the analyses are given in Table 3.1, where for mere thermoplasticity the damage deterioration effect is cancelled.

Table 3.1: Material parameters for the example problem.

Parameter	Symbol	Magnitude	Unit
Bulk modulus	H	164.206	GPa
Shear modulus	μ	80.1938	GPa
Flow stress	τ_0	0.450	GPa
Saturation stress	τ_∞	0.715	GPa
Linear hardening	K	0.12914	GPa
Hardening exponent	δ	16.93	-
Density	ρ	7.8×10^9	$\mathrm{Ns^2/mm^2}$
Damage multiplier	a	0.1	-
Damage exponent	s	1.0	-
Coefficient of thermal expansion	α^t	1×10^{-5}	$\mathrm{K^{-1}}$
Conductivity	k	45.0	N/sK
Specific capacity	C_v	0.46×10^9	$\mathrm{mm^2/s^2K}$
Hardening softening	w_h	0.002	$\mathrm{K^{-1}}$
Damage softening	w_d	0.002	$\mathrm{K^{-1}}$

Figure 3.3.a, b, c and d, respectively show the resultant deformed mesh profiles and the damage contours of the geometric imperfection, thermal triggering, damage triggering type 1 and type 2 methods for Δu=6 (mm). Starting with, it can be observed that, proposed necking triggering methods are capable of successfully developing the neck by means of breaking up the stress uniformity over the problem domain. Central damage accumulation is due for all of the models. Maximum radial thinning occurs in the geometric imperfection method with 3.61 (mm) where the minimum occurs in the damage triggering type 1 with 2.38 (mm). Specimens belonging to thermal triggering and damage triggering type 2 methods experience a thinning of 3.07 (mm) and 2.07 (mm), respectively. The differences in the radial reductions are accompanied by different central damage intensities. As expected, maximum damage accumulation is seen in the geometric imperfection method. The rest follows the order of the magnitude of the experienced radial reductions, which changes the effective stress contributions to damage accumulation considerably.
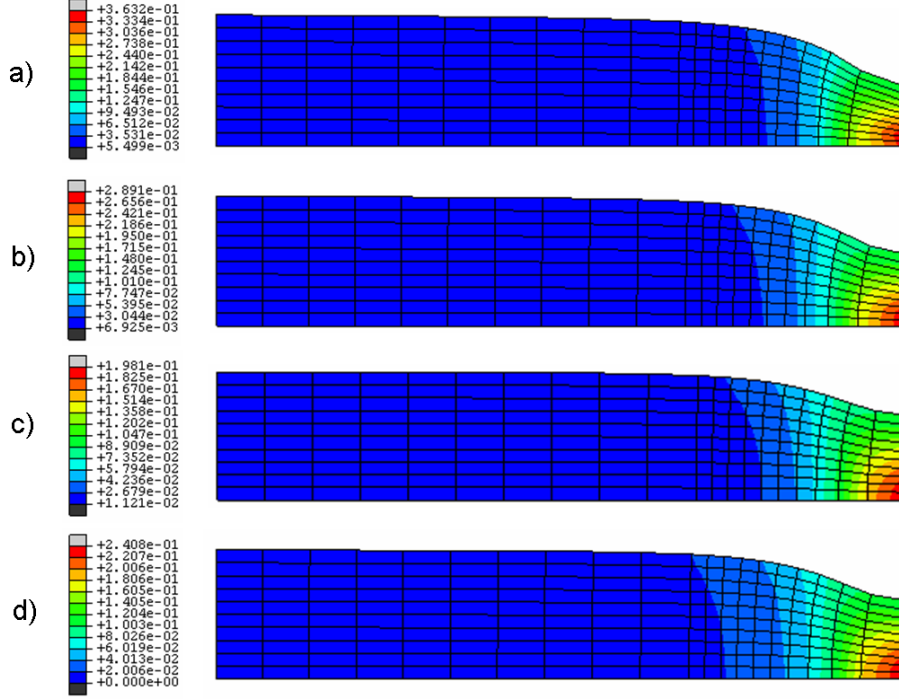
Figure 3.3: Contour plots of the damage distribution at $\Delta u=6$, a) Geometric imperfection method, b) Thermal triggering method, c) Damage triggering type 1, d) Damage triggering type 2.

Figure 3.4.a and b show, respectively, the resultant load-displacement and central temperature increase history curves. Due to considerable initial central area loss in the geometric imperfection method, regarding load values of the load-displacement curve follows a considerably lower trend compared to the other cases. Besides, the peak is reached at an earlier displacement state. The latest peak is reached by the damage triggering type 1 where the given initial centrally distributed damage is considerably small. These results are compatible with the maximum and minimum central thinning of the geometric imperfection and damage triggering type 1 methods, illustrated in Figure 3.3. These results are in accordance with the radial thinning values given. The model with the earlier neck emanation experiences further radial thinning and damage accumulation for a given time at the domain of post peak response. The slopes of the central temperature history curves experience an increase at the point where the peak load response is reached. Besides the apparent shift of the bifurcation points among the curves of different necking triggering methods, the similarity of the

105

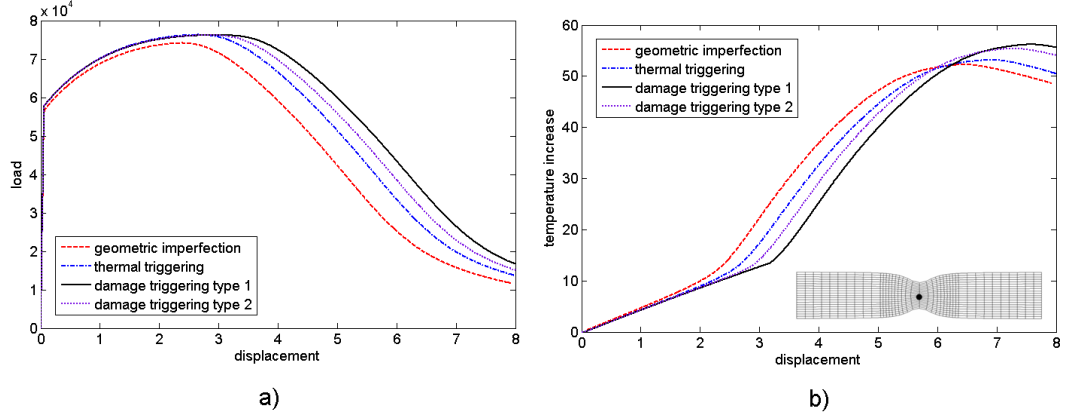post peak trends of both the load-displacement diagrams and the temperature history diagrams is noteworthy.

Figure 3.4: History plots for damage-coupled axi-symmetric necking problem, a) Load-displacement curves, b) Temperature increment evolution at center.

3.5.2 Localization of a Plane Strain Strip

This part is composed of two case studies based on tension of a plane strain strip. Initially a validation study is performed which relies on the comparison of the current thermoplastic material model with the built in model in ABAQUS. Then, the observation of mesh dependence in the localization of deformation and damage together with the investigation of the performance of the viscous regularization take place.

For both of the problems, the geometry, displacement and thermal boundary conditions are the same as those in the previous section (Figure 3.1) where in the current case the quarter is assumed for a plane strain case. Unless otherwise stated, the material parameters are the ones given in Table 3.1. Element CPE4T is used, which is 4-node plane strain thermally coupled quadrilateral with bilinear displacement and temperature interpolations. In the models thermal triggering method is utilized.

106

3.5.2.1 Validation of the Thermoplastic Code

Mere heat source is assumed to be the plastic work with the TAYLOR-QUINNEY empirical constant as, $\chi = 0.90$. Damage evolution is bypassed for this set of analyses. In two additional analyses PERZYNA type viscous regularization[11] is utilized with $\eta = 500$ and $\eta = 1000$. A fixed 10×20 mesh is used.

The load-displacement and the central temperature increment history plots are given in Figure 3.5.a and b respectively. As seen the curves of the ABAQUS built-in model which utilizes the corotational formulation and current hyperelastic thermoplastic results are in perfect correlation. The effect of viscosity is also illustrated in the plots. The abrupt loss in the load carrying capacity together with necking is precluded in the viscously regularized solutions.
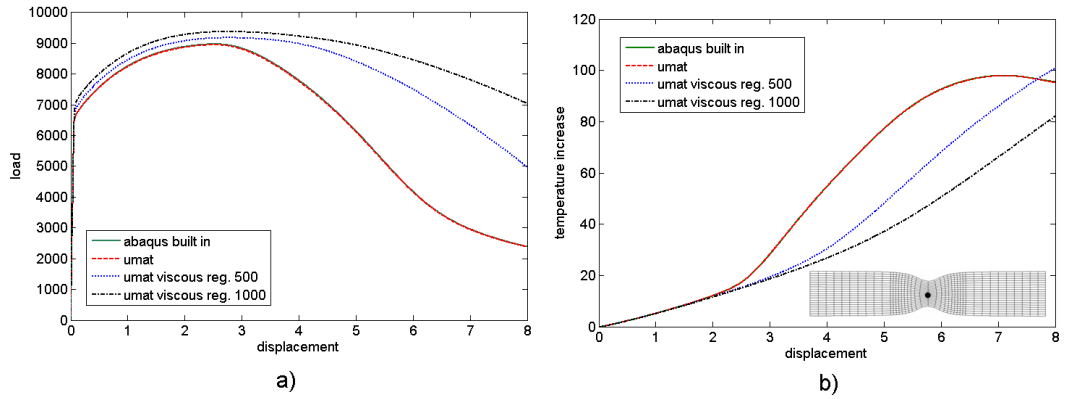

Figure 3.5: History plots for thermoplastic plane strain strip tension problem, a) Load-displacement curves, b) Temperature increment evolution at center.

In Figure 3.6.a, b, c and d deformed meshes together with temperature contour plots can be seen. Figure 3.6.a and b belong to ABAQUS built-in model and present thermoplastic model respectively. Figure 3.6.c and d respectively belong to the results for thermo-viscoplastic solutions with $\eta = 500$ and $\eta = 1000$ utilizing the developed subroutine.

---

[11] In the most general case, instantaneous elasticity and inviscid plasticity bound the expansion of the damage affected yield surface with $0 \leq \eta \leq \infty$.
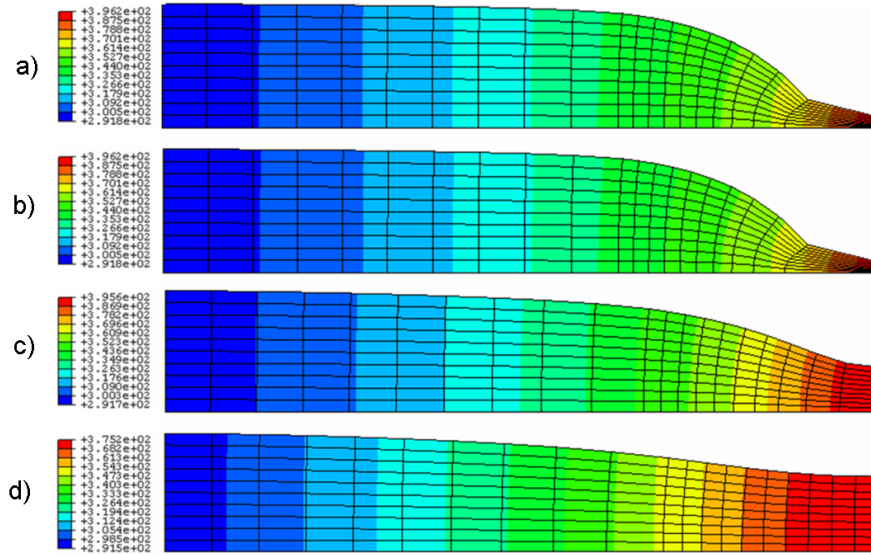
Figure 3.6: Contour plots of temperature distribution at $\Delta u = 8$.

The same order is valid also for the equivalent plastic strain contour plots given in Figure 3.7. All results belong to $\Delta u = 8$ (mm). As seen again, ABAQUS built-in model and the thermoplastic code that was implemented in this study, give perfectly matching results where the extremes are located at the center, as expected. The figures show that together with the inclusion of viscosity, highly localized behavior of the rate independent analyses diffuse; that is, the deformation localized at the elements of the central band is distributed over a wider band. This also decreases the radius reduction at the center. In the inviscid analyses, intensities of both the maximum equivalent plastic strain and the temperature are higher than those of viscous analysis.

3.5.2.2 Mesh Dependency and Viscous Regularization of the Softening Response

In the second problem, the mesh dependency of the doubly induced softening mechanism due to temperature and damage is tested together with the regularization effect of viscosity, where $\eta = 500$. 10×20, 15×30 and 20×40 meshes, shown in Figure 3.8.a,
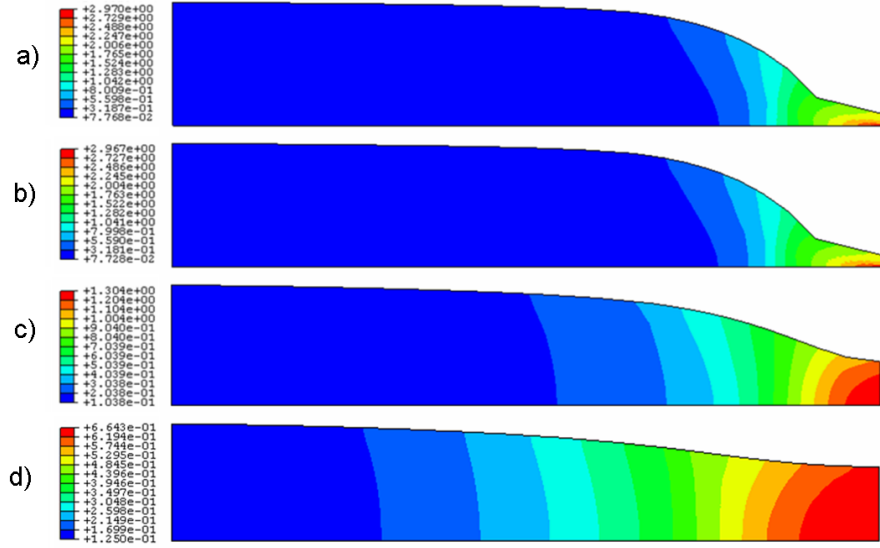
Figure 3.7: Contour plots of equivalent plastic strain distribution at $\Delta u=8$.

b and c, respectively, are used. The heat source is the one presented in the current thesis which is composed of plastic and damage dissipation contributions.
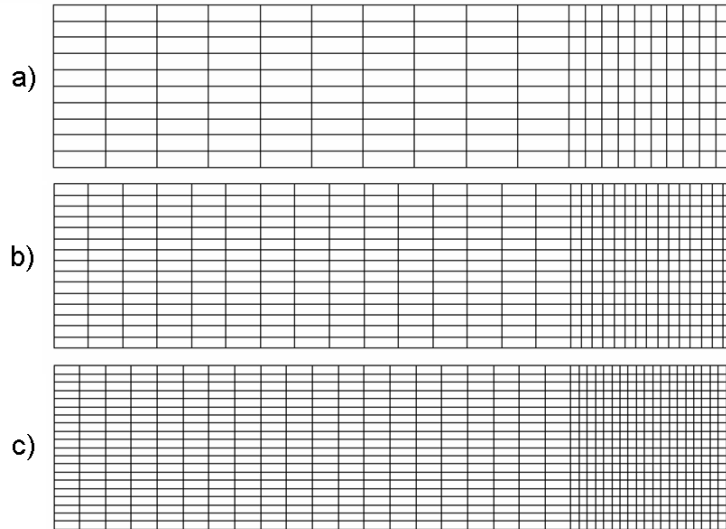

Figure 3.8: FE meshes, a) 10x20, b) 15x30 and c) 20x40.

Figure 3.9.a and b show load-displacement curves for inviscid and viscous solutions,

respectively. In the non-regularized behavior the branching among solutions start just after the peak whereas in the viscously regularized softening behavior, the branching is delayed considerably until which the mesh dependence is postponed and completely healed. Thus, one may conclude that, the viscous regularization cannot cure the pathological mesh dependence for the whole range of deformation, which means it only works partially. This is parallel to the observations in the literature on viscous regularization, [195]. In the rate independent solution, together with the refined mesh the analysis is terminated at a lower load level at smaller deformations. Besides, the post peak response has a sharper decrease compared to the rate dependent solution.
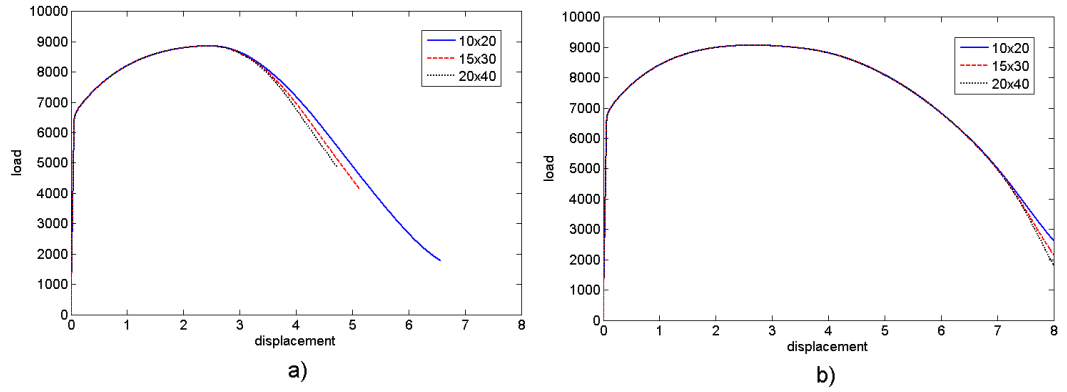

Figure 3.9: Load-displacement curves for damage-coupled plane strain strip tension problem, a) Rate independent solution, b) Viscous solution.

Figure 3.10 and 3.11 show damage contour plots, respectively, for inviscid and viscous solutions at $\Delta u = 4$ (mm) for different mesh refinement levels. For the non-regularized solution given in Figure 3.10, together with mesh refinement, both the intensity and the pattern of the damage becomes strongly mesh dependent, where a localized deformation, in the form of a shear band having an orientation of 45° with respect to the vertical axis, is observed. The width of this band is primarily a function of mesh size.
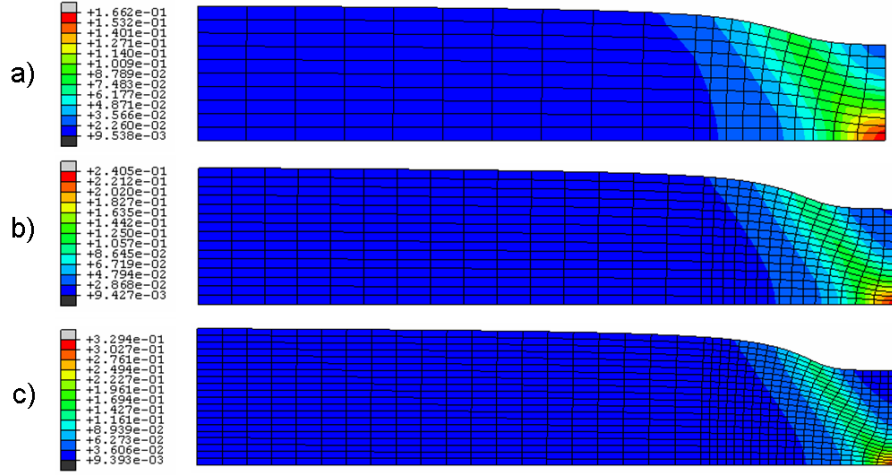
Figure 3.10: Contour plots of damage distribution at $\Delta u = 4$, Rate independent solution.

Together with the introduction of viscosity, this localized deformation problem is transformed into a diffuse necking problem as seen in Figure 3.11. Accordingly, both the distribution and the intensities of the damage field and the deformation pattern at $\Delta u = 4$ (mm) are in perfect correlation, which is confirmed by the load-displacement plots given in Figure 3.9.
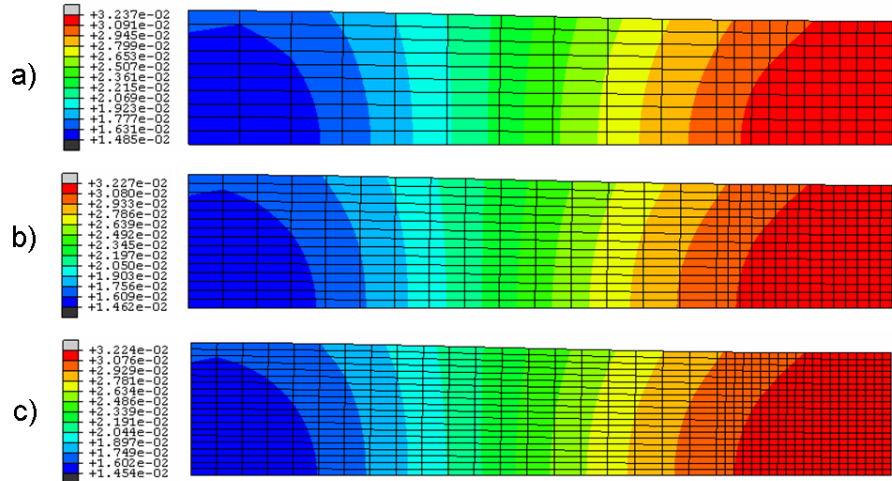

Figure 3.11: Contour plots of damage distribution at $\Delta u = 4$, Viscous solution.

111

3.6 Conclusion

In this chapter, an extension of [162] and its follow up works [9], [10], to the damage-coupled thermo-mechanical response is proposed. It is shown that, once the extensive property of the entropy is exploited, together with a temperature dependent damage dissipation potential, its decomposition into elastic, plastic and damage portions is possible, which depend on their regarding structural changes. Besides it is shown that, in addition to those mutual interactions of the mechanical and thermal fields presented in [162], there exists damage induced effects on thermal and other mechanical fields besides their effects on damage fields. Adiabatic formulations are also presented. The framework utilizes a principal axes formulation where the stresses are derived utilizing a hyperelastic potential quadratic elastic HENCKY strains. This supplies handiness in derivations and implementation of the framework. The resulting thermo-mechanical problem is solved for a staggered approach with the isothermal split where the derived forms are implemented as ABAQUS `UMAT` and `UMATH` subroutines and utilized in a set of example problems. The problems reveal that, for a quasi-static analysis, doubly softening mechanism is prone to the problem of spurious mesh dependence due to the loss of ellipticity of the IBVP. The use of PERZYNA type viscous regularizations however is efficient to an extent for the purpose of localization limitation. Two necking triggering methods in addition to the proposed ones in the literature are also added to the example problems, which are analogically linked to the geometrical imperfection method and thermal boundary fix methods which are already presented in the literature.

CHAPTER 4

MODELING CHEVRON CRACKS

4.1 Introduction

In metal forming processes, the aim is not to exhaust the formability reserve of the material. Once the reserve is exhausted, the physical properties are degraded or even cracks occur resulting in a defected product. The forming design aims defining appropriate kinematics, and predicting forces and stresses which do not induce excessive damage accumulation. This requires the knowledge on micro-mechanism of the material weakening.

In the present chapter, numerical damage analysis including discontinuous crack formation in the process of direct axi-symmetric extrusion with explicit FEM, is aimed. Besides, devising FEM as an economical and practical tool for manufacturing safe products without defects, by means of systematic construction of chevron free production curves or conduction of counter pressure, is presented[1].

By definition, direct axi-symmetric extrusion, classified as a massive metal forming process, is an area reduction method where a round billet is forced by a ram through a conical die. The process geometry is given in Figure 4.1. Two deterioration zones, as possible crack emanation regions, are typical for an extrusion process, which are surface and center. The cracks occurred accordingly are named as surface cracks (also named as snake skin, or fir-tree) or central bursts (also named as chevrons), respectively. The driving parameters affecting the mechanism of failure through redistribution of the mechanical and thermal fields are semi-cone die angle, i.e. α, area

---

reduction, i.e. $1 - [d_1/d_0]^2$, lubrication (friction), temperature, and mechanical and micro-structural quality of the raw material[2]. Resultant surface damage accumulations are due to surface tearing/shearing in the die exit zones where unloading strains (elastic) form tensile residual pressures. Central damage accumulations are due to positive central hydrostatic pressures in die reduction zones accompanied by plastic flow. This internal cracks result in a drastic reduction in the service capacity of the product. Investigation of these hidden cracks, to avoid the faulty product transfer to market, requires, nondestructive ultrasonic testing on every one of products, [201], which is neither practical nor cheap. Thus, proper investigation is required on the governing mechanisms of damage accumulation in extrusion.
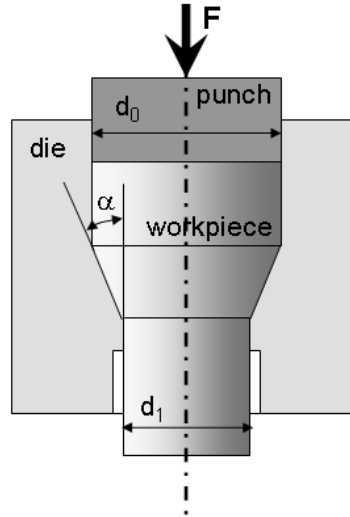
Figure 4.1: Geometry of the forward extrusion process.

The defect formations in extrusion processes have been of interest since early experimental investigations of [82]. Analytical works of [13] materialized upper bound theorem to separate safe and unsafe regions on the plane of semi-cone die angle and area reduction ratio. [200] expanded this work to give account for hardening. Without specific reference to the material, [175] created a similar diagram for spherical dies

---

[2] Like grain size and morphology, non-metallic inclusion content, [89], see e.g. [101] for inclusion of particulate reinforcement.

making use of numerical analysis[3]. According to these studies, the favorable central bursting conditions are the ones with low area reductions and high semi-cone angles, see e.g. [89], [6], [201], among others. Usually, increasing area reduction together with friction has an effect of damage transfer from interior to billet face, motivating superficially dominated deterioration and surface cracks, [101].

For a practising engineer, such forming limit diagrams are quite useful in avoiding defected products. In this context, the macro crack emanation and its propagation may seem to be of second interest, compared to investigating damage accumulation mechanisms to define barriers between safe and unsafe, [89]. However, the prediction and control of cracks gains importance expanding the application area to include deteriorative processes such as machining, orthogonal cutting or blanking, [36]. In the literature, considerable labor is devised for numerical prediction of damage in forward extrusion. Table 4.1 summarizes a number of up to date chronologically ordered numerical damage analysis of extrusion and drawing[4] processes. In Table 4.1, the listed references are evaluated according to the investigated process (extrusion or drawing, abbreviated as ext. or drw., respectively), damage model utilized, inclusion of the thermal and friction effects in the analysis, and finally macro crack formation and the method of crack modeling in use. The deletion procedures utilized are element deletion (Elem. Del.), element degradation (Elem. Deg.) and node separation (Node Sep.). The methods have relative advantages and disadvantages.

In presenting the periodic central bursts, the present work utilizes a LEMAITRE-variant local isotropic damage strongly coupled to a physically sound finite strain hyperelastic-plastic framework through a single VON MISES yield potential. A principal axes formulation, which provides convenience in active-passive damage evolutionary forms, besides in formulation of finite plasticity (the detailed evaluation of the principal stress space formulation for finite plasticity is elsewhere, [80]), is constructed in an EUCLIDEAN setting. It is shown that the active-passive evolutionary conditions controlled by the crack closure parameter have an important effect on the damage ac-

---

[3] See also e.g. [101] in which the [201] diagram is reproduced for reinforced metal matrix composites where strain hardening and friction is neglected, or the envelope curves plotted in [89] utilizing a FM model which is COCKROFT LATHAM model.

[4] Drawing is very similar to extrusion where the driving force is applied to the front tip of the billet creating a tension dominated zone unlike extrusion where the force is applied from the rear tip to result in mainly a compression dominated zone, this gives rise to higher possibility of central crack formation increasing the extent of material regions subjected to positive hydrostatic stresses.

cumulation zones. In the case of complete crack closure, the internal character is amplified rather than the superficial one.

Both explicit and implicit FE solution schemes are conducted, where crack propagation and contact conditions are efficiently resolved. The discrete crack formations are carried out applying element deletion procedure[5], where the elements whose GAUSS points have reached the critical damage threshold are eliminated from the analysis, for the explicit procedure and ramped stiffness degradation, where the elastic properties of the GAUSS points which have reached the critical damage threshold are degraded, for the implicit procedure.

The outline of the rest of this chapter is as follows. Utilizing identical theoretical steps for mathematical material model development as in the case for isothermal theory, numerical treatment of the algorithmic forms in the explicit finite element solution environment is given in § 4.2. A detailed analysis of the discrete chevron predictions under the effect of certain process and material parameters is given in § 4.3.

---

[5] The element deletion procedure is served as a built in procedure in many widely used commercial packages, see e.g., ABAQUS/Explicit, MSC.Marc and Deform2D, among others.

Table 4.1: Numerical damage investigation for direct extrusion/drawing.

ID	Reference	Process	Model	Temperature	Friction	Macro Crack	/	Method
1	Aravas [1986]	Ext.	MDM	–	–	–	/	–
2	Liu and Chung [1990]	Ext.	FM	–	✓	–	/	–
3	Giardini et al. [1994]	Ext.	FM	–	✓	–	/	–
4	Ceretti et al. [1996]	Ext.	FM	✓	✓	✓	/	Elem. Del.
5	Lim and Dunne [1997]	Ext.	MDM	–	–	–	/	–
6	Lee and Hahm [1997]	Ext./Drw.	MDM	–	✓	–	/	–
7	Gelin [1998]	Ext.	MDM	–	–	–	/	–
8	Choi et al. [1998]	Ext.	FM	–	–	–	/	–
9	Srikanth and Zabaras [1999]	Drw.	MDM	✓	✓	–	/	–
10	Komori [1999]	Drw.	MDM	–	✓	✓	/	Node Sep.
11	Ko and Kim [2000]	Ext./Drw.	FM	–	✓	–	/	–
12	Hambli and Badie-Levet [2000]	Ext.	CDM	–	✓	–	/	–
13	Reddy et al. [2000]	Drw.	FM/CDM	–	✓	–	/	–
14	Komori [2003]	Drw.	FM/MDM	–	✓	✓	/	Node Sep.
15	Saanouni et al. [2004]†	Ext.	CDM	–	✓	✓	/	Elem. Del.
16	McAllen and Phelan [2005]	Drw.	MDM+FM	–	✓	✓	/	Elem. Deg.
17	Chamacho et al. [2006]	Drw.	FM	–	–	–	/	–
18	McVeigh and Liu [2006]	Ext.	MDM	✓	✓	✓	/	Elem. Del.
19	McAllen and Phelan [2007]	Drw.	MDM+FM	–	✓	✓	/	Elem. Deg.
20	Soyarslan et al. [2008]	Ext.	CDM	–	✓	✓	/	Elem. Del.

†In Saanouni et. al. [2004], although a thermo-mechanical framework is presented, the extrusion process is simulated for isothermal conditions, thus, the thermal effects on the chevron prediction are not investigated.

4.2 Explicit FE Formulation

The generalized momentum balance in an EULERIAN description, so-called the strong form, reads,

$$\text{div } \boldsymbol{\sigma} + \rho\boldsymbol{\zeta} = \rho\boldsymbol{\gamma}, \tag{4.1}$$

where $\boldsymbol{\sigma}$ denotes the CAUCHY stress tensor defined at current configuration. ρ is the density, whereas $\boldsymbol{\zeta}$ and $\boldsymbol{\gamma}$ are the body forces and accelerations respectively. Multiplying both sides by a sufficiently smooth virtual velocity field, $\boldsymbol{\eta}$, integrating at the current configuration and applying the divergence theorem, one carries out the following weak statement of the (global) equilibrium of the body,

$$\begin{aligned}
g(\boldsymbol{\varphi}, \boldsymbol{\eta}) = \int_{\boldsymbol{\varphi}(\mathfrak{B})} \boldsymbol{\sigma} : \text{grad}\boldsymbol{\eta}\, dv - \int_{\boldsymbol{\varphi}(\mathfrak{B})} \rho\boldsymbol{\zeta} \bullet \boldsymbol{\eta}\, dv - \int_{\boldsymbol{\varphi}(\partial\mathfrak{B}_{\boldsymbol{\sigma}})} \bar{\mathbf{t}} \bullet \boldsymbol{\eta}\, da \\
+ \int_{\boldsymbol{\varphi}(\mathfrak{B})} \rho\boldsymbol{\gamma} \bullet \boldsymbol{\eta}\, dv = 0,
\end{aligned} \tag{4.2}$$

in which $\boldsymbol{\eta}$ satisfies the condition, $\boldsymbol{\eta} = \mathbf{0}$, at $\boldsymbol{\varphi}(\partial\mathfrak{B}_{\boldsymbol{u}})$, where $\boldsymbol{\varphi}(\partial\mathfrak{B}_{\boldsymbol{u}}) \subset \boldsymbol{\varphi}(\partial\mathfrak{B})$ denotes the part of the boundary, $\boldsymbol{\varphi}(\partial\mathfrak{B})$, on which the DIRICHLET boundary conditions are specified with the prescribed displacements, $\bar{\boldsymbol{u}}$. NEUMANN type boundary conditions acts on $\boldsymbol{\varphi}(\partial\mathfrak{B}_{\boldsymbol{\sigma}}) \subset \boldsymbol{\varphi}(\partial\mathfrak{B})$ with the tractions, $\bar{\mathbf{t}} = \boldsymbol{\sigma} \bullet \mathbf{n}$, where $\mathbf{n}$ denotes the spatial normal vector. The boundary parts satisfy the conditions, $\boldsymbol{\varphi}(\partial\mathfrak{B}_{\boldsymbol{u}})\bigcup\boldsymbol{\varphi}(\partial\mathfrak{B}_{\boldsymbol{\sigma}}) = \boldsymbol{\varphi}(\partial\mathfrak{B})$ and $\boldsymbol{\varphi}(\partial\mathfrak{B}_{\boldsymbol{u}})\bigcap\boldsymbol{\varphi}(\partial\mathfrak{B}_{\boldsymbol{\sigma}}) = \emptyset$. In a compact setting, (4.2) stands for the principle of virtual power,

$$\mathfrak{P} = \delta\mathfrak{P}^{int} - \delta\mathfrak{P}^{ext} + \delta\mathfrak{P}^{kin} = 0, \tag{4.3}$$

where $\delta\mathfrak{P}$, $\delta\mathfrak{P}^{int}$, $\delta\mathfrak{P}^{ext}$ and $\delta\mathfrak{P}^{kin}$ respectively denote virtual total, virtual internal, virtual external and virtual kinetic (inertial) power, with

$$\delta\mathfrak{P}^{int} = \int_{\boldsymbol{\varphi}(\mathfrak{B})} \boldsymbol{\sigma} : [\text{grad}\,\boldsymbol{\eta}]^{\text{sym}}\, dv, \tag{4.4}$$

$$\delta\mathfrak{P}^{ext} = \int_{\boldsymbol{\varphi}(\mathfrak{B})} \rho\boldsymbol{\zeta} \bullet \boldsymbol{\eta}\, dv + \int_{\boldsymbol{\varphi}(\partial\mathfrak{B}_{\boldsymbol{\sigma}})} \bar{\mathbf{t}} \bullet \boldsymbol{\eta}\, da, \tag{4.5}$$

$$\delta\mathfrak{P}^{kin} = \int_{\boldsymbol{\varphi}(\mathfrak{B})} \rho\boldsymbol{\gamma} \bullet \boldsymbol{\eta}\, dv. \tag{4.6}$$

with $\boldsymbol{\sigma} : [\text{grad}\,\boldsymbol{\eta}]^{\text{skw}} = 0$, due to symmetry of $\boldsymbol{\sigma}$. Application of the finite element discretization, with the subdivision of the domain, i.e. $\mathfrak{B}$, into non-overlapping subdomains (elements), i.e. $\mathfrak{B}^e$, where $\mathfrak{B} = \mathbf{A}_{e=1}^{n_{el}}\mathfrak{B}^e$, and representing the vector of

approximation functions with $\mathbf{N}^e$, and discrete gradient operator (strain displacement matrix) with $\mathbf{B}^e$, one obtains the following semi-discrete momentum equation[6],

$$\mathbf{F}^{int} - \mathbf{F}^{ext} + \mathbf{M} \bullet \ddot{\mathbf{u}} = \mathbf{0}, \tag{4.7}$$

in which $\mathbf{F}^{int}$, $\mathbf{F}^{ext}$ and $\mathbf{M}$ denote the internal loads, externally applied loads and the mass matrix respectively. Explicit definitions for $\mathbf{F}^{int}$ and $\mathbf{F}^{ext}$ can be given as follows,

$$\mathbf{F}^{int} = \mathop{\mathbf{A}}_{e=1}^{n_{el}} \left[\int_{\varphi(\mathfrak{B}^e)} \mathbf{B}^{e,t} \bullet \boldsymbol{\sigma}^e dv^e \right], \tag{4.8}$$

$$\mathbf{F}^{ext} = \mathop{\mathbf{A}}_{e=1}^{n_{el}} \left[\int_{\varphi(\mathfrak{B}^e)} \mathbf{N}^{e,t} \bullet \rho \boldsymbol{\zeta} \, dv^e + \int_{\varphi(\partial \mathfrak{B}^e_\sigma)} \mathbf{N}^{e,t} \bullet \bar{\mathbf{t}} \, da^e \right]. \tag{4.9}$$

$$\tag{4.10}$$

Finally $\mathbf{M}$ reads,

$$\mathbf{M} = \mathop{\mathbf{A}}_{e=1}^{n_{el}} \left[\int_{\varphi(\mathfrak{B}^e)} \rho \, \mathbf{N}^{e,t} \bullet \mathbf{N}^e dv^e \right]. \tag{4.11}$$

Solution of the resultant problem is possible through implicit or explicit procedures. Making use of an explicit FE procedure, serves advantages for the problems involving severe discontinuities, where an implicit solution scheme may fail to converge. Besides, the resolution of the complicated contact conditions are more efficiently handled compared to implicit procedures. The memory saving behavior for very large problems and amenability to parallelization are other apparent advantages of the explicit codes. Moreover, since the momentum iterations are irrelevant, the procedure does not require computation of the material tangent matrix. This is advantageous for especially the mathematically complicated material models, where a closed form expression for the material consistent moduli is not available[7]. Although there exists a minimum for the time step which preserves conditional stability, [77], in the context of slow (quasi-static) processes, where the inertia effects can be discarded, increasing the density (mass scaling), or the loading rate, artificially, may help expanding this

---

[6] $\mathbf{A}$ denotes the assembly operator, [78].

[7] It should be noted that, once closed form solution is not available, a material independent numerical means of computation of the algorithmic tangent moduli, which depends on the sensitivity analysis of the algorithmic stress terms with respect to the change in the deformation measures is possible, see e.g. [120] or [138], among others. The performance of such approximations depends on the selected step size; such that, convergence qualities close to the quadratic one, handled with the analytically computed tangent moduli, may be supplied.

limitation, which accelerates the process solution. For explicit FE applications in bulk metal forming, reader may refer to [151] and [150].

For the temporal discretization, a notation where, $[\bigstar]_{n-1/2}$, $[\bigstar]_n$, $[\bigstar]_{n+1/2}$ and $[\bigstar]_{n+1}$ give the definitions of any variable denoted by $[\bigstar]$, at times $t_{n-1/2}$, t_n, $t_{n+1/2}$ and t_{n+1}, respectively, is followed. Using an explicit time integration scheme, the kinematics can be integrated with central differences as

$$\mathbf{u}_{n+1} = \dot{\mathbf{u}}_n + \Delta t_{n+1} \, \dot{\mathbf{u}}_{n+1/2}, \tag{4.12}$$

where

$$\dot{\mathbf{u}}_{n+1/2} = \dot{\mathbf{u}}_{n-1/2} + \frac{\Delta t_{n+1} + \Delta t_n}{2} \, \ddot{u}_n, \tag{4.13}$$

$$\ddot{u}_n = \mathbf{M}^{-1} \bullet (\mathbf{F}_n^{int} - \mathbf{F}_n^{ext}), \tag{4.14}$$

with $\mathbf{u}$, $\dot{\mathbf{u}}$ and $\ddot{\mathbf{u}}$ representing displacement, velocity and acceleration vectors, respectively. The algorithmic setting requires the determination of the current state at time t_{n+1}, from a presumably known state at time t_n. As a first step, in a strain driven procedure, $\mathbf{u}_{n+1}$, i.e. the deformation at $\Delta t = t_{n+1} - t_n$, is integrated using (4.12), where the local integration algorithms follow the ones presented in Chapter 2, thus are not involved here.

4.3 Predicting Chevron Cracks

The given framework in Chapter 2 is implemented as a user defined material subroutine, VUMAT, for ABAQUS/Explicit, for return mapping in the company of reduced equation couple, together with the simultaneous solution scheme listed in Table 2.6. The code is materialized in the simulation of a set of damage accumulation studies in axi-symmetric forward extrusion, for a single pass reduction of the billet. A large strain explicit solution procedure is followed. CAX4R elements, which stand for 4-node bilinear axi-symmetric quadrilateral elements with reduced integrations, are utilized together with a combined stiffness-viscous hourglass control (where the weight factor is selected as 0.5). The friction at the interfaces are modeled with COULOMB friction with μ^f denoting the coefficient of friction. A double precision computation is sought, with second order accuracy and distortion control. The conducted simulations aim to investigate the effects of certain phenomena, such as friction and crack

closure parameter, on damage accumulation zones, and frequency and morphology of the obtained crack.

4.3.1 Single Pass Reduction of 100Cr6

4.3.1.1 Explicit FE approach

The problem geometry and the boundary conditions are given in Figure 4.2, where a mesh size of 0.2 mm is utilized in the simulations. A velocity controlled loading is applied.
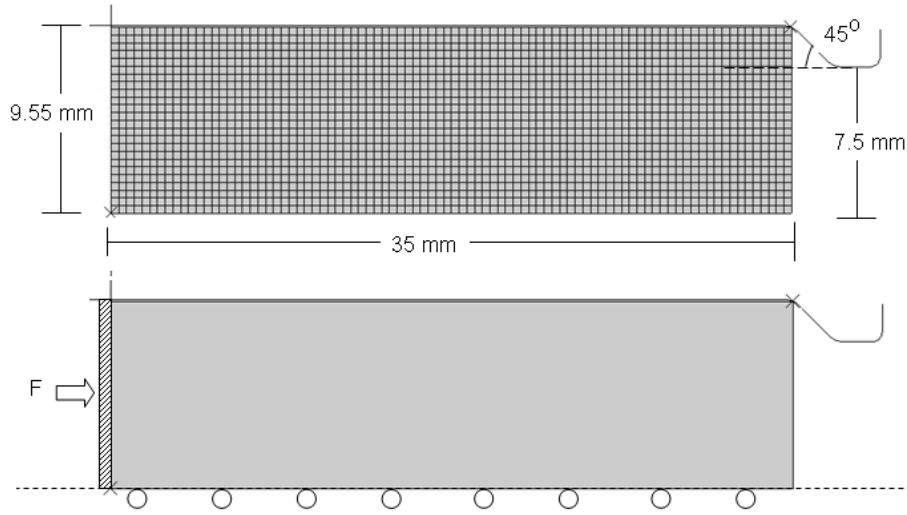

Figure 4.2: Problem dimensions, mesh and the boundary conditions of the single pass axi-symmetric extrusion problem, mesh size=0.2 mm.

Bearing steel 100Cr6 is selected as a material, for which the experimental chevron outputs are available. For the material plasticity parameters, the outcomes of the standard upsetting experiments are utilized, as given in Table 4.2. Neglecting damage accumulation with void nucleation as a consequence of shear decohesion under

Table 4.2: Material parameters for 100Cr6.

Parameter	Symbol	Magnitude	Unit
Bulk modulus	H	175.0	GPa
Shear modulus	μ	80.7692	GPa
Linear hardening	K	0.1151	GPa
Saturation stress	τ_∞	0.9879	GPa
Flow stress	τ_0	0.752	GPa
Saturation parameter	δ	14.3	-
Damage parameter	a	0.3	-

compressive stresses with the presumption of perfect frictionless upsetting conditions, damage is assumed not to affect the parameter identification for plasticity, with the aid of complete crack closure effect. Coming to damage, for the simplest possible damage rate form, in the crack propagation problems, the single parameter, a, is selected as $a = 0.3$ as also given in Table 4.2. Damage coupled and uncoupled flow curves are given in Figure 4.3 (left) for the selected material parameters for the simple plane strain loading of a unit square shown on the figure, utilizing a single finite element having a single GAUSS point. Figure 4.3 (right) shows the concave-up nature of the damage-equivalent plastic strain curve for the whole range of damage accumulation. Admittedly, at this stage of preliminary studies, in the selection of the damage parameter a, the obtained cracks patterns are utilized assuming complete crack closure effect with $h = 0$, where the cracks are supplied with removal of the elements with integration points, satisfying $D \geq D_{cr}$. Without detailed reference to the underlying micro-structure, $D_{cr} = 0.27$ is selected, taking into account the listed critical damage values of certain materials, [99]. Proper selection of h, a and D_{cr} requires further experimental studies. Besides, more complicated damage evolutionary forms, which are nonlinear in Y, may be selected, which can be adapted into the listed framework easily.
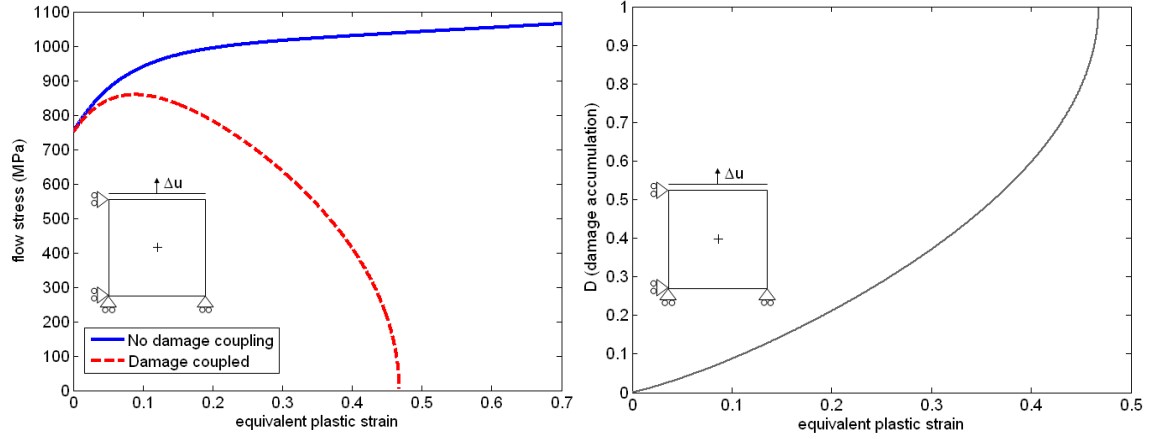
Figure 4.3: (left) Flow curve for 100Cr6, (right) Damage-equivalent plastic strain curve.

Figures 4.4 and 4.5 belong to the frictionless extrusion simulations, where the critical damage value is relaxed to $D_{cr} = 1.0$, which is never actually reached, not to create cracks. Neglecting friction at this stage, aims, isolating the system from additional effects of external agencies in addition to precluding any additional punch force demands. Accordingly, selecting the crack closure parameter, h, as, $h = 0$, the damage deriving stress mechanisms are investigated. Figure 4.4 shows the positive portions of the principal stresses which contribute to the evolution of damage.
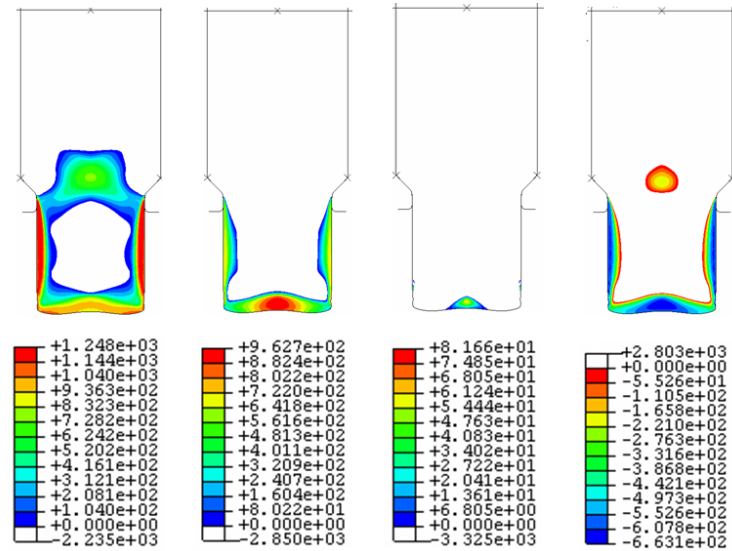

Figure 4.4: From left to right, tensile portions of max, mid and min principal and hydrostatic stresses. An intermediate step of simulations without crack formation, mesh size=0.2 mm., μ^f=0.

The central damage accumulation given in Figure 4.5 reveals that, although at the die exit surface involves considerable amount of tensile residual stresses, damage is centrally located where equivalent plastic strain rate at the reduction zone meets with positive tensile principal stress components. In the current geometry, the maximum principal stress seems to be the mere damage source. The hydrostatic stress field plots also show the central location of the tensile triaxial stress field.
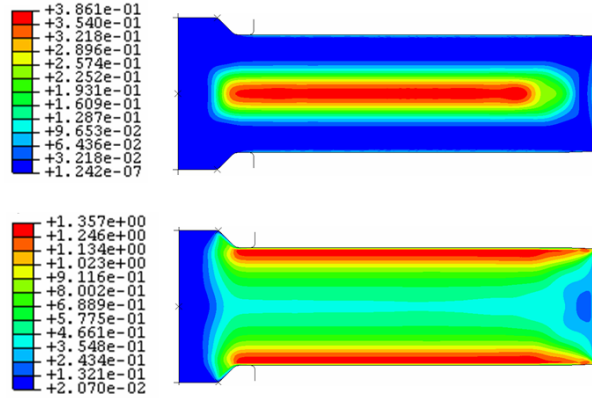

Figure 4.5: Damage and equivalent plastic strain accumulation. Final step of simulations without crack formation, mesh size=0.2 mm., μ^f=0.

The given damage accumulation is utilized to produce cracks by simply reducing D_{cr}, from 1.0 to 0.27, and applying element deletion for the elements where the damage accumulation on the Gauss point comes out to be higher than the threshold. Removal of a finite element from the existing mesh affects the mass matrix and the internal force vector with elimination of the regarding Gauss point from the computational stack. Accordingly, the mass and the internal force contributions of the deleted element are not assembled[8]. The obtained cracks, together with damage and equivalent strain fields are listed in Figures 4.6 and 4.7 throughout the process history. As seen in Figure 4.6, after the occurrence of any free surface by production of a crack, the accumulation of the central damage to produce another crack requires a certain period. This *time to accumulation* creates the periodicity of the discrete crack formation.

---

[8]   Adaptive element sizing gains importance at this point for a smooth solution, where the destabilizing effects of the element removable are scaled by the element size.
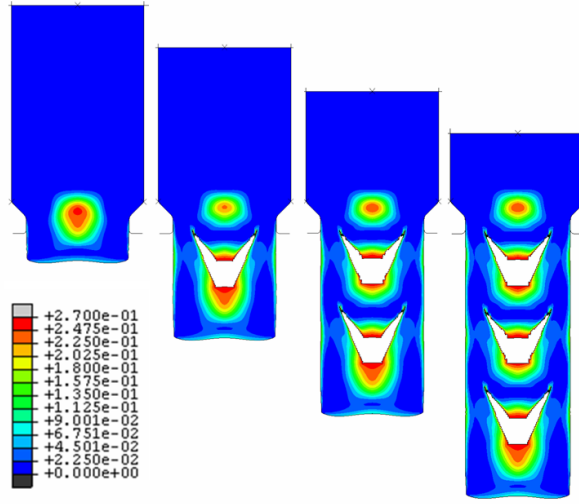
Figure 4.6: Damage accumulation that generate cracks throughout the process history, mesh size=0.2 mm., μ^f=0.

Figure 4.7 shows that, the distribution of the equivalent plastic strains are affected by the central bursts. The crack tip experiences a considerable plastic strain concentration.
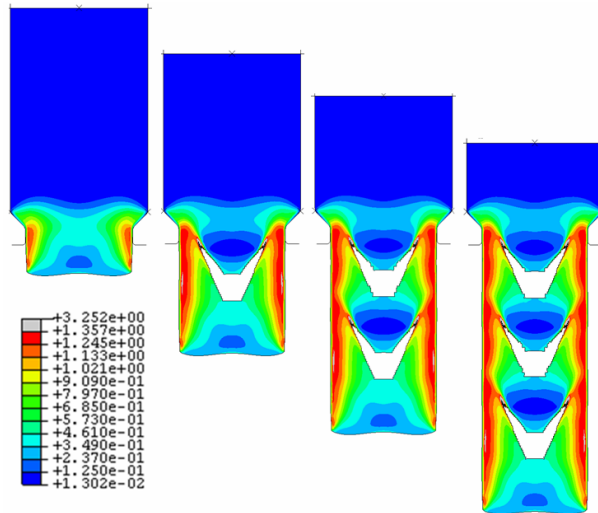

Figure 4.7: Equivalent plastic strain accumulation throughout the process history, mesh size=0.2 mm., μ^f=0.

A comparison between the simulations with crack formation and the ones without crack formation is quite intuitive. Figure 4.8 shows the punch displacement versus punch force demand curves for crack producing and non-producing simulations. Comparison of the plotted curve trends reveals that, the frequency of the oscillations of the force-displacement curve of the crack involving simulation is in accordance with the crack periodicity. The emanation of the force reduction after every oscillatory peak is coincident with the discrete central macro-crack nucleation. The force-displacement curve of the crack-free simulation, on the other hand, follows a constant trend at the steady state, which is typical for a frictionless axi-symmetric extrusion test.
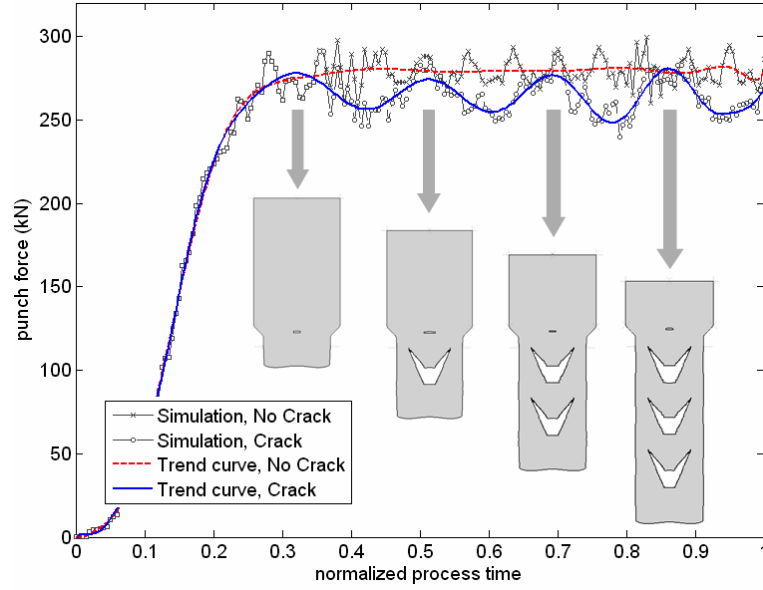

Figure 4.8: Punch force as a function of (normalized) punch displacement, mesh size=0.2 mm, μ^f=0.

The element deletion procedure is criticized for its violation of mass conservation. Figure 4.9, which shows the deleted elements for the frictionless analysis mapped on the undeformed mesh, is used to clarify the extent of this violation. This is to show that, in the meridian plane the large crack gap is not completely due to the deleted elements, but it is primarily due to the separation (displacement, falling apart) of the produced free surfaces, under the redistribution of stress fields. Consequently, together with the efficiency served by element deletion in crack propagation problems, one concludes that, this violation is justifiable. Besides, the deleted material percent

can be calibrated through proper damage controlled adaptive remeshing schemes, which allocate the smallest possible element size to the maximum damage area, see e.g. [27] and [155].
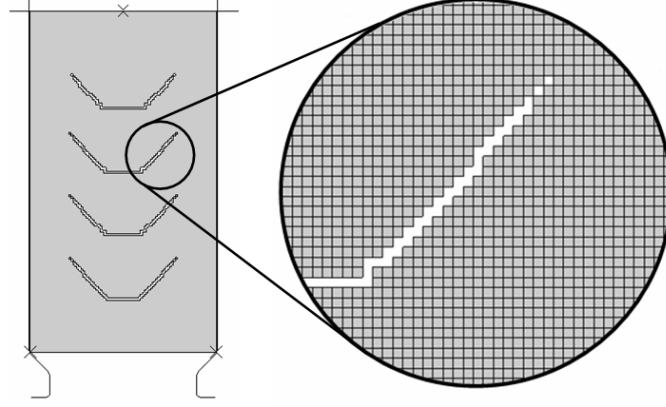

Figure 4.9: Extent of deleted elements, shown on the undeformed mesh, mesh size=0.2 mm, μ^f=0.

Figure 4.10 shows the periodic character of the radial displacement response of the top surface, for the frictionless simulation. This phenomenon stands for the bamboo lines observed on the surface of the extruded specimens which involve internal cracks. For crack-free extrudates, such radial surface oscillations are irrelevant.

The effect of the crack closure parameter, h, is investigated utilizing 0.4 mm. mesh, and frictionless conditions. Simulations are conducted for $h = 0.0$, $h = 0.1$, $h = 0.2$, $h = 1.0$ where the resultant radial extrudate damage accumulations are plotted on a logarithmic scale. To observe the full extent of the closure parameter, the damage rate multiplier a is selected as $a = 0.003$, where damage growth is significantly decelerated. The results, given in Figure 4.10, show the major effect of crack closure parameter on damage accumulation zones. For complete crack closure, i.e. $h = 0$, central accumulation governs whereas making use of standard LEMAITRE form, i.e. $h = 1.0$, surface damage dominates. For $h = 0.10$ the central and surfacial damage accumulations are nearly equal[9]. In obtaining the cracks carried out in the current

---

[9]   The works of [72] has the applications of standard LEMAITRE model where significant dam-

research, a complete crack closure is assumed. Moreover, for $h = 0.20$, which is the proposed crack closure parameter for most of the metals, [98], surfacial rather than central cracks can be carried out as shown in the plot. Thus, proper determination of the crack closure parameter as a material constant requires significant research.
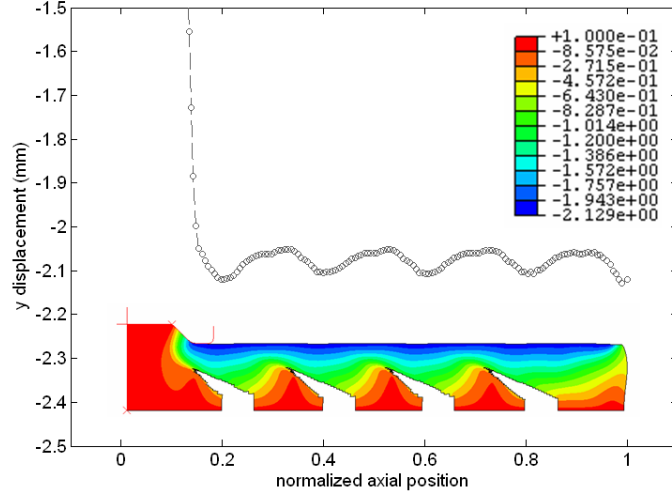

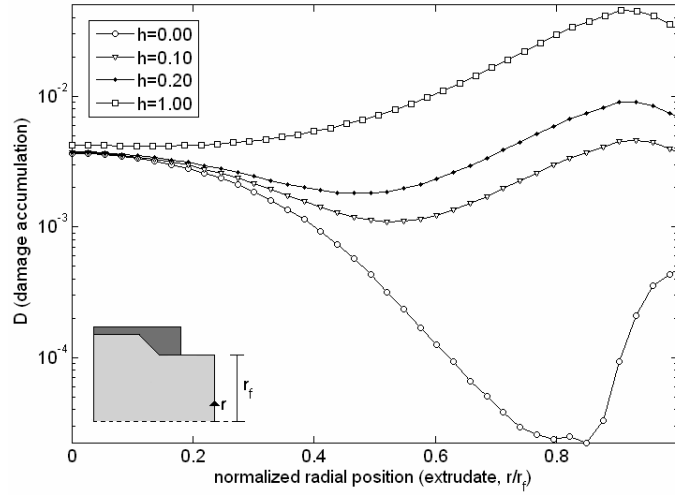Figure 4.10: Radial displacement at the billet surface, mesh size=0.2 mm, μ^f=0.

Figure 4.11: Effect of the crack closure parameter on extrudate radial damage distribution (steady state), mesh size=0.4 mm, μ^f=0.

age accumulation is observed for even not very steep die angles. The main reason, as reveals this observation, is dematerialized crack closure effect.

The effect of friction at the die-billet interface is also investigated. For this purpose, a set of simulations for a set of friction coefficients, such as $\mu^f = 0$, $\mu^f = 0.02$, $\mu^f = 0.04$, $\mu^f = 0.06$ and $\mu^f = 0.08$, are utilized. The resultant crack patterns are given in Figure 4.12. Accordingly, it can be concluded that, wider and more frequent central cracks are due, with the reduction of friction. These results are in complete accordance with those listed in [155].

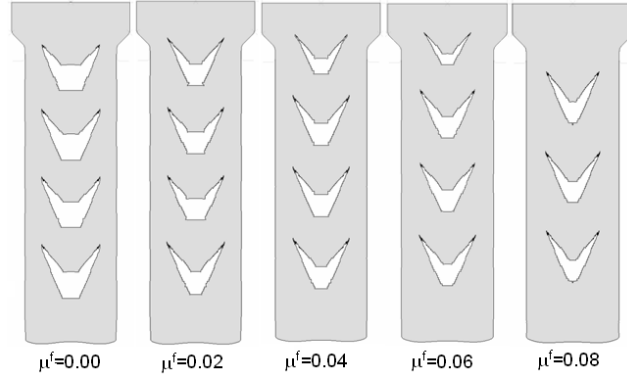Figure 4.12: Effect of friction on discrete crack morphologies and frequencies, mesh size=0.2 mm.

Figure 4.13 shows that, the periodicity of the discrete cracks, for $\mu^f = 0.04$, are compatible with the experimental observations. This represents the predictive performance of the selected damage model.
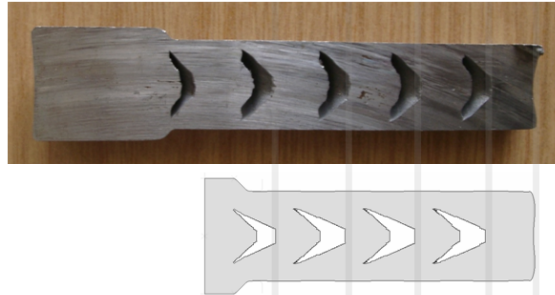

Figure 4.13: Comparison of the handled discrete crack periodicity, mesh size=0.2 mm, μ^f=0.04.

The effect of friction on central and surfacial damage formations can more clearly be seen in Figures 4.14, where observations for $\mu^f = 0$ and $\mu^f = 0.08$ are compared. Also, for these simulations, the variations of the observed damage distributions follow a similar frequency pattern with the observed cracks. Besides, with increased friction, an anticipated increase in the surface damage formation occurs.
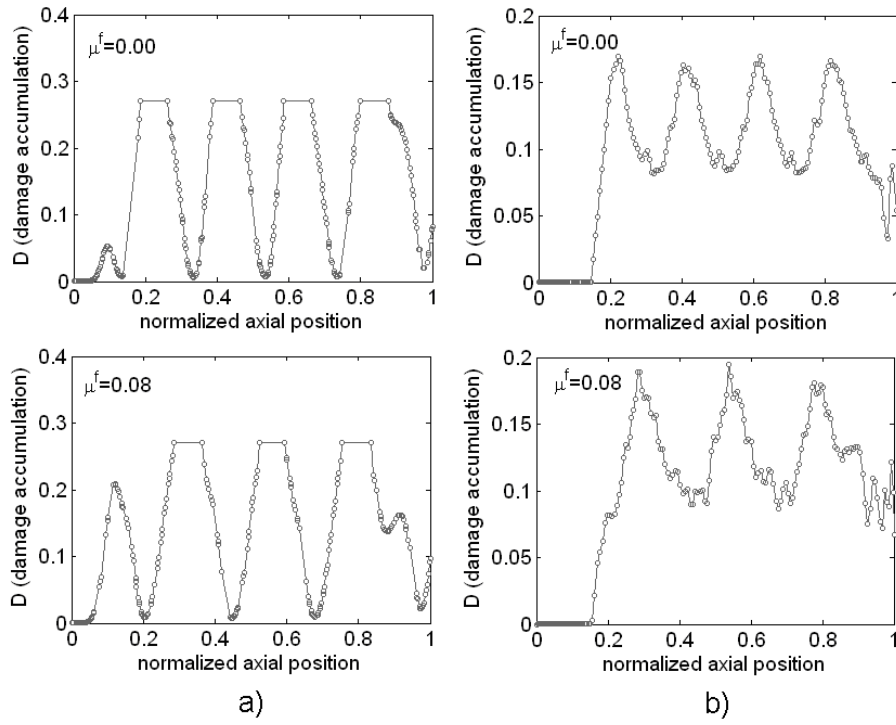
Figure 4.14: Effect of friction on damage distributions, a) center, b) surface, mesh size=0.2 mm.

In order to observe the effect of isotropic hardening regime on damage accumulation profile in extrusion, a set of simulations are run for a mere saturation type hardening plasticity model with different exponents. The yield stress is assumed to be 750 MPa whereas the saturation stress is taken as 950 MPa. Selected exponents define how fast the hardening curve levels off to the saturation stress. Related hardening curves are shown in Figure 4.15.

Figure 4.15: Hardening curves for the selected saturation paramers.

Resulting steady state radial damage and equivalent plastic strain distributions are given in Figure 4.16.a and b respectively, for frictionles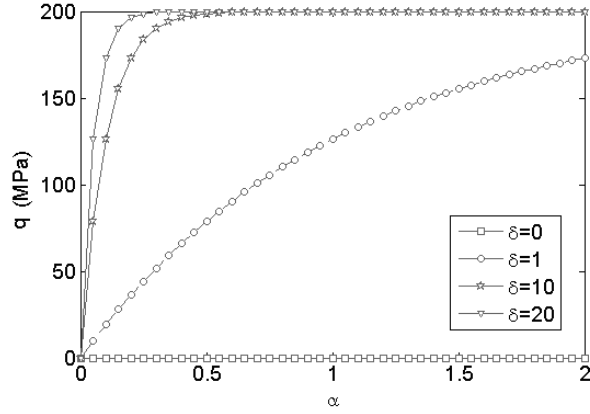s simulations. It is observed that, although the differences among radial equivalent plastic strain distributions are hardly observed, there occurs a marked disparity among radial damage distributions. Accordingly, central damage accumulation is increased for plastic hardening regimes with rapid saturation. This is due to the stress field distributions over the problem domain under the effect of further resistance to flow together with a rapidly governed plastic hardening. The experiences of the author show that, once the material has a mild hardening regime, the surface flow governs whereas a nonuniform equivalent plastic strain distribution occurs for steady state sections. For steeper hardening regimes, a more uniform flow distribution may be carried out with enhanced central flow. The consequence of this observation shows itself in occurrence of various extrudate tip shapes which can take a form in between concave or convex morphologies.

4.3.1.2   Implicit FE approach

Current section involves an attempt for the resolution of the presented problem in the preceding section, using the implicit finite element setup proposed in Chapter 2. In accordance with the previous section, the problem is first solved for no crack formation, and the results of the implicit scheme are utilized in comparison studies
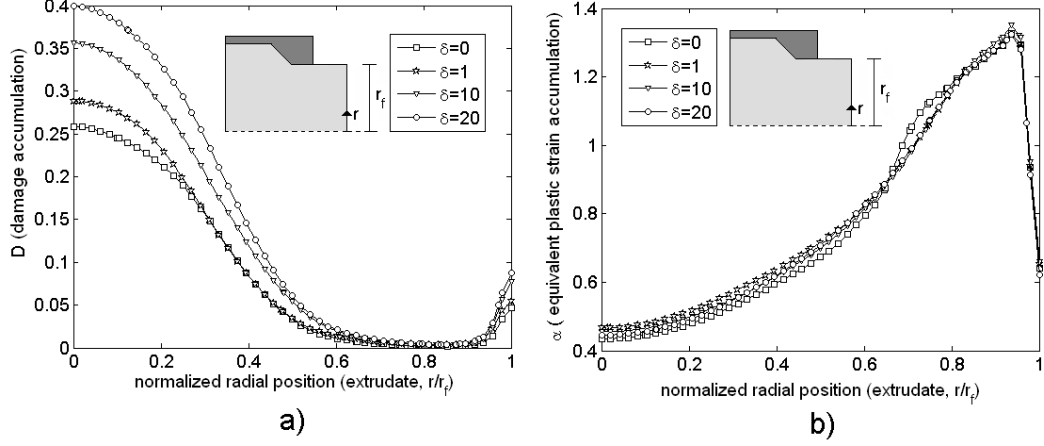
131

Figure 4.16: Steady state radial distributions of, a) Damage, b) Equivalent plastic strain, $\mu^f=0$.

with those of explicit scheme. Admitting the apparent difference in element technologies, utilizing different numerical integration order for ABAQUS/Standard and ABAQUS/Explicit[10], to the author's knowledge, this is the first implicit/explicit comparison study for damage accumulation and crack formation in extrusion processes. In the second part, cracks are carried out by assignment of a critical damage limit, together with the so-called element degradation method[11]. The outcomes are also compared with those carried out with the explicit scheme results which are realized using the element deletion technique using ABAQUS/Explicit. In order to appropriately[12] supply stiffness and load carrying capacity degradation, a ramped degradation of the elastic constants is applied, where at every iteration in a load increment, which is sufficiently small, the elasticity modulus of a failed GAUSS point is reduced to 50% of the previous step. At the end, an elastic GAUSS point persists where the elastic stiffness is about 1e-3 of its initial value, which is a sufficiently close approximation.

---

[10] In the analyses, for ABAQUS/Standard, CAX4 elements are employed which are 4-node bilinear axi-symmetric quadrilaterals with full integration, whereas for ABAQUS/Explicit CAX4R elements which stand for reduced integration 4-node bilinear axi-symmetric quadrangulars with a combined stiffness-viscous hourglass control are utilized. Element type CAX4 is not available in ABAQUS/Explicit, for ABAQUS Version 6.5-1.

[11] For variants of the current utilization of the element degradation method, see e.g. [112] and [113].

[12] A built in element deletion procedure together with the implicit solution scheme is not supported. Thus the deletion requires multiple restart analysis together with MODEL CHANGE and REMOVE ELEMENT commands. Although by scripting this can be achieved without user intervention, element deletion does not guarantee convergence. For certain cases, zero pivoting may occur as a result of under-constrained degrees of freedom. Stiffness degradation is relatively fast compared to element deletion due to no necessity for termination of the analysis upon element failure. However abrupt stiffness and stress drop may introduce ill-conditioning to the system.

Since the degrees of freedoms are still supplied with a small but nonzero stiffness, zero pivoting due to under-constraints does not occur.

Frictionless interface conditions are assumed. The problem geometry and the boundary conditions are the ones given in the previous section. Mesh size of 0.30 mm is utilized in both of the ABAQUS/Standard and ABAQUS/Explicit simulations. A velocity controlled loading is applied. The crack closure parameter is selected as, $h = 0$, where only the positive (tensile) portions of the principal stresses are assumed to contribute to damage evolution.

Figure 4.17.a and b show the damage distributions for implicit and explicit analyses for crack free simulations, respectively. It is notable that, the contours are in perfect correlation where the halves appear as the mirror images of each other. This correlation is a clue for the correction of the implemented codes in implicit and explicit simulations.
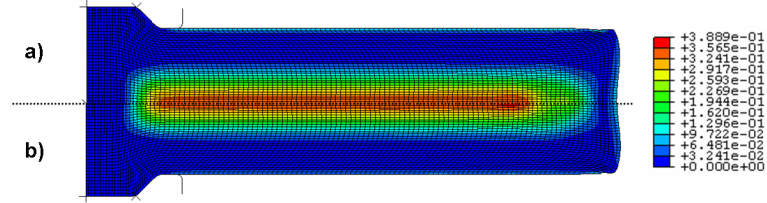
Figure 4.17: Damage contour plots, a) ABAQUS/Standard + UMAT, b) ABAQUS/Explicit + VUMAT.

Figure 4.18.a and b, respectively show the radial distributions of the equivalent plastic strain and damage at a certain section which has reached the steady state, for implicit and explicit analyses. As seen, the outcomes are in a good correlation, where the slight differences seem to emerge due to the different element technologies and global solution scheme differences of CAX4 of ABAQUS/Standard and CAX4R of ABAQUS/Explicit.
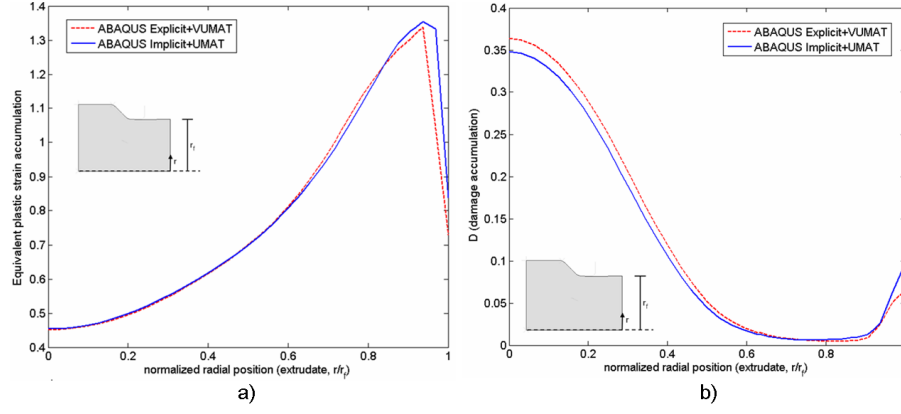
Figure 4.18: Steady state radial distributions of, a) Equivalent plastic strains, b) Damage.

The force demand curves for implicit and explicit analyses are given in Figure 4.19. Due to the boundary condition discontinuity, the curved die surface cannot be traced by the quadrilateral elements exactly. This is the reason for the element size dependent oscillatory load response in the implicit solution, [197]. Due to the sensitivity of the explicit analysis for such discontinuities, although the trend is similar, the kinks in the diagram are larger. In both of the analyses, the driving load saturates to a steady state which is expected for a friction-free extrusion.

Figure 4.19: Punch force-normalized process time curves for implicit and explicit analyses without crack formation.

The given damage accumulation is utilized to produce cracks by simply applying a critical damage threshold, $D_{cr} = 0.27$, and applying element degradation for implicit analysis and element deletion for explicit analysis to the GAUSS points which violate the crit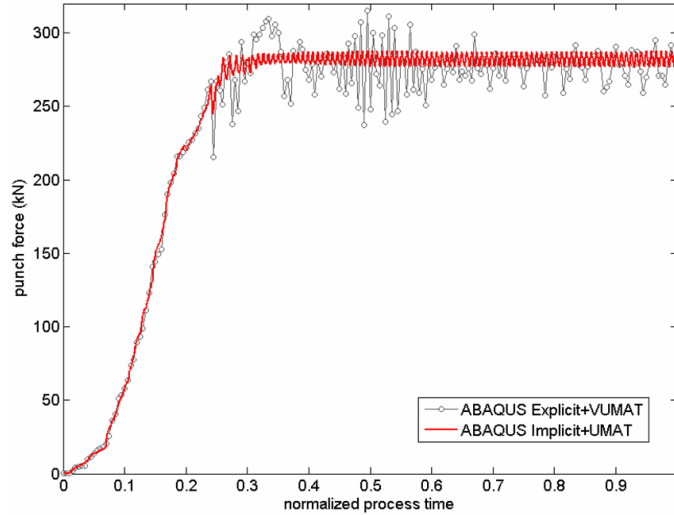ical limit. Figure 4.20 shows the mechanism of crack occurrence, where the left halves demonstrate the positive portions of the hydrostatic stresses over the deformed mesh and the right halves show the accumulated damage contours. The discontinuous accumulation of the damage is in accordance with the crack periodicity.
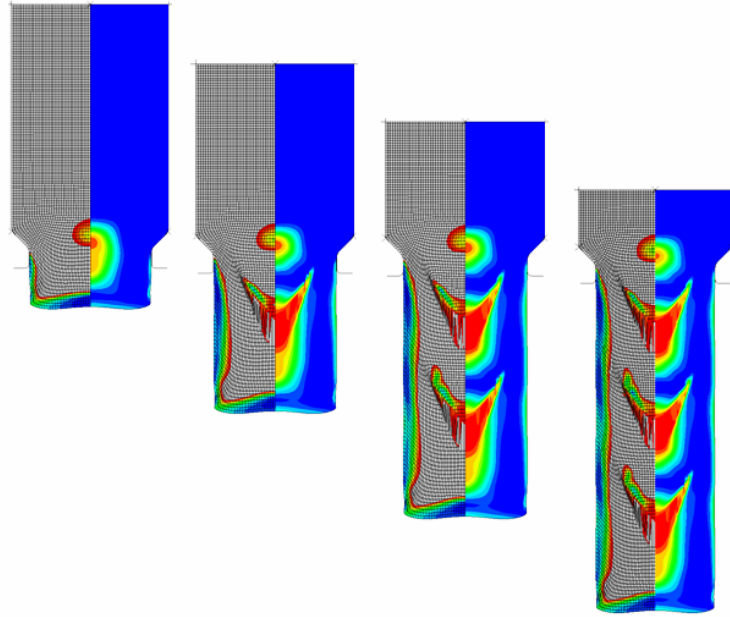
Figure 4.20: Distributions of positive portions of the hydrostatic pressures (left halves) and accumulated damage (right halves) throughout the process history.

The respective chevron patterns of implicit and explicit schemes are given in Figure 4.21.a and b. For a detailed comparison, Figure 4.21.c and d are included which correspond to the crack patterns for undeformed and deformed meshes, in which left halves belong to the implicit and right halves to the explicit solution schemes. As seen in Figure 4.21.a, the periodicity and the morphology of the chevron cracks are well-captured. This proves the capability of the ramped element stiffness degradation method in crack propagation problems. The comparison between results belonging to implicit and explicit schemes shows that, although the emanation of the very first

cracks coincides in both solution schemes, there occurs an accumulated gap in between every successive chevron. This is a result of the difference in the crack tip propagation of the implicit and explicit schemes, where, in the implicit scheme, in which the stiffness degradation is utilized, the extent of the crack tip propagation is larger in both radial and longitudinal direction, which is due to the difference in element technologies besides the macro-crack simulation techniques. Accordingly, in the implicit scheme, each crack is delayed in an accumulated manner, due to the fact that, the extension of free surface by means of further propagated crack tip postpones central damage accumulation. It is also notable that, with the element deterioration method, the extent of deteriorated elements has a larger proportion as compared to the deleted elements of explicit schemes, which makes use of element deletion. This may be one of the reasons for the further crack tip extension in the implicit scheme.
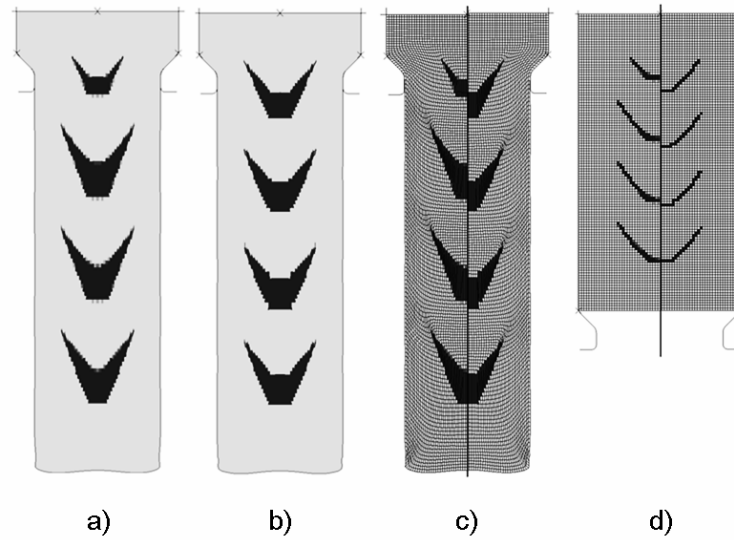
Figure 4.21: Crack morphologies, a) ABAQUS/Standard + `UMAT`, b) ABAQUS/Explicit + `VUMAT`, c) Mirror comparison of implicit (left) and explicit (right) analyses results on deformed mesh, d) Mirror comparison of implicit (left) and explicit (right) analyses results on undeformed mesh.

Figure 4.22 shows the punch load-normalized process time diagrams for implicit solutions. This figure clearly demonstrates the characteristic differences between the force demand curves of chevron-free and chevron-involving extrusions. Once the sizes of the

central cracks are considerable, there occurs apparent oscillations whose periodicities match with those of discrete cracks.

A final note is on the comparison of the force demand, and radial deformation of the billet surface curves of implicit and explicit schemes. The oscillatory behavior is also observed in the radial deformation of the billet surface, which is in correlation with the experimental facts. Besides, the observations listed in the previous paragraphs agree well with the force demand curves given in Figure 4.23.a and b, where the propagating shifts between the oscillations of both the force demand curves and the radial deformation of the billet surface curves of implicit and explicit solutions are respectively given. For a better match between the crack patterns carried out, the methods of crack simulation should be refined. Besides, certain enhancements such as adaptive mesh refinement can be devised.
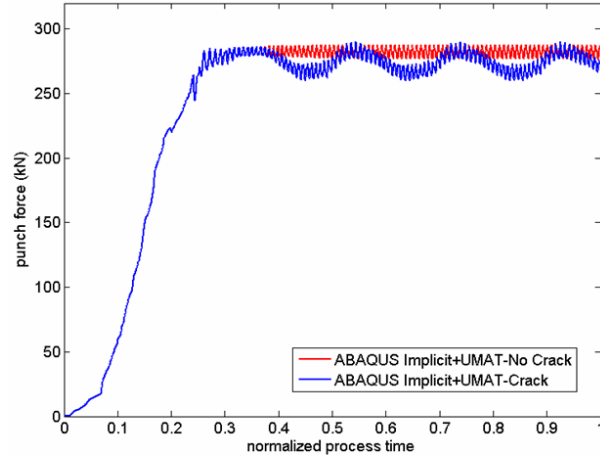
Figure 4.22: Punch force-normalized process time curves for implicit analyses with and without crack formation.

4.3.2   Double Pass Reduction of Cf53

This section is devoted to the simulation of double pass reduction of Cf53, where the material parameters are listed in Table 4.3.
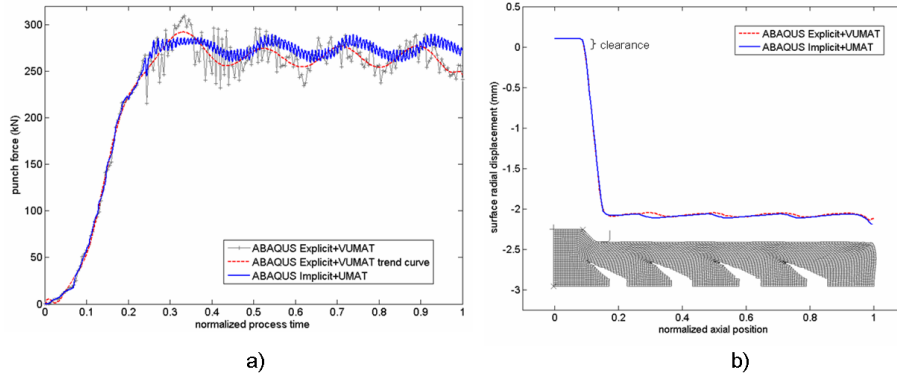
Figure 4.23: Oscillations in a) Punch force-normalized process time curves, b) Radial deformation of the billet surface curves, of implicit and explicit analyses.

Table 4.3: Material parameters for Cf53.

Parameter	Symbol	Magnitude	Unit
Bulk modulus	H	175.0	GPa
Shear modulus	μ	80.7692	GPa
Linear hardening	K	0.0223	GPa
Saturation stress	τ_∞	0.9354	GPa
Flow stress	τ_0	0.6259	GPa
Saturation parameter	δ	10.1	-
Damage parameter	a	0.7	-

Figure 4.24 gives the geometrical setting of the problem. In the analysis CAX4R elements are utilized where the details are the ones given for the single pass simulations with explicit framework.
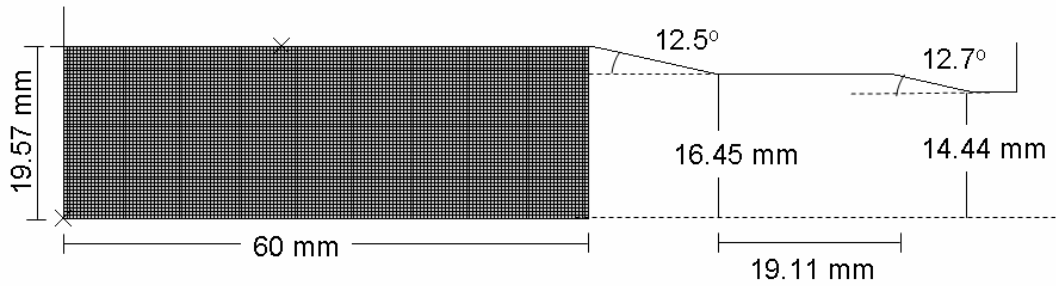
Figure 4.24: Problem dimensions and the mesh of the double pass axi-symmetric extrusion problem, mesh size=0.4 mm.

138

The simulations show that, in both of the passes, for the damage model which merely gives account for damage occurrence driven by tensile principle stress states, central damage accumulation is due. The crack threshold is not satisfied at the first pass. However in the second pass, with further damage accumulation, the cracks can be carried out. Figure 4.25 shows how the mechanism of damage accumulation is realized.
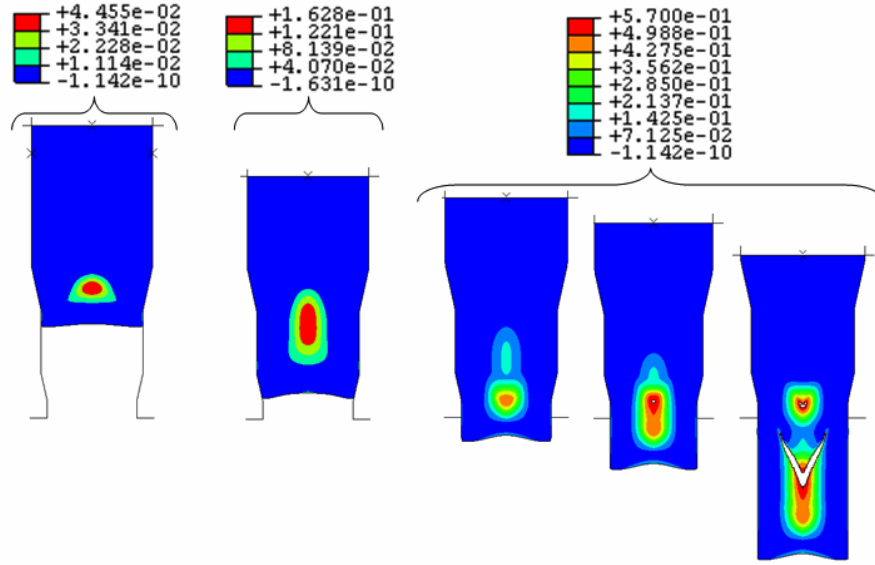
Figure 4.25: Damage accumulation and crack propagation at different stages of double reduction of Cf53.

Equivalent plastic strain distributions at various stages of the simulation are given in Figure 4.26. Together with crack occurrence, significant plastic strain concentration occurs at the crack tip, as anticipated and observed from the previously given single extrusion of 100Cr6 simulations with cracks.

The punch force demand curve is given in Figure 4.27, where the central crack occurrence instances are also marked. It is seen that although the simulation is conducted making use of an explicit scheme, the scatters of the graphs are in tolerable ranges. Together with the comparison of the internal strain energy and kinetic energy curves,
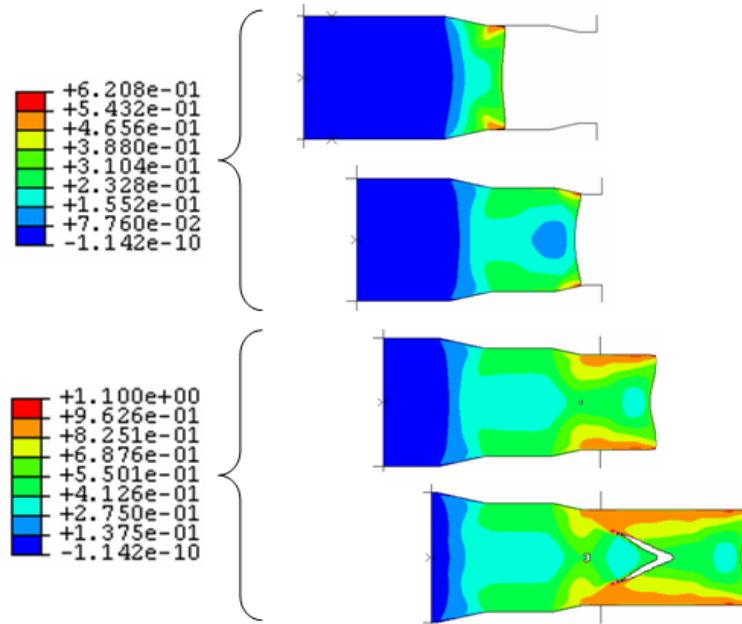
Figure 4.26: Equivalent plastic strain accumulation and crack propagation at different stages.

it is seen that the inertia effects are sufficiently decreased, thus the quasi-static analysis is safely and physically realistically realized.
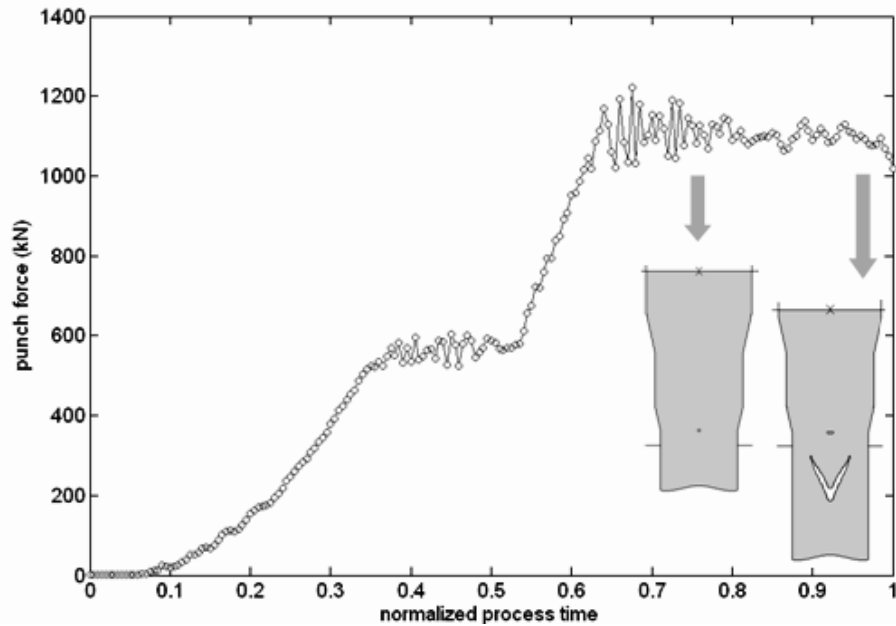
Figure 4.27: Punch force as a function of normalized process time.

Figure 4.28 shows that, crack periodicities carried out for a mesh size of 0.4 mm, D_{cr}=0.57, h=0.0 and μ_f=0.03 are in well accordance with the experimental outputs.

Figure 4.28: Comparison of the experimental and numerical cracks.

4.4 Avoiding Chevron Cracks

4.4.1 Numerical Chevron-Free Production Curves

Through a set of simulations for different semi-cone die angles and area reduction ratios, an AVITZUR-like chevron-free production curve can be produced. Accordingly, by means of simulations materializing CDM, admissible die angle-area reduction combinations can be identified without need for repeated experiments. As stated previously, such diagrams are quite valuable for a practising engineer by accelerating the process geometry decision step considerably. As far as the production costs are concerned, a numerical method supplies a much more economical solution.

Figure 4.29.a shows iso-curves for maximum steady state central damage values that occur in frictionless extrusion of 100Cr6, which is carried out by scanning a predefined grid at the die angle-area reduction plane for certain combinations through simulations. An explicit FE procedure is utilized in the simulations. It is seen that,

most desirable conditions with smallest central damage accumulation occur for small die angles and high area reduction ratios. Critical damage threshold is satisfied for cases where high reduction ratios meet with high die angles. Figure 4.29.b shows the scanned grid points on the plane where safe (without crack formation) and unsafe (with crack formation) simulations are also marked.
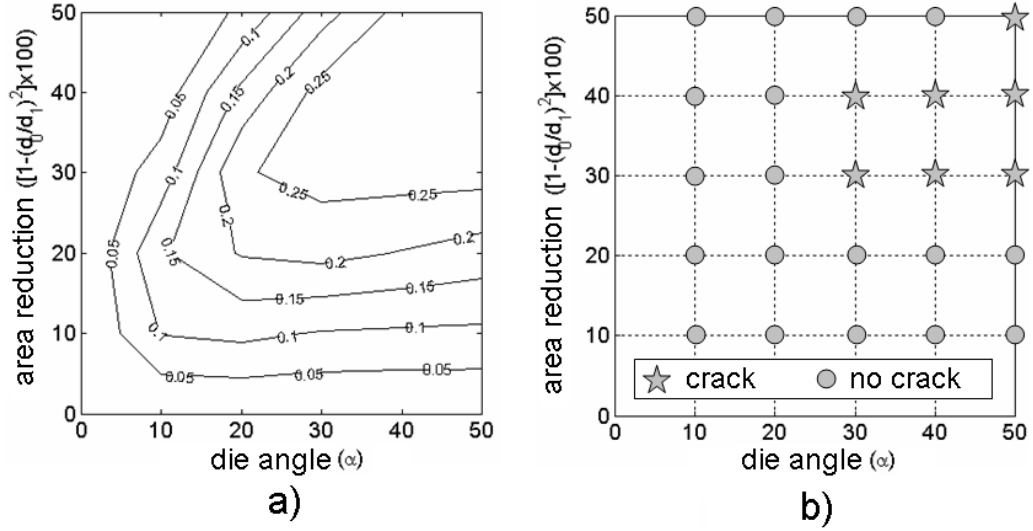
Figure 4.29: a) Iso-damage contours for maximum central damage accumulation at steady-state, b) Simulations with and without cracks, $\mu^f=0$.

4.4.2 Avoiding Chevrons by Means of Counter Pressure

In this section it is demonstrated that, application of counter pressure introduces a marked decrease in the central damage accumulation, which in turn increases the formability of the material through keeping the central tensile triaxiality in tolerable limits. It is also shown that, for a crack involving process, through systematic increase of the counter pressure, the crack sizes diminish; where at a certain level of counter pressure chevron cracks can be completely avoided. Since, in avoiding cracks, the main motivation is to obtain a hydrostatic compression at the forming zone, for fixed die geometry and process parameters one could supply additional central compression by means of employing counter pressure at the extruded nose part of the workpiece. The

experimental studies of [191], [192], [193] show that, application of counter pressure promotes material formability in extrusion by which it becomes possible to extrude even relatively brittle materials, like MMC of aluminum alloy matrix with SiC particles, similar to low carbon steels, where the cracks are suppressed. Moreover, it is demonstrated in these studies that, counter pressure application results in decreased die exit residual tensile stresses and more homogeneous plastic deformation distributions at the extrudate where strain gradients are lowered. Besides its advantages, counter pressure increases the punch force demand of the process and thus has certain limits governed by the allowable punch and die stresses[13].

To the author's knowledge, there exist no numerical studies on the use of counter pressure to give account for defect-free extrusion. Accordingly, in this follow up section, the aim is to investigate what (explicit) finite element method suggests on the role of counter pressure in suppressing crack formations in axi-symmetric forward extrusion. For this purpose, for single pass reduction of 100Cr6, it is shown that, proper application of counter pressure suppresses central crack formation completely, by keeping the forming zone hydrostatic stress levels in tolerable limits. The deviations of crack morphologies and sizes with counter pressure application are also examined. Figure 4.30 shows the employed axi-symmetric model boundary conditions, where for counter pressure a rather simplistic approach, in which a compressive normal traction is applied at the workpiece nose with an opposing direction to the punch movement direction, is pursued. Such an application of the counter pressure in the form of normal compressive surface pressure deviates from the actual practice where a counter punch is utilized. However, various trials of the authors show that, simulations involving a counter pressure applied through a counter deformable body increases the computational time considerably due to additional contact iterations, where, although the nose deformation pattern may depart at high pressure levels in between two methods, these differences diminish at distances sufficiently far away from the nose due to SAINT-VENANT's principle.

---

[13] Counter pressure application is also employed as a precision extrusion method, where the underfilling defects are eliminated, [132]. However this type of utilization falls beyond the context of this study.
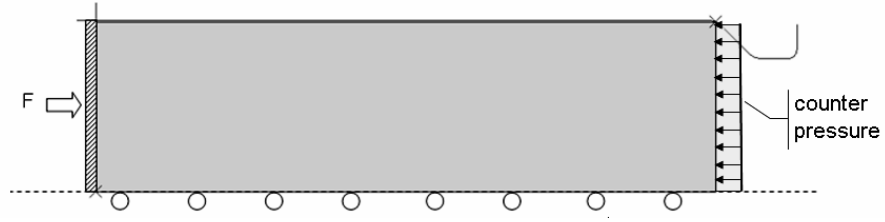
Figure 4.30: Application of the counter pressure.

Starting with, frictionless workpiece-die interface is assumed for a clear demonstration of the central damage accumulation mechanism. Without any counter pressure, with the aid of positive triaxial stress state which meets with plastic flow at the forming zone, a localized damage growth is observed, as demonstrated in Figure 4.31.a, b and c, which respectively represent the iso-curves for positive hydrostatic stress, equivalent plastic strain rate and damage rate, one step before the first element deletion, i.e. occurrence of the first crack. At the die exit, there exists a small amount of surface deterioration due to residual tensile stresses. At Figure 4.31.d and e, total equivalent plastic strain and total damage iso-curves are given, respectively. As seen, central damage rates accumulate to create a continuous damage zone at the central region. It is not hard to guess that, when this value exceeds the critical threshold, together with coalescence of micro-voids, macro-crack formations in the form of chevrons take place.
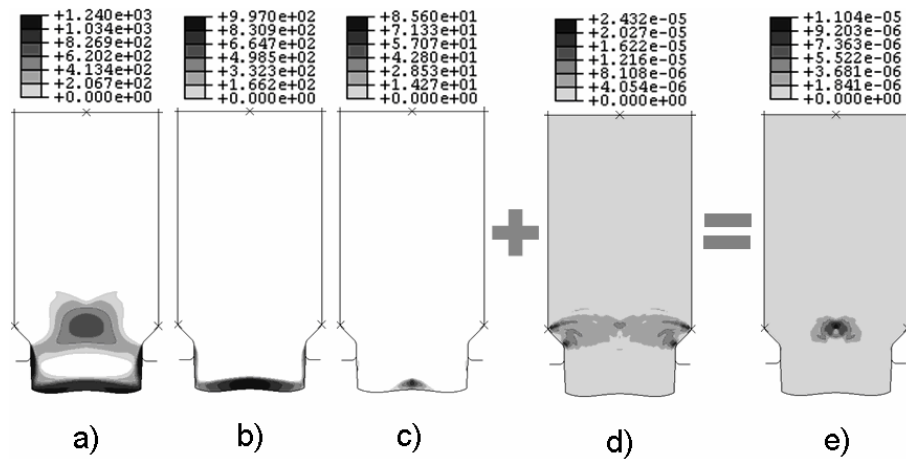
Figure 4.31: Isomaps for no counter pressure, $\mu^f=0$.

When a counter pressure of 200 MPa is applied to the frictionless simulation, a decrease is observed in both the intensity and area extent of the central positive hydrostatic stresses, for the same time increment, as seen in Figure 4.32.a. This amounts for a noticeable decrease in the damage rates, as seen in Figure 4.32.c, where the effectiveness of the counter pressure application is clearly observed.
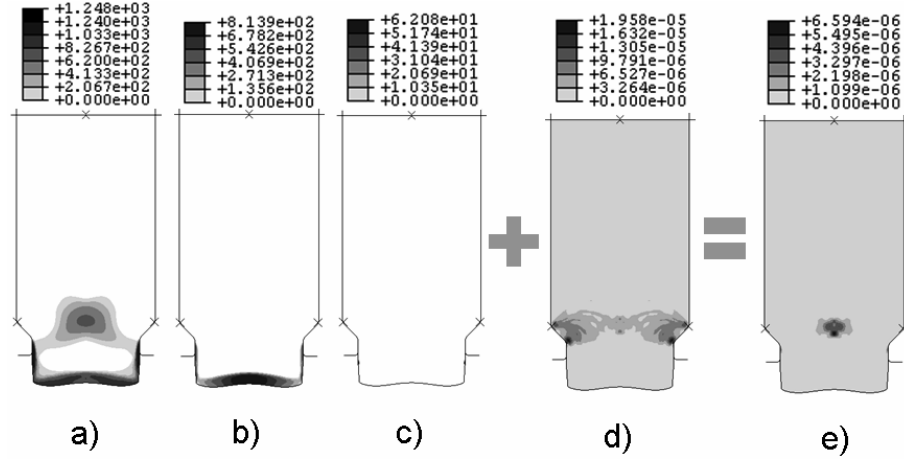
Figure 4.32: Isomaps for counter pressure=200 MPa, μ^f=0.

For the same time step, hydrostatic stress and damage growth distributions for a certain path defined at the axis of symmetry on the forming zone are respectively given in Figure 4.33.a and b, for different counter pressure values. Figure 4.33.a shows that, for a counter pressure of 400 MPa, triaxial stress distribution over the path is kept compressive through the anticipated stress increase in the central zone in the compressive direction by means of counter pressure employment. Consequent damage rates, given in Figure 4.33.b, although show a considerable decrease with increasing counter pressure, do not boil down to zero for 400 MPa counter pressure. This is due to the fact that, in the selected mathematical damage model, damage evolution depends on the sign of each principal stress component but not merely the sign of the pressure.
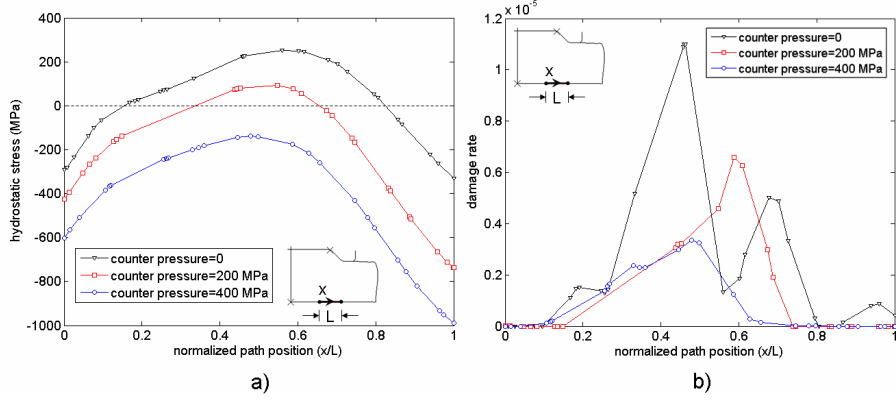
Figure 4.33: Central line, a) hydrostatic stress, b) damage rate values, for different counter pressure levels, μ^f=0.

In order to further evaluate the effectiveness of intensity of the counter pressure, analyses for different counter pressure magnitudes, ranging from 0 to 200 MPa, are conducted for frictionless and frictional conditions. As given in Figure 4.34, for frictionless conditions, it is seen that, a counter pressure of 200 MPa suffices to suppress crack formation. This finding is analogous to the experimental findings of WAGENER and his colleagues which show the efficiency of the counter pressure in promotion of the material formability in cold extrusion. It should be noted that, damage accumulation at the center is not completely bypassed however decreased under the crack threshold, where the material integrity at the macro-scale is preserved. The experiences of the author show that, for the selected damage model, the counter pressure values that should completely withdraw the central damage accumulation should be considerable, which in turn require unreasonable punch force demands and thus become impractical. Besides, die and punch stress limitations act as the main obstacles for excessive amplification of counter pressures. Figure 4.34 also represents the effect of the counter pressure intensity on crack morphologies. Accordingly, the outputs suggest that, the crack opening and the crack half width, measured as the arithmetic mean of first three cracks, show a monotonic decrease with increased counter pressure, which is physically reasonable, thus anticipated. It is notable that, unlike friction, counter pressure does not seem to have an effect on the periodicity of the cracks.

146
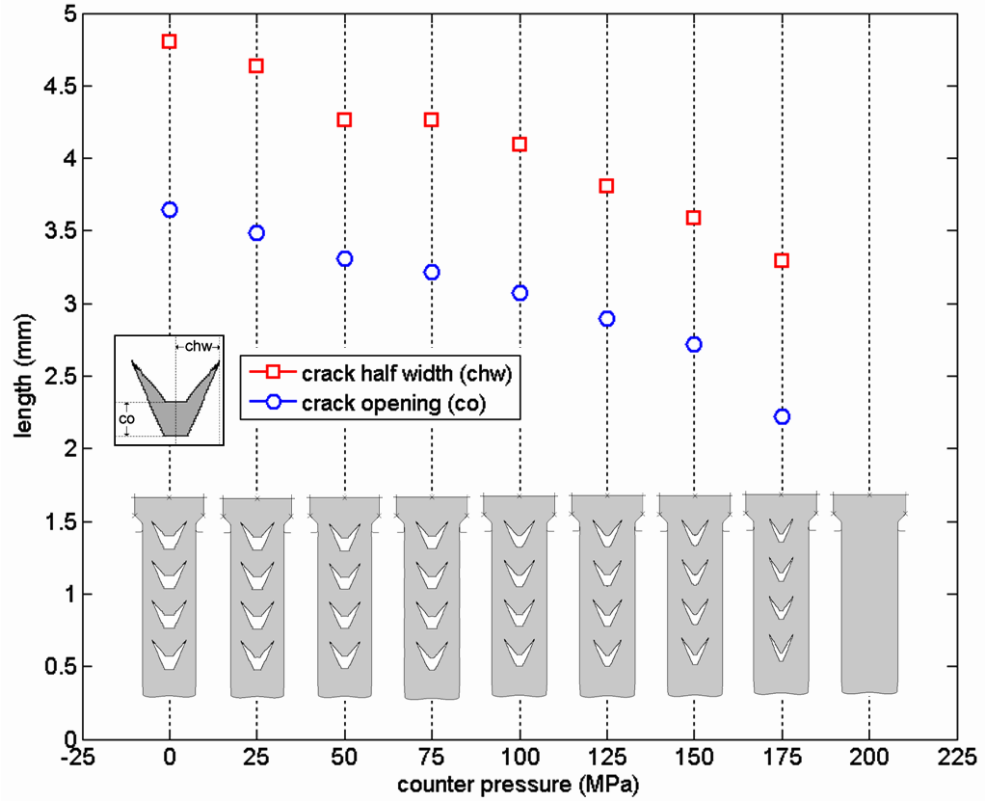
Figure 4.34: Mean crack dimensions and crack patterns for various counter pressure levels, μ^f=0.

For frictionless simulations, the punch force-normalized process time curves are given in Figure 4.35 for the analyses without counter pressure and with counter pressure of 100 MPa and 200 MPa. Crack involving simulations experience an oscillatory behavior whereas in the simulation without any cracks, no oscillations are observed where a steady trend is captured in the absence of friction. Moreover, the extent of the oscillations is strictly dependent on the internal crack size, where in the simulations with larger cracks, oscillations become more dominant compared to those with smaller cracks. The anticipated increase in the punch force demand with increasing counter pressure values reminds one that, in the actual applications, reasonable counter pressure values should be selected for feasibility.

Once a friction of μ^f=0.04 is applied at die-workpiece interface, crack patterns for
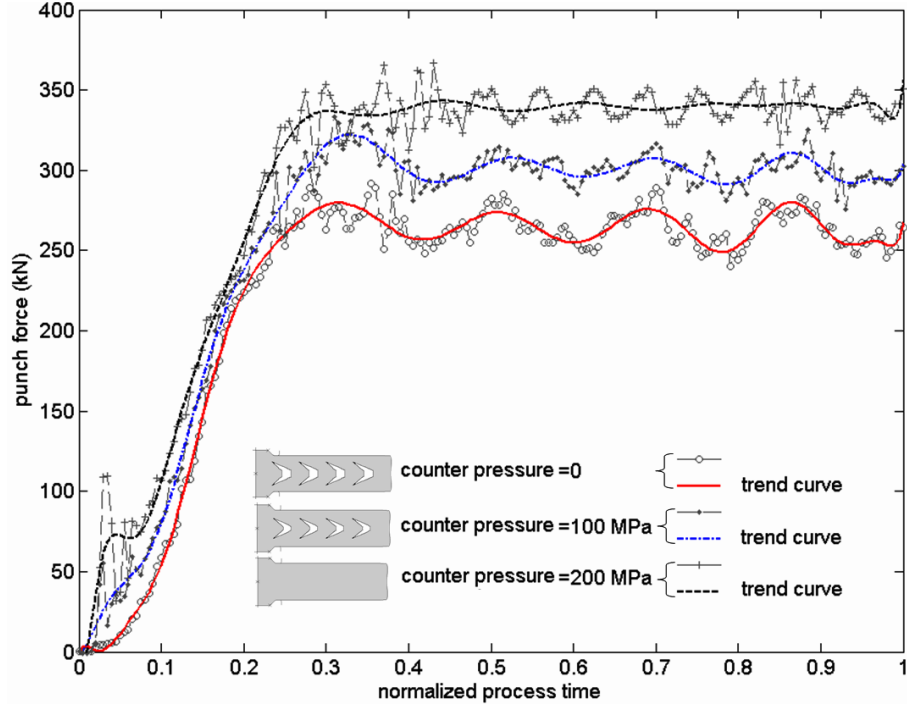
Figure 4.35: Punch force demand curves for different counter pressure levels, $\mu^f=0$.

different counter pressure values take the form demonstrated in Figure 4.36. A remarkable point is that, in the presence of friction, the counter pressure required for the crack-free simulations decreases considerably from 200 MPa to 125 MPa. This is due to the fact that both friction and counter pressure act analogically similar, as a counter force agent which works in opposite direction with respect to the applied external pressure of the punch. Another point is that, with the increase of friction, damage accumulation zones are carried over to the surface rather than center. Thus under frictional conditions, cracks can be healed with employment of a reduced counter pressure. The change of the crack sizes as a function of the applied counter pressure follows a similar trend with the frictionless simulations.

For the frictional conditions, the punch force-normalized process time diagrams are given in Figure 4.37, for the analyses without counter pressure and with counter pressure for 75 and 125 MPa, respectively. In accordance with the previous outcomes,
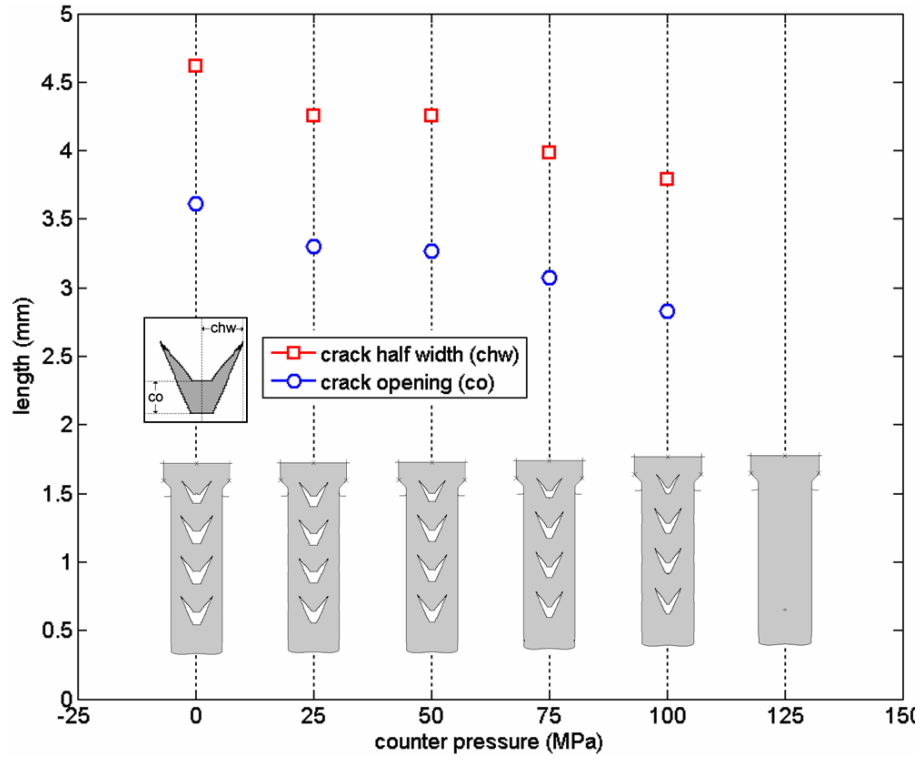
Figure 4.36: Mean crack dimensions and crack patterns for various counter pressure levels, μ^f=0.04.

the crack size dependent oscillations in the force demand diminish with smaller cracks. In addition to the counter pressure, the effect of friction also increases the peak load levels for analyses. Besides, due to friction, the steady trend of the frictionless force demand curve now experiences a monotonic drop off with the reduction of contacting surfaces.

Figure 4.38 is to compare the crack morphologies for frictional and frictionless analysis, at different counter pressure values. The dimensions of the cracks in frictional simulations come out to be considerably small compared to frictionless simulation results, which is anticipated.
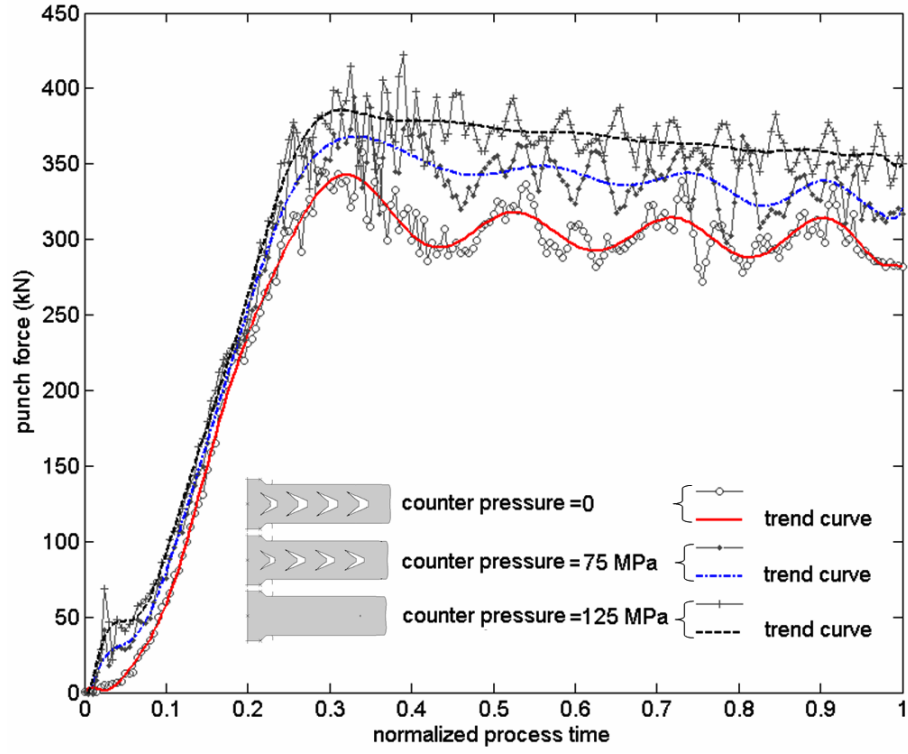
Figure 4.37: Punch force demand curves for different counter pressure levels, $\mu^f=0.04$.
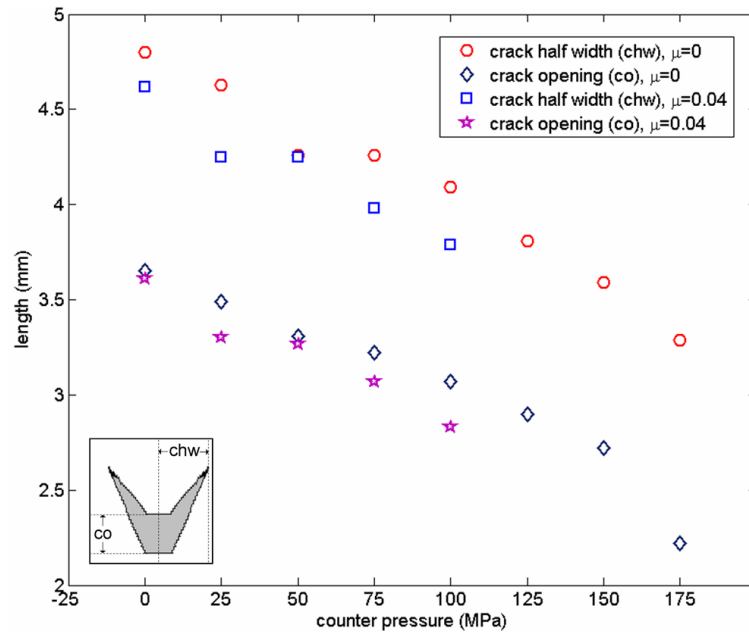
Figure 4.38: Mean crack dimensions for various counter pressure levels and friction coefficients.

As previously shown in Figure 4.33.a and b, employment of counter pressure, although heals crack occurrence for certain intensities, does not necessarily eliminate the cen-

tral damage accumulation completely. Figure 4.39 shows the damage iso-error plots for certain counter pressure levels in frictionless and frictional simulations. As seen, for both $\mu^f=0$, and $\mu^f=0.04$, once the counter pressure is 100 MPa, discontinuous chevron crack formations arise. For these cases, damage iso-curves have a discontinuous structure, similar to the crack patterns, where maximum damage values occur at the crack free-surfaces. The cracks are eliminated for a counter pressure of 200 MPa, at both of the frictional conditions. It is remarkable that, this time central damage accumulation has a continuous distribution. Another notable point is that, central damage intensities in the frictional case are less than those seen in the frictionless simulation, which is in agreement with the previously stated observations.
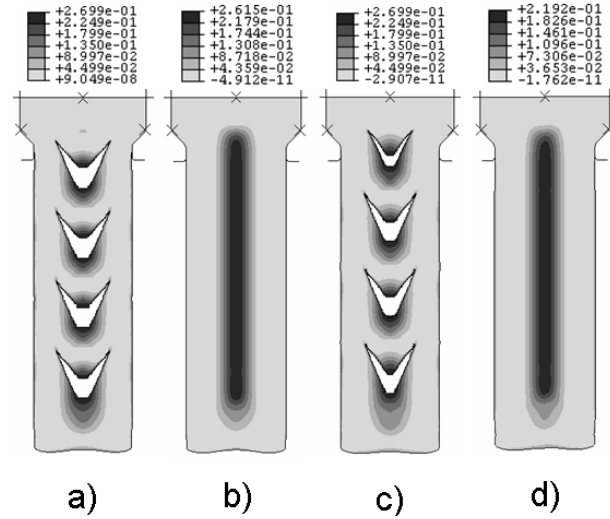
Figure 4.39: Damage contours, a) counter pressure=100 MPa, $\mu^f=0$, b) counter pressure=200 MPa, $\mu^f=0$, c) counter pressure=100 MPa, $\mu^f=0.04$, d) for counter pressure=200 MPa, $\mu^f=0.04$.

Our final attempt is investigation of the steady state radial damage and equivalent plastic strain distributions for chevron-free simulations subjected to frictionless and frictional conditions, as given in Figure 4.40 and 4.41 respectively. Damage plots, given in Figure 4.40, reveal that, for both frictionless and frictional simulations, counter pressure decreases damage accumulation in both center and surface considerably. A comparison of Figure 4.40.a and b shows that, for equal levels of counter pressure,

frictional interface conditions result in lower central however higher surface damage accumulations, compared to the frictionless conditions which is in accordance with the previous observations.
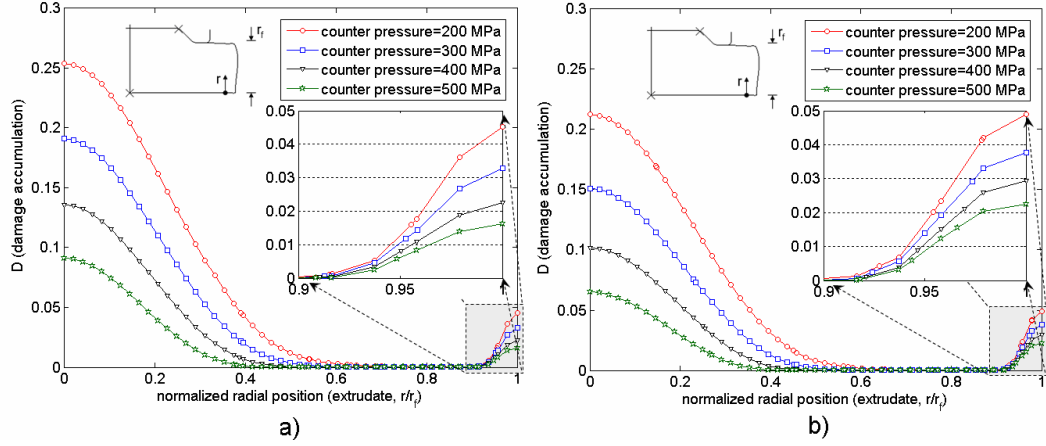
Figure 4.40: Radial damage distribution for different counter pressure levels (steady state), a) $\mu^f=0$, b) $\mu^f=0.04$.

Coming to Figure 4.41, current employment of counter pressure introduces a difference in central equivalent plastic strain accumulations for both frictionless and frictional experiments, where with the increase of applied pressure, central plastic flow is promoted which, although slightly, decreases the overall radial equivalent plastic strain gradients. This is also in accordance with the experimental findings of WAGENER and his colleagues, where uniform equivalent plastic strain distributions are carried out with the aid of counter pressure employment. Besides, it is shown that, unlike center, friction introduces a marked increase in the plastic strain intensities at the surface region. Accordingly the distribution of equivalent plastic strain has a steeper trend at the half radial distance closer to the surface.
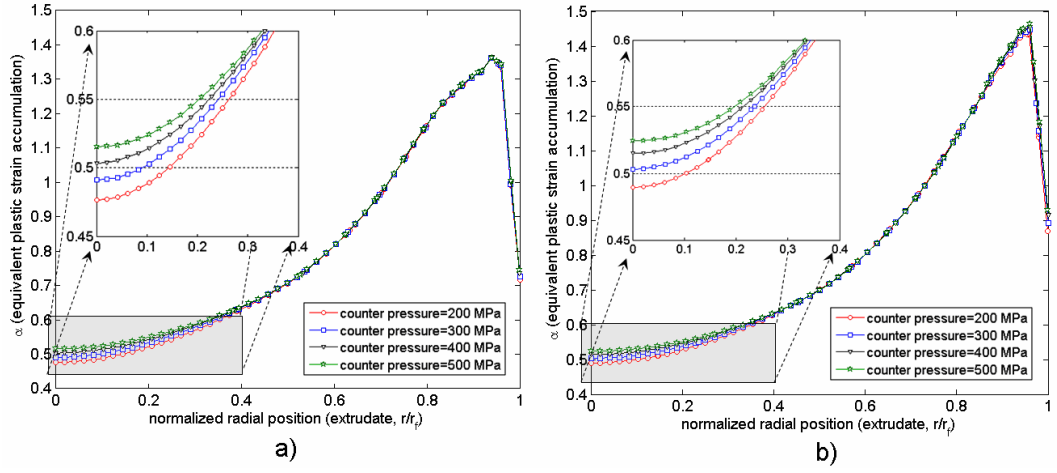
Figure 4.41: Radial equivalent plastic strain distribution for different counter pressure levels (steady state), a) $\mu^f=0$, b) $\mu^f=0.04$.

4.5 Conclusion

In this chapter, numerical prediction of the periodic central bursts in the direct axi-symmetric extrusion is presented. For this purpose, a framework, based on a LEMAITRE-variant (in its simplest form) local isotropic damage strongly coupled to a physically sound finite strain hyperelastic-plastic formulation through a single VON MISES yield potential, is derived. The derived forms are implemented as `VUMAT` user defined material subroutines, for ABAQUS/Explicit code, and `UMAT` subroutines for ABAQUS/Standard. Discrete crack formation in single pass reduction of 100Cr6 and in double pass reduction of Cf53 is modeled by making use of element deletion procedure supported by ABAQUS/Explicit and a developed ramped stiffness degradation method implemented in ABAQUS/Standard. It is shown that, supplied central bursts are in correlation with the experimental facts. The investigations of the researchers show that, the crack closure parameter, controlling the quasi-unilateral evolutionary forms damage, has an important affect on the damage accumulation zones determining the central or superficial character. Besides, the effect of many process parameters, like friction, die geometry, material hardening regime, on damage distribution is investigated. Two promising and economic methods for avoiding chevron cracks are proposed in the context of FE analysis, which are creation of numerically handled chevron free production curves and application of counter pressure. Clearly, for industrial use, the numerical production of the defect free production curves, taking

153

the change of many previously mentioned process parameters into account, is possible. It is shown that, chevron crack formations can be prevented at the expense of increased load demand, not mentioning the mechanism complications, by devising counter pressure, which helps keeping the tensile triaxial stress fields under tolerable limits. Further micro-mechanical and experimental research should be conducted for proper determination of the material parameters of the actual material together with more advanced damage rate forms.

CHAPTER 5

CLOSURE and FUTURE PERSPECTIVES

5.1 Closure

An extensive theoretical and numerical study on modeling isotropic ductile damage for finite strain plasticity is presented. For this purpose a framework for damage coupled hyperelastic-(visco)plasticity is presented in principal axes in an EUCLIDEAN setting in a local basis. The unified functional framework for the governing functions of plasticity and damage does not assume particular restrictions on the forms. This gives rise to implementation of a broad range of damage and plasticity models, strongly coupled through a single yield surface. It is shown that, principal axes formulation provides convenience in active-passive damage evolutionary conditions which depends on eigen-projections besides finite hyperelastic-plastic framework, reducing tensorial differentials to simple differentials with respect to scalars. Inclusion of thermal effects is also presented. Unilateral damage evolutionary forms are given with special emphasis on the practicality and efficiency of formulations in principal axes. Moreover local integration procedures are summarized starting from a full equation set which are simplified step by step initially to two and finally to one. Also different operator split methodologies such as elastic predictor-damage plastic corrector (simultaneous plastic-damage solution scheme) and elastic predictor-plastic corrector-damage deteriorator (staggered plastic-damage solution scheme) are given. To this end regarding consistent material moduli are derived. The models are implemented as user defined material subroutines for ABAQUS and MSC.Marc. The efficiency and the predictive performances of the models are studied with a set of sample problems.

155

5.2   Future Perspectives

Following topics constitute current and future research interests,

- Extension of the thermo-mechanical setting to include material anisotropy, where damage induced anisotropic behavior together with hyperelastic and plastic anisotropies will also be developed.

- Investigations on additional damage models, which are micro-mechanically based.

- Nonlocal material modelling with special emphasis of the ellipticity and hyperbolicity loss in the IBVPs of quasi static and dynamic frameworks, respectively. Besides, investigation of localization limiting properties of the integral and gradient localizers.

- Evaluation of local integration algorithms together with efficiency and accuracy observations.

- Use of adaptive mesh refinement methods with consistent error measures for crack propagation.

- Extension of the explicit adiabatic framework to cope with impact and projectile penetration problems.

- Material parameter identification through inverse methods.

REFERENCES

[1] ABAQUS User Subroutines Reference Manual - ABAQUS Version 6.6, [2006]: ABAQUS, Inc.

[2] ABU AL-RUB, R. K.; VOYIADJIS, G. Z. [2003]: "On the coupling of anisotropic damage and plasticity models for ductile materials", *International Journal of Solids and Structures*, Vol. 40, 2611–2643.

[3] ANAND, L. [1979]: "On Hencky's Approximate Strain-Energy Function for Moderate Deformations", *ASME Journal of Applied Mechanics*, Vol. 46, 78–82.

[4] ANAND, L. [1986]: "Moderate Deformations in Extension-Torsion of Incompressible Isotropic Elastic Materials", *Journal of the Mechanics and Physics of Solids*, Vol. 34, 293–304.

[5] ANDRADE PIRES, F. M.; DE SOUZA NETO, E. A.; OWEN, D. R. J. [2004]: "On the finite element prediction of damage growth and fracture initiation in finitely deforming ductile materials", *Computer Methods in Applied Mechanics and Engineering*, Vol. 193, 5223–5256.

[6] ARAVAS, N. [1986]: "The analysis of void growth that leads to central bursts during extrusion", *Journal of Engineering for Ind*, Vol. 34, 55–79.

[7] AREIAS, P. M. A.; CÉSAR DE SÁ, J. M. A.; CONCEIÇÃO ANTÓNIO, C. A. [2003]: "A gradient model for finite strain elastoplasticity coupled with damage", *Finite Elements in Analysis and Design*, Vol. 39, 1191–1235.

[8] ARGYRIS, J. H.; DOLTSINIS, J. ST. [1981]: "On the natural formulation and analysis of large deformation coupled thermomechanical problems", *Computer Methods in Applied Mechanics and Engineering*, Vol. 25, 195–253.

[9] ARMERO, F.; SIMÓ, J. C. [1993]: "A new unconditionally stable fractional step method for non-linear coupled thermomechanical problems", *International Journal for Numerical Methods in Engineering*, Vol. 35, 737–766.

[10] ARMERO, F.; SIMÓ, J. C. [1993]: "A priori stability estimates and unconditionally stable product formula algorithms for nonlinear coupled thermoplasticity", *International Journal of Plasticity*, Vol. 9, 749–782.

[11] ASARO, R. J. [1983]: "Micromechanics of crystals and polycrystals. *Advances in Applied Mechanics*, Vol. 23, 1–115.

[12] AURICCHIO, F.; TAYLOR, R. L. [1999]: "A return-map algorithm of general associative isotropic elastoplastic materials in large deformation regimes", *International Journal of Plasticity*, Vol. 15, 1359–1378.

[13] AVITZUR, B. [1968]: "Analysis of central bursting defects in extrusion and wire drawing", *Journal of Mechanics and Physics of Solids*, Vol. 90, 79–91.

[14] BAKER, G.; DE BORST, R. [2005]: "An anisotropic thermomechanical damage model for concrete at transient elevated temperatures", *Philosophical Transactions of the Royal Society A*, Vol. 363, 2603–2628.

[15] BAKHSHI-JOOYBARI, M. [2002]: "A theroretical and experimental study of friction in metal forming by the use of the forward extrusion process", *Journal of Materials Processing Technology*, Vol. 125-126, 369–374.

[16] BASARAN, C.; NIE, S. [2004]: "An irreversible thermodynamics theory for damage mechanics of solids", *Intertational Journal of Damage Mechanics*, Vol. 13, 205–223.

[17] BAŽANT, Z. [2000]: "Structural stability", *International Journal of Solids and Structures*, Vol. 37, 55–67.

[18] BELLENGER, E.; BUSSY, P. [1998]: "Plastic and viscoplastic damage models with numerical treatment for metal forming processes", *Journal of Materials Processing Technology*, Vol. 80-81, 591–596.

[19] BERSKI, S.; DYJA, H.; BANASZEK, G.; JANIK, M. [2004]: "Theoretical analysis of bimetallic rods extrusion process in double reduction die", *Journal of Materials Processing Technology*, Vol. 153-154, 583–588.

[20] BIELSKI, J.; SKRZYPEK, J. J.; KUNA-CISKAL, H. [2006]: "Implementation of a model of coupled elastic-plastic unilateral damage material to finite element code", *International Journal of Damage Mechanics*, Vol. 15, 5–39.

[21] BIGONI, D.; ZACCARIA, D. [1994]: "Eigenvalues of the elastoplastic constitutive operator", *Z. angew. Math. Mech.*, Vol. 74, No. 8, 355–357.

[22] BONNET, J.; WOOD, R.[1997]: *Nonlinear Continuum Mechanics for Finite Element Analysis*, Cambridge University Press.

[23] BONORA, N. [1997]: "A nonlinear *CDM* model for ductile failure", *Engineering Fracture Mechanics*, Vol. 58, 11–28.

[24] BONORA N.; GENTILE D.; PIRONDI A.; NEWAZ G. [2005]: "Ductile damage evolution under triaxial state of stress: theory and experiments", *International Journal of Plasticity*, Vol. 21(5), 981–1007.

[25] BONORA N.; RUGGIERO A.; ESPOSITO L.; GENTILE D. [2006]: "CDM modeling of ductile failure in ferritic steels: Assessment of the geometry transferability of model parameters", *International Journal of Plasticity*, Vol. 22(11), 2015–2047.

[26] BORJA, R. I.; SAMA, K. M.; SANZ, P. F. [2003]: "On the numerical integration of three-invariant elastoplastic constitutive models", *Computer Methods in Applied Mechanics and Engineering*, Vol. 192, 1227–1258.

[27] BOROUCHAKI, H.; LAUG, P.; CHEROUAT, A.; SAANOUNI, K. [2005]: "Adaptive remeshing in large plastic strain with damage", *International Journal for Numerical Methods in Engineering*, Vol. 63, 1–36.

[28] Børvik, T.; Hopperstad, O. S.; Berstad, T.; Langseth, M. [2001]: "Numerical solution of plugging failure in balistic penetration", *International Journal of Solids and Structures*, Vol. 38, 6241–6264.

[29] Børvik, T.; Hopperstad, O. S.; Berstad, T.; Langseth, M. [2002]: "Perforation of 12mm thick steel plates by 20mm diameter projectiles with flat, hemispherical and conical noses Part II: numerical simulations", *International Journal of Impact Engineering*, Vol. 27, 37–64.

[30] Brozzo, P.; Deluca, B.; Rendina, R. [1972]: "A new method for the prediction of formability limits in metal sheets, sheet metal forming and formability", *Proceedings of the Seventh Biannual Conference of the International Deep Drawing Research Group*.

[31] Brünig, M. [2003]: "An anisotropic ductile damage model based on irreversible thermodynamics", *International Journal of Plasticity*, Vol. 19, 1679–1713.

[32] Brünig, M.; Ricci, S. [2005]: "Nonlocal continuum theory of anisotropically damaged metals. *International Journal of Plasticity*, Vol. 21, 1346–1382.

[33] Camacho, A. M.; Gonzáles, C.; Rubio, E. M.; Sebastián, M. A. [2006]: "Influence of geometrical conditions on central burst appearance in axisymmetric drawing procsses", *Journal of Materials Processing Technology*, Vol. 177, 304–306.

[34] Čanadija, M.; Brnić, J. [2004]: "Associative coupled thermoplasticity at finite strain with temperature-dependent material parameters", *International Journal of Plasticity*, Vol. 20, 1851–1874.

[35] Cervera, M.; Chiumenti, M.; de Saracibar, A. C. [2004]: "Shear band localization via local J2 continuum damage mechanics", *Computer Methods in Applied Mechanics and Engineering*, Vol. 193, 849–880.

[36] Ceretti, E.; Taupin, E.; Altan, T. [1997]: "Simulation of metal flow and fracture applications in orthogonal cutting, blanking, and cold extrusion", *Annals of the CIRP*, Vol. 46, 187–190.

[37] César de Sá, J. M. A.; Areias, P. M. A.; Zheng, C. [2006]: "Damage modelling in metal forming problems using an implicit non-local gradient model", *Computer Methods in Applied Mechanics and Engineering*, Vol. 195, 6646–6660.

[38] Chaboche, J. L. [2003]: Chapter 2.04, Damage Mechanics. In: Comprehensive Structural Integrity. Elsevier Ltd., 213–284.

[39] Chandrakanth, S.; Pandey, P. C. [1993]: "A new ductile damage evolution model", *International Journal of Fracture*, Vol. 60, R73–R76.

[40] Chandrakanth, S.; Pandey, P. C. [1995]: "An exponential ductile continuum damage model for metals", *International Journal of Fracture*, Vol. 72, 293–310.

[41] Chen, C. C.; Oh, S. I.; Kobayashi, S. [1979]: "Ductile fracture in axisymmetric extrusion and drawing", *J. Eng. Ind.*, Vol. 101, 13–35.

[42] CHEN, D.; SYU, S.; WU, C.; LIN S. [2007]: "Investigation into cold extrusion of aliminum billets using three-dimensional finite element method", *Journal of Materials Processing Technology*, Vol. 192-193, 188–193.

[43] CHEROUAT, A.; SAANOUNI, K.; HAMMI, Y. [2002]: "Numerical improvement of thin tubes hydroforming with respect to ductile damage", *International Journal of Mechanical Sciences*, Vol. 44, 2427–2446.

[44] CHEROUAT, A.; SAANOUNI, K.; HAMMI, Y. [2003]: "Improvement of forging process of a 3D complex part with respect to damage occurence", *Journal of Materials Processing Technology*, Vol. 142, 307–317.

[45] CHORIN, A. J.; HUGHES, T. J. R.; MCCRACKEN, M. F.; MARSDEN, J. E. [1978]: "Product formulas and numerical algorithms", *Communications on Pure and Applied Mathematics*, Vol. XXXI, 205–256.

[46] COCKROFT, M. G.; LATHAM, D. J. [1968]: "Ductility and the workability of metals", Journal of the Institute of Metals Vol. 96, 33–39.

[47] COLEMAN, B.; GURTIN, M.[1967]: "Thermodynamics of internal state variables", *The J. Chemical Physics*, Vol. 47, 597–613.

[48] DA CUNDA, L. A. B.; BITTENCOURT, E.; CREUS, G. [1998]: "Analysis of ductile damage coupled with thermoplasticity by the FEM", In: IDELSOHN, S.; OÑATE, E.; DVORKIN, E. (Eds.), Computational Mechanics New Trends and Applications, CIMNE, Barcelona, Spain, 1–13.

[49] DHAR, S.; SETHURAMAN, R.; DIXIT, P. [1996]: "A continuum damage mechanics model for void growth and micro-crack initiation", *Engineering Fracture Mechanics*, Vol. 53, 917–928.

[50] DOGHRI, I. [2000]: *Mechanics of Deformable Solids, Linear and Nonlinear, Analytical and Computational Aspects*, Springer-Verlag, Berlin Heidelberg.

[51] DRABEK, T.; BÖHM, H. J. [2005]: "Damage models for studying ductile matrix failure in composites", *Computational Materials Science*, Vol. 32, 329–336.

[52] ELGUETA, M.; CORTÉS, C. [1999]: "Application of continuum damage theory in metalforming processes", *Journal of Materials Processing Technology*, Vol. 95, 122–127.

[53] EKH, M.; LILLBACKA, R.; RUNESSON, K. [2004]: "A model framework for anisotropic damage coupled to crystal (visco)plasticity", *International Journal of Plasticity*, Vol. 20, 2143–2159.

[54] EKH, M.; MENZEL, A. [2006]: " Efficient iteration schemes for anisotropic hyperelasto-plasticity", *International Journal for Numerical Methods in Engineering*, Vol. 66, 707–721.

[55] ENAKOUTSA, K.; LEBLOND, J. B.; PERRIN, G. [2007]: "Numerical implementation and assessment of a phenomenological nonlocal model of ductile rupture", *Computer Methods in Applied Mechanics and Engineering*, Vol. 196, 1946–1957.

[56] ENGELEN, R. A. B. [2005]: *Plasticity induced damage in metals*, PhD thesis, Technische Universiteit Eindhoven

[57] ETEROVIC, A. L.; BATHE, K., J. [1990]: "A hyperelastic-based large strain elasto-plastic constitutive formulation with combined isotropic-kinematic hardening using the logarithmic stress and strain measures", *International Journal of Numerical Methods in Engineering*, Vol. 30, 1099–1114.

[58] FREUDENTHAL, A. M. [1950]: *The Inelastic Behavior in Solids*, Wiley, New York.

[59] GANAPATHYSUBRAMANIAN, S.; ZABARAS, N. [2003]: "Computational design of deformation processes for materials with ductile damage", *Computer Methods in Applied Mechanics and Engineering*, Vol. 192, 147–183.

[60] GANCZARSKI, A. [2003]: "Chapter 10. Thermo-Damage Coupling Modelling and Applications for Creep Conditions", In: SKRZYPEK, J. J; GANCZARSKI, A. W. (Eds.), Anisotropic Behavior of Damaged Materials, Springer-Verlag Berlin Heidelberg, 317–349.

[61] GELIN, J. C. [1998]: "Modelling of damage in metal forming simulations", *Journal of Materials Processing Technology*, Vol. 80–81, 24–32.

[62] GIARDINI C.; CERETTI, E.; MACCARINI, G. [1995]: "Formability in extrusion forging: the influence of die geometry and friction conditions", *Journal of Materials Processing Technology*, Vol. 54, 302–308.

[63] GOIJAERTS, A. M.; GOVAERT, L. E.; BAAIJENS, F. P. T. [2001]: "Evaluation of ductile fracture models for different metals in blanking", *J. Mater. Process. Technol.*, Vol. 110, 312–323.

[64] GOLOGANU, M.; LEBLOND, J.-B.; PERRIN, G.; DEVAUX, J. [1997]: "Transverse ductility of metal matrix composites", In: SUQUET, P. (Eds.), Continuum Micromechanics, CISM Lecture Series, Springer, 61–130.

[65] GUNAWARDENA, S. R.; JANSSON, S.; LECKIE, F. A. [1991]: "Transverse ductility of metal matrix composites", In: HARITOS, K.; NEWAZ, K.; MALL, S. (Eds.), Failure Mechanisms in High Temperature Composite Naterials, ASME, New York, NY, 23–30.

[66] GUO, Y. B.; YEN, D. W. [2004]: "A FEM study on mechanisms of discontinuous chip formation in hard machining", *Journal of Materials Processing Technology*, Vol. 155–156, 1350–1356.

[67] GUO, Y. B.; YEN, D. W.; WOODBURY, K. A. [2004]: "Dynamic material behavior modeling using internal state variable plasticity and its applications in hard machining", *Journal of Manufacturing Science and Engineering*, Vol. 128, 749–759.

[68] GURSON, A. L. [1977]: "Continuum theorie of ductile rupture by void nucleation and growth: Part I. Yield criteria and flow rules for porous ductile media", *J. Eng. Mater. Technol. Trans. ASME*, Vol. 99, 2–15.

[69] HAKANSSON, P.; WALLIN, M.; RISTINMAA, M.[2005]: "Comparison of isotropic hardening and kinematic hardening in thermoplasticity", *International Journal of Plasticity*, Vol. 21, 1435–1460.

[70)] HAKANSSON, P.; WALLIN, M.; RISTINMAA, M.[2006]: "Thermomechanical response of non-local porous material", *International Journal of Plasticity*, Vol. 22, 2066–2090.

[71] HAMBLI, R.; POTIRON, A. [2000]: "Finite element modelling of sheet-metal blanking operations with experimental verification", *Journal of Materials Processing Technology*, Vol. 102, 257–265.

[72] HAMBLI, R.; BADIE-LEVET, D. [2000]: "Damage and fracture simulation during the extrusion process", *Computer Methods in Applied Mechanics and Engineering*, Vol. 186, 109–120.

[73] HAMBLI, R. [2001]: "Comparison between Lemaitre and Gurson damage models in crack growth simulation during blanking process", *International Journal of Mechanical Sciences*, Vol. 43, 2769–2790.

[74] HANCOCK, J. W.; MACKENZIE, A. C. [1950]: "On the mechanisms of ductile fracture in high-strength steels subjected to multi-axial stress states", *Journal of Mechanics and Physics of Solids*, Vol. 24, 147–169.

[75)] HANSEN, N. R.; SCHREYER, H. L. [1994]: "A thermodynamically consistent framework for theories of elastoplasticity coupled with damage", *International Journal of Solids and Structures*, Vol. 31, 359–389.

[76] HILL, R. [1950]: *The Mathematical Theory of Plasticity*, Oxford University Press, London.

[77] HUGHES, T. J. R. [1983]: "Analysis of transient algorithms with particular reference to stability behavior", In: BELYTSCHKO, T.; HUGHES, T. J. R. (Eds.), Computational Methods for Transient Analysis, North-Holland, 67–155.

[78] HUGHES, T. J. R. [2000]: *The Finite Element Method–Linear Static and Dynamic Finite Element Analysis*, Dover Publishers, New York.

[79] IBRAHIMBEGOVIĆ, A. [1994]: "Equivalent spatial and material descriptions of finite deformation elastoplasticity in principal axes", *International Journal of Solids and Structures*, Vol. 31, 3027–3040.

[80] IBRAHIMBEGOVIĆ, A.; GHARZEDDINE, F. [1999]: "Finite deformation plasticity in principal axes: from a manifold to the Euclidean setting", *Computer Methods in Applied Mechanics and Engineering*, Vol. 171, 341–369.

[81] IBRAHIMBEGOVIĆ, A.; CHORFI, L. [2000]: "Viscoplasticity model at finite deformations with combined isotropic and kinematic hardening", *Computers and Structures*, Vol. 77, 509–525.

[82] JENNISON, H. C. [1930]: "Certain types of defects in copper wire caused by improper dies and drawing practice", *Proc. Inst. Metal Div. AIME*, Vol. 89.

[83] JIRÁSEK, M.; BAŽANT, Z. [2001]: *Inelastic Analysis of Structures*, John Wiley and Sons, England.

[84] JOHNSON, G. R.; COOK, H. W [1985]: "Fracture Characteristics of Three Metals Subjected to Various Strains, Strain Rates, Temperature and Pressures", *Engineering Fracture Mechanics*, Vol. 21(1), 31–48.

[85] Ju, J. W. [1989a]: "Energy-based coupled elastoplastic damage models at finite strains", *Journal of Engineering Mechanics*, Vol. 115, 2507–2525.

[86] Ju, J. W. [1989b]: "On energy-based coupled elastoplastic damage theories: constitutive modelling and computational aspects", *International Journal for Solids and Structures*, Vol. 25, 803–833.

[87] Ju, J. W. [1990]: "Isotropic and anisotropic damage variables in continuum damage mechanics", *Journal of Engineering Mechanics*, Vol. 116, 283–287.

[88] Kachanov, L. M. [1958]: "Time of the rupture process under creep conditions", *Izv. Akad. Nauk. SSR*, Vol. 8, 26–31.

[89] Ko, D.; Kim, B. [2000]: "The prediction of central burst defects in extrusion and wire drawing", *Journal of Materials Processing Technology*, Vol. 102, 19–24.

[90] Komori, K. [1999]: "Simulation of chevron crack formation and evolution in drawing", *International Journal of Mechanical Sciences*, Vol. 41, 1499–1513.

[91] Komori, K. [2003]: "Effect of ductile fracture criteria on chevron crack formation and evolution in drawing", *International Journal of Mechanical Sciences*, Vol. 45, 141–160.

[92] Krajcinovic, D. [1996]: *Damage Mechanics*, Elsevier, Amsterdam.

[93] Krieg, R. D.; Krieg, D. B. [1977]: "Accuracies of numerical solution methods for the elastic-perfectly plastic model", *J. Pressure Vessel Tech., A.S.M.E.*, Vol. 99, 510–515.

[94] Lee, E. H. [1969]: "Elasto-plastic deformation at finite strains", *ASME Journal of Applied Mechanics*, Vol. 36, 1–6.

[95] Lemaitre, J. [1971]: Evaluation of dissipation and damage in metals. In: Proceedings of I.C.M. 1, Kyoto, Japan.

[96] Lemaitre, J. [1985]: "A continuous damage mechanics model for ductile fracture", *Journal of Engineering Materials and Technology, Transactions of ASME*, Vol. 107, 83–89.

[97] Lemaitre, J.; Chaboche, J. [1990]: *Mechanics of Solid Materials*, Cambridge University Press, Cambridge.

[98] Lemaitre, J. [1996]: *A Course on Damage Mechanics*, Springer-Verlag, Berlin.

[99] Lemaitre, J.; Desmorat, R. [2005]: *Engineering Damage Mechanics*, Springer-Verlag, Berlin Heidelberg.

[100] Lestriez, P.; Saanouni, K.; Mariage, J. F.; Cherouat, A. [2004]: "Numerical prediction of ductile damage in metal forming proceses including thermal effects", *International Journal of Damage Mechanics*, Vol. 13, 59–80.

[101] Lim, L. G.; Dunne, F. P. E. [1997]: "Modelling central bursting in the extrusion of particulate reinforced metal matrix composite materials", *Int. J. Mach. Tools Manufact.*, Vol. 37, 901–915.

[102] Lin R. C.; Brocks W.; Betten J. [2006]: "On internal dissipation inequalities and finite strain inelastic constitutive laws: Theoretical and numerical comparisons", *International Journal of Plasticity*, Vol. 22, 1825–1857.

[103] Lin, J.; Liu, Y.; Dean, T. A. [2005]: "A review on damage mechanisms, models and calibration methods under various deformation conditions", *International Journal of Damage Mechanics*, Vol. 14, 299–319.

[104] Lubarda, V. A.; Krajcinovic, D.; Mastilovic, S. [1994]: "Damage model for brittle elastic solids with unequal tensile and compressive strength", *Engineering Fracture Mechanics*, Vol. 49, 681–697.

[105] Lubliner, J. [1984]: "A maximum-dissipation principle in generalized plasticity", *Acta Mechanica*, Vol. 52, 225–237.

[106] Lubliner, J. [1990]: *Plasticity Theory*, Macmillan Publishing Company, New York.

[107] Lämmer, H.; Tsakmakis, Ch. [2000]: "Discussion of coupled elastoplasticity and damage constitutive equations for small and finite deformations", *International Journal of Plasticity*, Vol. 16, 495–523.

[108] Mackerle, J. [2006]: "Finite element modelling and simulation of bulk material forming", *International Journal for Computer-Aided Engineering and Software*, Vol. 23, 250–342.

[109] Marsden, J. E.; Hughes, T. J. R. [1994]: *Mathematical Foundations of Elasticity*, Dover, New York.

[110] Mathews, J. H.; Fink, K. D. [1999]: *Numerical Methods Using MATLAB*, Prentice Hall, Upper Saddle River, NJ.

[111] Maugin, G. A. [1992]: *The Thermomechanics of Plasticity and Fracture*, Cambridge University Press, Cambridge.

[112] McAllen, P. J.; Phelan, P. [2005]: "Ductile fracture by central bursts in drawn 2011 aliminium wire", *International Journal of Fracture*, Vol. 135, 19–33.

[113] McAllen, P. J.; Phelan, P. [2007]: "Numerical analysis of axisymmetric wire drawing by means of a coupled damage model", *Journal of Materials Processing Technology*, Vol. 183, 210–218.

[114] McVeigh, C.; Liu, W. K. [2006]: "Prediction of central bursting during axisymmetric cold extrusion of a metal alloy containing particles", *International Journal of Solids and Structures*, Vol. 43, 3087–3105.

[115] Mediavilla, J. [2005]: *Continuous and discontinuous modelling of ductile fracture*, PhD thesis, Technische Universiteit Eindhoven.

[116)] Mediavilla, J.; Peerlings, R. H. J.; Geers, M. G. D. [2006]: "A nonlocal triaxiality-dependent ductile damage model for finite strain plasticity", *Computer Methods in Applied Mechanics and Engineering*, Vol. 195, 4617–4634.

[117] Menzel, A.; Steinmann, P. [2001]: "A theoretical and computational framework for anisotropic continuum damage mechanics at large strains", *International Journal of Solids and Structures*, Vol. 38, 9505–9523.

[118] Menzel, A.; Ekh, M.; Runesson, K.; Steinmann, P. [2005]: "A framework for multiplicative elastoplasticity with kinematic hardening coupled to anisotropic damage", *International Journal of Plasticity*, Vol. 21, 397–434.

[119] Miehe, Ch. [1994]: "Aspects of the formulation and finite element implementation of large strain isotropic elasticity", *International Journal for Numerical Methods in Engineering*, Vol. 37, 1981–2004.

[120] Miehe, Ch. [1996]: "Numerical application of algorithmic (consistent) tangent moduli in large-strain computational inelasticity", *Computer Methods in Applied Mechanics and Engineering*, Vol. 134, 223–240.

[121] Miehe, Ch. [1998]: "Comparison of two algorithms for the computation of fourth-order isotropic tensor functions", *Computers and Structures*, Vol. 66, 37–43.

[122] Moritoki, H.; Okuyama, E. [1998]: "Prediction of central bursting in extrusion", *Journal of Materials Processing Technology*, Vol. 80-81, 579–584.

[123] Mousavi, S. A. A. A.; Feizi, H.; Madoliat, R. [2007]: "Investigations on the effects of ultrasonic vibrations in extrusion process", *Journal of Materials Processing Technology*, Vol. 187-188, 657–661.

[124] MSC.Marc Volume A: Theory and User Information, [2006]: MSC.Software Corporation.

[125] MSC.Marc Volume D: User Subroutines and Special Routines, [2006]: MSC.Software Corporation.

[126] Nahshon, K.; Hutchinson, J. W. [2008]: "Modification of the Gurson Model for shear failure ", *European Journal of Mechanics - A/Solids*, Vol. 27, 1–17.

[127] Needleman, A. [1988]: "Material rate dependence and mesh sensitivity in localization problems", *Computer Methods in Applied Mechanics and Engineering*, Vol. 67, 69–85.

[128] Nesnas, K.; Saanouni, K. [2002]: "Integral formulation of coupled damage and viscoplastic constitutive equations", *International Journal of Damage Mechanics*, Vol. 11, 367–397.

[129] Norasethasopon, S.; Yoshida, K. [2008]: "Prediction of chevron crack initiation in inclusion copper shaped-wire drawing", *Engineering Failure Analysis*, Vol. 15, 378–393.

[130] Ogden, R. W. [1984]: *Non-Linear Elastic Deformations*, Ellis Horwood Limited, Chichester.

[131] Ortiz, A.; Popov, E. P. [1985]: "Accuracy and stability of integration algorithms for elastoplastic constitutive relations", *International Journal for Numerical Methods in Engineering*, Vol. 21, 1561–1576.

[132] OSAKADA, K.; MATSUMOTO, R.; OTSU, M.; HANAMI, S. [2005]: "Precision extrusion methods with double axis servo-press using counter pressure", *Annals of the CIRP*, Vol. 1, 245–248.

[133] OTTOSEN, N. S.; RISTINMAA, M. [2005]: *The Mechanics of Constitutive Modelling*, Elsevier.

[134] OTTOSEN, N., S.; RUNESSON, K. [1991]: "Acceleration waves in elasto-plasticity", *International Journal of Solids and Structures*, Vol. 28, No. 2, 135–159.

[135] OYANE, M. [1972]: "Criteria of ductile fracture strain", *Bulletin of JSME*, Vol. 15, 1507–1513.

[136] OYANE, M.; SATO, T.; OKIMOTO, K.; SHIMA, S. [1979]: "Criteria for ductile fracture and their applications", *J. Mech. Work. Technol.*, Vol. 4, 65–81.

[137] PENG, X.; QIN, Y.; BALENDRA, R. [2003]: "FE analysis of springback and secondary yielding effect during forward extrusion", *Journal of Materials Processing Technology*, Vol. 135, 211–218.

[138] PÉ REZ-FOGUET, A.; RODRÍGUEZ-FERRAN, A.; HUERTA, A. [2000]: "Numerical differentiation for local and global tangent operators in computational plasticity", *Computer Methods in Applied Mechanics and Engineering*, Vol. 189, 277–296.

[139] PERZYNA, P. [1968]: "Fundamental problems in viscoplasticity", *Advances in Applied Mechanics*, Vol. 9, 243–322.

[140] PERZYNA, P. [1990]: "Constitutive equations of dynamic plasticity", In: KLEIBER, M.; KÖNIG, J.A. (Eds.), Inelastic Solids and Structures, Antoni Sawczuk Memorial Volume, Pineridge Press, Swansea, UK, pp. 111–129.

[141] PIRONDI, A.; BONORA, N.; STEGLICH, D.; BROCKS W.; HELLMANN, D. [2006]: "Simulation of failure under cyclic plastic loading by damage models", *International Journal of Plasticity*, Vol. 22(11), 2146–2170.

[142] PLANCAK, M. [1990]: "Stress distribution within the specimen in cold forward extrusion of steel", *Journal of Materials Processing Technology*, Vol. 24, 387–394.

[143] PROT, V.; SKALLERUD, B.; HOLZAPFEL, G. A. [2007]: "Transversely isotropic membrane shells with application to mitral valve mechanics. Constitutive modelling and finite element implementation", *International Journal for Numerical Methods in Engineering*, (in press).

[144] RABOTNOV, Y. [1968]: "Creep rupture", In: HETENYI, M.; VINCENTI, W. (Eds.), Applied Mechanics. Proceedings of the 12th International Congress of Applied Mechanics, Springer-Verlag, Berlin, 342–320.

[145] RAGAB, A. R.; SAMY, S. N.; SALEH, CH. A. R. [2005]: "Prediction of central bursting in drawing and extrusion of voided metals", *J. Manufacturing Science and Engineering, ASME*, Vol. 127, 698–702.

[146] RAJAK, S. A.; REDDY, N. V. [2005]: "Prediction of internal defects in plane strain rolling", *Journal of Materials Processing Technology*, Vol. 159, 409–417.

[147] RECKWERTH, D.; TSAKMAKIS, CH. [2003]: "The principle of generalized energy equivalence in the continuum damage mechanics", In: HUTTER, K.; BAASER, H., Eds. *Deformation and Failure in Metallic Materials*, Springer-Verlag Berlin Heidelberg, 381–406.

[148] REESE, S.; WRIGGERS, P. [1997]: "A material model for rubber-like polymers exhibiting plastic deformation: computational aspects and a comparison with experimental results", *Computer Methods in Applied Mechanics and Engineering*, Vol. 148, 279–298.

[149] RICE, J. R.; TRACEY, D. M. [1969]: "On the ductile enlargement of voids in triaxial stress fields", *Journal of Mechanics and Physics of Solids*, Vol. 17, 201–217.

[150] ROJEK, J.; ZIENKIEWICZ, O. C.; OÑATE, E.; POSTEK, E. [2001]: "Advances in FE explicit formulation for simulation of metalforming processes", *Journal of Materials Processing Technology*, Vol. 119, 41–47.

[151] ROJEK, J.; OÑATE, E.; POSTEK, E. [1998]: "Application of explicit FE codes to simulation of sheet and bulk metal forming processes", *Journal of Materials Processing Technology*, Vol. 80-81, 620–627.

[152] ROUSSELIER, G. [1987]: "Ductile fracture models and their potential in local approach of fracture", *Nucl. Eng. Design*, Vol. 105, 97–111.

[153] SAANOUNI, K.; HAMMI, Y. [2000]: "Numerical simulation of damage in metal forming processes", In: BENALLAL, A. (Eds.), Continuous Damage and Fracture, Elsevier, Amsterdam, 353–363.

[154] SAANOUNI, K.; CHABOCHE, J. L. [2003]: Chapter 3.06, Computational Damage Mechanics: Application to Metal Forming Simulation. In: Comprehensive Structural Integrity. Elsevier Ltd., 319–374.

[155] SAANOUNI, K.; MARIAGE, J. F.; CHEROUAT, A.; LESTRIEZ, P. [2004]: "Numerical prediction of discontinuous central bursting in axisymmetric forward extrusion by continuum damage mechanics", *Computers and Structures*, Vol. 82, 2309–2332.

[156] SALEH, CH. A. R.; RAGAB, A. R.; SAMY, S. N. [2005]: "Prediction of void growth in drawing and extrusion of voided metals", *Mechanics of Materials*, Vol. 37, 915–924.

[157] SHABAIK, A. H. [1991]: "Mechanics of plastic deformation in metal forming processes: Experimental and numerical methods", *Journal of Materials Processing Technology*, Vol. 27, 3–24.

[158] SIMÓ, J. C. [1988a]: "A framework for finite strain elastoplasticity based on a maximum plastic dissipation and the multiplicative decomposition. Part I: Continuum Formulation", *Computer Methods in Applied Mechanics and Engineering*, Vol. 66, 199–219.

[159] Simó, J. C. [1988b]: "A framework for finite strain elastoplasticity based on a maximum plastic dissipation and the multiplicative decomposition. Part II: Computational aspects", *Computer Methods in Applied Mechanics and Engineering*, Vol. 68, 1–31.

[160] Simó, J. C.; Govindjee, S. [1991]: "Non-linear B-stability and symmetry preserving return mapping algorithms for plasticity and viscoplasticity", *International Journal for Numerical Methods in Engineering*, Vol. 31, 151–176.

[161] Simó, J. C. [1992]: "Algorithms for multiplicative plasticity that preserve the form of the return mappings of the infinitesimal theory", *Computer Methods in Applied Mechanics and Engineering*, Vol. 99, 61–112.

[162] Simó, J. C.; Miehe, Ch. [1992]: "Associative coupled thermoplasticity at finite strains: Formulation, numerical analysis and implementation", *Computer Methods in Applied Mechanics and Engineering*, Vol. 98, 41–104.

[163] Simó, J. C. [1994]: "Topics on the numerical analysis and simulation of plasticity", In: Ciarlet, P.G.; Lions, J.L. (Eds.), Handbook of numerical analysis, Elsevier Science Publishers, North Holland, Vol. III.

[164] Simó, J. C.; Hughes, T. J. R. [1998]: *Computational Inelasticity*, Springer-Verlag, Berlin.

[165] Simó, J. C.; Ju, J. W. [1989]: "On continuum damage-elastoplasticity at finite strains", *Computational Mechanics*, Vol. 5(5), 375–400

[166] Simó, J. C.; Taylor, R. L. [1985]: "Consistent tangent operators for rate-independent elastoplasticity", *Computer Methods in Applied Mechanics and Engineering*, Vol. 48, 101–118.

[167] Simó, J. C.; Taylor, R. L. [1991]: "Quasi-incompressible finite elasticity in principle stretches: continuum basis and numerical algorithms", *Computer Methods in Applied Mechanics and Engineering*, Vol. 85, 273–310.

[168] Simone, A. [2003]: *Continuous-Discontinuous Modelling of Failure* , PhD Thesis, Technische Universiteit Delft.

[169] Skrzypek, J. J.; Ganczarski, A. [1999]: *Modelling of Material Damage and Failure of Structures*, Springer-Verlag, Berlin.

[170] de Souza Neto, E. A.; Perić, D. [1994]: "A computational model for ductile damage at finite strains: Algorithmic issues and applications", *Engng. Comput.*, Vol. 11, 257–281.

[171] de Souza Neto, E. A.; Perić, D. [1995]: "A computational framework for a class of fully coupled models for elastoplastic damage at finite strains with reference to the linearization aspects", *Computer Methods in Applied Mechanics and Engineering*, Vol. 130, 179–193.

[172] de Souza Neto, E. A. [2002]: "A fast, one-equation integration algorithm for the Lemaitre ductile damage model", *Communications in Numerical Methods in Engineering*, Vol. 18, 541–554.

[173] Soyarslan, C.; Tekkaya, A. E.; Akyuz, U. [2008]: "Application of Continuum Damage Mechanics in discontinuous crack formation: Forward extrusion chevron predictions", *Journal of Applied Mathematics and Mechanics / Zeitschrift für Angewandte Mathematik und Mechanik*, Vol. 88, 436–453.

[174] Srikanth, A.; Zabaras, N. [1999]: "A computational model for the finite element analysis of thermoplasticity coupled with ductile damage at finite strains", *International Journal for Numerical Methods in Engineering*, Vol. 45, 1569–1605.

[175] Sriram, S.; Van Tyne, C. J. [2002]: "Criterion for prevention of central bursting in forward extrusions through spherical dies using the finite element method", *J. Manufacturing Science and Engineering, ASME*, Vol. 124, 65–70.

[176] Stabler, J.; Baker, G. [2000]: "Fractional step methods for thermomechanical damage analyses at transient elevated temperatures", *International Journal for Numerical Methods in Engineering*, Vol. 48, 761–785.

[177] Staub, C.; Boyer, J. C. [1998]: "A ductile growth model for elasto-plastic material", *Journal of Materials Processing Technology*, Vol. 77, 9–16.

[178] Steglich, D.; Pirondi, A.; Bonora, N.; Brocks, W. [2005]: "Simulation of failure under cyclic plastic loading by damage models", *International Journal of Solids and Structures*, Vol. 42(2), 337–351.

[179] Stein, E.; Müller-Hoeppe, N. [1991]:"A concept for modelling and computation of finite inelastic deformations", in: Brüller, O., Mannl, V., Najar, J., Eds. *Advances in Continuum Mechanics*, 88–99. Springer-Verlag Berlin Heidelberg.

[180] Stein, E.; Steinmann, P.; Miehe, Ch. [1995]: "Instability phenomena in plasticity: Modelling and computation", *Computational Mechanics*, Vol. 17, 74–87.

[181] Steinmann, P.; Miehe, Ch.; Stein, E. [1994]: "Comparison of different finite deformation inelastic damage models within multiplicative elastoplasticity for ductile material", *Computational Mechanics*, Vol. 13, 458–474.

[182] Tai, W. H. [1990]: "Plastic damage and ductile fracture in mild steels", *Engineering Fracture Mechanics*, Vol. 37(4), 853–880.

[183] Taylor, G. I.; Quinney, M. A. [1933]: "The latent energy remaining in a metal after cold working", *Proc. Roy. Soc. London Ser. A*, A 143, 307–325.

[184] Tie-Jun, W. [1990]: "A new ductile fracture theory and its applications", *Engineering Fracture Mechanics*, Vol. 42, 177–183.

[185] Tiernan, P.; Hillery, M. T.; Draganescu, B.; Gheorghe, M. [2005]: "Modelling cold extrusion with experimental verification", *Journal of Materials Processing Technology*, Vol. 168, 360–366.

[186] Tveergaard, V.; Needleman A. [1984]: "Analysis of the cup-cone fracture in a round tensile bar", *Acta Metall.*, Vol. 32, 157–169.

[187] VAZ JR., M.; OWEN, D. R. J. [2001]: "Aspects of ductile fracture and adaptive mesh refinement in damaged elasto-plastic materials", *International Journal for Numerical Methods in Engineering*, Vol. 50, 29–54.

[188] VENKATA REDDY, N.; DIXIT, P. M.; LAL, G. K. [2000]: "Ductile fracture criteria and its prediction in axisymmetric drawing", *International Journal of Machine Tools and Manufacture Design, Research and Application*, Vol. 40, 95–111.

[189] VOYIADJIS, G. Z.; ABU AL-RUB, R. K.; PALAZOTTO, A. N. [2004]: "Thermodynamic formulations for non-local coupling of viscoplasticity and anisotropic viscodamage for dynamic localization problems using gradient theory", *International Journal of Plasticity*, Vol. 20, 981–1038.

[190] VOYIADJIS, G. Z.; DORGAN, R. K. [2007]: "Framework using functional forms of hardening internal state variables in modeling elasto-plastic-damage behavior", *International Journal of Plasticity*, Vol. 20, 981–1038.

[191] WAGENER, H. W.; HAATS, J.; WOLF, J. [1992]: "Increase of workability of brittle materials by cold extrusion", *Journal of Materials Processing Technology*, Vol. 32, 451–460.

[192] WAGENER, H. W.; WOLF, J. [1993]: "Cold forging of MMCs of aluminium alloy matrix", *Journal of Materials Processing Technology*, Vol. 37, 253–265.

[193] WAGENER, H. W.; HAATS, J. [1995]: "Crack prevention and increase of workability of brittle materials by cold extrusion", *in: Material Processing Defects, Elsevier Science B. V.*, pp. 373–385.

[194] WALLIN, M.; RISTINMAA, M. [2007]: "An alternative method for the integration of continuum damage evolution laws", *Computational Mechanics*, Vol. 41, 347–359.

[195] WANG, W. M.; SLUYS, L. J.; DE BORST, R. [1997]: "Viscoplasticity for instabilities due to strain softening and strain-rate softening", *International Journal of Numerical Methods in Engineering*, Vol. 40, 3839–3864.

[196] WEBER, G.; ANAND, L. [1990]: "Finite deformation constitutive equations and a time integration procedure for isotropic, hyperelastic-viscoplastic solids", *Computer Methods in Applied Mechanics and Engineering*, Vol. 79, 173–202.

[197] WERTHEIMER, T. B. [1982]: *Problems in Large Deformation Elasto-plastic Analysis Using the Finite Element Method*, PhD thesis, Standord University.

[198] WRIGGERS, P.; MIEHE, CH.; KLEIBER, C.; SIMÓ, J. C. [1992]: "On the coupled thermodynamic treatment of necking problems via finite element methods", *International Journal for Numerical Methods in Engineering*, Vol. 33, 869–883.

[199] ZHU, Y. Y.; CESCETTO, S. [1995]: "A fully coupled elasto-visco-plastic damage theory for anisotroic materials", *International Journal of Solids and Structures*, Vol. 32, 1607–1641.

[200] ZIMERMAN, Z.; AVITZUR, B. [1970]: "Analysis of central bursting defects in extrusion and wire drawing", *J. Eng. Ind.*, Vol. 90, 135–145.

[201] ZIMERMAN, Z.; DARLINGTON, H.; KOTTCAMP, E. H. [1971]: "Selection of operating parameters to prevent central bursting defects during cold extrusion", In: HOFFMANNER, A.L. (Eds.), Metal Forming - Interrelations between Theory and Practice Plenum Press, New York-London, 47–62.

APPENDIX A

EXPONENTIAL MAPPING

Let y be a function of time, and take a linear ODE in the standard form as,

$$\frac{dy}{dt} + p(t)\,y = q(t).$$

(A.1)

Specify an IVP as a combination of the given ODE with $q(t) = 0$ and an initial value defined at time $t = 0$,

$$\frac{dy}{dt} + p(t)\,y = 0, \qquad \text{where} \quad y(0) = y^{tri}.$$

(A.2)

The solution of the ODE is to be found by applying an integrating factor of $\exp[\int p(t)dt]$ and multiplying both sides following form is carried out,

$$\begin{aligned}
0 &= \exp[\int p(t)dt]\,\frac{dy}{dt} + \exp[\int p(t)dt]\,p(t)\,y \\
&= \exp[\int p(t)dt]\,\frac{dy}{dt} + \frac{d}{dt}\left[\exp[\int p(t)dt]\right]y \\
&= \frac{d}{dt}\left[\exp[\int p(t)dt]\,y\right].
\end{aligned}$$

(A.3)

Integrating both sides will yield,

$$\exp[\int p(t)dt]\,y = C,$$

(A.4)

where C is the constant of integration and will trivially be found using the following form,

$$\exp[\int_0^t p(t)dt]\,y(t) = C,$$

(A.5)

and specifying for $t = 0$ by substituting $y(0) = y^{tri}$

$$\begin{aligned}
C &= \exp[\int_0^0 p(t)dt]\,y(0) \\
&= \exp[0]\,y^{tri} \\
&= y^{tri}.
\end{aligned}$$

(A.6)

Substituting the final form in A.4 we find the solution as

$$y(t) = \exp\left[-\int p(t)dt\right] y^{tri}. \tag{A.7}$$

Using $\int p(t)dt \approx p(t)\Delta t$ for a typical time step Δt, we can finalize the integration by exponential mapping as follows,

$$y(\Delta t) = \exp\left[-p(t)\Delta t\right] y^{tri}. \tag{A.8}$$

If the ODE is defined in a nonconventional setting as commonly seen in rate definitions as,

$$\frac{dy}{dt} = r(t)\, y, \tag{A.9}$$

then the solution will require a simple sign change which may seem to be a minor modification however drastically changes the picture if mistakenly handled,

$$y(\Delta t) = \exp[r(t)\Delta t].\, y^{tri} \tag{A.10}$$

APPENDIX B

ABAQUS IMPLEMENTATION

Current framework is implemented into `UMAT` and `UMATH` subroutines for ABAQUS. A detailed representation of implementation conventions can be found in [1]. For the thermo-mechanical resolution of the problem, the derived staggered approach stands for the `SEPERATE` solution flag in ABAQUS. For the mechanical problem update of stresses, `STRESS`, and material tangent matrix, `DDSDDE`, is crucial. For the thermal problem, definitions of the mechanical dissipation, `RPL`, and the thermal tangent, `DRPLDT`, suffice. These definitions are supplied with appropriate update of state variables which monitor the irreversible micro-structural processes. Below, mapping is supplied among already derived expressions and ABAQUS subroutine variables.

For continuum elements ABAQUS requires JAUMANN rate form for stress integrations, for which the proper material tangent matrix `DDSDDE` should be introduced. In the above derived forms, the consistent material tangent supports the OLDROYD rate of the KIRCHHOFF stress. Accordingly a modification is required for the currently derived OLDROYD type tangent, $\mathbf{c}_{MM}$, to reach the JAUMANN type operator, $\overset{\triangledown}{\mathbf{c}}_{MM}$, in order to supply compatibility. Table B.1 gives this conversion where $\overset{\circ}{\boldsymbol{\tau}}$ and $\overset{\triangledown}{\boldsymbol{\tau}}$ stand for the objective OLDROYD and JAUMANN rates of the KIRCHHOFF stress tensor respectively,

Table B.1: Objective rates expressions and related constitutive tensor transformations.

Objective Rate	Explicit Form	Material Tangent Moduli
$\overset{\circ}{\boldsymbol{\tau}} := \mathbf{c}_{MM} : \mathbf{d} \rightsquigarrow$	$\dot{\boldsymbol{\tau}} - \boldsymbol{\tau} \bullet \mathbf{l}^t - \mathbf{l} \bullet \boldsymbol{\tau}$	$[\mathbf{c}_{MM}]_{ijkl}$
$\overset{\triangledown}{\boldsymbol{\tau}} := \overset{\triangledown}{\mathbf{c}}_{MM} : \mathbf{d} \rightsquigarrow$	$\dot{\boldsymbol{\tau}} - \boldsymbol{\tau} \bullet \mathbf{w} - \mathbf{w} \bullet \boldsymbol{\tau}$	$[\overset{\triangledown}{\mathbf{c}}_{MM}]_{ijkl} = [\mathbf{c}_{MM}]_{ijkl} + [\boldsymbol{\tau}]_{ik}[\mathbf{1}]_{jl} + [\mathbf{1}]_{ik}[\boldsymbol{\tau}]_{lj}$

Final attempt should be applied to the standard arguments to gather the matrix form for `DDSDDE` from the tensorial expression $\overset{\triangledown}{\mathbf{c}}_{MM}$.

For the thermal part of the problem, `RPL` stands for the mechanical dissipation, Ω^{mech}. `DRPLDT` is c_{TT} indeed. Through `UMATH` the linear FOURIER heat conduction with damage deterioration is implemented.

APPENDIX C

AUXILIARY DERIVATIONS

C.1 Isothermal Conditions

C.1.1 Local Tangent

Components for the local Jacobian, for the simultaneous local integration scheme, can be given as,

$$\frac{\partial r_{1,n+1}}{\partial \Delta\gamma} = \frac{2}{3} K''(\alpha_{n+1}) + 2\mu \frac{1}{(1 - D_{n+1})}, \tag{C.1}$$

$$\frac{\partial r_{1,n+1}}{\partial D_{n+1}} = 2\mu \frac{\Delta\gamma}{(1 - D_{n+1})^2}, \tag{C.2}$$

$$\frac{\partial r_{2,n+1}}{\partial \Delta\gamma} = -g_{n+1} - \Delta\gamma \frac{g_{n+1}}{\partial \Delta\gamma}, \tag{C.3}$$

$$\frac{\partial r_{2,n+1}}{\partial D_{n+1}} = 1 - \Delta\gamma \frac{g_{n+1}}{\partial D_{n+1}}, \tag{C.4}$$

where $K''(\alpha) = \partial^2 K(\alpha)/\partial \alpha^2$.

C.1.2 Global Tangent

Derivations required for the global tangent are,

$$\frac{\partial r_{1,n+1}}{\partial \epsilon_{n+1,B}^{tri}} = -2\mu \, n_{n+1,B}, \tag{C.5}$$

$$\frac{\partial r_{2,n+1}}{\partial \epsilon_{n+1,B}^{tri}} = -\Delta\gamma \frac{\partial g_{n+1}}{\partial \epsilon_{n+1,B}^{tri}}. \tag{C.6}$$

For a general damage rate form, $g = g(Y_{n+1}; \alpha_{n+1}, D_{n+1})$. In the current setting one may use $g = g(Y_{n+1}(\epsilon_{n+1,A}^{tri}; \Delta\gamma, D_{n+1}), \Delta\gamma, D_{n+1})$, together with chain rule of

differentiation, to reach the following expressions,

$$\frac{\partial g_{n+1}}{\partial \epsilon_{n+1,B}^{tri}} = g'_{n+1} \frac{\partial Y_{n+1}}{\partial \epsilon_{n+1,B}^{tri}}, \tag{C.7}$$

$$\frac{\partial g_{n+1}}{\partial \Delta\gamma} = \frac{\partial g_{n+1}}{\partial \Delta\gamma} + g'_{n+1} \frac{\partial Y_{n+1}}{\partial \Delta\gamma}, \tag{C.8}$$

$$\frac{\partial g_{n+1}}{\partial D_{n+1}} = \frac{\partial g_{n+1}}{\partial D_{n+1}} + g'_{n+1} \frac{\partial Y_{n+1}}{\partial D_{n+1}}, \tag{C.9}$$

where, $g' = \partial g / \partial Y_{n+1}$. Derivations of the following partial differentials are also required,

$$\frac{\partial \tilde{\tau}_{n+1,A}}{\partial \epsilon_{n+1,B}^{tri}} = H + 2\mu\,\delta_{AB}^{dev} - 2\mu\left\{\frac{\Delta\gamma}{(1-D_{n+1})}\frac{2\mu}{\left\|\tilde{s}_{n+1}^{tri}\right\|}\left[\delta_{AB}^{dev}\right.\right. \tag{C.10}$$
$$\left.\left.-n_{n+1,A}\,n_{n+1,B}\right]\right\}$$

$$\frac{\partial \tilde{\tau}_{n+1,A}}{\partial \Delta\gamma} = -2\mu\frac{1}{(1-D_{n+1})}n_{n+1,A}, \tag{C.11}$$

$$\frac{\partial \tilde{\tau}_{n+1,A}}{\partial D_{n+1}} = -2\mu\frac{\Delta\gamma}{(1-D_{n+1})^2}n_{n+1,A}. \tag{C.12}$$

C.1.3   Derivations for, $Y = Y^{d,+}$

In the present context, the specific damage conjugate variable is selected as the thermodynamically consistent one with the crack closure effect, given in (2.29). Hence any of the following,

$$\frac{\partial Y_{n+1}^{d,+}}{\partial \epsilon_{n+1,B}^{tri}}, \; \frac{\partial Y_{n+1}^{d,+}}{\partial \Delta\gamma}, \; \frac{\partial Y_{n+1}^{d,+}}{\partial D_{n+1}}, \tag{C.13}$$

will exploit the chain rule as follows,

$$\frac{\partial Y_{n+1}^{d,+}}{\partial(\bullet)} = \sum_{A=1}^{3} \frac{\partial Y_{n+1}^{d,+}}{\partial \tilde{\tau}_{n+1,A}}\frac{\partial \tilde{\tau}_{n+1,A}}{\partial(\bullet)}, \tag{C.14}$$

where $(\bullet)$ represents one of $\epsilon_{n+1,B}^{tri}$, $\Delta\gamma$ or D_{n+1}. Accordingly one may derive the following,

$$\frac{\partial Y_{n+1}^{d,+}}{\partial \tilde{\tau}_{n+1,A}} = \frac{(1+\nu)}{E}\langle\tilde{\tau}_{n+1,A}\rangle - \frac{3\nu}{E}\langle\tilde{p}\rangle + h\frac{(1+\nu)}{E}\langle-\tilde{\tau}_{n+1,A}\rangle - h\frac{3\nu}{E}\langle-\tilde{p}\rangle, \tag{C.15}$$

which concludes the formulations.

C.1.4 Kinematic Hardening

Analogical to the rate expression for the left CAUCHY-GREEN deformation tensor,

$$
\begin{aligned}
\partial_t \mathbf{b}^e &= \partial_t \mathbf{F} \bullet \mathbf{G}^p \bullet \mathbf{F}^t + \mathbf{F} \bullet \partial_t \mathbf{G}^p \bullet \mathbf{F}^t + \mathbf{F} \bullet \mathbf{G}^p \bullet \partial_t \mathbf{F}^t \\
&= \partial_t \mathbf{F} \bullet \mathbf{F}^{-1} \bullet \mathbf{F} \bullet \mathbf{G}^p \bullet \mathbf{F}^t + \mathbf{F} \bullet \partial_t \mathbf{G}^p \bullet \mathbf{F}^t + \mathbf{F} \bullet \mathbf{G}^p \bullet \mathbf{F}^t \bullet \mathbf{F}^{-t} \bullet \partial_t \mathbf{F}^t \\
&= \mathbf{l} \bullet \mathbf{b}^e + \mathbf{F} \bullet \partial_t \mathbf{G}^p \bullet \mathbf{F}^t + \mathbf{b}^e \bullet \mathbf{l}^t.
\end{aligned} \tag{C.16}
$$

one can construct the rate expression for the strain like expression responsible for the kinematic hardening,

$$
\begin{aligned}
\partial_t \mathbf{z} &= \partial_t \mathbf{F} \bullet \mathbf{\Xi} \bullet \mathbf{F}^t + \mathbf{F} \bullet \partial_t \mathbf{\Xi} \bullet \mathbf{F}^t + \mathbf{F} \bullet \mathbf{\Xi} \bullet \partial_t \mathbf{F}^t \\
&= \partial_t \mathbf{F} \bullet \mathbf{F}^{-1} \bullet \mathbf{F} \bullet \mathbf{\Xi} \bullet \mathbf{F}^t + \mathbf{F} \bullet \partial_t \mathbf{\Xi} \bullet \mathbf{F}^t + \mathbf{F} \bullet \mathbf{\Xi} \bullet \mathbf{F}^t \bullet \mathbf{F}^{-t} \bullet \partial_t \mathbf{F}^t \\
&= \mathbf{l} \bullet \mathbf{z} + \mathbf{F} \bullet \partial_t \mathbf{\Xi} \bullet \mathbf{F}^t + z \bullet \mathbf{l}^t.
\end{aligned} \tag{C.17}
$$

This parallelism in between derivations can be captured for the LAGRANGEAN dissipation expressions. Accordingly for plastic dissipation one has,

$$
\begin{aligned}
\mathbf{S} : \frac{1}{2} \mathbf{C} \bullet \partial_t \mathbf{G}^p \bullet \mathbf{G}^{p,-1} &= \left[\mathbf{F}^{-1} \bullet \boldsymbol{\tau} \bullet \mathbf{F}^{-t} \right] : \frac{1}{2} \left[\mathbf{F}^t \bullet \mathbf{F} \right] \bullet \left[\mathbf{F}^{-1} \bullet \mathcal{L}_v \mathbf{b}^e \right. \\
&\quad \left. \bullet \mathbf{F}^{-t} \right] \bullet \left[\mathbf{F}^{-1} \bullet \mathbf{b}^e \bullet \mathbf{F}^{-t} \right]^{-1} \\
&= \mathbf{F}^{-1} \bullet \boldsymbol{\tau} \bullet \mathbf{F}^{-t} : \frac{1}{2} \mathbf{F}^t \bullet \underbrace{\mathbf{F} \bullet \mathbf{F}^{-1}}_{= \mathbf{I}} \bullet \mathcal{L}_v \mathbf{b}^e \\
&\quad \bullet \underbrace{\mathbf{F}^{-t} \bullet \mathbf{F}^t}_{= \mathbf{I}} \bullet \mathbf{b}^{e,-1} \bullet \mathbf{F} \\
&= \mathbf{F}^{-1} \bullet \boldsymbol{\tau} \bullet \mathbf{F}^{-t} : \frac{1}{2} \mathbf{F}^t \bullet \mathcal{L}_v \mathbf{b}^e \bullet \mathbf{b}^{e,-1} \bullet \mathbf{F} \\
&= \mathrm{tr} \left[\mathbf{F}^{-1} \bullet \boldsymbol{\tau} \bullet \mathbf{F}^{-t} \bullet \frac{1}{2} \mathbf{F}^t \bullet \mathcal{L}_v \mathbf{b}^e \bullet \mathbf{b}^{e,-1} \bullet \mathbf{F} \right] \\
&= \mathrm{tr} \left[\mathbf{F}^{-1} \bullet \boldsymbol{\tau} \bullet \frac{1}{2} \underbrace{\mathbf{F}^{-t} \bullet \mathbf{F}^t}_{= \mathbf{I}} \bullet \mathcal{L}_v \mathbf{b}^e \bullet \mathbf{b}^{e,-1} \bullet \mathbf{F} \right] \\
&= \mathrm{tr} \left[\boldsymbol{\tau} \bullet \frac{1}{2} \mathcal{L}_v \mathbf{b}^e \bullet \mathbf{b}^{e,-1} \right] \\
&= \boldsymbol{\tau} : \left[-\frac{1}{2} \mathcal{L}_v \mathbf{b}^e \bullet \mathbf{b}^{e,-1} \right],
\end{aligned} \tag{C.18}
$$

whereas for the kinematic hardening counterpart one has,

$$
\begin{aligned}
\mathbf{A} : \frac{1}{2}\mathbf{C} \bullet \partial_t \mathbf{\Xi} \bullet \mathbf{\Xi}^{-1} &= \left[\mathbf{F}^{-1} \bullet \boldsymbol{\beta} \bullet \mathbf{F}^{-t}\right] : \frac{1}{2}\left[\mathbf{F}^t \bullet \mathbf{F}\right] \bullet \left[\mathbf{F}^{-1} \bullet \pounds_v \mathbf{z}\right. \\
&\qquad \left. \bullet \mathbf{F}^{-t}\right] \bullet \left[\mathbf{F}^{-1} \bullet \mathbf{z} \bullet \mathbf{F}^{-t}\right]^{-1} \\
&= \mathbf{F}^{-1} \bullet \boldsymbol{\beta} \bullet \mathbf{F}^{-t} : \frac{1}{2}\mathbf{F}^t \bullet \underbrace{\mathbf{F} \bullet \mathbf{F}^{-1}}_{=\mathbf{I}} \bullet \pounds_v \mathbf{z} \\
&\qquad \bullet \underbrace{\mathbf{F}^{-t} \bullet \mathbf{F}^t}_{=\mathbf{I}} \bullet \mathbf{z}^{-1} \bullet \mathbf{F} \\
&= \mathbf{F}^{-1} \bullet \boldsymbol{\beta} \bullet \mathbf{F}^{-t} : \frac{1}{2}\mathbf{F}^t \bullet \pounds_v \mathbf{z} \bullet \mathbf{z}^{-1} \bullet \mathbf{F} \\
&= \operatorname{tr}\left[\mathbf{F}^{-1} \bullet \boldsymbol{\beta} \bullet \mathbf{F}^{-t} \bullet \frac{1}{2}\mathbf{F}^t \bullet \pounds_v \mathbf{z} \bullet \mathbf{z}^{-1} \bullet \mathbf{F}\right] \\
&= \operatorname{tr}\left[\mathbf{F}^{-1} \bullet \boldsymbol{\beta} \bullet \frac{1}{2}\underbrace{\mathbf{F}^{-t} \bullet \mathbf{F}^t}_{=\mathbf{I}} \bullet \pounds_v \mathbf{z} \bullet \mathbf{z}^{-1} \bullet \mathbf{F}\right] \\
&= \operatorname{tr}\left[\boldsymbol{\beta} \bullet \frac{1}{2}\pounds_v \mathbf{z} \bullet \mathbf{z}^{-1}\right] \\
&= \boldsymbol{\beta} : \left[-\frac{1}{2}\pounds_v \mathbf{z} \bullet \mathbf{z}^{-1}\right].
\end{aligned}
\tag{C.19}
$$

C.2 Thermo-coupled Conditions

C.2.1 Mechanical Tangent Moduli

For a given principal stress component, $\tau_{n+1,\,A}$, one has,

$$
\frac{\partial \tau_{n+1,\,A}}{\partial \epsilon_{n+1,\,B}^{e,\,tri}} = (1 - D_{n+1})\frac{\partial \tau_{n+1,\,A}^{tri}}{\partial \epsilon_{n+1,\,B}^{e,\,tri}} - 2\mu\Delta\gamma\,\frac{\partial n_{n+1,\,A}}{\partial \epsilon_{n+1,\,B}^{e,\,tri}}, \tag{C.20}
$$

$$
\frac{\partial \tau_{n+1,\,A}}{\partial \Delta\gamma} = -2\mu\,n_{n+1,\,A}, \tag{C.21}
$$

$$
\frac{\partial \tau_{n+1,\,A}}{\partial D_{n+1}} = -\tau_{n+1,\,A}^{tri}. \tag{C.22}
$$

Using $\delta_{AB}^{dev} = \delta_{AB} - \frac{1}{3}$, with δ_{AB} representing the KRONECKER delta which is given as,

$$
\delta_{AB} = \begin{cases} 1, & \text{if } A = B; \\ 0, & \text{otherwise.} \end{cases} \tag{C.23}
$$

Accordingly one can find,

$$
\frac{\partial \tau_{n+1,\,A}^{tri}}{\partial \epsilon_{n+1,\,B}^{tri}} = H\left[1 - 3\,\alpha^t(\theta - \theta_0)\frac{\log[J^e] - 2}{J^e}\right] + 2\mu\delta_{AB}^{dev}, \tag{C.24}
$$

$$
\frac{\partial n_{n+1,\,A}}{\partial \epsilon_{n+1,\,B}^{tri}} = \frac{2\mu}{\|\tilde{\mathbf{s}}_{n+1}^{tri}\|}\left[\delta_{AB}^{dev} - n_{n+1,\,A}\,n_{n+1,\,B}\right]. \tag{C.25}
$$

179

C.2.2   Thermal Tangent Modulus

In the view of (3.92), for a given inelastic dissipation, Ω_{n+1}^{mech}, one has,

$$\frac{\partial \Omega_{n+1}^{mech}}{\partial \theta_{n+1}} = \frac{\Delta\gamma}{\Delta t}\left[\sqrt{\frac{2}{3}}\tau_0'(\theta_{n+1}) + \kappa a'(\theta_{n+1})\right] + \frac{\partial \Omega_{n+1}^{mech}}{\partial Y_{n+1}^d}\frac{\partial Y_{n+1}^d}{\partial \theta_{n+1}}, \qquad (C.26)$$

$$\frac{\partial \Omega_{n+1}^{mech}}{\partial \Delta\gamma} = \frac{1}{\Delta t}\left[\sqrt{\frac{2}{3}}\tau_0(\theta_{n+1}) + \kappa a(\theta_{n+1})\right] + \frac{\partial \Omega_{n+1}^{mech}}{\partial Y_{n+1}^d}\frac{\partial Y_{n+1}^d}{\partial \Delta\gamma}, \qquad (C.27)$$

$$\frac{\partial \Omega_{n+1}^{mech}}{\partial D_{n+1}} = \kappa\frac{\Delta\gamma}{\Delta t}\frac{a(\theta_{n+1})}{(1-D_{n+1})} + \frac{\partial \Omega_{n+1}^{mech}}{\partial Y_{n+1}^d}\frac{\partial Y_{n+1}^d}{\partial D_{n+1}}, \qquad (C.28)$$

with

$$\kappa = \frac{1}{(1-D_{n+1})}\left[\frac{Y_{n+1}^d}{a(\theta_{n+1})}\right]^{s+1}, \qquad (C.29)$$

$$\frac{\partial \Omega_{n+1}^{mech}}{\partial Y_{n+1}^d} = \frac{\Delta\gamma}{\Delta t}\frac{(s+1)}{(1-D_{n+1})}\left[\frac{Y_{n+1}^d}{a(\theta_{n+1})}\right]^{s}, \qquad (C.30)$$

and $\tau_0'(\theta_{n+1}) = -w_0\tau_0(\theta_0)$, and $a'(\theta_{n+1}) = -w_d a(\theta_0)$. For the local tangent, additional derivations include the following,

$$\frac{\partial r_{1,n+1}}{\partial \theta_{n+1}} = \sqrt{\frac{2}{3}}\left[\tau_0'(\theta_{n+1}) + \frac{\partial K_{n+1}'}{\partial \theta_{n+1}}\right], \qquad (C.31)$$

$$\frac{\partial r_{2,n+1}}{\partial \theta_{n+1}} = -\Delta\gamma s\frac{1}{(1-D_{n+1})}\frac{a'(\theta_{n+1})}{a(\theta_{n+1})}\left[\frac{Y_{n+1}^d}{a(\theta_{n+1})}\right]^{s} + \frac{\partial r_{2,n+1}}{\partial Y_{n+1}^d}\frac{\partial Y_{n+1}^d}{\theta_{n+1}}, \quad (C.32)$$

and

$$\frac{\partial Y_{n+1}^d}{\theta_{n+1}} = \frac{\partial \tilde{\Psi}^{td}(J_{n+1}^e, \theta_{n+1})}{\partial \theta_{n+1}} = -3\,H\,\alpha^t\frac{\log[J^e]}{J^e}. \qquad (C.33)$$

C.2.3   Rate of Inelastic Entropies

In view of the given dissipation potentials, $\tilde{\phi}$ and ϕ^d, one has,

$$\frac{\partial \tilde{\phi}}{\partial \theta} = -\sqrt{\frac{2}{3}}\frac{\partial y(q,\theta)}{\partial \theta}, \qquad (C.34)$$

$$\frac{\partial \phi^d}{\partial \theta} = \left.\frac{\partial \phi^d}{\partial \theta}\right|_{Y^d} + \frac{\partial \phi^d}{\partial Y^d}\frac{\partial Y^d}{\partial \theta} \qquad (C.35)$$

$$= \frac{\omega_d a(\theta_0)}{(1-D)}\left[\frac{Y^d}{a(\theta)}\right]^{s+1} + \frac{1}{(1-D)}\left[\frac{Y^d}{a(\theta)}\right]^{s}\frac{\partial Y^d}{\partial \theta},$$

where,

$$\frac{\partial y(q,\theta)}{\partial \theta} = \frac{\partial}{\partial \theta}[\tau_0(\theta) - q(\alpha,\theta)] = -\left[\omega_0\tau_0(\theta_0) - \omega_h q(\alpha,\theta_0)\right], \qquad (C.36)$$

and

$$\frac{\partial Y^d}{\partial \theta} = \frac{\partial \tilde{\Psi}^{td}}{\partial \theta} = -3 \, H \, \alpha^t \frac{\log[J^e]}{J^e}, \tag{C.37}$$

Accordingly following time rate of change of the plastic entropy is carried out,

$$\frac{\partial \eta^p}{\partial t} = \dot{\gamma}^{\,vp} \sqrt{\frac{2}{3}} \left[\omega_0 \tau_0(\theta_0) - \omega_h q(\alpha, \theta_0) \right], \tag{C.38}$$

which is identical to [162]. The growth of the inelastic entropy associated with damage is,

$$\frac{\partial \eta^d}{\partial t} = \frac{\omega_d a(\theta_0)}{(1-D)} \left[\frac{Y^d}{a(\theta)} \right]^{s+1} - 3 \, H \, \alpha^t \frac{1}{(1-D)} \left[\frac{Y^d}{a(\theta)} \right]^s \frac{\log[J^e]}{J^e}. \tag{C.39}$$

C.2.4 Plastic Dissipation

Using the proposed von Mises yield potential, one may derive the following equivalence for the plastic portion of the dissipation expression,

$$\begin{aligned}
\Omega^{mech,p} &= \boldsymbol{\tau} : \underbrace{\left[-\frac{1}{2} \pounds_v \mathbf{b}^e \bullet \mathbf{b}^{e,-1} \right]}_{\dot{\gamma} \frac{\partial \tilde{\phi}}{\partial \tilde{\tau}}} + q \underbrace{\frac{\partial \alpha}{\partial t}}_{\dot{\gamma} \frac{\partial \tilde{\phi}}{\partial q}} \tag{C.40} \\
&= \boldsymbol{\tau} : \left[\frac{\dot{\gamma}}{(1-D)} \frac{\tilde{\mathbf{s}}}{\|\tilde{\mathbf{s}}\|} \right] + q(\alpha, \theta) \left[\sqrt{\frac{2}{3}} \dot{\gamma}^{vp} \right] \\
&= \dot{\gamma}^{vp} \|\tilde{\mathbf{s}}\| + \sqrt{\frac{2}{3}} \dot{\gamma}^{vp} q(\alpha, \theta) \\
&= \dot{\gamma}^{vp} \sqrt{\frac{2}{3}} \tau_0(\theta),
\end{aligned}$$

with $\dot{\gamma}^{vp} \tilde{\phi} = 0$ also $\tilde{\boldsymbol{\tau}} = \boldsymbol{\tau}/(1-D)$, $\tilde{\boldsymbol{\tau}} = \tilde{p}\mathbf{1} + \tilde{\mathbf{s}}$ and $\tilde{p}\mathbf{1} : \tilde{\mathbf{s}} = \mathbf{0}$, and consequently $[\boldsymbol{\tau}/(1-D)] : \tilde{\mathbf{s}} = \tilde{\mathbf{s}} : \tilde{\mathbf{s}} = \|\tilde{\mathbf{s}}\|^2$.

C.2.5 Thermal State

For the given potentials $\Psi^{td}(J^e, \theta)$ and $\Psi^t(\theta)$, one may derive the following expressions,

$$\frac{\partial \tilde{\Psi}^{td}(J^e_{n+1}, \theta_{n+1})}{\partial \theta_{n+1}} = -3 \, H \alpha^t \frac{\log[J^e]}{J^e}, \tag{C.41}$$

$$\frac{\partial \Psi^t(\theta_{n+1})}{\partial \theta_{n+1}} = -C_v \log \left[\frac{\theta}{\theta_0} \right]. \tag{C.42}$$

VITA

PERSONAL INFORMATION

Surname, Name: Soyarslan, Celal

Nationality: Turkish (TC)

Date and Place of Birth: 7 December 1977 , Elazığ

Marital Status: Single

Phone: +90 312 586 83 52

Fax: +90 312 586 80 91

email: csoyarslan@atilim.edu.tr

EDUCATION

Degree	Institution	Year of Graduation
MS	METU, Civil Eng.	2002
BS	METU, Civil Eng.	2000
High School	Yalova High School, Yalova	1995

WORK EXPERIENCE

Year	Place	Enrollment
2006-Present	Atılım Univ., Manuf. Eng.	Instructor
2000-2006	METU, Civil Eng.	Research Assistant

FOREIGN LANGUAGES

Advanced English, Intermediate German.

PUBLICATIONS

1. SOYARSLAN, C.; TEKKAYA, A. E.; AKYUZ, U. [2008]: "Application of Continuum Damage Mechanics in discontinuous crack formation: Forward extrusion chevron predictions", *Journal of Applied Mathematics and Mechanics / Zeitschrift für Angewandte Mathematik und Mechanik*, Vol. 88, 436–453.

HOBBIES

Reading, Programming, Running, Movies.